Université du Québec
Institut National de la Recherche Scientifique
Centre Énergie, Matériaux et Télécommunications

Heterostructure Nanomaterials for Efficient Photoelectrochemical Devices

Par

Faying Li

Thèse présentée pour l'obtention du grade
De Philosophiae Doctor (Ph.D.)
en sciences de l'énergie et des matériaux

Jury d'évaluation

Président du jury et examinateur interne	Prof. Shuhui Sun INRS-EMT, Université du Québec
Examinateur externe	Prof. Mohamed Siaj Université du Québec à Montréal
Examinateur externe	Prof. Paolo Fornasiero University of Trieste
Directeur de recherche	Prof. Federico Rosei INRS-EMT, Université du Québec
Codirecteur de recherche	Prof. Qin Wei University of Jinan, China

ACKNOWLEDGEMENTS

I am honored to accomplish my Ph.D. program at Institut National de la Recherche Scientifique, Énergie Matériaux Télécommunications (INRS-EMT), University of Québec, Varennes, Canada. First, I would like to express my deepest and most sincere gratitude to my supervisor, Prof. Federico Rosei, for his patient guidance and support during my Ph.D. studies and research. In scientific research, Prof. Rosei not only provided me with systematic guidance and inspiration but also provided me with the required and unique research environment for my research project. In addition, he has always been a strong supporter and friend when I need help. It is the most valuable experience in my life to be able to study under his guidance.

Meanwhile, I would like to express my sincere thanks to my co-supervisor Prof. Qin Wei from the University of Jinan, China, for giving me invaluable suggestions and encouragement.

Besides my supervisors, I would like to acknowledge my sub-group leader Dr. Daniele Benetti. His endless effort in improving the quality of my research project by giving me some novel ideas makes me explore a fascinating scientific field.

I would like to thank Prof. Andreas Ruediger and Prof. Sergei Manzhos for working early on my doctoral examination. They gave me a lot of inspiration for my groundwork. I would like to thank all the staff at INRS-EMT, especially Dr. Christophe Chabanier for his work on X-ray diffraction, X-ray photoelectron spectroscopy, and ultraviolet photoelectron spectroscopy.

I am grateful to all the group members from Nano-FemtoLAB and other collaborators for their support and help throughout my Ph.D. work. I feel lucky to be part of such a hardworking supportive and inspiring group with postdoctoral fellows and graduate students, including Dr. Lei Jin, Dr. Lucas V. Besteiro, Dr. Gurpreet S.Selopal, Dr. Chao Wang, Dr. Xin Tong, Dr. Yufeng Zhou, Dr. Wei Huang, Dr. Hui Zhang, Dr. Kanghong Wang, Dr. Tingzhou Yang, Li Shi, Xin Liu, Jiabin Liu, Na Xu, Omar Abdelkarim, et al. In addition, I wish to acknowledge the scholarships from CSC and the Fonds de recherche du Québec Nature et Technologies (FRQNT) for supporting my Ph.D. study.

Last but not least, I am grateful to my beloved parents Guorong Zhang and Yipei Li, my wife Min Zhang, and My baby Zitong Li for their unconditional love, support, and encouragement, which are important parts of my study life abroad. I wish to thank my other family members and friends for their continuous love and heartfelt support.

RÉSUMÉ

La production d'hydrogène solaire photoélectrochimique (PEC) est une voie prometteuse pour convertir l'énergie solaire en énergie chimique en utilisant des semi-conducteurs comme matériaux actifs. Dans le processus de fractionnement de l'eau PEC, l'efficacité de conversion de l'énergie solaire en énergie hydrogène est principalement déterminée par l'absorption de la lumière des photocatalyseurs, la séparation et la migration des porteurs photogénérés et la catalyse de surface. Cependant, les performances sont encore loin d'être satisfaisantes en raison d'une plage d'absorption limitée et d'une recombinaison de charge rapide. Par conséquent, l'élargissement efficace de la plage spectrale d'absorption des photocatalyseurs et la suppression de la recombinaison de charge des paires électron-trou photogénérées sont deux moyens importants d'améliorer l'efficacité de conversion photoélectrique des matériaux semi-conducteurs à base de PEC. Par rapport aux photocatalyseurs à composant unique, les photocatalyseurs à hétérostructure qui combinent au moins deux matériaux fonctionnels dans un système ont reçu plus d'attention au cours de la dernière décennie grâce à l'effet synergique. Cette thèse explore comment les matériaux semi-conducteurs hétérostructurés interagissent les uns avec les autres, et comment des propriétés telles que la gestion de la lumière et l'injection de charge peuvent être contrôlées en modulant de manière appropriée les interfaces des nanomatériaux pour améliorer les performances du dispositif PEC. Les points quantiques à zéro dimension (0D QD) ont été reconnus comme l'un des photosensibilisateurs les plus prometteurs pour la fabrication de photoélectrodes, grâce à leurs propriétés optiques uniques et évolutives où l'absorption et la photoluminescence des QD sont réglables en composition et en taille, étendant la plage d'absorption de l'ultraviolet au visible et aussi au proche infrarouge (UV-VIS-NIR). De plus, étant donné que la structure en couches bidimensionnelle (2D) est bénéfique pour raccourcir le temps et la distance de transport de charge, les hétérojonctions basées sur des matériaux 2D peuvent présenter une séparation et un transfert de charge plus efficaces.

L'hétérostructure à base d'interfaces 0D/2D est particulièrement intéressante du fait de la possibilité de construire facilement des interfaces intimes, qui peuvent inhiber la recombinaison des porteurs. J'ai d'abord synthétisé une hétérojonction 0D/2D, qui a été construite par des QD de chalcogénure métallique 0D et des nanofeuillets Zn-MoS_2 2D hiérarchiques (NS). L'effet du PbS, du CdS et de leurs composites core-shell PbS@CdS QDs est analysé en les déposant sur des NS Zn-MoS_2 à l'aide d'un procédé in situ. Cette hétérojonction distinctive peut tirer parti des capacités de collecte de lumière des QD avec les performances catalytiques du Zn-MoS_2. Par rapport à Zn-MoS_2, Zn-MoS_2/PbS et Zn-MoS_2/CdS, l'hétérostructure 0D/2D obtenue basée sur le

composite Zn-MoS_2/PbS@CdS a un photocourant considérablement amélioré. L'effet synergique entre l'hétérojonction 0D/2D, la plage d'absorption étendue des QD et le fort couplage et l'alignement des bandes entre eux conduisent à des performances PEC solaires supérieures. Ce travail peut fournir une nouvelle plate-forme pour construire des nanohybrides 0D/2D multifonctionnels pour des applications optoélectroniques, non limitées aux dispositifs PEC.

De nos jours, la majorité des QD utilisés dans les dispositifs de génération d'hydrogène PEC sont basés sur des matériaux contenant des métaux lourds, tels que Pb et Cd. Malheureusement, l'utilisation de ces matériaux entrave leur potentiel de développement commercial en raison de problèmes de santé et d'environnement. En utilisant une procédure d'échange de cations assistée par modèle, nous avons développé des QD $CuInSe_2$/$(CuInSe_xS_{1-x})_5$/$CuInS_2$ respectueux de l'environnement basés sur une architecture multicouche à gradient, présentant une absorption optique et une photoluminescence (PL) dans le proche infrarouge (NIR).) Propriétés. Les QD NIR sont utilisés comme sensibilisateurs pour le TiO_2 mésoporeux et pour la production d'hydrogène PEC. Basé sur l'architecture à gradient, le dispositif PEC a montré une amélioration de 200 % par rapport aux QD $CuInSe_2$ à cœur simple et de 73 % par rapport à la structure cœur/coquille. L'amélioration est attribuée à un alignement de bande électronique par étapes favorable et à un taux de transfert d'électrons amélioré avec l'incorporation de couches de gradient interfaciales. Ces résultats pourraient ouvrir la voie à la synthèse de QD sans métaux lourds, présentant une large application dans les technologies optoélectroniques émergentes.

Combinez les stratégies mentionnées ci-dessus, une approche d'injection à chaud est utilisée pour synthétiser des QD sans métaux lourds $CuInS_2$ dopés au Zn 0D hautement monodispersés, qui sont ensuite ancrés sur des NS hiérarchiques 2D / 2D MoS_2 / rGO via une méthode facile assistée par sonication pour développer un 0D /Interface d'hétérojonction 2D/2D pour la séparation de l'eau PEC. La structure interfaciale et l'alignement des bandes entre les QD 0D proposés et les NS MoS_2/rGO 2D/2D sont conçus en modulant le rapport molaire Zn pendant la synthèse des QD. Les positions des bandes d'énergie des points quantiques après dopage sont étudiées et discutées en détail. Comme preuve de concept, la photoanode 0D/2D/2D optimisée présente une activité PEC presque 5 fois plus élevée que les NS MG/$CuInS_2$ et MoS_2/Zn-$CuInS_2$ en raison de l'absorption de lumière améliorée, de la séparation de charge efficace et de la transmission. On observe que le dopage au Zn et l'introduction de graphène jouent un rôle essentiel dans l'amélioration des performances de l'hétéro-structure proposée, la réduction de la recombinaison des porteurs de charge et l'amélioration de la récolte de la lumière solaire. Ce travail montre comment le contrôle de l'alignement optimal des bandes et de l'additif de carbone

peut faciliter le transfert de charge, permettant le développement de dispositifs PEC hautement efficaces basés sur un nanocomposite à hétérostructure 0D/2D/2D.

Mots-clés: Photoélectrochimique; Fractionnement de l'eau; Séparation des charges; Transmission de charge, plage d'absorption de la lumière; Hétéro-structure; 0D/2D; Points quantiques; QD core-shell; dichalcogénure de métal de transition; Se doper; Alignement de bande réglable; QD à gradient; Calcul théorique.

ABSTRACT

Photoelectrochemical (PEC) solar-driven hydrogen production is a promising route to convert solar energy into chemical energy using semiconductors as active materials. In the process of PEC water-splitting, the conversion efficiency of solar energy to hydrogen energy is mainly determined by the light absorption of photocatalysts, the separation and migration of photogenerated carriers, and surface catalysis. However, the performance is still far from satisfactory due to a limited absorption range and rapid charge recombination. Therefore, effectively expanding the absorption spectral range of photocatalysts and suppressing the charge recombination of photogenerated electron-hole pairs are two essential ways to improve the photoelectric conversion efficiency of semiconductor materials based on PEC. Compared to single-component photocatalysts, heterostructure photocatalysts that combine at least two functional materials in one system have received more attention in the last decade thanks to the synergistic effect. This thesis explores how heterostructure semiconducting materials interact with each other, and how properties such as light management and charge injection can be controlled by appropriately modulating the interfaces of nanomaterials to improve the performance of the PEC device. Zero-dimensional quantum dots (0D QDs), have been recognized as one of the most promising photosensitizers for photoelectrodes fabrication, thanks to their unique and scalable optical properties where absorption and photoluminescence of the QDs are composition and size-tunable, extending the absorption range from ultraviolet to Visible and also Near-infrared (UV-VIS-NIR). In addition, since the two-dimensional (2D) layered structure is beneficial for shortening the charge transport time and distance, heterojunctions based on 2D materials can exhibit more efficient charge separation and transfer.

Heterostructure based on 0D/2D interfaces is particularly interesting due to the possibility of easily constructing intimate interfaces, which can inhibit carrier recombination. First, I synthesized a 0D/2D heterojunction, which was constructed by 0D metal chalcogenide QDs and hierarchical 2D Zn-MoS_2 nanosheets (NSs). The effect of PbS, CdS, and their composite core-shell PbS@CdS QDs is analyzed by depositing them onto Zn-MoS_2 NSs using an in situ process. This distinctive heterojunction can leverage the light-harvesting capabilities of QDs with the catalytic performance of Zn-MoS_2. Compared to Zn-MoS_2, Zn-MoS_2/PbS, and Zn-MoS_2/CdS, the obtained 0D/2D heterostructure based on the composite Zn-MoS_2/PbS@CdS has a significantly enhanced photocurrent. The synergistic effect between 0D/2D heterojunction, the extended absorption range of QDs, and the strong coupling and band alignment between them lead to superior solar-

driven PEC performance. This work can provide a new platform to construct multifunctional 0D/2D nanohybrids for optoelectronic applications, not limited to PEC devices.

Nowadays, the majority of the QDs used in devices for PEC hydrogen generation are based on heavy-metal-containing materials, such as Pb and Cd. Unfortunately, using these materials hampers their perspective to be commercially developed due to health and environmental concerns. By using a template-assisted cation exchange procedure, we developed eco-friendly $CuInSe_2/(CuInSe_xS_{1-x})_5/CuInS_2$ QDs based on a gradient multi-shell architecture, exhibiting tunable Near Infra-Red (NIR) optical absorption and photoluminescence (PL) properties. The NIR QDs are used as sensitizers for mesoporous TiO_2 and employed for PEC hydrogen production. The PEC device based on the gradient architecture showed a 200 % improvement compared to the simple core $CuInSe_2$ QDs and 73 % compared to the core-shell structure. The enhancement is ascribed to favorable stepwise electronic band alignment and improved electron transfer rate by incorporating interfacial gradient layers. These results could pave the way for synthesizing heavy-metal-free QDs, exhibiting broad application in emerging optoelectronic technologies.

Combine the strategies mentioned above, a hot injection approach is utilized to synthesize highly monodisperse 0D Zn doped $CuInS_2$ heavy-metal free QDs, which are then anchored on hierarchical 2D/2D MoS_2/rGO NSs via a facile sonication-assisted method to develop a 0D/2D/2D heterojunction interface for PEC water splitting. The interfacial structure and band alignment between the proposed 0D QDs and 2D/2D MoS_2/rGO NSs is engineered by modulating the Zn molar ratio during the QDs synthesis. The energy band positions of QDs after doping is investigated and discussed in detail. As proof of concept, the optimized 0D/2D/2D photoanode exhibit almost 5 times higher PEC activity than MG/$CuInS_2$ and MoS_2/Zn-$CuInS_2$ NSs due to the enhanced light absorption, efficient charge separation, and transmission. It is observed that the Zn doping and the introduction of graphene play an essential role in enhancing the performance of the proposed heterostructure, reducing the recombination of charge carriers, and improving the harvesting of sunlight. This work shows how the control of optimum band alignment and carbon additive can facilitate charge transfer, allowing the development of high-efficient PEC devices based on 0D/2D/2D heterostructure nanocomposite.

Keywords: Photoelectrochemical; Water splitting; Charge separation; Charge transmission, Light absorption range; Heterostructure; 0D/2D; Quantum dots; core-shell QDs; Transition metal dichalcogenide; Doping; Band alignment tunable; Gradient QDs; Theoretical calculation.

TABLE OF CONTENT

LIST OF TABLE

LIST OF FIGURE

Figure 4.1 (a) Schematic diagram of sequential cation exchange procedures for synthesis of $CuInSe_2/(CuInSe_xS_{1-x})_5/CuInS_2$ QDs. Representative TEM images of: (b) CdSe, the insets is the HR-TEM image displaying the (111) plane of ZB CdSe; (c) $CdSe/(CdS)_6$ and (d) $CdSe/(CdSe_xS_{1-x})_5/CdS$ QDs before cation exchange, the insets are the HR-TEM images showing the (002) plane of WZ CdS. TEM images of (e) $CuInSe_2$, the insets is the HR-TEM image exhibiting the (111) plane of ZB $CuInSe_2$; (f) $CuInSe_2/(CuInS_2)_6$ and (g) $CuInSe_2/(CuInSe_xS_{1-x})_5/CuInS_2$ QDs, the insets are the HR-TEM image showing the (002) plane of hexagonal WZ $CuInS_2$ after cation exchange. The cartoons in the inset of the TEM images show the schematic QD.

Fig. 4.2 Size distribution of as-synthesized QDs corresponded to TEM imagine (Fig. 1, in manuscript). The QDs before cation exchange: (a) CdSe, (b) $CdSe/(CdS)_6$ and (c) $CdSe/(CdSe_xS_{1-x})_5$@CdS QDs. After cation exchange: (d) $CuInSe_2$; (e) $CuInSe_2/(CuInS_2)_6$ and (f) $CuInSe_2/(CuInSe_xS_{1-x})_5/CuInS_2$ QDs.

Figure 4.3 (a) XRD patterns of CdSe QDs before SILAR and after SILAR treatment with six layer CdS shell or five alloyed shell with $CdSe_xS_{1-x}$ interfacial layer and another CdS layer. The Joint Committee on Powder Diffraction Standards (JCPDS) card files for CdSe (00190191, cyan for ZB and 08-459, pink dashed for WZ) and CdS (01-077-2306, yellow for WZ) are shown for identification; (b) XRD patterns of QDs after sequential cation exchange: $CuInSe_2$ QDs (black curve), $CuInSe_2/(CuInS_2)_6$ QDs (red curve), $CuInSe_2/(CuInSe_xS_{1-x})_5/CuInS_2$ QDs (green curve); The Joint Committee on Powder Diffraction Standards (JCPDS) card files for cubic ZB phase of $CuInSe_2$ (blue curve, JCPDS card no. 01-074-9867) and hexagonal WZ phase of $CuInS_2$ (pink curve, JCPDS card no. 01-077-9459).

Figure 4.4 SAED patterns of (a) $CuInSe_2$, (b) $CuInSe_2/(CuInS_2)_6$ QDs and (c) $CuInSe_2/(CuInSe_xS_{1-x})_5/CuInS_2$ QDs, which are consistent with the XRD patterns in Fig. 4.3b.

Figure 4.5 EDS spectra of (a) $CuInSe_2$ QDs, (b) $CuInSe_2/(CuInS_2)_6$ QDs and (c) $CuInSe_2/(CuInSe_xS_{1-x})_5/CuInS_2$ QDs.

Figure 4.6 High-resolution XPS spectra of a $CuInSe_2/(CuInSe_xS_{1-x})_5/CuInS_2$: (a) Survey, (b) Cu, (c) In, (d) Se, and (e) S.

Figure 4.7 (a) Absorption and PL spectra of CdSe (black curve), $CdSe/(CdS)_6$ (red curve), and $CdSe/(CdSe_xS_{1-x})_5/CdS$ (blue curve). (b) Absorption and PL spectra of $CuInSe_2$ (green curve), $CuInSe_2/(CuInS_2)_6$ (cyan curve), and $CuInSe_2/(CuInSe_xS_{1-x})_5/CuInS_2$ (magenta curve). (c) Transient PL spectra of CdSe (black curve), $CdSe/(CdS)_6$ (red curve) and $CdSe/(CdSe_xS_{1-x})_5/CdS$

LIST OF ABBREVIATIONS

Abbreviations	Meaning
0D	zero dimensional
1D	one dimensional
2D	two dimensional
3D	three dimensional
CB	conduction band
CBD	chemical bath deposition
CE	counter electrode
CO_2	carbon dioxide
CTAB	cetyltrimethylammonium bromide
CV	cyclic voltammetry
DA	direct adsorption
DSSCs	dye-sensitized solar cells
EDS	energy-dispersive X-ray spectroscopy
EIS	electrochemical impedance spectroscopy
EPD	electrophoretic deposition
FTO	fluorine-doped tin oxide
FWHM	full width at half maximum
GC	gas chromatograph
H_2	hydrogen
HER	H_2 evolution reaction
ICP-OES	inductively coupled plasma optical emission spectrometry
IPA	isopropanol
IPCE	incident-photon-to-current-efficiency

IR ····· infrared

JCPDS ····· joint committee on powder diffraction standards

LED ····· light-emitting device

LSV ····· linear sweep voltammetry

MOF ····· metal-organic frameworks

N_2 ····· nitrogen gas

NHE ····· normal hydrogen electrode

NIR ····· near infrared

O_2 ····· oxygen

OA ····· oleic acid

ODE ····· octadecene

OER ····· O_2 evolution reaction

OLA ····· oleylamine

PEC ····· photoelectrochemical

PC ····· photoelectrochemical

PCE ····· photo conversion efficiency

PL ····· photoluminescence

Pt ····· platinum

PV ····· photovoltaic systems

QDs ····· quantum dots

QDSCs ····· QD-sensitized solar cells

QE ····· quantum efficiency

QY ····· quantum yield

Redox ····· reduction-oxidation

RHE ····· reversible hydrogen electrode

SA ····· sacrificial reagents

SAED ····· selected area electron diffraction

SEM ····· scanning electron microscope

SHE ····· standard hydrogen electrode

SILAR ····· successive ion layer adsorption and reaction

SNR ····· high signal to noise ratio

STH ····· solar to hydrogen conversion efficiency

TEM ····· transmission Electron Microscopy

TiO_2 ····· Titanium dioxide

TOP ····· trioctylphosphine

TOPO ····· trioctyl phosphine oxide

UV ····· ultraviolet

VB ····· valence band

WZ ····· wurtzite

XPS ····· X-ray photoelectron spectrometry

XRD ····· X-ray diffraction

ZB ····· zinc blend

1 INTRODUCTION AND BACKGROUND

1.1 Clean and renewable energy

Abundant and economical energy is the lifeline of modern civilization, and energy production and utilization are also indicators of a country's progress. Nowadays, any development is premised on energy, and life without energy will be unimaginable for human beings. At present, the energy consumption to maintain the modern lifestyle of humans still mainly depends on primary non-renewable energy sources fossil fuels such as oil, coal, and natural gas, especially in transportation and industry.[1] For example, oil power is used almost for any moving machine, making it uniquely versatile. Machines powered by oil are ubiquitous, such as planes manning people across the widest oceans at nearly the speed of sound, and factory machines producing and transporting food and daily necessities non-stop. Obviously, we are living in the oil age, but the oil age is coming to an end. The steady growth of the human population over the last century has led to the depletion of global fossil fuel reserves due to the ever-increasing human demand for energy. Fossil fuels are facing accelerated depletion and pose serious environmental problems and threats to the global climate. If oil production remains constant until its reserves are exhausted, it can only last for 51 years. Likewise, natural gas stored on Earth can be used for 53 years, while coal stored on Earth can be used for 114 years.[2] Almost everyone realizes that during human existence, oil and natural gas will become scarce and expensive. The limited reserves of fossil fuels will not be able to meet the increasing energy demand, which will lead to a serious energy crisis (an energy crisis occurs whenever the readily available supply of certain fuels or other energy commodities falls below the current demand in a given location). At the same time, the exhaust gas emitted by the consumption of fossil fuels seriously pollutes the environment and threatens human health, and even causes malignant diseases such as cancer.

Thus, it is urgent to develop green and sustainable technologies for clean energy production and environmental remediation, for the purpose of the long-term development of human society. In recent years, renewable energy resources have drawn lots of attention because they are relatively green and sustainable, such as solar energy, wind power, hydropower, biomass, and geothermal energy. Among them, solar energy is considered to be an ideal energy source to solve the energy crisis and environmental problems in the 21st century because of its abundance (Figure 1.1).[3] According to reports, the amount of solar energy radiated on the surface of planet earth in 1 hour (4.3×10^{20} J) is comparable to all of the energy currently consumed on the planet in 1 year ($\sim 5.7 \times 10^{20}$ J).[4]

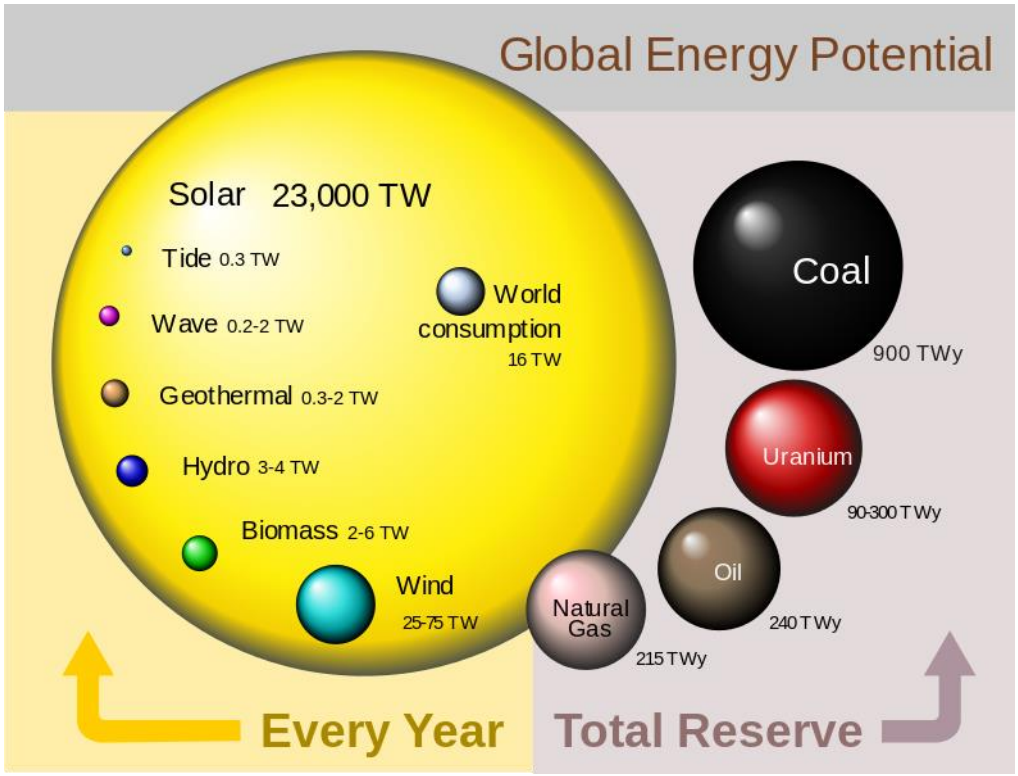

Figure 1.1 Global Energy Potential: comparison of renewable and conventional energy sources. For renewable, the amount of energy is shown per year, while for conventional sources the total reserve is displayed. Figure 1.1 Reproduced with permission from Global Energy Potential 2014.

The intermittency of solar radiation, coupled with the need for transportation and nighttime use, drives the prospect of artificially converting solar energy into storable energy. Solar energy can be stored as potential energy, kinetic energy, thermal energy, and chemical energy. Compared to other energy forms, storing solar energy in chemical form has tremendous advantages in terms of energy density, storage time, and mobility. Among various chemical energy forms, solar hydrogen (H_2) is a substantial energy carrier, avoiding the introduction of carbon sources. Combining the other advantages of H_2, such as high energy storage densities of 143 KJ/g, ease of transportation, and cost-effectiveness, and the only by-product is water, the conversion of solar energy into H_2 appears to be one of the most attractive solutions.[5]

To accelerate the deployment of hydrogen production by renewable solar energy, several technologies including photocatalytic (PC), photoelectrochemical (PEC), and photovoltaic-electrolysis (PV-E) routes, have been competitively developed.[6] However, it remains a significant challenge to construct a sufficiently efficient and stable solar-to-hydrogen (STH) energy conversion device.[7] To date, the state-of-the-art STH values of particulate photocatalysts are still

around 1%, leaving huge research and development gaps for practical application.[8, 9] Whereas, the obtained highest STH efficiency values (AM 1.5G) for PV-E, PV-PEC and PEC tandem cells are 30%, 19.3% and 13.1%, respectively, using III–V semiconductors (GaInNAs, GaAs, GaInP, etc.) as the light absorbers.[10-13] Even though water-splitting devices have been recently reported that the highest STH efficiency by PV-E system, the cost (US $8 per kg) is much higher than PC and PEC (US $3 per kg).[7, 13]

The water redox reaction that occurs in the PEC system is performed on two surfaces with different configurations (photoanode and photocathode) respectively, which greatly simplifies the subsequent gas separation process and facilitates the engineered production of hydrogen and/or oxygen. Whereas both HER and OER half-reactions take place on the surface of suspending photocatalyst particles in the PC system, leading to the evolution of a mixture of oxygen and hydrogen. Considering the higher cost of PV-E and lower STH conversion efficiencies of PC, the PEC approach integrates the light absorption and electrochemical process of the PV-E process into a single and monolithic unit via a direct semiconductor-electrolyte interface to reduce the cost, while having a distinct advantage over PC system in that the H_2 and O_2 evolution half-reactions occur on two different electrodes and are separated physically.[14] Furthermore, an external or self-bias voltage can also be incorporated into the PEC cell configuration, which can compensate for the potential deficiency and improve the exciting electron-hole separation and transfer efficiency.[15]

1.2 Photoelectrochemical hydrogen generation

1.2.1 Working Principle of PEC Water Splitting

PEC H_2 production is widely regarded as a promising approach to producing clean solar fuels that could partially address the challenges posed by growing global energy demand and climate change. The PEC water-splitting process is the direct conversion of solar energy into chemical energy in the form of hydrogen using semiconductor materials.[16] As early as 1968, oxygen evolution was observed by illuminating electrodes made of the rutile form of TiO_2 in solution.[17] In 1972, Fujishima and Honda first demonstrated photo-assisted electrochemical water splitting using an n-type rutile TiO_2 under ultraviolet (UV) light illumination, essentially marking the dawn of the development of the PEC system.[18] Since the pioneering work of PEC water splitting using TiO_2 as the photoanode in 1972, the research on semiconductor photocatalysts has entered a new era.[19, 20] Simultaneously, the STH conversion efficiency also increased to more than 13 % for the PEC system.[11] Figure 1.2 shows the PEC water splitting system configuration based on TiO_2

photoelectrode. Generally, in a conventional PEC system, there is at least one photoelectrode capable of absorbing light, and the other electrode can be a counter electrode (CE) on which another half-reaction occurs (more complex configurations may involve photoanode-photocathode pairs and /or multiple photoelectrodes). The conductive electrode substrate supporting the semiconductor photocatalyst can be a silicon substrate,[21] or a glass coated with a conductive layer, such as fluorine-doped tin oxide (FTO) and indium tin oxide (ITO). The electrodes are immersed in the electrolyte and the outer circuit could be closed by electrical contact.

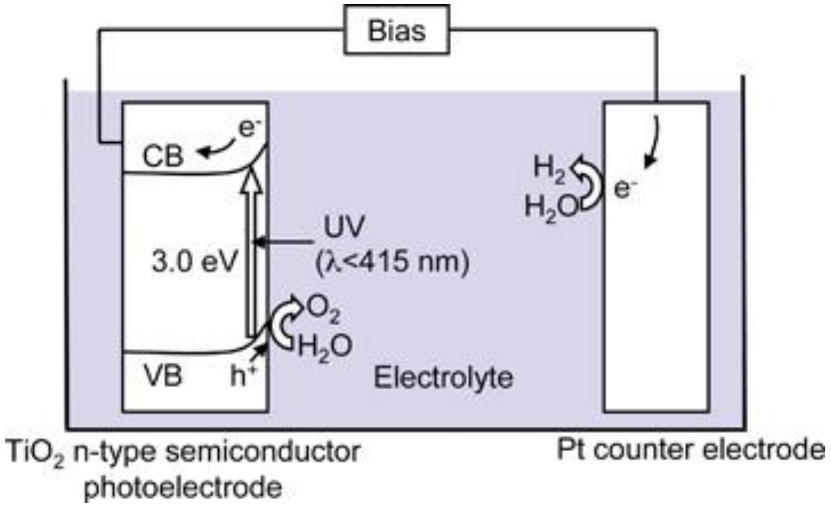

Figure 1.2 Honda–Fujishima effect-water splitting using a TiO_2 photoelectrode.[22]

Figure 1.3 shows the schematic representation of the PEC water-splitting process which consists of three major processes. (1) Light harvesting processes. Under light irradiation, photons with high-energy ($h\nu \geq$ bandgap, E_g) are first absorbed by the photoanode composed of n-type semiconductors (light harvesting process), followed by photo-excited charge carrier generation. The electrons are excited from the valence band (VB) to the conduction band (CB) of the semiconductor. (2) Charge separation and transfer process. The electron transfer occurs between the semiconductor and the electrolyte solution, thereby the Fermi level of the system is equilibrated with the redox potential of the electrolyte solution. Therefore, in bulk/single crystal material, the depletion layer formed at the semiconductor-electrolyte interface leads to energy band bending at the surface that facilitates the separation of photogenerated electrons and holes. Separation and migration of charge carriers to the electrode surface by the internal or external bias applied by the circuit, including the transport of photo-excited electrons from the photoanode to the counter electrode by an external circuit. (3) Surface reaction process. The electrons and

holes perform chemical redox reactions at the surface of the semiconductor photoanode and the platinum cathode.[23, 24] The photo-excited electrons accumulated on the surface of the counter electrode are injected into the electrolyte to reduce the H^+ ions to H_2 at the surface of the counter electrode. Simultaneously, the holes on the surface of the photoanode are involved in the oxygen evolution reaction. In addition, the electrolytes are essential in the PEC system for charge transfers. Due to the low conductivity of high-quality deionized water (about 0.05 μS/cm) at 25 °C, it is usually necessary to add ions (such as salts, acids, bases, etc.) to the electrolyte solution to increase its conductivity. Furthermore, during the PEC process, the photogenerated charge carriers travel through a “long journey” for the water splitting reaction, and charge recombination may occur in the inner bulk of the semiconductor, the semiconductor/substrate interface and the semiconductor/electrolyte interface, resulting in an inefficient PEC performance.[25] Therefore, effectively suppressing the above-mentioned charge recombination is essential to achieving efficient PEC performances. It is worth noting that in some cases, a redox couple that works as a sacrificial agent (hole sacrificial electrolytes, such as Na_2S and Na_2SO_3) is necessary to be added to the electrolyte to impede the charge recombination.[24] Some sulfides and organic agents can also act as electrolytes; where there is no oxygen evolution, due to the oxidation potential of water being more positive than these materials.

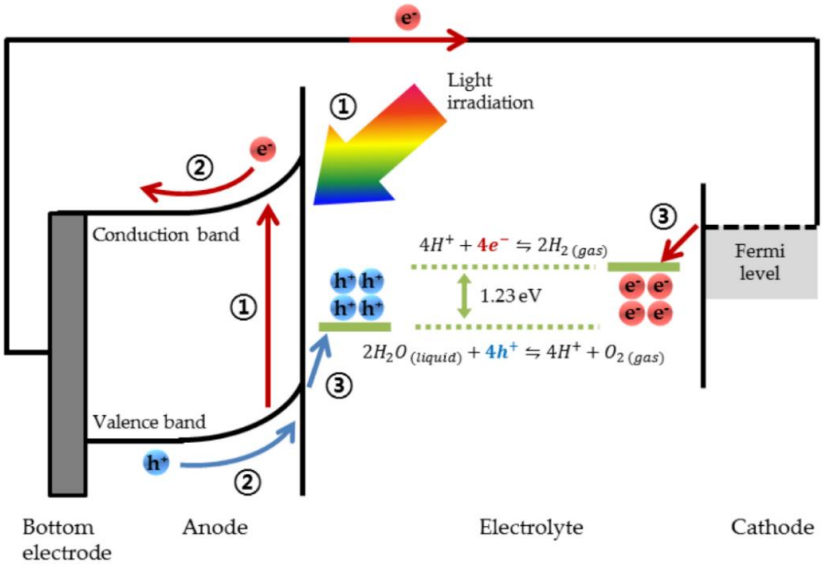

Figure 1.3 Schematic representation of the PEC water-splitting process in a common PEC water-splitting system consisting of a photoanode and a metal counterpart.[26]

In the PEC system, the required free energy change (ΔG) of converting one molecule H_2O to H_2 and 1/2 O_2 under standard conditions is 237.2 kJ mol^{-1}, which is calculated based on the Nernst

equation, corresponds to ΔE° = 1.23 V per electron transferred. Ideally, a single semiconductor used for PEC water splitting should satisfy certain conditions, such as with a band gap energy (Eg) large enough to split water (Eg >1.23 V) with the conduction band edge energy (E_{CB}) and valence band-edge energy (E_{VB}) straddling the electrochemical potentials E° ($H+/H_2$) and E° (O_2/H_2O).[27] However, under standard conditions, due to the thermodynamic energy loss (0.3-0.4 eV) during carrier transport and the overpotential requirement for surface reaction kinetics (0.4-0.6 eV), the minimum bandgap should be >1.8 V for a single semiconductor (to drive the reaction at a reasonable rate, actually higher much more). Whereas, there is a trade-off between the size of the bandgap and the amount of light that can be absorbed, with large bandgaps absorbing less light and leading to fewer efficiencies.[6] Therefore, Solar-driven water splitting can be achieved with a single semiconductor with a large bandgap (>1.8 eV) and/or by combining two or more semiconductors in tandem PEC cells by integrated oxygen-donating photoanode and hydrogen-donating counter electrode.[27] The tandem configuration allows the use of semiconductors with smaller band gaps and access to a larger portion of the solar spectrum than using a single semiconductor.[28]

1.2.2 Challenge of PEC Water Splitting

Controlling the properties of semiconductors is the primary concern in developing materials for solar water splitting. Accordingly, based on the comprehensive considerations of the PEC process mentioned in section 1.2.1, effectively expanding the absorption spectral range of photocatalysts and suppressing the recombination of photogenerated electron-hole pairs are crucial ways to improve the PEC performances. For decades, researchers have carried out a large number of theoretical and experimental studies, exploring a series of modification methods such as ion doping/defect regulation,[29, 30] noble metal modification,[31] dye sensitization,[32] semiconductor compounding,[33] supported co-catalyst,[34] etc., to achieve the purpose of extending the spectral absorption range to the visible light region and blocking the recombination of photogenerated electron-hole pairs to improve the activity of photo-splitting water.[35, 36] Among them, the more important modification strategies are: (1) energy band modulating, including ion doping, non-stoichiometry and oxygen vacancies approach to expand the absorption spectral range by creating surface defects and bulk defects.[29, 30] However too many defects can act as recombination centers for photogenerated carriers, limiting the further improvement of their performance. (2) introducing co-catalysts (Au, Ag, Pt, Pd, etc.), which not only serve as a good transport channel at the interface for charge carriers but also reduce the activation overpotential and provide more active sites. However, the high cost of precious metals limits their practical use.

(3) Constructing a heterojunction, accelerating the separation of electron-hole pairs by combining two or more semiconductors with matching energy bands.

Although previous research has made some progress, the degree of efficiency improvement is very limited, and the practical application of PEC water splitting still faces significant challenges. Compared to more traditional approaches, such as PV-E (more than 10%)[37], PEC-based systems still suffer from low STH conversions. As a result, there is still much work to be done, such as the development of new photocatalysts with specific structures and new photocatalytic reaction systems. These will be the focus of future water photolysis research.

In practical applications, the performance of PEC water separation systems is determined by the ability to harvest solar energy for hydrogen production using semiconductor photocatalysts. Low-cost fabrication processes utilizing existing, inexpensive, and environmentally friendly nanomaterials have the potential to make PEC devices a reliable alternative, both economically and environmentally.

1.3 Heterostructure Nanomaterials

1.3.1 Definition of nanomaterials and classfication

According to the definition adopted by the European Commission (October 18, 2011), nanomaterials are powdered, agglomerated natural or artificial materials composed of elementary particles with at least one or more three-dimensional dimensions ranging from 1 nm to 100 nm, and the total number of these elementary particles is required to account for more than 50% of the total number of particles in the entire material. The precisely engineered nanomaterials are considered to be the cornerstone of modern high-tech applications, such as biological imaging,[38] biosensors,[39] fuel cells,[40] lithium-ion batteries,[41] luminescent solar concentrators[42], and solar cells, etc.[43] According to confined dimensionality in which the charge carriers or excitons are free to move,[44] nanomaterials can be classified into zero-dimensional (0D), one-dimensional (1D), and two-dimensional (2D) and three-dimensional (3D) nanomaterials. (Table 1.1).

Table 1.1 Classification of nanomaterials

Classification	Representative	Numbers of dimensions in quantum confinement
0D nanomaterials	Quantum Dots (QDs)	3

1D nanomaterials	Nanowires/rods/tubes	2
2D nanomaterials	Nanosheets/ hierarchical	1
3D nanomaterials	Bulk materials	0

Quantum confinement is an important effect in semiconductor materials, which can adjust the photoelectric properties of semiconductor materials when the size of a metal ion is less than or equal to the exciton Bohr radius. In general, when a semiconductor is irradiated by an incident photon with energy higher than its band gap, the electrons will be excited to CB and leave a hole in the VB, which these two oppositely charged particles are attracted by the Coulomb force. The photogenerated electron-hole pair is called an exciton, while the distance between the excited electron in CB and the hole in VB is called Bohr radius, which depends on the effective mass of electrons and holes in a specific material, as shown in the following formula:

$$r_B = \frac{\varepsilon h^2}{\pi e^2}\left(\frac{1}{m_e^*} + \frac{1}{m_h^*}\right)$$

Where r_B is the exciton Bohr radius, ε is the dielectric constant of the corresponding materials, h is Planck's constant, e is the electronic charge, m_{e*} and m_{h*} are the effective masses of electron and hole, respectively. Charge carriers are spatially confined when one or more dimension sizes of semiconductor nanocrystals are reduced to the same magnitude as the exciton Bohr radius.[45] The density of the state (DOS) function describes the number of states available in the system and is the key to determining the carrier concentration and energy distribution in semiconductors. The properties of nanomaterials are shape-dependent, which is induced by their particular DOS, making them promising as building blocks of emerging technologies. As shown in Figure 1.4, the electronic DOS of 3D bulk semiconductors is continuous, and the corresponding bandgap energy of the semiconductor is composition-dependent due to the absence of confinement of the exciton in three dimensions. In particular, the insets of Figure 1.4, report a cartoon showing the corresponding spatial confinement with quantum confinement directions defined by arrows. The exciton is spatially confined in one dimension (thickness direction) of 2D quantum well/nanosheets (NSs), while it is fully confined to two dimensions (cross-sectional direction) of 1D quantum nanowires, respectively. In addition, in the case of 0D QDs, all the available states exist only in discrete energies due to electrons being spatially confined in all three dimensions. This allows the mobility of electrons and holes to be confined to specific energy levels, affecting

the electrical and optical properties. Therefore, nanomaterials of different dimensions possess significantly different optical and electronic properties, which makes them promising in the field of solar technologies application. In addition, various methods, including doping[29-32], alloying[33-35], ion exchange[36-38], and heterodeposition[39] have been employed to obtain multicomponent nanomaterials.

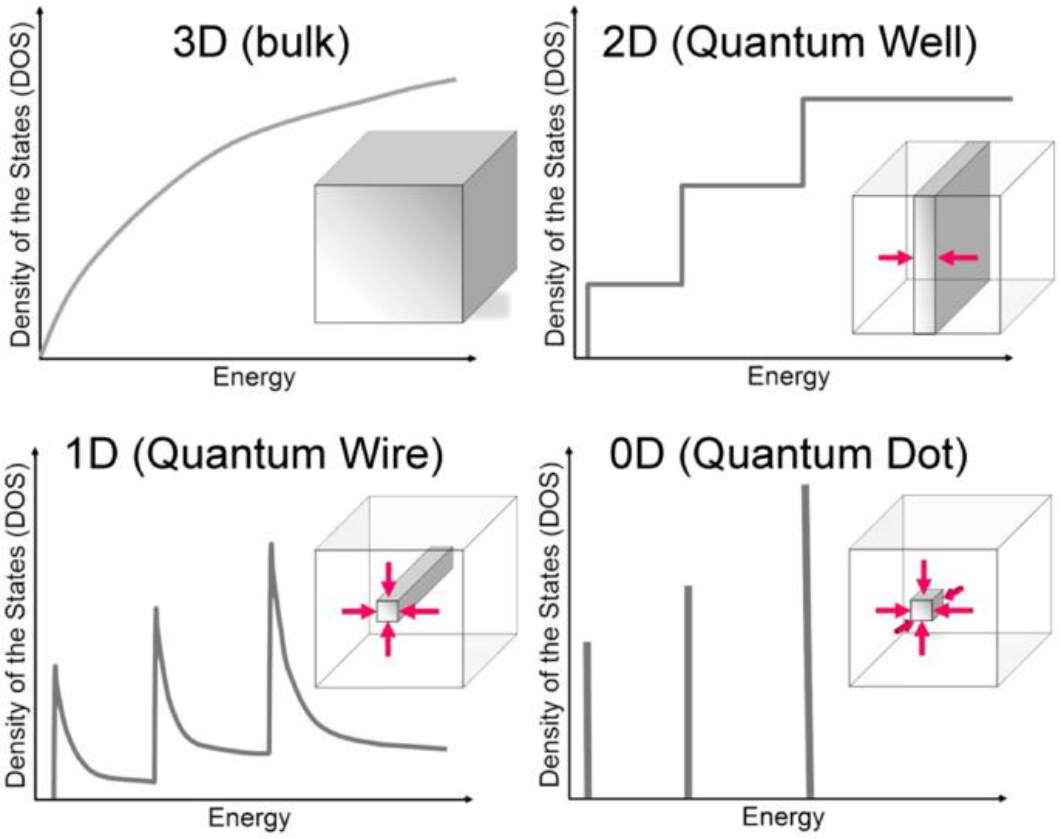

Figure 1.4 Schematic illustration of DOS as a function of energy on dimensionality.[44]

1.3.2 Materials requirement for PEC

Since the pioneering discovery of the photolysis of water by titanium dioxide (TiO_2) in 1972, TiO_2-based photoelectrodes have been intensively investigated for water splitting, due to their many excellent properties, such as being composed of earth-abundant, non-toxic elements, and photochemical stability under either strongly acidic or alkaline conditions. However, due to its wide band gap (3.2 eV for the anatase phase and 3.0 eV for the rutile phase), only UV light (5% of the solar spectrum) can be absorbed, resulting in a low theoretical STH efficiency (η = 1.3% for anatase and 2.2% for rutile). In the last decades, varieties of materials were investigated and

used for PEC water splitting. According to the composition, photocatalysts can be generally categorized into three types: metal oxides, metal chalcogenides, and metal-free photocatalysts.

As aforementioned, the most important aspect of PEC water splitting is the selection of suitable photoelectrodes material. An ideal photoelectrode requires semiconductor materials that possess the following characteristics:

(1) Appropriate band gap energy and band position. Sunlight is composed of 5% ultraviolet (300-400nm), 43% visible light (400-780nm), and 52% infrared radiation (700-2500nm). According to the relationship between the bandgap energy and the absorption onset: $Eg=1240/\lambda_{Onset}$. Thus, the light absorption range depends on the band gap of the semiconductor. In addition, due to the rapid decrease of solar intensity below 390 nm according to the solar spectrum, the optimal upper limit of the bandgap energy is 3.2 eV. The reduction potential of the proton is located at 0 V vs. NHE while the O_2/H_2O potential is 1.23 V vs. NHE at pH = 0, the theoretical minimum band gap for the water splitting requires the lowest energy incident photon of 1.23 eV. However, due to the thermodynamic energy loss (0.3-0.4 eV) during carrier transport and the overpotential requirement for surface reaction kinetics (0.4-0.6 eV), a minimum band gap of ~1.8 eV is required for a single photocatalyst. Thus, a single photocatalyst for one-step excitation of overall water splitting under visible light irradiation must meet several rigorous prerequisites, including having a band gap larger than 1.8 eV but smaller than 3.2 eV and that straddles the reduction and oxidation potentials of the water. Whereas, in the dual-particle system, the redox mediator relaxes the confinement and the sum of the voltages of the two particles provides the driving force for the overall water splitting.

(2) Efficient charge carrier separation and transport. In general, rapid charge carrier recombination is the main factor responsible for the low STH efficiencies. Therefore, an effective strategy to accelerate the charge carrier separation and transport is required, which depends on the intrinsic properties (carrier mobility) and the extrinsic properties (crystallinity and nanostructure). The photocatalysts with smaller sizes in some dimensions, such as 0D QDs, 1D nanowires,[46, 47] or 2D NSs[48], can minimize the diffusion distance of excitation-generated electrons and holes in the transport, thus reducing the recombination rate.

In addition, to improve the charge separation efficiency of PEC systems, many useful strategies have been investigated, such as constructing heterojunctions at the interface of different photocatalysts to form a built-in electric field to provide a driving force for charge separation.[36, 49]

(3) Strong catalytic activity and stability. Appropriately fast surface reaction kinetics can avoid the accumulation of surface charges, which otherwise can lead to electron-hole recombination and photo-corrosion.

Furthermore, from an economic and environmental perspective, the required photoelectrode materials should be low-cost and composed of earth-abundant, non-toxic elements for practical applications. This is critical in proving the argument for scaling up solar fuel equipment in an economical way. From an application point of view, a favorable band alignment must be able to balance the carrier separation, confinement, as well as recombination. To reduce the photogenerated electron-hole recombination, the construction of heterostructure is a promising strategy thanks to the appropriate band alignment. Simultaneously, the non-ideal band positions of most materials with respect to the thermodynamic water splitting potentials is one reason why it is advantageous to use two photo-absorbers in series. In this way, each semiconductor needs to have only one band (either the conduction or the valence band) that is suitable for the respective reaction.[6]

1.3.3 Heterostructures for PEC

"*The interface is the device*", as Herbert Kroemer said in his Nobel Lecture, the semiconductor interface plays a crucial role in modern electronic and optoelectronic devices.[50, 51] Generally, utilizing heterojunctions in semiconductor devices can generate nearly arbitrary and continuous bandgap variations in contrast to single-component semiconductors, whose bandgap tuning is limited by their inherent properties.[52] Therefore, coupling wide bandgap semiconductors with narrow bandgap semiconductors and constructing heterostructures with matched band alignments is a promising strategy to improve the PEC performance by accelerating charge carrier separation and transfer. In general, according to distinct bandgap offsets, the heterojunctions formed by two semiconductors can be classified into three patterns: straddling gap (type I), staggered gap (Type II), and broken gap (Type III) heterostructures (Figure 1.5a). For Type-I heterojunctions, the conduction band minimum (CBM) of one semiconductor is higher than another semiconductor while the valence band maximum (VBM) is lower, resulting in both the electrons and holes tending to transfer to the latter, as shown in Figure. 1.5a. Therefore, Type-I heterojunctions have been widely used in light-emitting devices and semiconductor lasers that require carrier recombination.

For Type-II heterojunctions, the bandgaps of the two semiconductors form a staggered band alignment, namely, the energies of both the CB and VB of one semiconductor are relatively higher

than that of the other semiconductor. Therefore, following the initial generation of charge carriers under the radiation, the photogenerated electrons and/or holes tend to transfer in opposite directions through the interface, resulting in the efficient spatial separation of charge carriers and subsequent formation of the built-in electric field.[53] This charge confinement is of great significance in certain optoelectronic devices, especially where light absorption or emission is involved, such as solar cells and PEC devices, since efficient regulation of carrier separation and transport determines the performance of these devices.[54] Furthermore, interfacial transitions can extend the spectral range to wavelengths longer than those defined by the band gap of any component.

In addition, if a staggered lineup is taken to the extreme, the result is a broken-gap lineup (Type III) in which the bottom of the conduction band on one side is lower than the top of the valence band on the other.

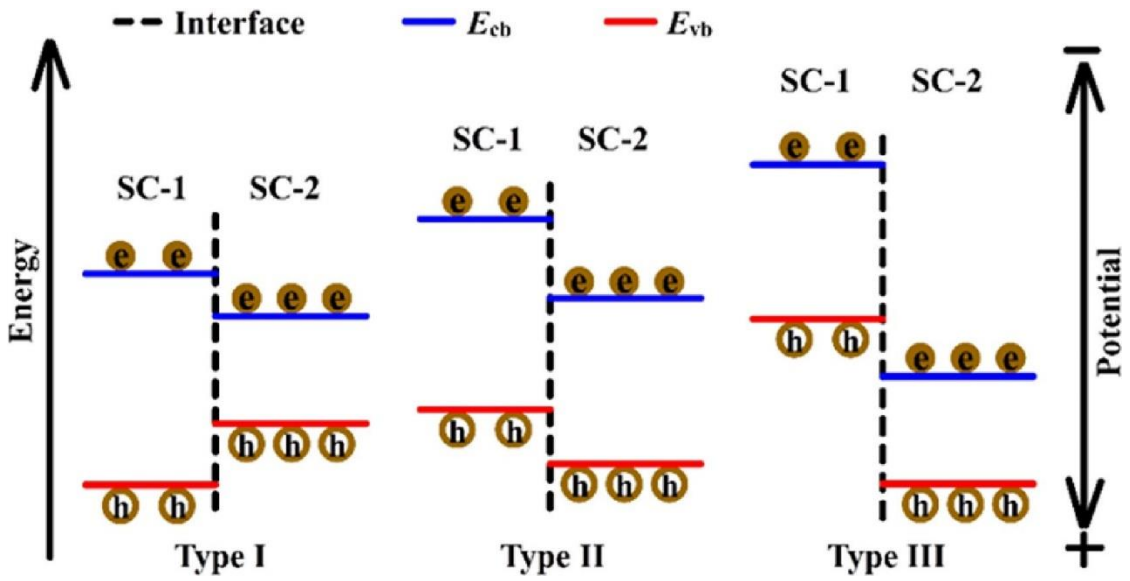

Figure 1.5 Schematic illustration of Type I, Type II, and Type III heterojunctions formed by the coupling of two semiconductors.[55]

Among these three types of heterostructure, the Type II heterostructure has proved a promising strategy to enhance the PEC performance thanks to the efficient spatial separation of photogenerated electron-hole pairs and reduced charge recombination.[56] The rich and diverse available combinations of semiconductor nanomaterials with unique intrinsic electro-optic properties, precise tuning of chemical compositions and crystal structures, interface strain

engineering, structural optimization, and external field excitation enable the rational design of type-II heterojunctions, to meet the specific requirements of various applications. Therefore, rational design strategies for type-II heterojunctions are crucial to obtaining desired properties required for PEC applications. The energy band alignment at the interface plays a crucial role in the carrier transfer properties and optoelectronic performance of the type-II heterojunction. As shown in Figure 1.6, after the junction reaches thermal equilibrium, the built-in potential causes band bending due to band offsets, which drives the photogenerated electrons and holes to move in the opposite direction, resulting in the spatial separation of electrons and holes in different sides of the heterostructure.[54, 57] Designing a favorable band alignment is of great importance to facilitate the charge carrier separation extraction for PEC devices.[58] From an application point of view, a favorable band alignment must be able to balance the carrier separation, confinement, as well as recombination. In particular, band alignment engineering typically relies on the intrinsic tuning of the composition of one or two semiconductor materials that form the interface. With the rapid development of diverse synthesis techniques, precise chemical composition tuning, such as doping and alloying, can provide a powerful strategy for the control of the desired band alignment.[59]

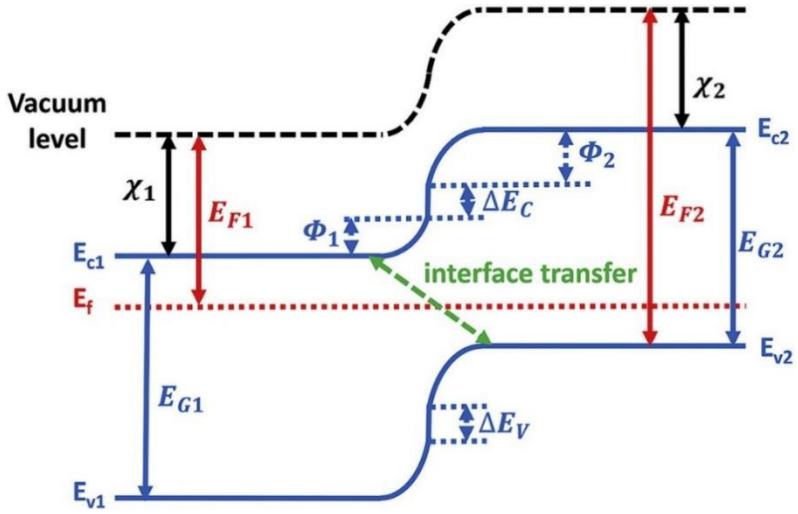

Figure 1.6 Schematic diagram of a typical type II heterojunction.[54]

1.3.4 0D/2D heterostructure

Although each class of low-dimensional structures possesses superior optical and electronic properties, there are also some inherent limitations. For instance, 0D materials may potentially exhibit higher emission quantum yields (QY) because carrier localization tends to suppress non-radiative recombination losses. Nevertheless, thin films of 0D materials generally have low carrier

mobilities due to large tunneling barriers.[54] 2D materials, especially some a-few-monolayer structures (eg. MoS_2, MoS_2, g-C_3N_4), usually do not provide sufficient light absorption for detection-related applications due to their small absorption cross section; and are more sensitive to structural defects, so they tend to produce lower light-emitting quantum yields. By combining nanomaterials of different dimensions, mixed-dimensional heterojunctions exhibit some unique properties, providing an option for bypassing the intrinsic limitations of a low-dimensional material.[60] Simultaneously, type II heterojunctions of different dimensions may generate discrete energy levels due to their different quantum confinement effects, causing the band structures to deviate from each other.[54] Since the surfaces of most low-dimensional materials are dangling bond-free, they can interact via van der Waals forces, resulting in 2D-0D, 2D-1D, and 2D-3D van der Waals heterojunctions.[60, 61] However, there are also some shortcomings of low-dimensional type II heterostructure.[62-64] For instance: (i) tendency to self-aggregate, greatly reducing their exposed surface area and active sites; (ii) instability relative to their bulk counterparts due to their large number of surface defects; (iii) easy recombination of photo-induced electron-hole pairs, leading to low charge utilization efficiency.[65] Therefore, structural optimization has a great impact on the optoelectronic properties of heterojunctions. One of the effective approaches to solve these problems is to deposit 0D nanoparticles on ultrathin two-dimensional (2D) NSs to obtain 0D/2D heterostructures, thanks to the larger surface area and better charge mobility of 2D NSs to load QDs uniform and reduce the charge recombination, respectively.[66] For example, benefiting from the strong and size-tunable optical absorption of 0D PbS QDs and the high carrier mobility of 2D MoS_2 monolayer, the hybrid 0D-2D PbS-MoS_2 heterojunction based photodetector exhibits excellent response up to 10^6 $A \cdot W^{-1}$.[67] The strong electronic coupling between both components not only enables the 0D NPs to have high dispersion and stability but also greatly improves their charge separation and transfer efficiency.[68]

The heterostructure based on 0D/2D interfaces is particularly interesting due to the possibility of easily constructing close interfaces. Generally, in the 0D-2D mixed dimensional heterostructure, the 0D materials commonly work as light absorption layers due to their higher absorption. Therefore, coating 0D materials on the surface of 2D materials is a common strategy to form 0D/2D heterostructures. Among a wide gamut of 0D/2D heterostructures, quantum dots (QDs)/NSs are promising for improving the photoexcited electrons/holes transfer due to their high charge mobility of 2D NSs.[69] In a QDs/NSs heterostructure, a very close interface between the two is created, and since processes such as exciton dissociation and charge injection are critically dependent on the QD-surface distance, they will be enhanced.[70] Further, the presence of a 2D material can provide several superior features (compared to 0D and 1D nanomaterials) such as

a significant increase in the material surface area, extended contact between the assembly and the electrolyte, and most remarkably, preferential electrical transport that can suppress charge carrier recombination and overall improve the functional PEC properties.[4, 71] Based on these advantages, the 0D/2D hybrid can combine the strong light harvesting capability of QDs with the catalytic performance of the 2D platform.

1.4 0D QDs

Quantum dots (QDs)-based heterostructures represent an excellent relevant model system for understanding and tuning the optoelectronic behavior, and provide a well-defined nanoscale interface analysis of opportunities for exciton dissociation and charge separation.[72] In particular, QDs-based components are often incorporated into optically related devices, including photovoltaics[73-75], light-emitting devices (LED)[76-78], PEC devices, and photosensors[79, 80], thanks to their tunable bandgap and ability to initiate multi-electron exciton generation.

1.4.1 Core QDs

Nanometer-sized QDs, sometimes called artificial atoms, exhibit fundamentally different properties compared to analogous bulk materials. QDs are typical 0D semiconductor nanocrystals, and their size in three dimensions is smaller than the exciton Bohr radius (the distance between e^- and h^+ pair) of their corresponding semiconductor materials.[81] Normally, the QDs are composed of II-VI, III-V, and IV-VI elements of the periodic table, and the size varying from 1 nm to about 20 nm. Unlike their bulk semiconductors, the most striking feature of QDs is their unique size-dependent optical properties, which result from the quantum confinement effect. In most semiconductors, quantum confinement occurs once the size is reduced to a few nanometers, resulting in the size-dependent optoelectronic properties of QDs.[81-83] For example, with the quantum confinement effect in these materials, the band gap between the VB and the CB widens with decreasing crystallite size,[84] leading to unique phenomena such as size-dependent fluorescence emission and size-tunable absorption properties.[81] Due to the quantum confinement effect, the excitons of QDs are spatially confined. In addition, inverse to the continuous energy band of bulk materials, the QDs present discrete energy levels because electrons are quantized to specific energies (Figure 1.7a). In general, the energy band gap of a quantum dot can be considered as the sum of the energy band gap of the bulk material, the exciton confinement energy, and the Coulomb attraction energy between electrons and holes in the spherical quantum dot, as shown in the following formula[85]:

$$\mathrm{Eg(QDs)} = \mathrm{Eg(bulk)} + \frac{h^2}{8R^2}\left(\frac{1}{m_e^*} + \frac{1}{m_h^*}\right) - \frac{1.8e^2}{4\pi\varepsilon R\varepsilon_0}$$

Where Eg(bulk) of the above formula is the band gap energy of the corresponding bulk material, h is the Plank constant, R is the radius of the spherical QDs, m_e* and m_h* are the effective mass of electron and hole, respectively, e is the charge of the electron, ε_0 and ε are the vacuum permittivity and permittivity of QDs, respectively.[85] In particular, the second and the third term correspond to the exciton confinement energy and the Coulomb attraction energy, respectively. It can be known from the above formula, that the band gap of QDs is tuned by modulation of the QDs size (R). It means the bandgap energy of QDs will increase with the QDs size decrease, because the merged energy bands gradually become discrete, as shown in Fig. 1.7 b. In addition, the optical properties of QDs are size-dependent, allowing their absorption and photoluminescence (PL) properties to be tuned over a broad spectral range by varying their size.[86] As shown in Figure 1.7 c, the absorption and PL emission wavelength of CdSe QDs can be tuned in the visible range from 450 nm to 750 nm (Eg = 1.76 eV for the bulk and r_{Bohr} = 4.8 nm) by modulating the CdSe size. Therefore, controllable synthesis of semiconducting chalcogenide QDs (such as CdSe, CdS, and PbS) can in principle be designed with different sized spans, matches, and even overlaps with the entire visible and NIR spectral range.[87] The unique size-dependent optical properties of QDs, combined with their cost-effectiveness, efficient charge generation, fast charge separation and transfer, make QDs extremely useful sensitizers in various types of optoelectronic devices.[88-90]

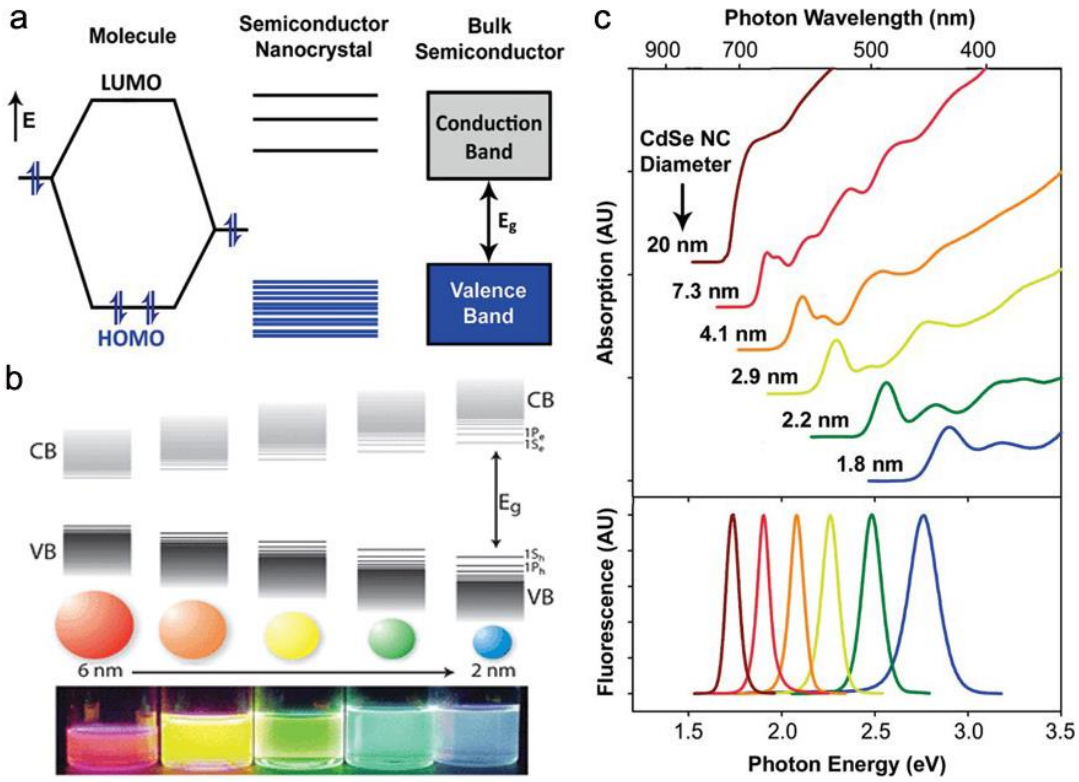

Figure 1.7 (a) Electronic energy states of a semiconductor in the transition from discrete molecules to nanosized crystals and bulk crystals. Blue shading denotes ground state electron occupation. (b) Schematic representation of the quantum confinement effect on the energy level structure of semiconductor material. The lower panel shows colloidal suspensions of CdSe nanocrystals of different sizes under UV excitation. (c) Absorption (upper) and fluorescence (lower) spectra of CdSe semiconductor nanocrystals show quantum confinement and size tunability. AU = arbitrary units. Figure 1.7 a and c were taken from reference [91] and Figure 1.7 b was taken from reference[92].

Figure 1.8 shows a diagram of the emission range of various representative QDs, including II-VI (e.g., Cd(Zn)X, X = S, Se, Te), III-V (e.g., InP, InAs, GaAs), IV-VI (e.g., PbX, X = S, Se, Te) and also alloyed I-III-VI ternary nanocrystals (e.g., CuInX, X = S, Se) semiconductors with different elemental composition. The absorption and PL emission of QDs can be tailored over the entire ultraviolet-visible-near-infrared (UV-VIS-NIR) region by modulating the size, composition and structure (e.g., involving core/shell structure), due to the quantum confinement.

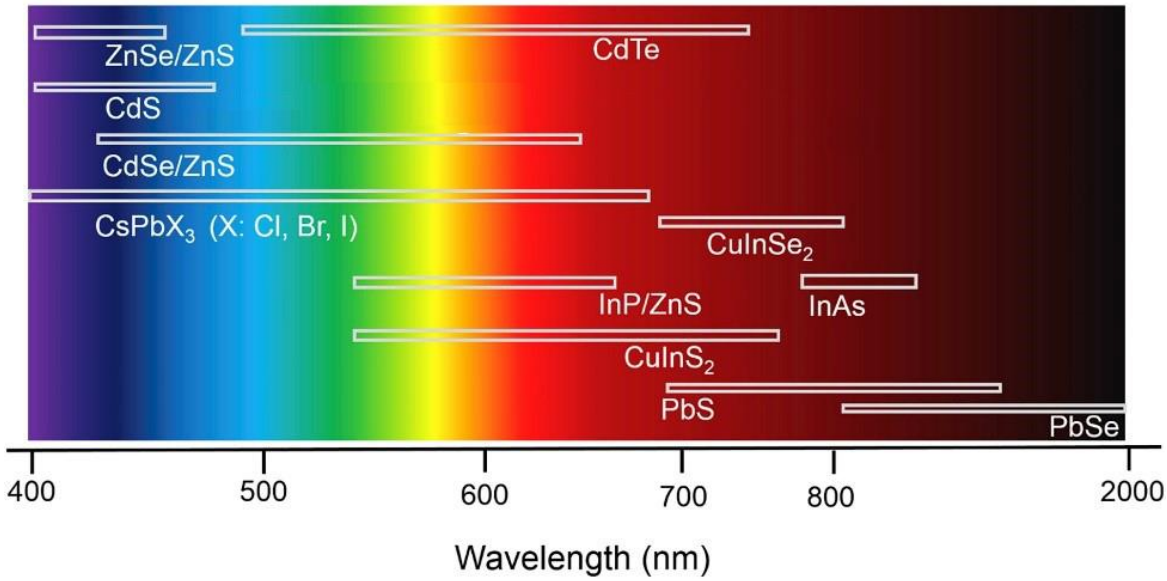

Figure 1.8 The emission range for representative QDs.[83]

1.4.2 Core-shell QDs

Due to the small size of the QDs (normally small than 20 nm), they present a relatively high surface-to-volume ratio. The surface organic ligands of QDs not only can stabilize colloidal QDs in the solution but also can passivate dangling bonds at the QDs surface, simultaneously.[93] However, the ligands on the surface of the QDs are relatively weak. Therefore, the properties of bare QDs covered with organic ligands are very sensitive to surface conditions, especially under illumination conditions. The surface ligand-associated traps and defects served as fast non-radiative de-excitation channels for photogenerated carriers, which may decrease the photo conversion efficiency (PCE), emission QY, and long-term photostability.[81] This issue can be addressed by growing epitaxial layers of inorganic shells covering the core to form a core-shell structure.[94-97] Therefore, a robust inorganic shell can protect the semiconductor core from surface defect states, trap sites, and environmental chemical states, reducing charge recombination. A general requirement for synthesizing core-shell nanocrystals with satisfactory optical properties is epitaxial shell growth. The growth of the shell can lead to the formation of strain and defect states at the core/shell interface or inside the shell. These can act as trap states of photogenerated carriers, leading to diminishing emission QY and reduced photostability.[93] Therefore, to minimize the formation of defect states at the core-shell interface or inside the shell, the core and shell materials should exhibit a small lattice mismatch. In addition, by choosing appropriate core-shell materials, the band alignment of the core and shell can be tuned to improve exciton separation and charge transfer.

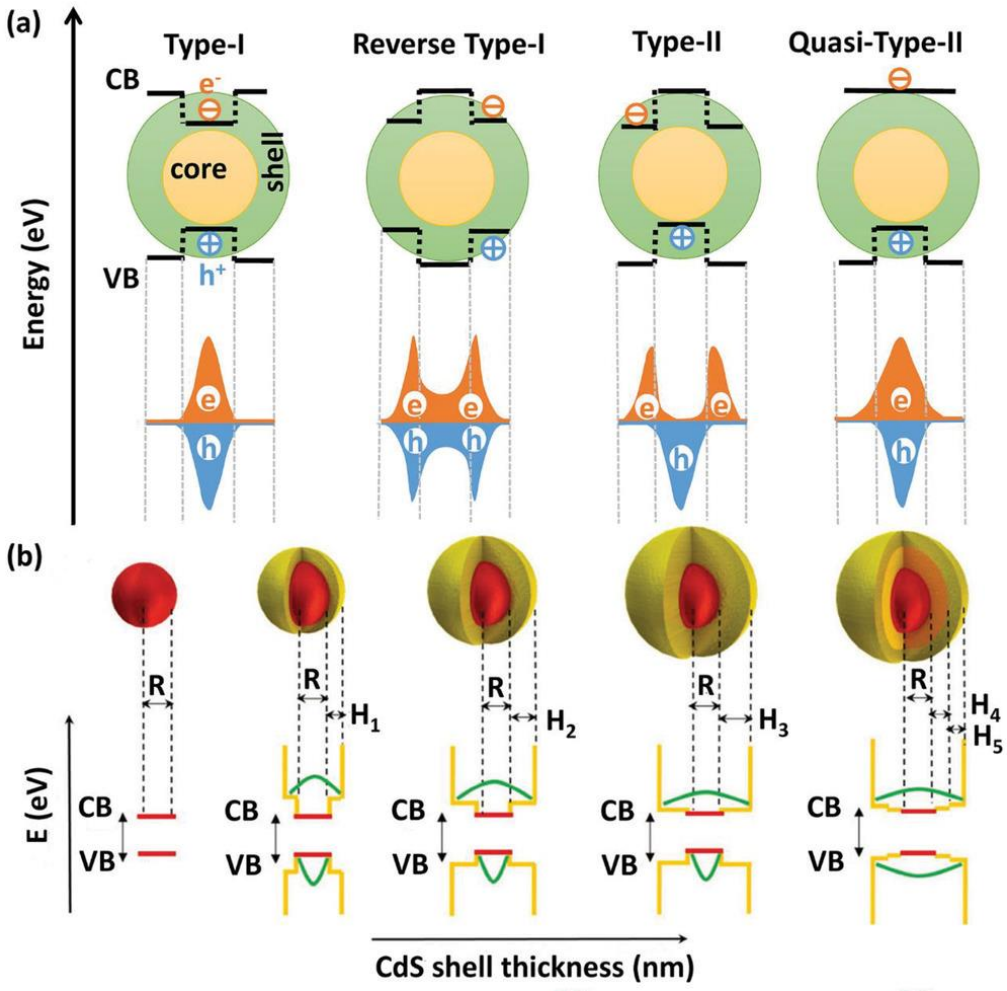

Figure 1.9 (a) Schematic representation of the exciton localization regimes in different types of core-shell QDs. The plus and minus signs represent the hole and the electron. (b) Schematic illustrations of engineering energy band alignment and carrier confinement properties of core-shell QDs with the shell thickness increase.[98]

As shown in Figure 1.9, the core-shell heterostructures are generally classified into type I, reverse type I, type II, and quasi-type II structures depending on the relative alignment of the CB and VB edges of the monomer bound at the interface.[99] In the type I structure core-shell QDs, the bandgap of the core is smaller than that of the shell, and both band edges of the core are located in the band gap of the shell, such as CdSe/ZnS.[100] Therefore, both electrons and holes are confined in the core region, resulting in less interaction of core-localized e-h pairs (excitons) with surface traps compared with bare QDs, resulting in improved PLQY and photothermal stability.

In contrast, in Reverse type I QDs, the bandgap of the shell is smaller than that of the core, and both band edges of the shell are all located within the band gap of the core, such as

CdS/CdSe.[101] In this case, the energy level alignment results in partial or complete delocalization of electrons and holes in the shell region (depending on the shell thickness), which facilitates efficient charge extraction and enhanced charge injection rates.[98, 102, 103] Particularly, by increasing the thickness of the narrow-bandgap shell, the significant extension of the absorption spectrum to the long wavelengths can benefit from the absorption contribution of the shell.[104]

In a typical type II structure, the CB or VB of the shell material is staggered with that of the core. The band alignment results in the spatial separation of electrons and holes into distinct regions of the core-shell structure. One carrier is mainly confined within the core, while the other is located within the shell, so that photogenerated electrons and holes can be spatially distributed, such as CdTe/CdSe.[95] In particular, the effective band gap of type II QDs is highly dependent on the band energy offset of the core-shell, which can be precisely adjusted by modulating core size and shell thickness.[105]

A special case is the quasi-type II. In this case, only one type of carrier can be confined within the core region, while the other one is partially delocalized over the core-shell region.[106] By suitable tailoring the shell thickness and electronic band structure, the excitons generated in the core can have significantly longer lifetimes than pure thin-shell QDs due to the efficient leakage of electrons in the shell, forming a quasi-type II Band arrangement. For example, the CdSe/CdS thin shell QDs belong to type II QDs, while the “giant” CdSe/CdS core-shell QDs have typical quasi-type II band alignment properties.[24, 106] The lifetime of excitons generated in the core can be significantly longer than pure thin-shell QDs.[24]

More importantly, the reduction in the spatial overlap between electron and hole wavefunctions can reduce their Coulomb interactions, increase the lifetime of exciton states, and delay the charge recombination process, thereby increasing electron transfer rates.[95, 105] According to the previous investigation, inverse type I, Type-II and quasi-Type-II core/shell heterostructure QDs are suitable for PEC systems thanks to the superior charge transfer performance, including CdS/CdSe QDs,[101] CdSe/CdS QDs[107], CdSe/CdSeS/CdS QDs[108].

As shown in Figure 1.10, as the thickness of the shell increases and the composition ratio is adjusted, the electronic band structure of the core/shell QDs changes, leading to the formation of a quasi-type II core/shell structure.[109, 110] Giant QDs present superior photo-physical/chemical stability, suppressed non-radiative Auger recombination, improved QY, and prolonged multiexciton lifetime compared to both core QDs and core/thin-shell QDs. However, such a core-shell interface suffers from surface defects induced during shell growth, mainly due to the lattice mismatch between core and shell layers.[111, 112] For instance, the lattice mismatch between the

CdSe and CdS (4.4%) results in the interfacial strain at the interface between the CdSe core and CdS shell,[112] causing the formation of interface defects and undesirable carrier confinement potential.[96] In addition, the absorption spectrum of CdSe/CdS core-shell QDs is dominated by the CdS shell (E_g = 2.49 eV) because the thick shell of CdS is located on the CdSe core QDs surface. Simultaneously, the thick CdS shell acts as a physical and energy barrier during electron/hole injection.[113] Therefore, it is necessary to optimize the electron/hole injection rate and effective surface passivation of CdSe/CdS core-thick shell QDs through interface engineering of core-shell structures. Recently, a graded interface layer between the core and shell has been introduced to address this problem. The graded layer can strongly suppress Auger recombination for both biexcitons and charged excitons.[114] According to the previous report,[108] the gradient multi-shell QDs can extend the absorption range compared to core-shell QDs. Gurpreet et al. incorporated $CdSe_xS_{1-x}$ interfacial layers between the CdSe core and CdS shell in heterostructured core/shell QDs to investigate the PEC performance (Figure 1.10). The result shows that the $CdSe_{0.5}S_{0.5}$ gradient shell based QDs (Figure 1.10 b) exhibit a broader absorption spectrum towards longer wavelength, and better carrier separation, injection and transport rate compared to core-shell QDs (Figure 1.10 a). To further improve the performance, they also engineered the $CdSe_xS_{1-X}$ interfacial layers by modulating the Se: S molar ratios during the growth of each interfacial layer. The resulting newly graded alloyed QDs (Figure 1.10 c) show a broader absorption response, higher electron-hole transfer rate and modified confinement potential as compared to $CdSe_{0.5}S_{0.5}$ graded QDs and core-shell QDs. It also causes more favorable band alignment, where the gradient layer can serve as a “ladder” for electrons to overcome the original high energy barrier. Therefore, by adding the alloyed interface layers, a gradient band structure is introduced that can significantly accelerate the charge carrier transition, leading to reduce charge recombination.[115] These results show that interface engineering can improve the optoelectronic properties of core-shell QDs, providing a promising approach to improve the performance of optoelectronic technologies based on QDs.

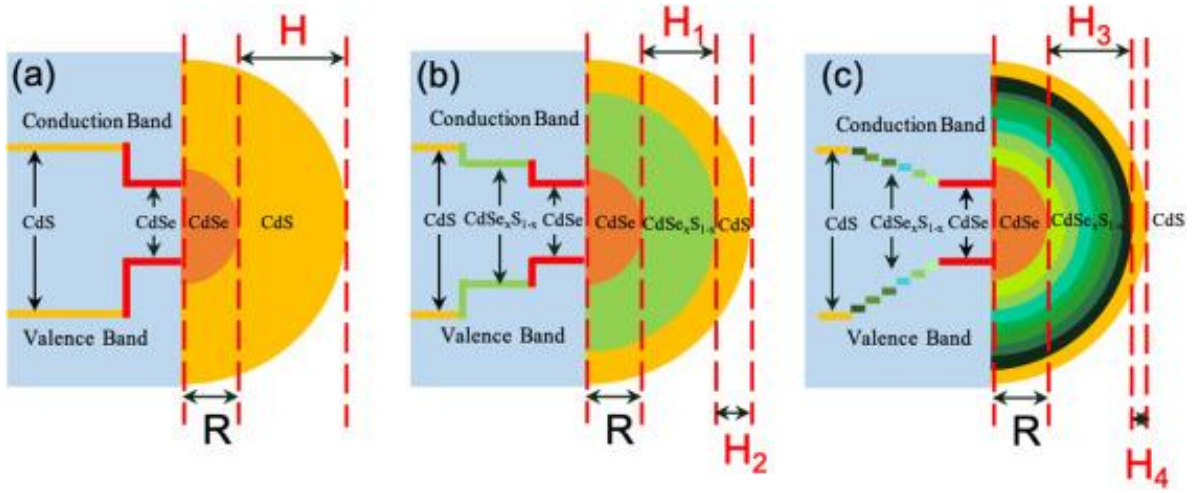

Figure 1.10 Schematic illustration of internal interfacial structures and carrier confinement potentials of QDs. R is the Radius of CdSe QDs and H is the shell thickness.[108]

1.3.3 Doped QDs

Element doping strategy also can improve the PEC performance by adjusting carrier transport, band structure, and surface active sites. In detail, the introduction of elements into the QDs can increase carrier density and further improve carrier transport performance. In addition, element doping in semiconductor QDs can also generate electronic states that allow for altered exciton recombination dynamics.[59, 116] For instance, the dopant could create electronic states in the intragap region of the QDs, altering the exciton recombination dynamics.[117] Thereby improving the light absorption capacity and the redox capacity of the photoelectrodes.

Doping with transition metal ions, such as manganese (Mn),[118, 119] copper (Cu)[117, 120] and zinc (Zn)[59, 121], allows modification of the electronic, magnetic, and photophysical properties of QDs. For example, Mn doping can significantly adjust the magnetic and electronic properties of Cu_2ZnSnS_4 and perovskite ($CsPbX_3$, $CsGeX_3$) nanocrystals.[119] Many types of optoelectronic devices use doped QDs as light collectors and show better performance than pure QDs, such as QDs-sensitized solar cells using Mn-doped CdS/CdSe QDs [118] and QDs-based luminescent solar concentrators (LSCs) using Mn-doped ZnSe QDs.[122]

Cu-doped ternary semiconductor nanocrystals have been recently developed as a kind of color-tunable and efficient light emitters.[123] By modulating the molar concentration of Cu dopants and varying the proportion of Zn: In, the UV-vis-NIR absorption and PL spectra window can extend to a wide light harvesting range to achieve the best use of solar energy. In addition, other unique advantages including the long carrier lifetime, and suitable band structure for water splitting,

suggest the enormous advantages of solar-driven PEC H_2 production.[124] Luo et al. demonstrate that the appropriate Cu doping to ZnInSe QDs could effectively extend the light absorption range by introducing an intra-bandgap state (Figure 1.11 a).[117] The optical properties, electronic structure, carrier lifetime and charge transport of QDs can be fine-tuned by optimizing the proportion of Cu ions and Zn: In atoms in the synthesis process. This improved carrier dynamics of Cu(5%): ZISe-1:4 QDs leads to the efficient separation of electron/hole pairs and provides sufficient time for charge carriers to participate in the PEC water-splitting reactions and result in the enhanced PEC performance (Figure 1.11 b and c).

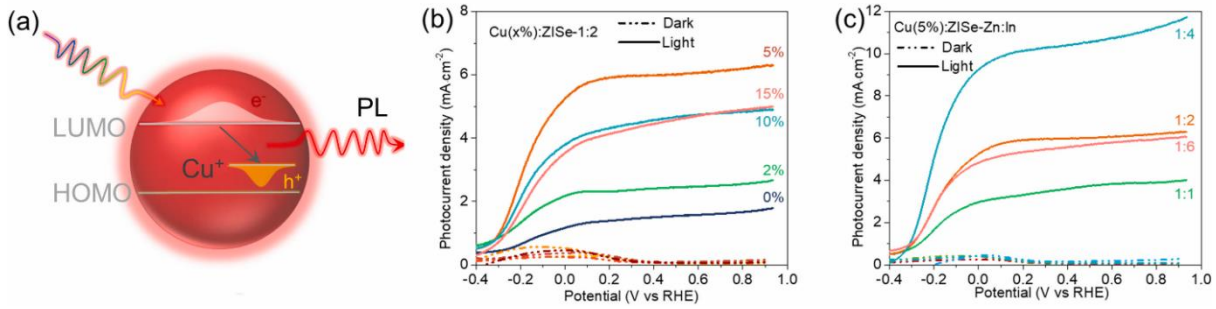

Figure 1.11 (a) Schematic of PL emission mechanism of Cu doped ZnInSe QDs; The current densities depending on (b) altered Cu molar percentage and (c) fixed Cu (5%) with altered Zn: In ratios of Cu doped ZnInSe QDs sensitized TiO_2 photoanodes.[117]

Simultaneously, previous works also have demonstrated that transition element Zn doped $CuInS_2$ and $CuInSe_2$ semiconductor nanocrystals possess the tuned band gaps and band position by modulating not only the size but also the compositions of particles.[59] At present, the $ZnCuInS_2$ QDs have been used successfully for QDs-sensitized solar cells.[125] For instance, it has been shown that the bandgap of Zn-doped $CuInS_2$ QDs can be tuned by modulating the Zn: Cu ratio, improving the PL properties.[121] Furthermore, the Zn doping could allow modulation of the conduction band edge for $ZnCuInSe_2$ QDs (Figure 1.12), increasing the energetic driving force for injecting photo-generated electrons from QDs into opportune charge transport materials, such as TiO_2.[125, 126]

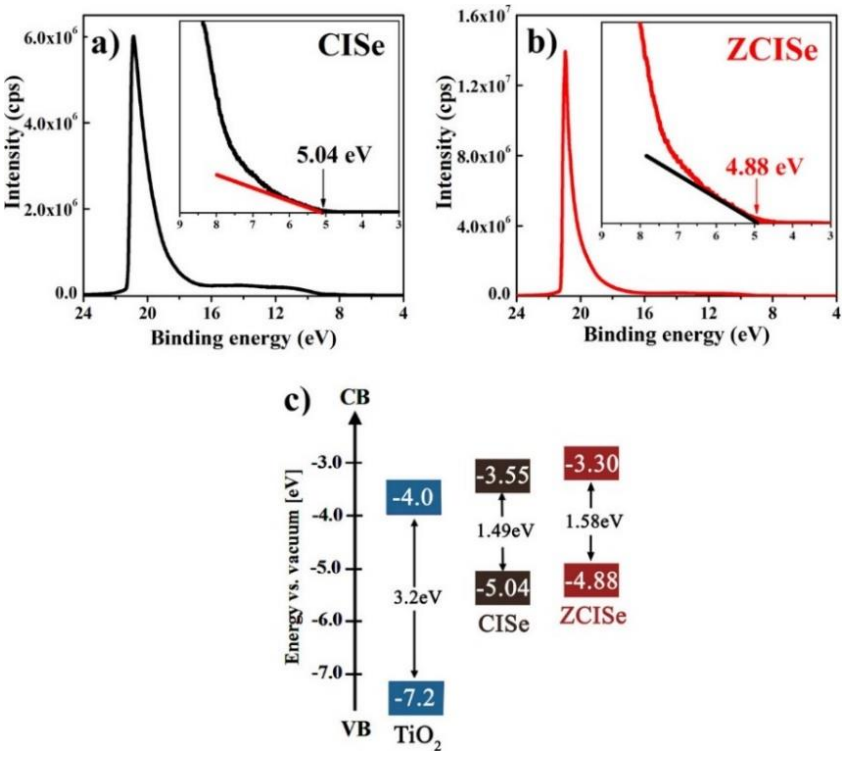

Figure 1.12 UPS spectra of CuInSe (a) and ZnCuInSe (b) QDs. (c) Schematic energy level diagrams of TiO_2, CuInSe, and $ZnCuInSe_2$ QDs.[59]

1.4.3 QDs synthesis

There are mainly two different routes for the QDs by wet chemistry method, namely, in-situ and ex-situ approaches.[83, 104, 127] The in-situ synthesis approach was widely used to prepare QDs-sensitized photo-electrodes, including chemical bath deposition (CBD)[128, 129] and successive ionic layer adsorption and reaction (SILAR)[127, 130]. These in-situ approaches allow the direct nucleation and growth of QDs on the matrix surface, resulting in the direct growth of QDs on mesoporous metal oxides such as TiO_2, ZnO, and SnO_2 photoelectrodes. In particular, this SILAR approach was proposed by Nicolau in 1985.[131] It is a heterogeneous chemical reaction in which cations and anions are absorbed in the solid-liquid interface.[57] In general, the SILAR reaction is as follows (Figure 1.13): $m[CLp]^{n+} + n[AL'q]^{m-} \rightarrow C_mA_n \downarrow + mpL + nqL'$. Where the L and L' represent different ligands, while the $[CLp]^{n+}$ and $[AL'q]^{m-}$ are cations and anions, respectively. After each soak, the substrate with core-shell/array should be rinsed with deionized water to remove the unreacted ions. Whereas in the QDs synthesis combined with the hot injection technique, a SILAR method can precisely control shell thickness layer-by-layer, in which cation and anion precursors are injected alternately so that only half of the monolayer is deposited at a time.[132] In-situ growth is a

double-edged sword because the prepared QDs by the in-situ approach possess a broad size distribution, but it has close contact and sharp interface with the matrix substrate, which is beneficial for processes such as exciton dissociation and charge injection because they are critically dependent on the QD-surface distance.[133]

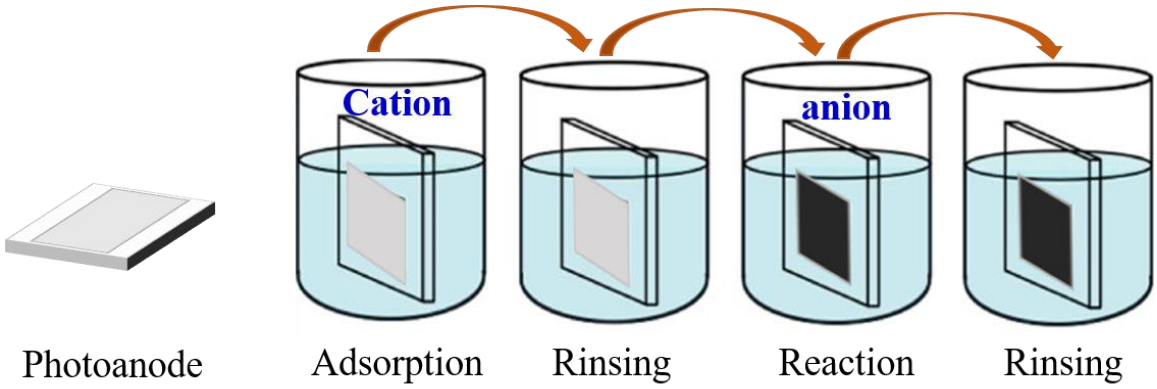

Figure 1.13 Schematic illustration of In-situ fabrication methods (SILAR) of QDs on photoanode.

For ex-situ synthesis colloidal QDs, the hot injection method is a significant representational strategy. Colloidal QDs synthesized by ex-situ approach, have the advantage of very narrow size distribution, which leads to well-defined optical and electronic properties in terms of exciton absorption peak and PL.[134] Normally, the hot injection method is usually carried out in an organic solvent, where the organometallic precursors are mixed in the presence of stabilizers such as surfactants (Figure 1.14). In a typical process, the mixture of cationic precursor and solvent is heated to a relatively high temperature to obtain a clear solution. Then, an inert gas was then added to prevent oxidation and the mixture was heated to a fixed high temperature (100~330°C). The non-metallic (anionic) precursor is then injected into the mixture for nucleation and growth.[135] More importantly, the size, shape and structure of QDs can be controlled by adjusting experimental parameters such as the types of precursors and surfactants, the molar ratio of precursors and concentration, the reaction temperature and reaction time, and further, their optical properties can be regulated. The QDs prepared by hot injection have a narrow size distribution and good crystallization. In addition, the prepared colloidal QDs reveal well-controlled optical and electronic properties in terms of absorption, PL, and lifetime. In this thesis, the colloidal QDs were prepared by the ex-situ hot injection approach.

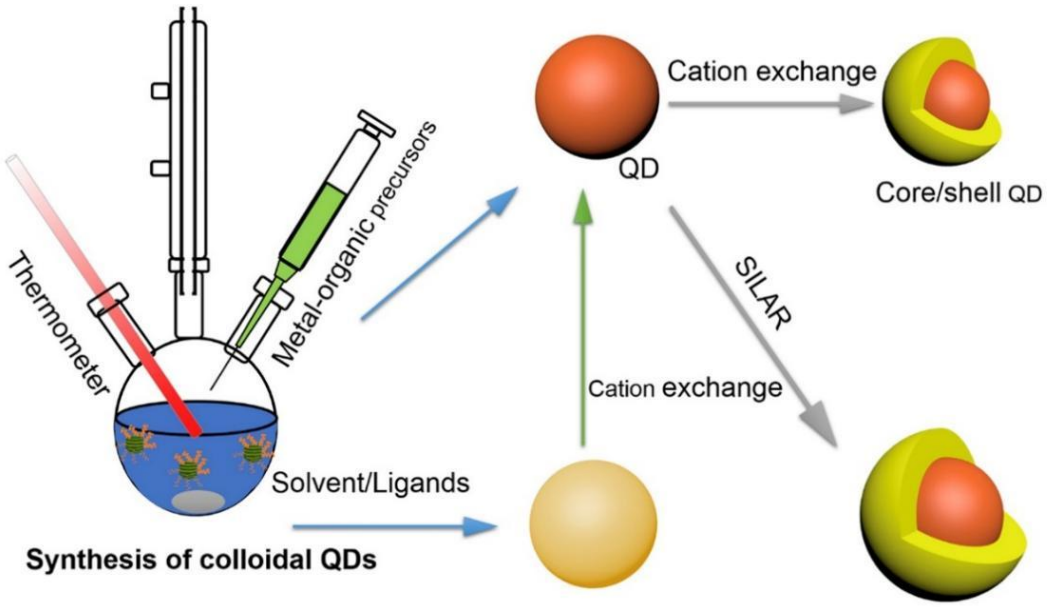

Figure 1.14 Schematic illustration of the Synthesis of Colloidal QDs. The core QDs can be synthesized via the hot injection approach. The core-shell structure can be obtained via both a cation exchange approach and a SILAR approach. Figure 1.14 was taken from reference.[83]

To synthesize core-shell or core-gradient shell-shell QDs, cation exchange and the SILAR approach are promising. Cation exchange provides a method for preparing materials that cannot be directly synthesized.[136, 137] Instead of depositing or growing the target material directly on the pre-existing material, the cation exchange method replaces the original cations with guest cations, resulting in the chemical conversion of one material to another. A notable example in this direction is partial cation exchange. The nanocrystals performed in this way can be transformed into alloy nanocrystals or various types of nano-heterostructures with core-shell, segmented, or striped structures.[137, 138] As an alternative to traditional synthesis methods, chemical transformation of existing nanostructures provides another efficient method for the synthesis of another nanostructured material with precise control of chemical composition, structure and morphology.[139] A significant advantage of the ion-exchange approach is the ability to create interfaces or heterojunctions within nanostructured materials through partial transformation.[140] Simultaneously, compared with the traditional epitaxial growth method of outgrowth, the ion exchange process is less regulated by the lattice parameters of the seed matrix due to its unique ingrowth mechanism.[54] For most semiconductor materials, the anions act as the structural framework, while the cations are relatively mobile in the crystal lattice. Therefore, chemical transformation by cation exchange is relatively easy to achieve. The rapid development of cation

exchange technology has greatly expanded the synthetic versatility of preparing heterojunctions, which was previously difficult or impossible to achieve.

The cation exchange approach was used to synthesize core-shell QDs, where the as-synthesized QDs are used as templates. For instance, this approach has been widely used to synthesize core-shell heterostructures of lead chalcogenides, such as PbS@CdS, and PbSe@CdSe, where the precursor of the cationic component of the shell material was introduced to partially replace the cations in the core material, while the anion sublattice is basically undisturbed (Figure 1.15a).[141, 142] In other words, shell growth is at the cost of sacrificing the crystal core by replacing the cation in the crystal core with the cation newly introduced in the solution. The overall size of the QDs does not change. The results show that the growth of the shell is accompanied by the decrease of core in the process of cation exchange. In other cases, it also can achieve the full cation exchange by controlling the ratio of cation, such as the CdTe to HgTe cation exchange (Figure 1.15b).[143]

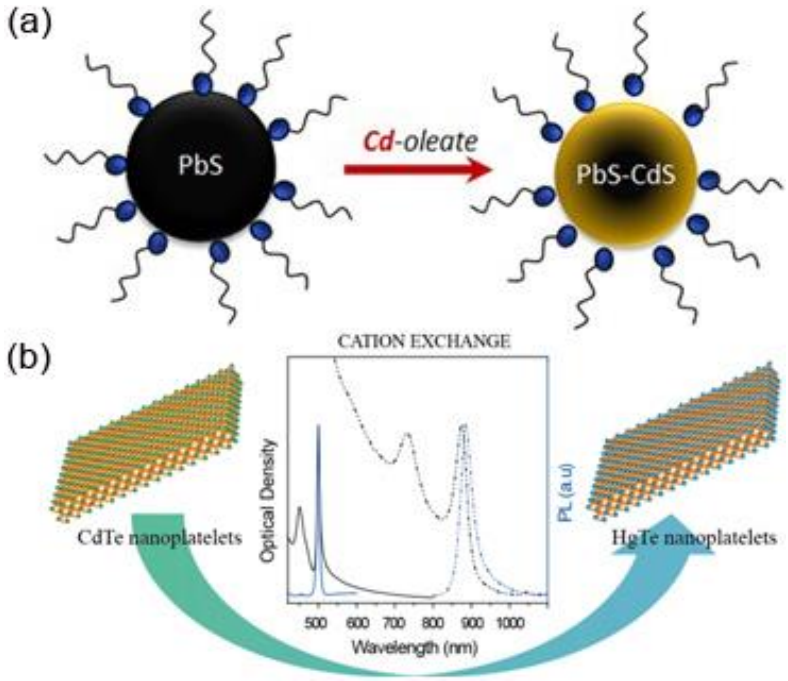

Figure 1.15 Schematically illustrates: (a) the Pb to Cd partial cation exchange on the PbS surface to prepare PbS@CdS core-shell QDs; [142] (b) fully cation exchange of CdTe to HgTe.[143]

The SILAR approach is also a representative and common approach to synthesizing core-shell or core-gradient shell-shell QDs. Shell growth is based on alternating injection of cationic and anionic precursors to form a monolayer at a time, which was initially applied for the CdSe@CdS

QDs synthesis.[144] Whereas in the QDs synthesis combined with the hot injection technique, a SILAR method can precisely control shell thickness layer-by-layer, in which air-stable cationic and anionic precursors are injected alternately so that only half of the monolayer is deposited at a time.[132] By temporally separating the growth of each half-monolayer, secondary nucleation is avoided, and the epitaxial semiconductor layer is more uniform. However, the high overgrowth temperature of the shell elements, which requires good thermal stability of the core, limits the selection of suitable materials in the core-shell architecture. In the process of SILAR coating, the core size is basically unchanged, and the shell thickness can be effectively adjusted in the monolayer.[144]

1.5 2D structure

Heterojunctions based on 2D materials have attracted extensive research interest due to their unique structures and excellent electronic and optoelectronic properties. In contrast to conventional epitaxially grown heterostructures of different materials, arbitrary combinations of 2D layer materials can be stacked mechanically via weak van der Waals interlayer interactions to form vertical heterojunctions without strict lattice matching constraints.[54] The construction of 2D layered composite photocatalysts can produce many unique properties that other types of semiconductor composite photocatalysts do not exist, which is beneficial to the improvement of photocatalytic performance, the adjustment of band gaps, and the formation of heterojunctions. In addition, the van der Waals heterojunctions provide a perfect platform for probing optoelectronic processes and underlying physical mechanisms at the atomic scale due to the structure of atomically thick layers.[54] Compared with 0D and 1D materials, 2D layered materials have many extraordinary advantages (Figure 1.16), which make them promising candidates for conducting high-performance energy conversion and environmental remediation applications. Generally, the 2D layered structure is conducive to shortening the transport time and distance of charge, resulting in more efficient charge separation and transfer.[71] Because the excited holes/electrons with long lifetimes and short travel are favorable for the oxidation/reduction reaction process. In addition, 2D layered materials possess larger specific surface areas than their bulk structures.[145, 146] Furthermore, some 2D layered materials (such as graphene) possess superior electrical conductivity and electron mobility due to the existence of a 2D π-conjugated structure, providing an ultrafast electron transfer platform to facilitate the separation and transfer of photogenerated charge carrier, reducing the recombination.[71, 147] The advent of van der Waals (vdW) bonded layered materials, such as graphene and transition metal dichalcogenides (TMDs)

has opened up a new era of atomically thin materials for fundamental scientific research and applied device design.[60]

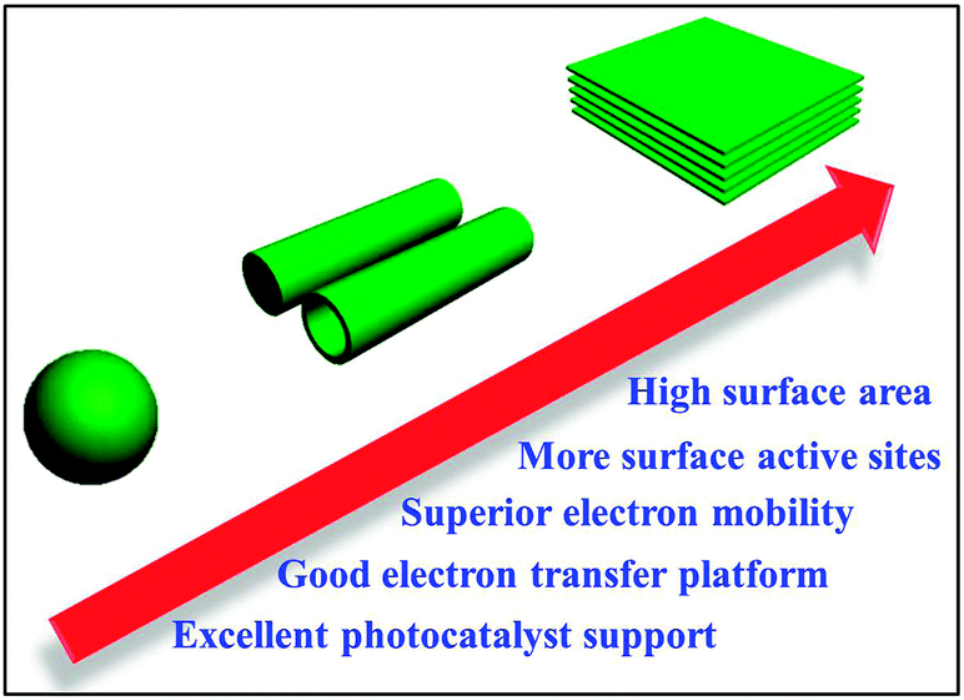

Figure 1.16 Schematic illustration of the advantages of 2D layered materials in comparison with 0D and 1D materials. The 2D layered materials possess large surface areas, more surface active sites and superior electron mobility, and can serve as good electron transfer platforms, and excellent photocatalyst supports.[148]

1.5.1 Graphene

Graphene, a typical two-dimensional (2D) layered material, has experienced a glorious era since it was first mechanically exfoliated from bulk graphite in 2004.[149] Graphene has a single atomic layer of carbon with all atoms covalently bonded in a honeycomb lattice, is a strictly 2D zero-bandgap semi-metal material with a small overlap between its CB and VB.[150] The absence of an electronic bandgap in graphene restricts its applicability as an absorber in solar energy conversion. However, charge carriers in graphene move with extraordinarily high mobility, making graphene a highly conductive-layered material. As a representative conductive carbonaceous matrix, 2D monolayer graphene has attracted increasing attention both in basic science and potential applications due to its unique structure and excellent performance such as high transparency (97.7% transmittance in the visible spectrum), high electrical conductivity ($\sim 10^4\ \Omega^{-1}\cdot cm^{-1}$), high specific surface area (2630 m^2/g), and superior chemical stability.[66, 151-154] In particular, graphene with a unique 2D microstructure and surface chemical structure, can inhibit the excessive growth

of guest species, thereby preparing ultra-thin nanostructures, which is conducive to enhancing reaction kinetics. Thus, graphene can be used not only as a substrate for epitaxial growth, but also as an electroactive material to improve electrical conductivity. In addition, it can use as an electron mediator for shuttling electrons, leading to effective separation of photo-generated carriers at the junction interface.[71, 147]

In addition to serving as a sink and shuttle of photo-excited electrons, the chemical bond and nano-Schottky interface formed at the contact between the semiconductor and graphene can also narrow the bandgap of the semiconductor hybrid to expand the absorption range, thus leading to enhanced PEC activity.[147, 155] For instance, Feng et al.[156] and Yu et al.[68] demonstrated that reduced graphene oxide could improve the PEC and photocatalytic water splitting performance of 2D/3D (3D nanostructured carbon supported on graphene) and 0D/2D (Pt/CdS/graphene) hybrids, respectively. Xiao et al. demonstrated a facile layer-by-layer self-assembly approach for the construction of well-defined graphene-CdS QDs multilayered films for photoanode.[157] According to the linear sweep voltammetry (LSV) (Figure 1.17 a) and electrochemical impedance spectroscopy (EIS) results (Figure 1.17 b), the graphene could improve the PEC performance and reduce the charge transfer resistance, by providing low-resistance channels to shuttle the photo-generated electrons and holes on the interfaces. Figure 1.17 c illustrates the PEC mechanism over the graphene-CdS QDs multilayered films based photoanode. The energy level diagram of the graphene-CdS QDs hybrid system is shown in Figure 1.17 c. It can be seen that the CB of the CdS QDs is located above the work function of graphene, indicating favorable charge transfers from the CB of the CdS QDs to graphene under light irradiation. The photoexcited electrons are captured by graphene and then can be swiftly transferred to the FTO substrate, thereby separating the photogenerated electron-hole carriers and generating photocurrents. In addition, graphene derivatives with similar properties also exhibited improved photostability of metal sulfides. For example, Jia et al. prepared N-doped graphene/CdS photocatalysts, in which N-graphene acts as an electron transfer channel to reduce the recombination of electron-hole pairs, the photocatalytic performance did not show any obvious decrease due to the presence of N-graphene.[158] Ning et al. demonstrate the synergistic effect in this ternary TiO_2/rGO/NiFe-layered double hydroxide (LDH) photoanode gives rise to a largely enhanced photoconversion efficiency (0.58% at 0.13 V) and photocurrent density (1.74 mA cm^{-2} at 0.6 V) (Figure 1.17 d) and also exhibits excellent stability with negligible photocurrent decay (3%) after 3 h of PEC water splitting reaction. Experimental results show that reduced graphene oxide (rGO) with a high work function (Figure 1.17 e) and superior electron mobility accepts photogenerated electrons from TiO_2 and enables fast electron transportation.[159] An experiment-calculation combination study

reveals a mechanism for enhancing the oxidation performance of PEC water is proposed, as shown in Figure 1.17 f. The superior electron mobility of rGO enables electrons to migrate rapidly to the collector, significantly inhibiting electron-hole recombination, and improving the charge separation efficiency and photostability. These studies highlight the advantages of graphene in inhibiting the recombination of photoinduced electron-hole pairs and suggest the promising potential for the use of graphene to improve photostability.

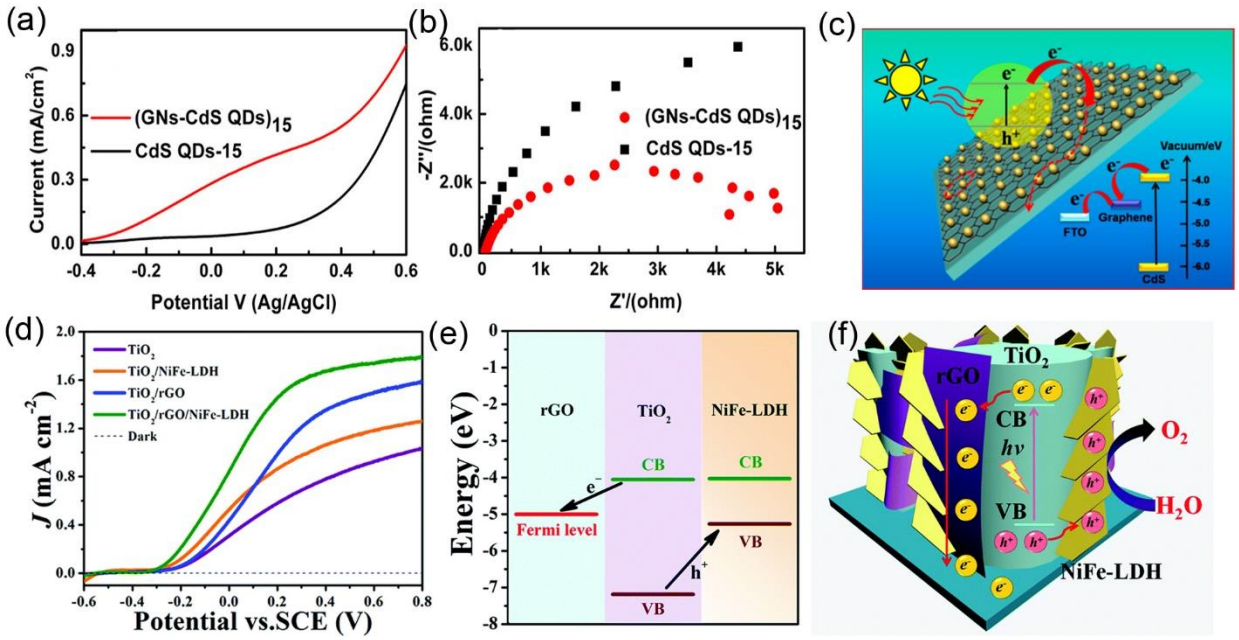

Figure 1.17 (a) Photocurrent–voltage curves *(J-V)* and (b) EIS Nyquist plots of CdS QDs film and graphene–CdS QDs multilayered film with the 15 deposition cycles in 0.1 M Na_2S aqueous solution under visible light irradiation (λ > 420 nm); (c) Schematic illustration of the PEC mechanism over the graphene-CdS QDs multilayered films.[157] (d) current-voltage (*J-V*) curves in 0.5 M Na_2SO_4 aqueous solution; (e) Band edge placement of TiO_2, rGO and NiFe-LDH; (f) a schematic illustration of the PEC water oxidation process in the TiO_2/rGO/NiFe-LDH core-shell NA photoanode.[159]

1.5.2 MoS_2

The rapid development of graphene research and the development of fabrication methods for ultrathin nanolayers has inspired the exploration of other 2D materials.[160] Transition metal dichalcogenides (TMDs) with a layered crystal structure, have recently received increasing attention not only as co-catalyst for PEC device but also as thin-film based photoelectrodes owing to their unique electronic and optical properties, such as high carrier mobility, strong light-matter interaction.[28]

Previous works show that 2D-TMDs are more sensitive to photons of different energies compared to graphene.[161, 162] Meanwhile, it is also demonstrated that the nested band structure of the 2D-TMDs induces strong interband absorption above the fundamental band gap.[163] Such properties enable 2D-TMDs, such as Molybdenum disulfide (MoS_2) exhibit a robust photon-electron coupling effect, leading to enhanced photoelectric reaction activity.[164] It has been found that the optical and physicochemical properties of MoS_2 could be easily adjusted by modulating the number of layers. The bulk MoS_2 is composed of a multi-layer structure, and the Mo atomic plane of the multi-layer structure is sandwiched between two S atomic planes, arranged in a trigonal prismatic arrangement, exhibiting an indirect-direct bandgap transition of 1.1~1.3 eV. The 2D MoS_2 nanosheet structure exhibits a direct band gap of 1.7~1.96 eV.[165, 166] Both computational and experimental studies have confirmed that the monolayer and few-layer MoS_2 possess suitable band edge positions for PEC water splitting.[167] The narrow-bandgap of few-layer MoS_2 can also expand the light absorption range of wide-bandgap semiconductors, thereby improving the utilization efficiency of light energy.

In addition, MoS_2 NSs are considered to be a promising photoanode material for PEC water splitting (as shown in Figure 1.18), due to their free energy of hydrogen adsorption being close to zero, which is quite close to Pt.[162] Therefore, constructing a hybrid heterojunction between MoS_2 and other semiconductors should be a promising approach to overcome the intrinsic limitations of some semiconductors and improve the PEC performances.[168]

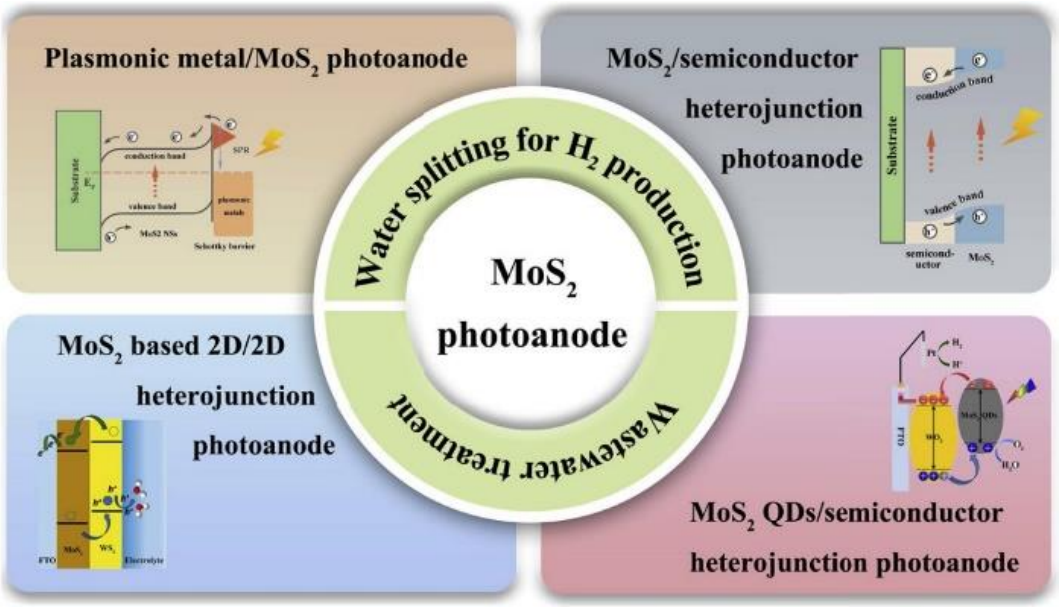

Figure 1.18 MoS_2-based photo-anode and application.[53]

To date, MoS_2-based semiconductor heterostructures with good photocatalytic or PEC properties, such as MoS_2/WS_2,[167] MoS_2/CdS,[169], MoS_2/PbS[67], and MoS_2/TiO_2,[170] have been successfully synthesized. In these structures, effective charge separation can be achieved by coupling two semiconductor structures with matched energy levels. In addition, as expected for the higher lying S 2p orbitals, the valence band edges of few-layers MoS_2 are much closer to the water oxidation potential, compared to metal oxide semiconductors,[167] which indicates potential use as photoanodes for water oxidation.[171] Many different morphologies for MoS_2 have been developed and used as visible light sensitizers in photocatalytic and PEC systems.[162, 172, 173] In particular, hierarchical structures of NSs assembled in flower-like morphology present a large surface area and good permeability, which can increase the active sites and light utilization rate through multiple scattering of incidence light, making them an ideal candidate for high-efficiency photocatalysts.[174, 175] In addition, the large surface area of 2D MoS_2 allows the robust anchoring of QDs onto its surface, which will facilitate efficient electron injection from QDs to 2D MoS_2.[48] Simultaneously, effective metal doping can also enhance the electrocatalytic activity, leading to better conductivity. It will effectively accelerate the charge transfer and reduce charge recombination. In addition, Shi et al. confirmed that the non-precious metal Zn doping in MoS_2 could effectively modulate the band position.[176]

For instance, Pesci et al. has demonstrated MoS_2/WS_2 type II heterojunction for efficient PEC devices (Figure 1.19 a and Figure 1.19 b).[167] As shown in Figure 1.19 c, the LSV of WS_2 and MoS_2 NSs films were recorded with the difference between light and dark current, corresponding to the photocurrent (see blue and black lines). Both thin films of solution-processed WS_2 and MoS_2 photoanodes show positive photocurrents under low overpotentials, with an onset at +0.6 V for WS_2 and +0.7 V for MoS_2 under simulated solar irradiation, respectively. In addition, the photocurrent generated by the MoS_2/WS_2 heterojunction is one order of magnitude larger than MoS_2 and twice higher than that WS_2 electrode. This significant enhancement could ascribe to the better band alignment formed at the interface of the two materials, which promotes electron-hole separation and prolongs the carrier's lifetime. Huang et al. constructed a photodetector based on MoS_2/graphene heterostructure and investigate the PEC mechanism.[177] Figure 1.19 d illustrates the schematic diagram of the proposed photodetector based on MoS_2/graphene heterostructure. Figure 1.19 e displays the LSV of the bare MoS_2, graphene, and MoS_2/graphene heterostructure respectively. A significant improvement in current density is observed in MoS_2/graphene heterostructure-based photoanode compared to bare MoS_2 and graphene-based photoanodes. Simultaneously, it is noteworthy that the photocurrent of the MoS_2/graphene heterostructure is about 2.5 times more than that of the bare MoS_2 and the photocurrent is very

stable without any obvious photocurrent decay (Figure 1.19 f). Therefore, MoS_2-based heterostructures are promising in the construction of highly efficient PEC devices.

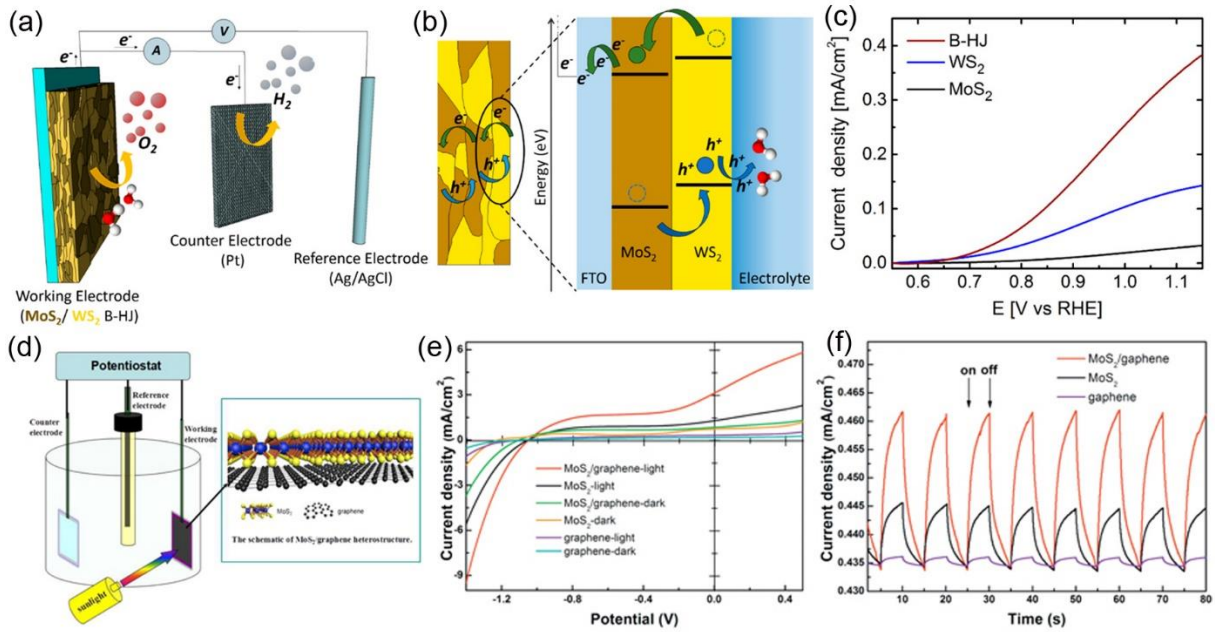

Figure 1.19 Illustration of (a) different PEC cell components (labeled) and (b) electronic band structure alignment of a type II junction and electron and hole dynamics; (c) LSV curves of MoS_2, WS_2, and MoS_2/WS_2 heterojunction based photoanodes under 1 sun irradiation (100 mW cm^{-2} under simulated AM 1.5G conditions) in mixed 0.5 M $NaClO_4$ electrolyte solution. (Milli-Q water, pH 1, $HClO_4$).[167] (d) A schematic diagram of the PEC-type photodetector with a model of the MoS_2/graphene heterostructure; (e) LSV curve vs. bias voltage and (f) photocurrent transient response of bare MoS_2, graphene and MoS_2/graphene heterostructure based photoelectrodes under sunlight irradiation (40 mW cm^{-2}) with zero bias voltage.[177]

1.6 Thesis Objectives

As discussed above, the consumption of non-renewable fossil fuels has caused serious energy crises and environmental pollution, which seriously threatens human health. Therefore, the development of green, environmentally friendly, and sustainable energy is imminent. Solar-driven PEC water splitting using semiconductor photoelectrodes is a promising approach for sustainable and environmentally friendly production of renewable energy fuels, such as H_2. Since the pioneering work of Fujishima and Honda in 1972, varieties of semiconductors have been used to construct photoelectrodes for PEC devices. Despite major progress, these materials still face several significant challenges. In particular: (1) metal oxides usually possess a large bandgap that limits sunlight absorption; (2) Not all semiconductors have a favorable band alignment to realize both redox processes (water reduction and oxidation); (3) low electrical conductivity and

limited hole diffusion length; (4) charge recombination can occur easily in the bulk and on the surface, limiting the efficiency of the system.

To address these above-mentioned challenges, semiconductor heterojunction-based PEC devices are promising candidates. Mixed-dimensional heterojunctions can utilize the synergistic effect of each component to enhance optoelectronic properties. To extend the absorption range, the 0D QDs were introduced to the heterojunction thanks to the tunable band position and absorption range due to the quantum confinement effect. However, the photocurrent density enhancement mechanism of different types of QDs (core-shell QDs, gradient QDs and doped QDs) in different heterojunctions remains to be explored.

Therefore, the objectives of this thesis are as follows:

(1) The first project intends to investigate the influence of band alignment to charge injection in 0D/2D heterostructure. Few works have reported 0D/2D hybrids of QDs/MoS_2, however to date, the role of different QDs and the band alignments between 0D QDs and 2D MoS_2 to enhance PEC performance is rarely investigated. Herein, we designed to modulate the charge injection of 0D/2D heterostructure by doping to adjust the band alignment between the proposed 0D/2D heterostructure. Because the appropriate band alignment between the heterostructure could accelerate the charge separation and reduce the charge recombination, further improving the PEC performances. In detail, we synthesize Zn-doped MoS_2 with tunable bandgap position by doping, then PbS@CdS core-shell QDs are loaded by *in-situ* method to construct 0D/2D heterojunction. The PEC performance enhancement mechanisms in this project were analyzed in detail.

(2) QDs with a gradient multi-shell have been developed and due to an improved band alignment and favorable charge transfer, devices based on these QDs have shown superior performance compared to the single core or core/shell QDs. At present, the majority of PEC systems based on QDs typically use heavy metal elements, such as Pb and Cd, which are toxic. However, to date, there are no reports on heavy-metal-free gradient multi-shell QDs as light harvesters for PEC devices. The development of heavy metal-free QDs for PEC applications is a major unresolved challenge in this field. For the second project, a sequential cation exchange approach was used to synthesize heavy metal-free, gradient multi-shell architecture $CuInSe_2/(CuInSe_xS_{1-x})_5/CuInS_2$ QDs. The photocurrent density enhancement mechanism is expounded through the experimental results combined with the theoretical calculation.

(3) Inspired by the first and second projects, in the third project, we design and synthesize Zn-doped $CuInS_2$ eco-friendly QDs and modulate the band position by different amounts of dopant. Subsequently, construct 2D/2D MoS_2/rGO heterojunctions to enhance the conductivity of MoS_2 to inhibit charge recombination. By constructing 0D/2D/2D heterojunctions, combined with their band alignment after different amounts of Zn doped eco-friendly QDs to investigate the PEC mechanism in detail. The distinctive 0D/2D/2D heterojunction can leverage the light-harvesting capabilities of QDs with the catalytic and conductivity performance of 2D NSs.

1.7 Thesis organization

This thesis is divided into seven parts and organized as follows:

Chapter 1 generally introduces the research background of this thesis and outlines the motivation and main goals for this work.

Chapter 2 describes the basic experimental reagent and the characterization methods for synthesized nanomaterials.

Chapter 3 reports the effects of metal chalcogenide QDs, such as PbS, CdS, and their composite PbS@CdS QDs, and the doping amounts of MoS_2 are analyzed and correlated to the change in PEC performance. After optimizing the Zn doping amount and the QDs composition, the PEC devices based on proper band alignment showed an outstanding 200% improvement in photocurrent density compared to the benchmark samples. We analyzed in detail the mechanisms that underpin this significant enhancement, ascribing it to the wide absorption range of QDs, the zinc coordinating sites of MoS_2 NS, and the creation of favorable stepwise electronic band alignment. This synergistic effect offered by the 0D/2D heterojunction improves the electron transfer rate and reduces the charge recombination, leading to superior solar-driven PEC performance. This work demonstrates a new platform for solar-to-hydrogen energy conversion from solution-processed MoS_2 hierarchical thin film and further provides insight into the importance of band alignment engineering to control photoelectrode performance. The publication related to this chapter is:

***Faying Li**, Daniele Benetti*, Min Zhang, Jinhui Feng, Qin Wei*, and Federico Rosei*. Modulating the 0D/2D Interface of Hybrid Semiconductors for Enhanced Photoelectrochemical Performances. Small Methods, 2021, 5(8), 2100109.*

Chapter 4 demonstrates a template-assisted cation exchange approach for the fabrication of eco-friendly $CuInSe_2$/$(CuInSe_xS_{1-x})_5$/$CuInS_2$ QDs based on a gradient multi-shell architecture,

exhibiting tunable Near Infra-Red (NIR) optical absorption and photoluminescence (PL) properties. We analyzed in detail the mechanisms that underpin this significant enhancement and are ascribed to a favorable stepwise electronic band alignment, which improves the electron transfer rate and reduces charge recombination, due to the incorporation of interfacial gradient layers. The experimental data on exciton kinetics are supported also by the theoretical analysis of the electron/hole (e/h) wave function. PEC devices based on our novel gradient architecture showed an outstanding 200% improvement in photocurrent density compared to single core $CuInSe_2$ QDs, as well as a 73% improvement compared to the core-shell $CuInSe_2/(CuInS_2)_6$ structure. These findings represent a promising new concept of using 'green' multi-shell QDs to enhance the performance and stability of PEC hydrogen production. The publication related to this chapter is:

***Faying Li**, Min Zhang, Daniele Benetti*, Li Shi, Lucas V. Besteiro, Hui Zhang, Jiabin Liu, Shuhui Sun, Qin Wei*, and Federico Rosei*. "“Green”, gradient multi-shell $CuInSe_2/(CuInSe_xS_{1-x})_5/CuInS_2$ quantum dots for photo-electrochemical hydrogen generation." Applied Catalysis B: Environmental, 2021, 280, 119402.*

Chapter 5 reports the modulation of a 0D/2D heterojunction using 0D metal chalcogenide quantum dots (QDs) and 2D Zn doped MoS_2 hierarchical NS, fabricating then photoanodes for hydrogen production. The optoelectronic properties and band alignment of colloidal $ZnCuInS_3$ QDs were adjusted by tuning the ratio of the Zn/Cu component (from 0/1 to 3/1). We also analyzed in detail the mechanisms that underpin this significant enhancement, ascribing it to the appropriate band alignment between the optimal QDs and MoS_2/rGO as well as the superior conductivity of GO to accelerate the charge transfer and reduce the photo-generated charge recombination. The publication related to this chapter is:

***Faying Li**, Daniele Benetti*, Min Zhang, Li Shi, Jinhui Feng, Qin Wei*, and Federico Rosei*. "Tunable 0D/2D/2D nanocomposite based on green Zn-doped $CuInS_2$ Quantum Dots and MoS_2/rGO as photoelectrodes for solar hydrogen production." ACS Applied Materials & Interfaces, 2022, 14(49), 54790–54802.*

Chapter 6 briefly summarizes the important contributions of my Ph.D. research work and discusses future challenges and perspectives in this field.

Most of the work in this thesis was performed by myself, Faying Li, however, some parts were also carried out through collaboration. Especially, Dr. Daniele Benetti discussed the experimental details with me and give some constructive suggestions. The theoretical calculations part of electron/hole wavefunctions in Chapter 4 were performed by Dr. Lucas V. Besteiro, at the time

working in our group at the INRS-EMT center. In this theoretical calculation part, Faying Li I only participated in developing the model and discussing the results. I did not conduct the simulations. In addition, Dr. Daniele Benetti helped with the description of theoretical calculation. Steady and transit PL measurements in this thesis were conducted by Jiabin Liu.

Following the main body of this thesis is an appendix providing a summary of this thesis in French according to INRS requirements.

2 MATERIALS AND CHARACTERIZATION

2.1 Chemicals and reagents

Ammonium tetrathiomolybdate ($(NH_4)_2MoS_4$, 99.97%), zinc nitrate hexahydrate ($Zn(NO_3)_2 \cdot 6H_2O$, 98%), lead(II) nitrate ($Pb(NO_3)_2$, 99%), cadmium nitrate tetrahydrate ($Cd(NO_3)_2 \cdot 4H_2O$, 99%), hydrazine monohydrate ($N_2H_4 \cdot H_2O$, 98%), zinc acetate dihydrate ($Zn(Ac)_2 \cdot 2H_2O$, 98%), selenium (Se, 99.5 %), sodium sulfide nonahydrate ($Na_2S \cdot 9H_2O$, 99.9%), sodium sulfite (Na_2SO_3, 98%), cadmium oxide (CdO, 99.99 %), trioctyl phosphine oxide (TOPO, 99 %), tetrakis(acetonitrile)copper(I)hexafluorophosphate ($[(CH_3CN)_4Cu]PF_6$, 97 %), sulfur powder (99.99 %), indium acetate ($In(AC)_3$, 99.99 %), hexadecyltrimethylammonium bromide (CTAB), acetone, ethanol, methanol, toluene, titanium tetrachloride ($TiCl_4$, 30 %), zinc acetate ($Zn(Ac)_2$, 99.99%), cupric acetate monohydrate ($Cu(Ac)_2$, 99.99%), sodium molybdate dehydrate ($Na_2MoO_4 \cdot 2H_2O$, 99.95%) and thiourea (≥99.0%) were purchased from Sigma-Aldrich.

N, N-Dimethylformamide (DMF, 99.8%) was purchased from Fisher Scientifique. Acetonitrile and hexane were purchased from Bio Basic. Oleic acid (OA, 90 %), 1-octadecene (ODE, 90 %), trioctyl phosphine (TOP, 97 %), oleylamine (OLA, 97 %), 1-dodecanethiol (DDT, 99.9 %) were purchased from Sigma-Aldrich. Methanol and acetone were purchased from VWR. All chemicals were used as received without further purification. Distilled water (18.25 MΩ) was used throughout the study. Fluorine-doped tin oxide (FTO) coated conducting glass substrates with sheet resistance 10 Ω/square were purchased from Pilkington glasses. Titania paste containing active anatase nanoparticles ~20 nm in diameter (18 NR-T) and a mixture of active anatase particles (~20 nm) and larger anatase scattering particles (~450 nm) paste (18 NR-AO) were purchased from Dyesol/GreatCell Solar (Queanbeyan, Australia). All chemicals were used as received, without further purification.

2.2 Materials Characterizations Methods

This section contains various physical characterization techniques for the morphology, structure, composition, and optical characterization of the synthesized nanomaterials and prepared photoanode in this work.

The scanning electron microscope (SEM) and energy dispersive X-ray spectroscopic (EDS) mapping were performed using a JSM-6900F microscope (Japan). Transmission electron microscopy (TEM) and high-resolution TEM (HR-TEM) images were performed using a JEOL 2100 F

TEM equipped with energy dispersive X-ray spectroscopy (EDS) and selected area electron diffraction (SAED). The FTO/Zn-MoS_2 photo-electrode was coated with the PbS@CdS QDs using SILAR process and was then peeled off and deposited on a TEM grid for the analysis. X-ray diffraction (XRD) patterns of powders were acquired using a Bruker D8 Advance X-ray diffractometer equipped with Cu K_α radiation ($\lambda = 0.15418$ nm). The XRD pattern of purified QDs film deposited on a glass substrate was performed using a Panalytical X-Pert PRO MRD with Cu K_α radiation source (λ = 0.15418 nm). Ultraviolet-visible- nearinfrared (UV-vis-NIR) absorption spectrum was carried out using a Cary 5000 UV-vis-NIR spectrophotometer (Varian). UV-visible diffuse reflectance spectroscopy (UV-VIS DRS) absorption spectra were also performed by using a Cary 5000 UV-vis-NIR spectrophotometer (Varian), equipped with an integrating sphere. The bandgap energy (E_g) of the as-synthesized semiconductors was determined from Tauc plots, i.e. $(\alpha h\nu)^2$ as a function of hv. Photoluminescence spectra (PL) and PL lifetime of the QDs in solution were performed using a Fluorolog-3 system (Horiba JobinYvon). Inductively coupled plasma optical emission spectrometry (ICP-OES) was performed using an Agilent 5100 ICP-OES system. X-ray Photoelectron Spectroscopy (XPS) was performed using a VG Escalab 220i-XL spectrometer equipped with hemispherical analyzer, applying a Twin Anode X-Ray Source. The C 1s peak (calibrated to a binding Energy=284.6 eV) was used as an intrinsic reference to rule out charging effects. Ultraviolet photoelectron spectroscopy (UPS) measurements were performed using an unfiltered Helium gas discharge lamp emitting predominantly at 21.22 eV to determine the VB position of as-prepared semiconductors. The zeta potential of the as-prepared MG and QDs in deionized water was carried out by using a Brookhaven Zeta Plus system in a standard 10 mm all-side-transparent polymethyl methacrylate cuvette. The Brunauer-Emmett-Teller (BET) surface area of prepared semiconductors was performed using a Quantachrome Autosorb-IQ-MP low temperature nitrogen sorption method.

3 MODULATING THE 0D/2D INTERFACE OF HYBRID SEMICONDUCTORS FOR ENHANCED PEC PERFORMANCES

In this chapter, a photoelectrode based on a 0D/2D heterojunction is constructed by 0D metal chalcogenide PbS@CdS core-shell QDs and hierarchical 2D Zn doped MoS_2 NSs to reduce the charge carrier recombination. However, the relationships between 0D/2D interface engineering and the photoactivity of these composites have not been systematically studied, and the PEC mechanism of these photoelectrodes is still poorly understood. In this regard, in this work, we investigate how modulation of the band energy of the QDs and the MoS_2 (by Zn doping) affect the charge transfer and thus the overall performance when used as photoelectrode in a PEC device for hydrogen generation. The PbS@CdS QDs act as well as light absorbers for extending absorption to the NIR. In the optimized photoanode, the 0D/2D interface between Zn-MoS_2 and QDs can present less stacking that can allow a more uniform dispersion of QDs, further, the 2D hierarchical nanoflower structure can effectively quench the photoluminescence of the QDs, accelerating the charge transfer and thereby inhibiting the recombination of photo-excited charges. Thanks to an improved charge transfer, the stability is also improved. These results suggest that heterojunctions and the synergetic effect of the 0D/2D interface could effectively improve the performance of PEC hydrogen production.

3.1 Experimental section

3.1.1 Preparation of 2D Zn-MoS_2 nano-hybrid

The Zn-MoS_2 nano-hybrid was synthesized according to a protocol described previously with some modifications.[178] Briefly, to obtain a 10% Zn doping, 8.45×10^{-5} mol of $(NH_4)_2MoS_4$ and 8.45×10^{-6} mol of $Zn(NO_3)_2\cdot6H_2O$ were dissolved into 10 mL of DMF by sonication for 15 min to achieve a clear and homogeneous solution. Subsequently, 0.1 mL of $N_2H_4\cdot H_2O$ was added to the mixture under vigorous stirring. The mixture was further sonicated for 10 min before transferring it to a 50 mL Teflon-lined stainless steel autoclave. Subsequently, the reaction was heated to 200 °C for 12 h and then cooled down to room temperature. The products were collected by several rinse centrifugation cycles with water and ethanol to remove impurities. Finally, the product was freeze-dried to obtain a black powder. For the preparation of different Zn doped MoS_2, different molar ratios of $Zn(NO_3)_2\cdot6H_2O$ (0.5:10, 1:10, 1.5:10, 2:10, and 3:10) with respect to $(NH_4)_2MoS_4$ were added to the reaction. Similarly, non-doped MoS_2 nanoflowers were prepared

similarly, without using $Zn(NO_3)_2 \cdot 6H_2O$. Finally, all the prepared nano-hybrids were calcinated in a tubular furnace at 350 °C for 1 h in the Ar atmosphere (heating rate: 5 °C/min).

3.1.2 Zn-MoS_2 film deposition

The FTO glass substrates were cleaned with triton, then with a mixture of methanol, acetone and isopropanol (1:1:2), rinsed with deionized water and dried in N_2 flow. Then, the cleaned FTO glass substrates were treated in a UV-ozone cleaner for 15 min to further eliminate surface organic contaminants. Subsequently, the Zn-MoS_2 thin films were deposited by a modified space-confined self-assembly method.[179] Typically, the cleaned FTO substrates are placed in a fritted glass funnel filled with two immiscible solvents to form a liquid-liquid interface.[179] In the case of Zn-MoS_2 dispersed in ethanol, the bottom phase was formed by water: acetonitrile (85:15, v / v, ~ 15 mL), while hexane (~10 mL) was used as the top phase. The Zn-MoS_2 ethanol solution (~1.0 mg/mL) was injected at the interface continuously until a compact film is formed. After the 2D self-assembly, first, the top liquid phase was removed using a pipette and then the bottom phase was removed by a low vacuum (~50 mbar) assisted filtration to allow the thin film formed at the interface to deposit on the substrates. Subsequently, the thin films deposited on the FTO substrates were allowed to dry at 150 °C for 15 min, followed by heating in Ar at 350 °C for 1 h to remove the residual solvent.

3.1.3 Preparation of photo-anode

Herein, an *in situ* SILAR approach was used to sensitize the FTO/Zn-MoS_2 photoanodes with QDs, to construct the specific 0D/2D heterojunction.[180] In general, for growing core PbS QDs, a 20 mM methanolic solution of $Pb(NO_3)_2$ and a 20 mM solution of $Na_2S \cdot 9H_2O$ in methanol/water (50:50, v/v) were used as the Pb^{2+} and S^{2-} precursors, respectively. For CdS shell growth, a 50 mM ethanolic solution of $Cd(NO_3)_2 \cdot 4H_2O$ and a 50 mM solution of $Na_2S \cdot 9H_2O$ in methanol/water (50:50, v/v) were used as the Cd^{2+} and S^{2-} precursor, respectively. For each SILAR cycle, the FTO/Zn-MoS_2 photoanode was dipped 1 min in the metallic precursor (either Pb^{2+} or Cd^{2+}) then, the photoanode was washed with the corresponding solvent to remove unabsorbed chemical and dried under N_2 flux. Subsequently, the same process was used for the sulfide precursor. For the growth of composite PbS@CdS QDs, the deposition of the CdS shell immediately followed the preparation of PbS core. To this end, we first completed the nucleation and growth of PbS core directly on the surface of Zn-MoS_2, then grew the external CdS shell. The PbS and CdS QDs

used in this work are grown with two and four SILAR cycles, respectively, while the composite PbS@CdS QDs were grown with two cycles of PbS followed by another four CdS SILAR cycles.

Previous work showed that a passivating ZnS capping layer on the surface of FTO/Zn-MoS_2/PbS@CdS photoanodes by SILAR inhibits photo-corrosion and further improves stability.[181, 182] In a typical SILAR deposition cycle, a 0.1 M methanolic solution of $Zn(Ac)_2$ and 0.1 M solutions of $Na_2S{\cdot}9H_2O$ in a mixture of methanol/water (1/1 v/v) were applied as a source of Zn^{2+} and S^{2-}, respectively. A single SILAR cycle consisted of 1 min dipping of the working electrode in the Zn^{2+} precursors, and subsequently in the S^{2-} precursors. After each bath, the photoanode was thoroughly rinsed by immersing it in the corresponding solvent, respectively, to remove the chemical residuals from the surface, then dried with N_2.

3.1.4 PEC Characterization

PEC cell performance was determined using a CHI-760D electrochemical workstation with a sweep rate of 20 mV/s. The working electrode was prepared by depositing the as-synthesized Zn-MoS_2 followed by the SILAR approach for PbS@CdS QDs on FTO glass. An Ag/AgCl electrode with saturated KCl and Pt wire electrode was used as the reference and counter electrode, respectively. The surface of the photo-anode was covered with an insulating epoxy resin, except for the active area (~0.30 cm^2), to avoid any direct contact between the electrolyte and the conductive back contact and/or the connecting wire. Typically, the electrolyte containing 0.25 M $Na_2S{\cdot}9H_2O$ and 0.35 M Na_2SO_3 after deoxygenating with highly pure N_2 for 30 min, which served as a sacrificial hole scavenger. In particular, the photocurrent density-voltage (J-V) curve was measured using a Compact Solar Simulator AAA (Sciencetech SLB-300A) under simulated sunlight (1 Sun = AM 1.5G, 100 mW cm^{-2}). To verify the standard 1 solar illumination (100 mW cm^{-2}) on the as-fabricated photoanode (working electrode) in the three-electrode system, a Si reference diode (Sciencetech) was used to adjust the distance between the solar simulator and photoanode before each measurement. Subsequently, the measured potential (vs Ag/AgCl) was converted to the RHE according to the following formula: $V_{RHE} = V_{Ag/AgCl} + 0.197+pH*(0.059)$. EIS was performed in the presence of 0.25 M $Na_2S{\cdot}9H_2O$ and 0.35 M Na_2SO_3 mixture (pH=12.5) under light by using a Gamry 1000E station with zero bias voltage vs Reference and a sweep in frequency from a range of 1 Hz to 100 kHz. The EIS data were fitted with Zview software. The EESA was obtained by a simple cyclic voltammogram (CV) method, which was carried out from -0.1 V to 0.1 V (vs Ag/AgCl) employing a redox probe of $[Fe(CN)_6]^{4-/3-}$ solution containing 0.1 M KCl. Then, a linear relationship between the scan rate and the current density is obtained from

the CV cycles of the non-faradaic processes. M-S measurement was carried out from -1.0 V to 0 V (vs Ag/AgCl) in a solution containing 0.5 M Na_2SO_4.

3.2 Result and Discussion

Previous work confirmed that metal doping can enhance electrocatalytic activity, yielding MoS_2 with better conductivity.[176, 183, 184] Doping accelerates the charge transfer and reduces charge recombination. In particular, it has been observed that non-precious metal Zn doping in MoS_2 can effectively modulate the band position.[176] In this work, the Zn-MoS_2 materials are synthesized by a one-pot solvothermal approach and samples with different % Zn are prepared (from 0% to 30%).

3.2.1 Microstructure and Morphology characterization

SEM and TEM imagings were used to investigate the morphology of the pristine MoS_2 and Zn-MoS_2 nanocrystals. As shown in Figure 3.1a, pure MoS_2 exhibits a nano-flower morphology. Each nanoflower is a hierarchical structure of 2D petal-like NSs with an average length of ~130 to 150 nm. After 10% Zn doping (10% is based on the precursors' ratio, the sample is labeled as 10 Zn-MoS_2), the morphology (Figure 3.1b) and size did not exhibit obvious change compared to pure MoS_2. The Brunauer-Emmett-Teller (BET) surface area results shown in Figure 3.1c reveal that the 10 Zn-MoS_2 sample possesses a larger BET surface area (47.9 m^2/g) compared to pristine MoS_2 (9.72 m^2/g), which could provide more contact areas for the nucleation of 0D QDs and for the electrolyte redox reaction while performing PEC tests.

Then, XRD characterization was applied to monitor crystal structure changes with increased Zn doping. As shown in Figure 3.1d, the undoped MoS_2 presents three distinct diffraction peaks corresponding to pristine MoS_2 (JCPDS Card No. 73-1508). At a low doping level (up to 10% Zn doping), Zn atoms are incorporated into the MoS_2 matrix without ZnS formation. In particular, the low intensity of the XRD peaks is due to the fact that the samples are polycrystalline. In addition, thin NSs are often deformed when they are repositioned as powder, and due to this deformation, their stacking periodicity will be disordered, leading to less intense XRD peaks. [185] Furthermore, the SAED pattern of the as-synthesized Zn-MoS_2 samples (Figure 3.1e) presents three obvious rings corresponding to (002), (100) and (110), further indicating polycrystalline Zn-MoS_2 in the hexagonal structure. Whereas for Zn doping amounts above 10 %, Zn starts to form a secondary impurity phase of ZnS. For example, the XRD spectrum of the 20 Zn-MoS_2 samples has three new diffraction peaks, corresponding to the (111), (220) and (311) peaks of cubic sphalerite ZnS [JCPDS Card No. 77-2100].

TEM (Figure 3.1f) and HRTEM images (Figure 3.1g) of 10 Zn-MoS_2 show significant ripples and wrinkles, indicating the presence of an ultrathin structure. The 2D petal-like NSs with a layer spacing ~ 0.66 nm can be assigned to the (002) crystalline plane of MoS_2.[176] The appearance of small NSs with sharp edges indicates a high degree of crystallization. Furthermore, consistent with XRD patterns showing no other obvious crystalline phases, 10 Zn-MoS_2 shows no obvious nanoparticles or large clusters appearing on its surface, confirming that no zinc sulfide compounds are formed on the surface. The energy dispersive X-ray spectroscopic (EDS) mapping analysis of 10 Zn-MoS_2 (Figure 3.1h) confirms the co-existence of Mo (indicated by green color), S (indicated by yellow color) and Zn (indicated by red color) elements in the sample. Clearly, the Zn elements are uniformly distributed in the NSs, indicating the successful Zn doping of MoS_2.

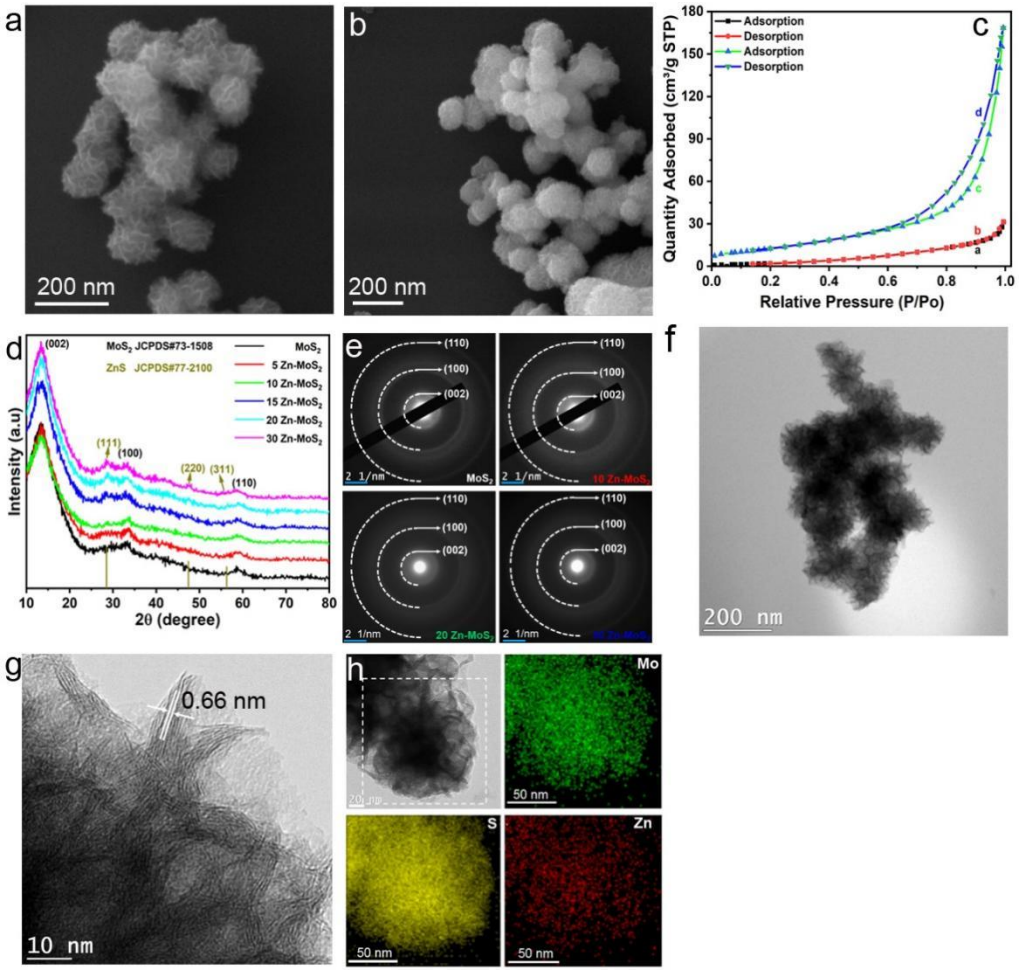

Figure 3.1. Morphological characterizations by SEM imaging: (a) pure MoS_2 nano-flowers and (b) 10 Zn-MoS_2 nanoflowers; (c) XRD of different zinc content doped MoS_2. (d) BET curves of MoS_2 (curve a, b) and 10Zn-MoS_2 (curve c, d), respectively. (e) SAED patterns of MoS_2, 10 Zn-MoS_2, 20 Zn-MoS_2 and 30 Zn-MoS_2. TEM (f) and HRTEM images (g) of 10 Zn-MoS_2; (h) Elemental mapping images of 10 Zn-MoS_2.

3.2.2 XPS characterization of Zn-MoS_2

The chemical state and phase state of Zn-MoS_2 were also investigated by X-ray photoelectron spectroscopy (XPS) analysis. The XPS survey spectrum of pure MoS_2 (black curve) and 10 Zn-MoS_2 (red curve) are presented in Figure 3.2a, indicating the presence of Mo, S and Zn elements. Figure 3.2b-e displays high-resolution spectra of Mo 3d, S 2p, O1s and Zn 2p for 10 Zn-MoS_2, respectively. Figure 3.2b reports detailed XPS scans of Mo 3d. The two distinct peaks around 232.6 eV and 229.5 eV with a 3.1 eV difference can be assigned to Mo $3d_{3/2}$ and Mo $3d_{5/2}$, respectively, confirming the presence of Mo^{4+}.[186] The peak around 226.7 eV can be indexed to S 2s. In addition, the weak peaks located at a higher binding energy at 233.5 eV and 235.9 eV are attributed to the Mo^{6+} oxidation state, indicating that the Mo edges are slightly oxidized which could be due to oxidation of the catalyst sample in air.[187] The peak of S 2p can be used to investigate the inner structure of MoS_2 and Zn-MoS_2. As shown in Figure 3.2c, the binding energy of S 2p splits into S $2p_{1/2}$ (163.3 eV) and S $2p_{3/2}$ (162.1 eV), consistent with the presence of S^{2-}.[188] Meanwhile, the small peak at a binding energy of 164.3 eV indicates the presence of bridging disulfides S_2^{2-} and/or apical S^{2-} ligands. [189] In addition, to elucidate the influence of different Zn concentrations on the chemical state, the S 2p peak with different doping was further analyzed. As shown in Figure 3.2f, the two distinct peaks around 163.5 eV and 162.3 eV correspond to the S 2p of pure MoS_2. With the increase of Zn doping, the binding energies of S 2p negatively shift indicating an increase of electronic density in MoS_2 after the incorporation of elemental Zn.[190] In addition, the O 1s spectrum of Zn-MoS_2 (Figure 3.2d) shows three peaks: the peaks located at 533.6 eV and 532.7 eV are assigned to absorbed water,[191] while the peak located at 530.8 eV is assigned to the Mo-O groups.[192] The Zn 2p spectrum (Figure 3.2e) exhibits the typical peaks of Zn $2p_{3/2}$ and Zn $2p_{1/2}$ with binding energies at 1022.3 eV and 1045.3 eV, indicating Zn has been successfully doped into MoS_2 nanoflowers, in agreement with EDS mapping (Figure 3.1h). Furthermore, the amount of Zn incorporation in Zn-MoS_2 can be calculated as 1.22 atom %, 2.23 atom % and 2.87 atom %, when 10%, 20%, 30% Zn ratio is used, respectively.

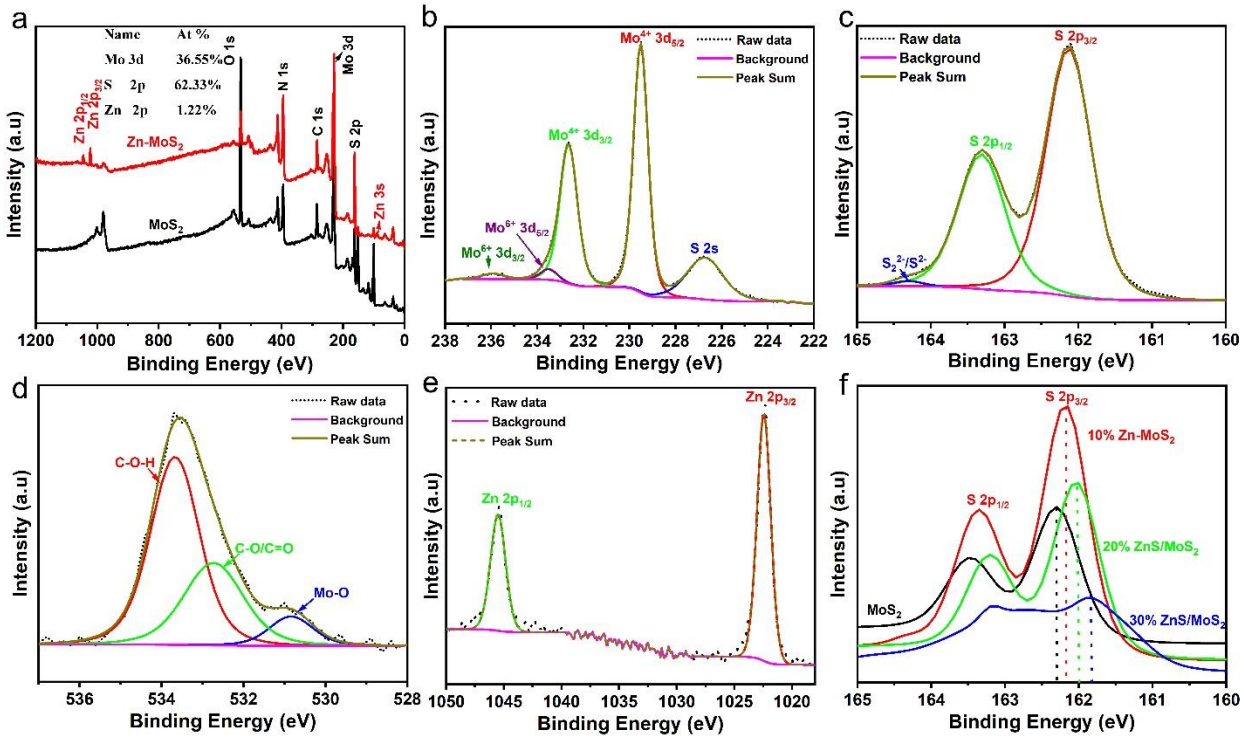

Figure 3.2 (a) XPS survey spectra of MoS_2 (black curve) and 10 Zn-MoS_2 (red curve); (b-e) Mo 3d, S 2p, O1s and Zn 2p XPS spectra of 10 Zn-MoS_2, respectively; (f) S 2p XPS spectra of MoS_2 and Zn-MoS_2 (10%, 20% and 30% Zn doped MoS_2).

Furthermore, to elucidate the influence of different Zn dopants concentrations on the chemical state, the S 2p was analyzed to probe the inner structure of Zn-MoS_2. As shown in Figure 3.2f, the two distinct peaks around 163.5 eV and 162.3 eV correspond to the S 2p of pure MoS_2. With the increase of Zn doping, the binding energies of S 2p negatively shift indicating an increase of electronic density in MoS_2 after the incorporation of elemental Zn.[190] The high-resolution S 2p XPS spectra of MoS_2 and Zn-MoS_2 (10%, 20% and 30%) are shown in Figure 3.3. Compared to pure MoS_2 (S $2p_{3/2}$ 162.3 eV, S $2p_{1/2}$ 163.5eV), S2p of 10 Zn-MoS_2 (S $2p_{3/2}$ 162.1 eV, S $2p_{1/2}$ 163.3eV) shows a negative shift, but only the Mo-S peaks are present without any obvious S 2p peak for the ZnS impurity. Whereas the S 2p of 20 Zn-MoS_2 exhibits a negative shift, that can be deconvoluted into four distinct peaks, which index to Zn-S bond (162.1eV, 163.5 eV) and Mo-S bond (162 eV, 163.2 eV), respectively. Similarly, the S 2p peaks for 30% Zn dopant further exhibit a negative shift and can as well be deconvoluted into the same four peaks: Zn-S bond (162.7eV, 163.7 eV) and Mo-S bond (161.9 eV, 163.1 eV), respectively.[193]

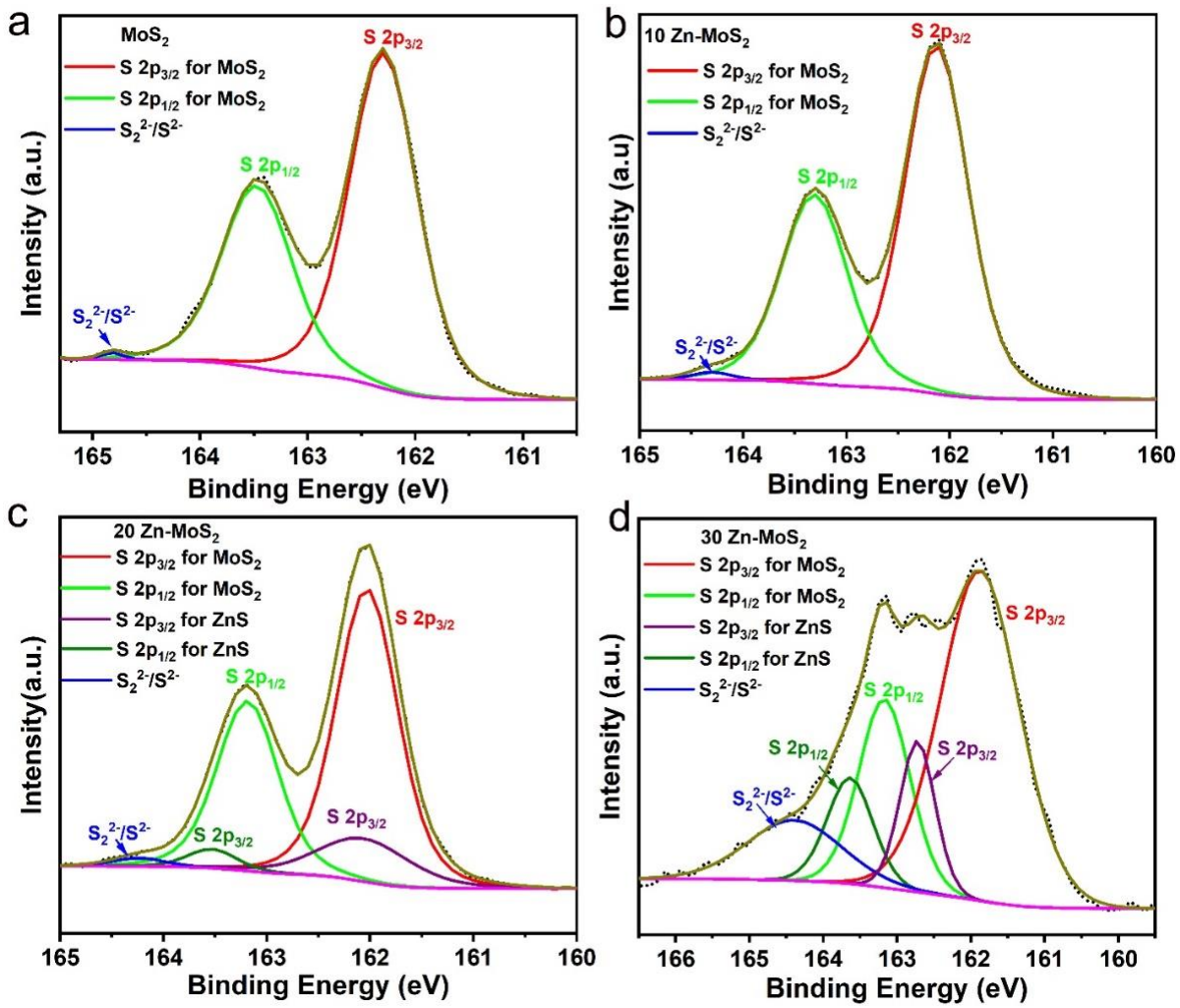

Figure 3.3 High resolution S 2p XPS spectra of MoS_2 (a) and 10 Zn-MoS_2 (b), 20 Zn-MoS_2 (c), 30 Zn-MoS_2 (d), respectively.

3.2.3 0D/2D heterostructure characterization

SILAR was used to grow PbS and CdS QDs. Due to the intrinsic nature of the SILAR process, the obtained QDs possess a large size dispersion.[180] In this case, a broad QDs size distribution could boost the light scattering ability because of the rough surface, thereby allowing more photons to be captured and utilized.[194] In this work, the proposed PbS@CdS nanocomposite system was obtained by first growing PbS with two SILAR cycles, followed by four CdS SILAR cycles. A ZnS layer was then added to reduce photo-corrosion to all photoanodes following previous procedures.[195] We expect the PbS core to nucleate directly on the Zn-MoS_2 surface, and be covered with a CdS layer that grows epitaxial over the PbS core.[196] Figure 3.4 a-c displays

TEM images of the PbS, CdS and PbS@CdS QDs, respectively. The QDs present an average size of (3.5 ± 0.5), (4.1 ± 0.5), and (5.0 ± 0.5) nm, respectively.

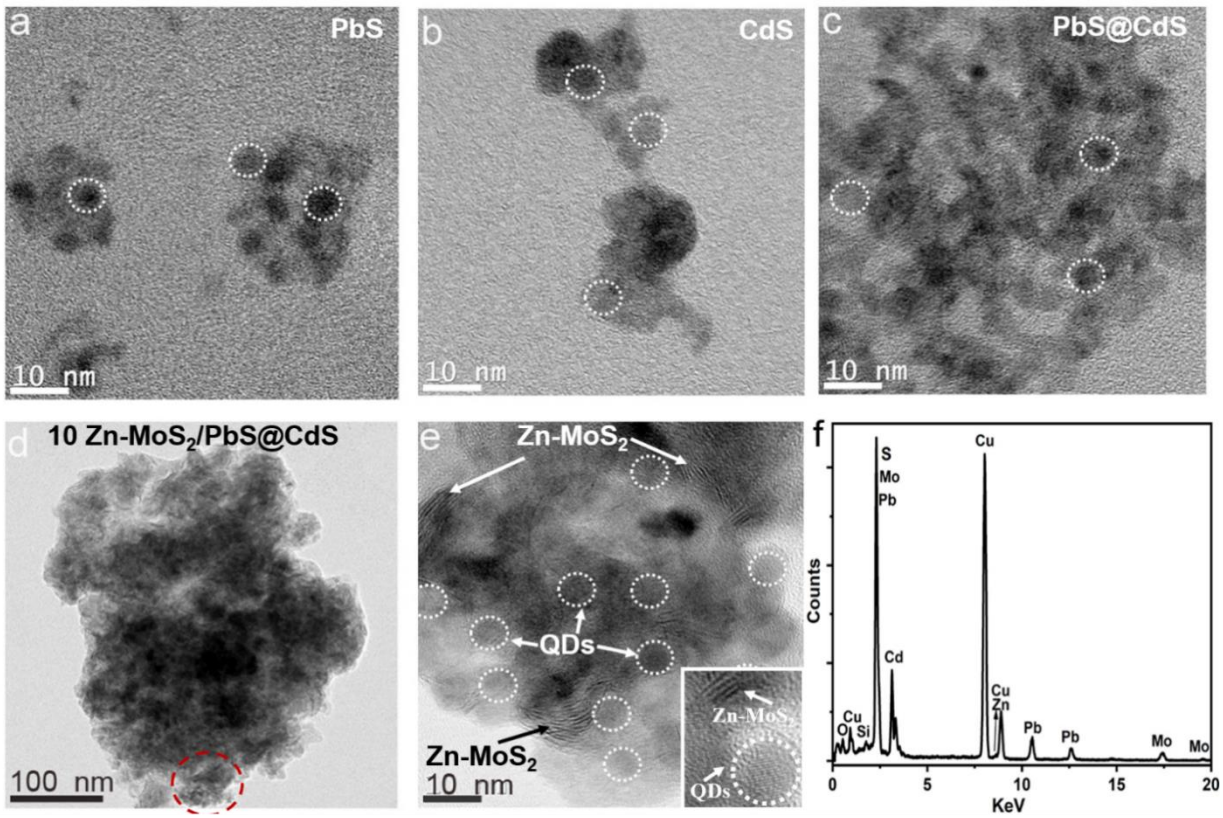

Figure 3.4 High-resolution TEM images: (a) PbS, (b) CdS, (c) PbS/CdS and (d-e) Zn-MoS_2/PbS@CdS; (f) EDS of Zn-MoS_2/PbS@CdS. The inset shows the Zn-MoS_2 and QDs separately.

In addition, Figure 3.4 d shows the TEM image of a 10 Zn-MoS_2 sensitized with PbS@CdS QDs. As shown in Figure 3.4 d, PbS@CdS QDs are present on the Zn-MoS_2 film surface, after SILAR deposition. A partially enlarged view of the red-circled area (Figure 3.4 e) clearly shows the 0D/2D assembly, the QDs are highlighted by superimposed circles, while the Zn-MoS_2 clearly exhibits a different lattice. PbS@CdS QDs are uniformly deposited on the Zn-MoS_2 surface. EDS analysis performed on 10 Zn-MoS_2/ PbS@CdS QDs shows the coexistence of Mo, S, Zn, Pb and Cd elements (Figure 3.4 f). The strong Cu signal originates from the Cu grid used for TEM imaging. The EDS mapping spectrum in Figure 3.5 shows the elemental composition of the film, confirming that the PbS@CdS QDs are successfully adsorbed on the Zn-MoS_2 film.

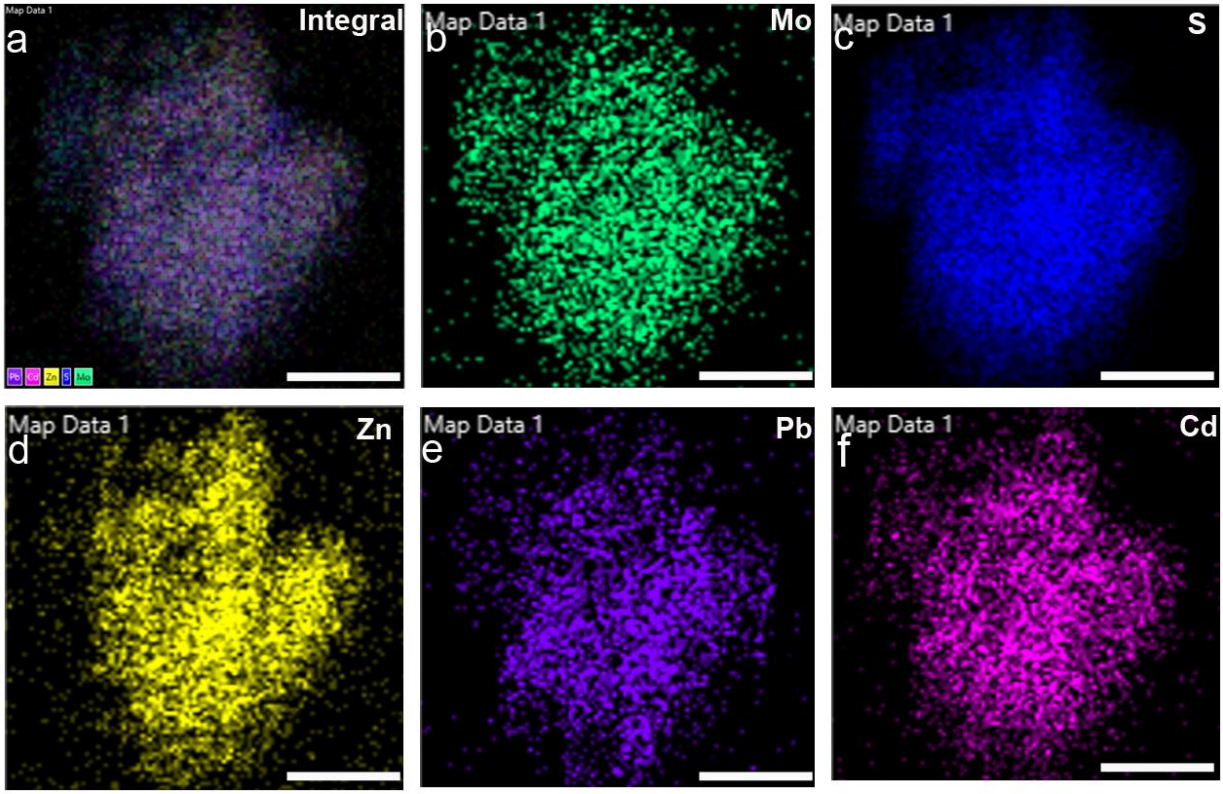

Figure 3.5 EDS mapping of 0D/2D 10Zn-MoS_2/PbS@CdS heterojunction element mapping images: (a) combined, (b) Mo, (c) S, (d) Zn, (e) Pb, (f) Cd, respectively. The scale bar is 100 nm. The sample was scraped from the photoelectrodes.

Furthermore, the XRD patterns (Figure 3.6) and XPS spectra (Figure 3.7) acquired from 10Zn-MoS_2/PbS@CdS also confirmed the successful preparation of 0D/2D heterostructures. XRD characterization was performed to investigate the nanocrystal structure variation after different SILAR processes. As shown in Figure 3.6, the 10Zn-MoS_2 film exhibited three distinct diffraction peaks of (002), (100) and (110), which also corresponds to pristine MoS_2 (JCPDS Card No. 73-1508). After two PbS SILAR approach to 10Zn-MoS_2, another five obvious diffraction peaks of (111), (200), (220), (311) and (222) corresponds to PbS (JCPDS Card No. 78-1897). Simultaneously, three diffraction peaks of (111), (220) and (311) were obtained when four CdS shells were covered on the 10Zn-MoS_2 film surface, which corresponds to CdS (JCPDS Card No. 75-0581). Moreover, it is obvious that the pristine diffraction peaks of MoS_2 are weak due to four CdS shells covering the 10Zn-MoS_2 film surface. As expected, the diffraction peaks of 10Zn-MoS_2/PbS@CdS are the combination of 10Zn-MoS_2, PbS and CdS, while the diffraction peaks of PbS are weak due to the PbS@CdS core-shell structure.

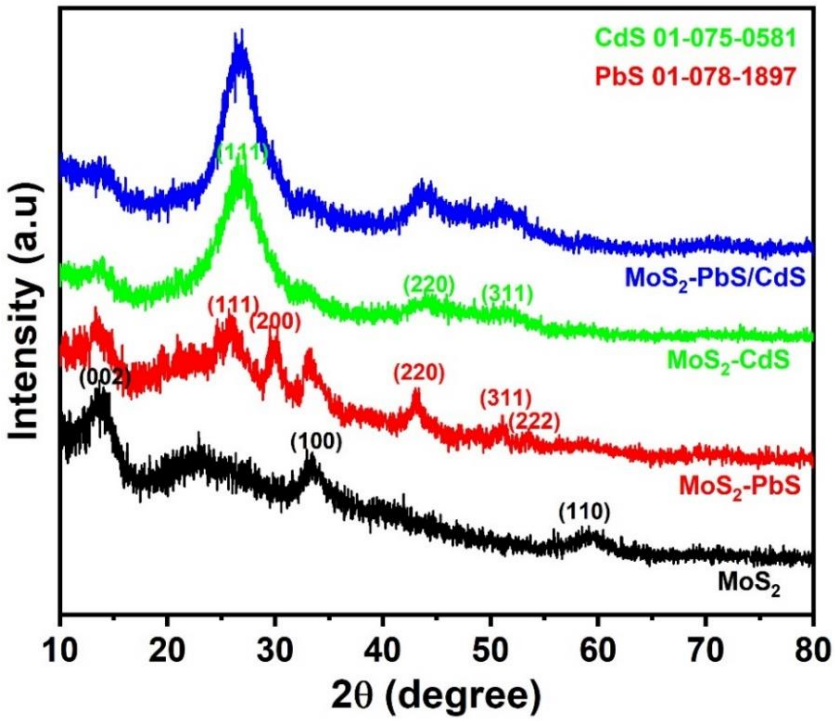

Figure 3.6 XRD spectra of 10Zn-MoS_2 (black curve), 10Zn-MoS_2/PbS (red curve), 10Zn-MoS_2/CdS (green curve), 10Zn-MoS_2/PbS@CdS (blue curve), respectively.

The chemical state and SILAR process of the as-synthesized photo-anode sensitized by different QDs was investigated by X-ray photoelectron spectroscopy (XPS). In particular, two PbS SILAR and four CdS SILAR were coated on the 10Zn-MoS_2 substrate surface in successive. As shown in Figure 3.7, the XPS survey spectrum of 10Zn-MoS_2 (black curve), 10Zn-MoS_2/PbS (red curve), 10Zn-MoS_2/CdS (green curve), 10Zn-MoS_2/PbS@CdS (blue curve) render the corresponding elements, respectively. Figure 3.7 b-f present the high-resolution XPS spectrum of Mo, S, Pb and Cd and Zn elements, respectively, which corresponded to 10Zn-MoS_2/PbS@CdS QDs. It confirmed the successful SILAR process of 0D QDs to 2D Zn-MoS_2 substrate. Especially, after the coating with PbS@CdS QDs, the HR-XPS peaks of Mo exhibit some difference compared to Zn-MoS_2 before sensitizing with QDs. As shown in Figure 3.7b, the two distinct peaks around 232.2 eV and 228.7 eV were corresponding to Mo $3d_{3/2}$ and Mo $3d_{5/2}$ of MoS_2, respectively, which can be relevant to Mo^{4+}.[197] Then, the binding energies of Mo 3d shows a little negatively shifted in 10Zn-MoS_2/PbS@CdS compared with the 10Zn-MoS_2, indicating the increase of electronic density after incorporation of PbS@CdS QDs. Especially, the intensity of S 2s peak around 225.7 eV exhibits a distinct increase, which can ascribe to the intensity of S^{2-} in PbS@CdS. Simultaneously, all of the element co-existence further confirmed the successful PbS@CdS

SILAR approach to 10Zn-MoS_2. Thus, all of the above results confirmed the successful SILAR approach.

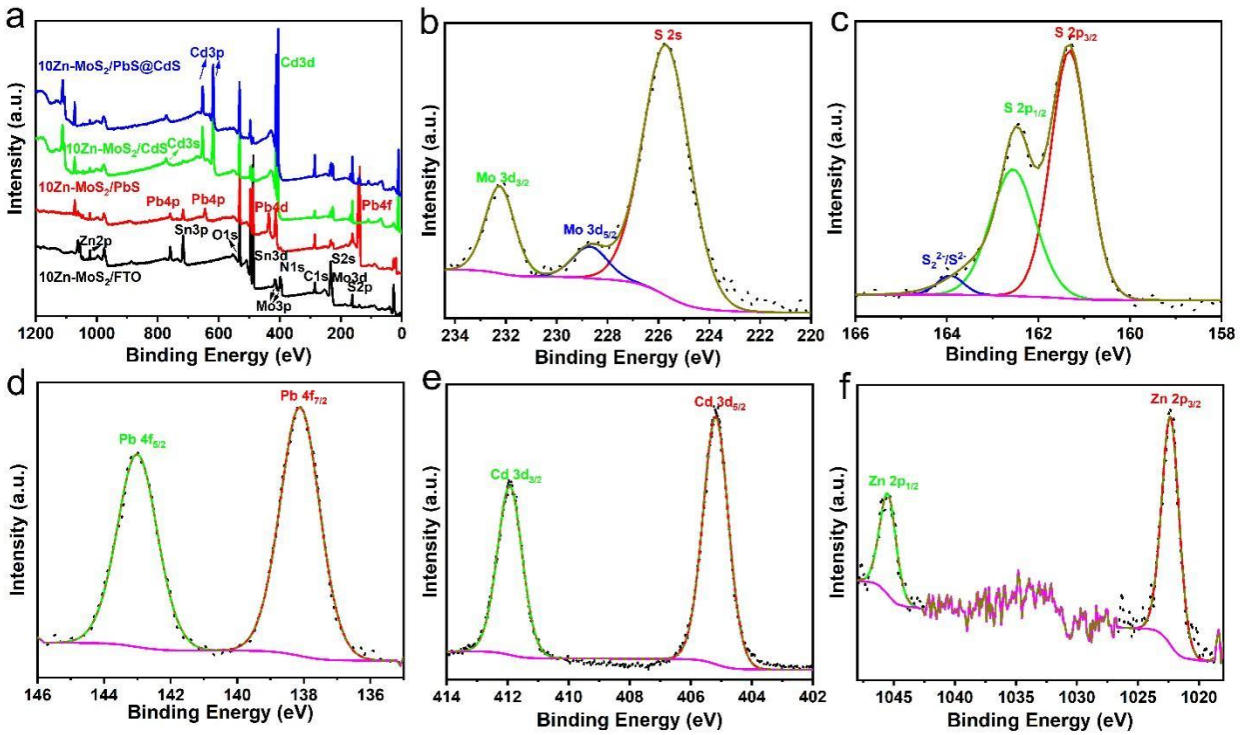

Figure 3.7 (a) XPS survey spectra of different QDs doped Zn-MoS_2 film on FTO substrate: 10Zn-MoS_2 (black curve), 10Zn-MoS_2/PbS (red curve), 10Zn-MoS_2/CdS (green curve), 10Zn-MoS_2/PbS@CdS (blue curve); HR-XPS spectra for (b-f) Mo 3d, S 2p, Zn 2p, Pb 4f and Cd 3d of 10Zn-MoS_2/PbS@CdS QDs, respectively.

3.3 PEC performance

A modified space-confined self-assembly method was used to prepare the photoanodes (see experimental for details).[179] As shown in Figure 3.8a, the process containing: injection of Zn-MoS_2 dispersion (pipette); flake confinement and self-assembly; hexane removal; acetonitrile removal and film deposition; and finally drying at 150 °C. Figure 3.8 b and c display the typical SEM images of the fluorine-doped tin oxide (FTO) before and after the deposition of Zn-MoS_2, respectively.

Figure 3.8b shows a typical SEM image of the FTO substrate before and after the deposition of Zn-MoS_2. The surface of FTO is not smooth and full of crystalline particles with sizes ranging from 50 to 250 nm (corresponding to Glass-1). The SEM image of FTO/Zn-MoS_2 was shown in Figure 3.8c. It is obvious that a few layers of Zn-MoS_2 NSs were successfully coated on the FTO surface (corresponding to Glass-2).

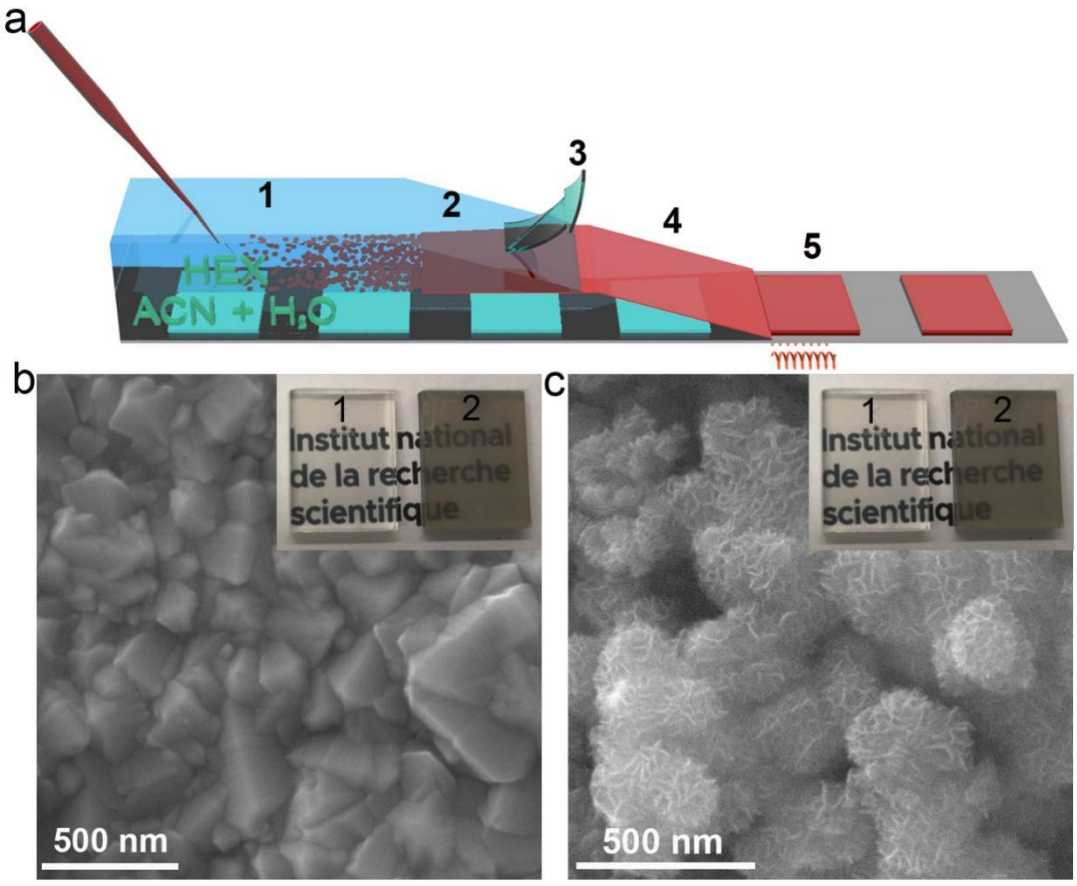

Figure 3.8 (a) The space-confined self-assembly approach for Zn-MoS_2 thin-film deposition; (b) SEM of FTO glass (corresponding to FTO-1); (c) SEM of Zn-MoS_2 deposited FTO (corresponding to FTO-2), the FTO is 1.5 cm*2cm.

The cross-sectional SEM image and corresponding EDS analysis of the PbS@CdS QDs sensitized 10Zn-MoS_2 photo-electrode are shown in Figure 3.9, showing a thickness of the deposited film of ~0.6 µm. The EDS spectra (Figure 3.9b) confirmed the presence of Mo, S, Zn, Pb, and Cd, respectively, consistent with the chemical composition in the QDs sensitized photoanode. The content of Zn is much higher due to a ZnS layer deposited on the surface of the photoanode to prevent the QDs from photocorrosion. In addition, the EDS mapping characterization (Figure 3.9c-h) also verified the presence of Mo, S, Zn, Pb, Cd and Sn, respectively. The Sn signal originates from the FTO glasses substrate. All the EDS analysis results confirm the homogeneous distribution of QDs on the mesoporous Zn-MoS_2 film, suggesting the successful deposition by the SILAR process.

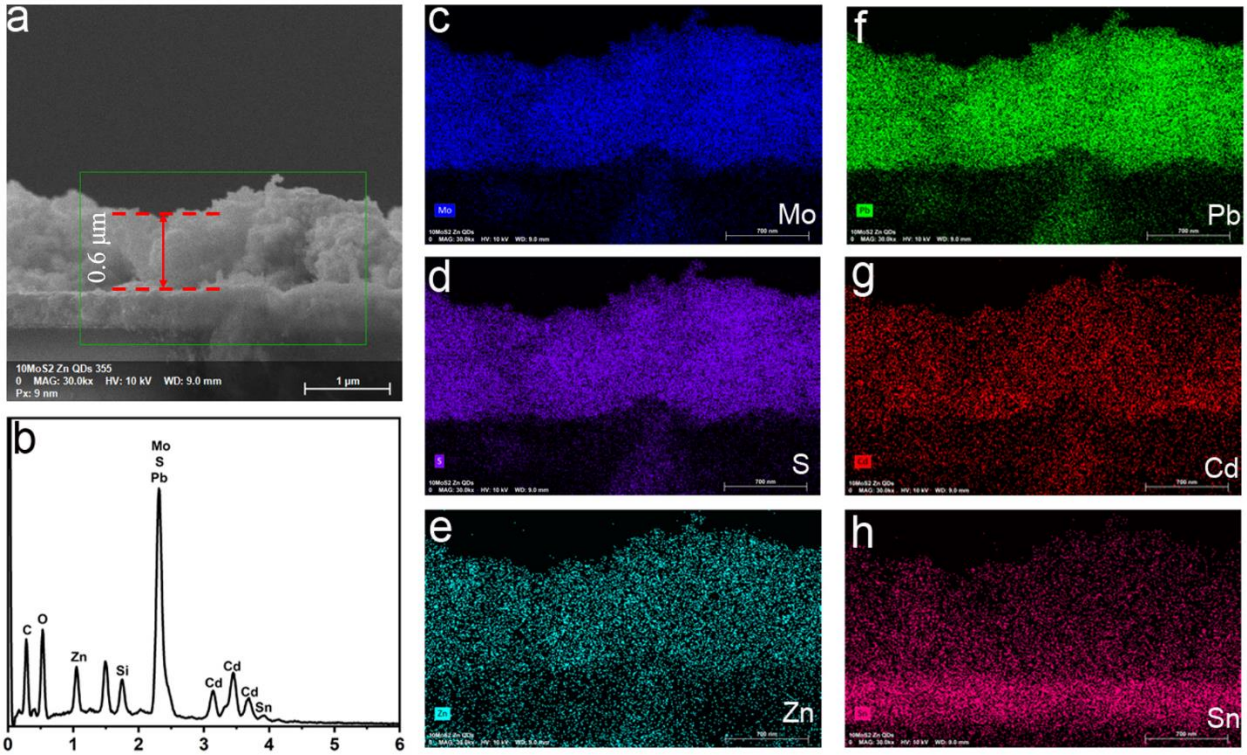

Figure 3.9 (a) Cross-sectional SEM image of 10Zn-MoS_2/PbS@CdS photo-anode. (b) EDS spectra of 10Zn-MoS_2/PbS@CdS photo-anode. (c-h) EDS mapping and relevant chemical composition.

To clarify the direction of charge injection, we performed Mott-Schottky (M-S) analysis and open-circuit potential (OCP) transient test on the prepared heterojunction film samples (Figure 3.10). The M-S plot was carried out to qualitatively investigate the conductivity types and the carrier concentration of Zn-MoS_2.[169] Usually, a positive slope in the linear segment of the M-S plot reflects the n-type property, while a negative slope indicates the p-type property of a semiconductor. According to the M-S equation, the charge carrier concentration (N) is a function of the inverse slope of the M-S linear graph (ie, N~slope^{-1}). Therefore, the value of this slope can be used to estimate the change in carrier concentration.[169, 198] The decrease in the slope value indicates an increase in the charge carrier concentration. As shown in Figure 3.10 a, the MoS_2 and 10Zn-MoS_2 film show a positive slope, indicating the n-type characteristic. The slope value of 10Zn-MoS_2 is smaller than that of the pure MoS_2 sample, suggesting an increase in carrier densities and the enhancement of conductivity after the Zn dopant. This result confirms the XPS results, in which it was observed that the electronic density increased in Zn-MoS_2 after the incorporation of Zn element. As shown in Figure 3.10 b, all the measured OCP based on different photo-anodes present a negative increase in voltage under light irradiation, indicating that the photogenerated

electrons are injected from the film into the FTO substrate, resulting in the formation of an anodic photocurrent.[199, 200] Simultaneously, the generated photo-voltage difference of the 10Zn-MoS_2/PbS@CdS sample (0.21 V vs Ag/AgCl) was larger than that of the Zn-MoS_2/PbS@CdS film sample (0.05 V vs Ag/AgCl) and 20 Zn-MoS_2/PbS@CdS film sample (0.12 V vs Ag/AgCl), suggesting that the prepared 10Zn-MoS_2/PbS@CdS sample will have remarkable photoelectric conversion ability.[198]

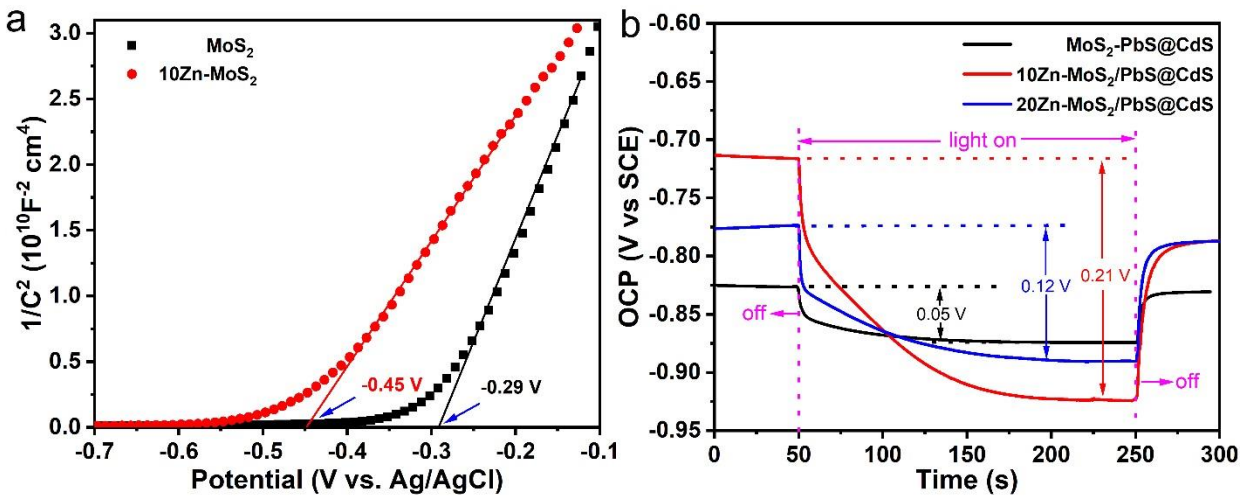

Figure 3.10 (a) Mott-Schottky plots collected on MoS_2 and 10Zn-MoS_2; (b) Transient OCP of different heterostructure films under dark and light illumination.

To test the PEC performances, the different photoanodes were investigated in electrolyte with a hole scavenger (0.25 M $Na_2S{\cdot}9H_2O$ and 0.35 M Na_2SO_3) by employing a typical three-electrode setup under dark and light conditions, including linear sweep voltammetry (LSV), chronoamperometry, and electrochemical impedance spectroscopy (EIS). Representative samples of pure MoS_2/PbS@CdS, Zn doped MoS_2/PbS@CdS (5%, 10%, 15%, 20%, 30% Zn dopant) were employed to study the effect of Zn dopants on the band alignment of the heterojunction and how it can affect the PEC performance. As shown in Figure 3.11a, the photocurrent density (J_{ph}) increases with the applied bias due to the enhancement in the generation and collection of photo-excited charge carriers. The LSV shows that the pure MoS_2/PbS@CdS sample generates a photocurrent of 0.08 mA cm^{-2} at 0.93 V versus the reversible hydrogen electrode (RHE) (0 V vs. the Ag/AgCl) under one sun illumination. The sample with 5 wt% Zn presents a photocurrent density of 0.16 mA cm^{-2}, an intermediate value between the one obtained for 0% and 10% Zn doping. By doping with 10% Zn, the J_{ph} showed a 3-fold increase, reaching a maximum photocurrent value of 0.25 mA cm^{-2} at 0.93 V, whereas for

higher amounts of Zn doping the performance decreased. In particular, the PEC performance decreases gradually with higher amounts of Zn doping of 15%, 20% and 30% reducing the photocurrent to 0.21 mA cm^{-2}, 0.18 mA cm^{-2} and 0.13 mA cm^{-2}, respectively. Thus, the maximum photocurrent (0.25 mA cm^{-2}) is obtained for 10 % Zn doped into MoS_2, whereas for lower/higher amounts of Zn the performance is lower.

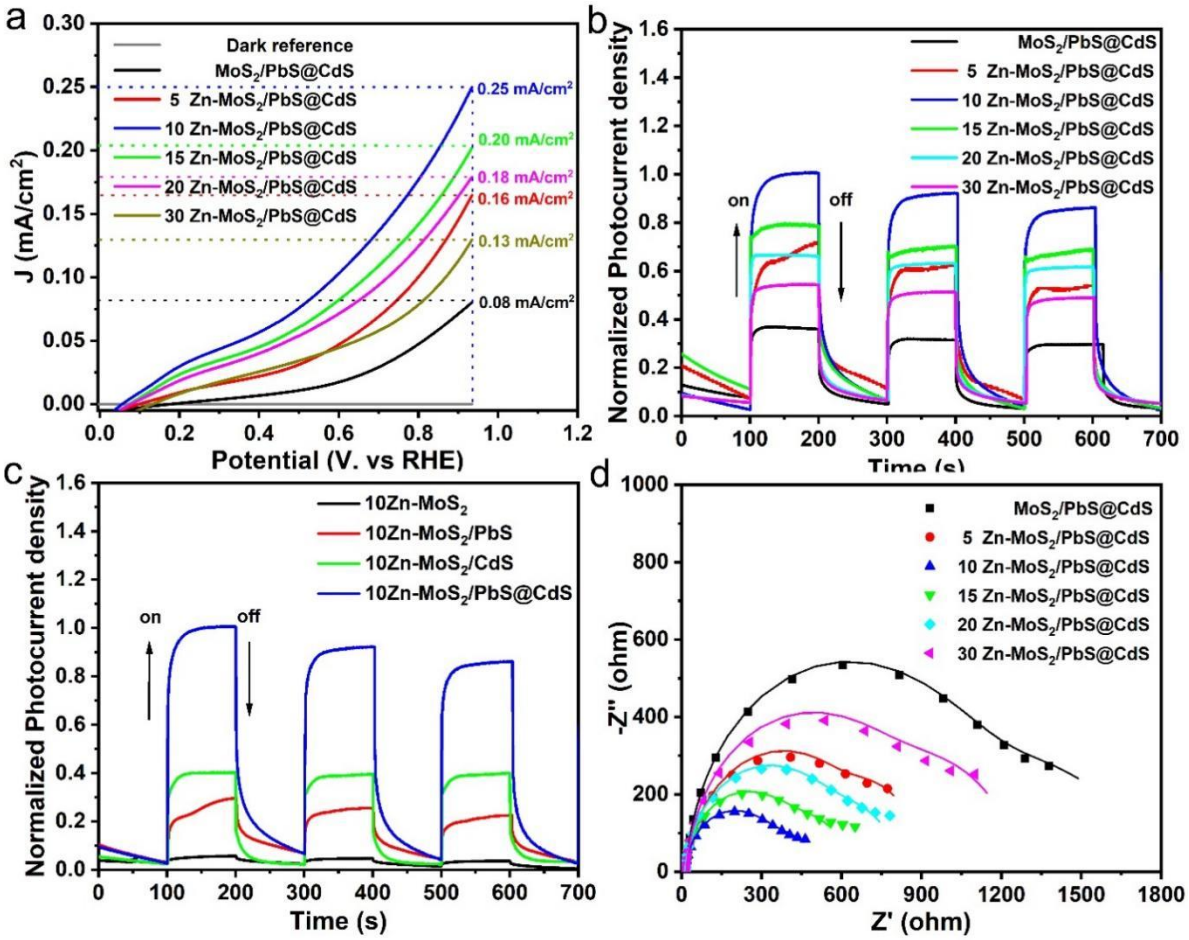

Figure 3.11. (a) LSV and normalized amperometric J-t cycles for PECs with different photo-anodes based on different Zn dopant MoS_2 sensitized by PbS@CdS QDs; (c) photo-anodes based on different QDs sensitized 10 Zn-MoS_2. (d) Nyquist plots of EIS with different electrodes under illumination, and fitting results are plotted as solid traces.

To further highlight the effect of Zn doping, the normalized chopped photocurrent (normalized amperometric i-t) at 0.93 V vs RHE is presented in Figure 3.11b. Compared to the dark current (OFF state), for all the samples the J_{ph} under illumination significantly increases (ON state). This confirms that the prepared Zn-MoS_2 are typically n-type, in agreement with the OCP result and M-S measurements.[201] In addition, the instantaneous increase in photocurrent suggests that the

semi-transparent film-based photoanodes are sensitive to light, and can effectively generate and separate electron-hole pairs and transfer electrons to the counter electrode. The addition of Zn modulates the photocurrent density by altering the conductivity and band alignment, with the 10 Zn-MoS_2/PbS@CdS sample showing the highest photocurrent density. The higher J_{ph} of 10 Zn-MoS_2/PbS@CdS can be ascribed to synergistic effects, such as: (i) the formation of an appropriate band alignment that accelerates the charge injection from the QDs to 10Zn-MoS_2, suppressing electron-hole recombination; (ii) the ultrathin layer also reduces the path that charges have to travel, thus reducing charge recombination.

We also evaluated the effect of the different metal chalcogenides QDs, PbS, CdS and their composite PbS@CdS, by fixing the Zn doping at 10%. As shown in Figure 3.11c, 10 Zn-MoS_2/PbS@CdS exhibits the highest saturated photocurrent compared to pure 10 Zn-MoS_2, 10 Zn-MoS_2/PbS or 10 Zn-MoS_2/CdS. The original data for Figure 3.11b and 3.11c are shown in Figure 3.12a and 12b, respectively. The PEC performance of only PbS and CdS QDs-based photoanodes were also investigated (Figure 3.12c and 3.12d, respectively).

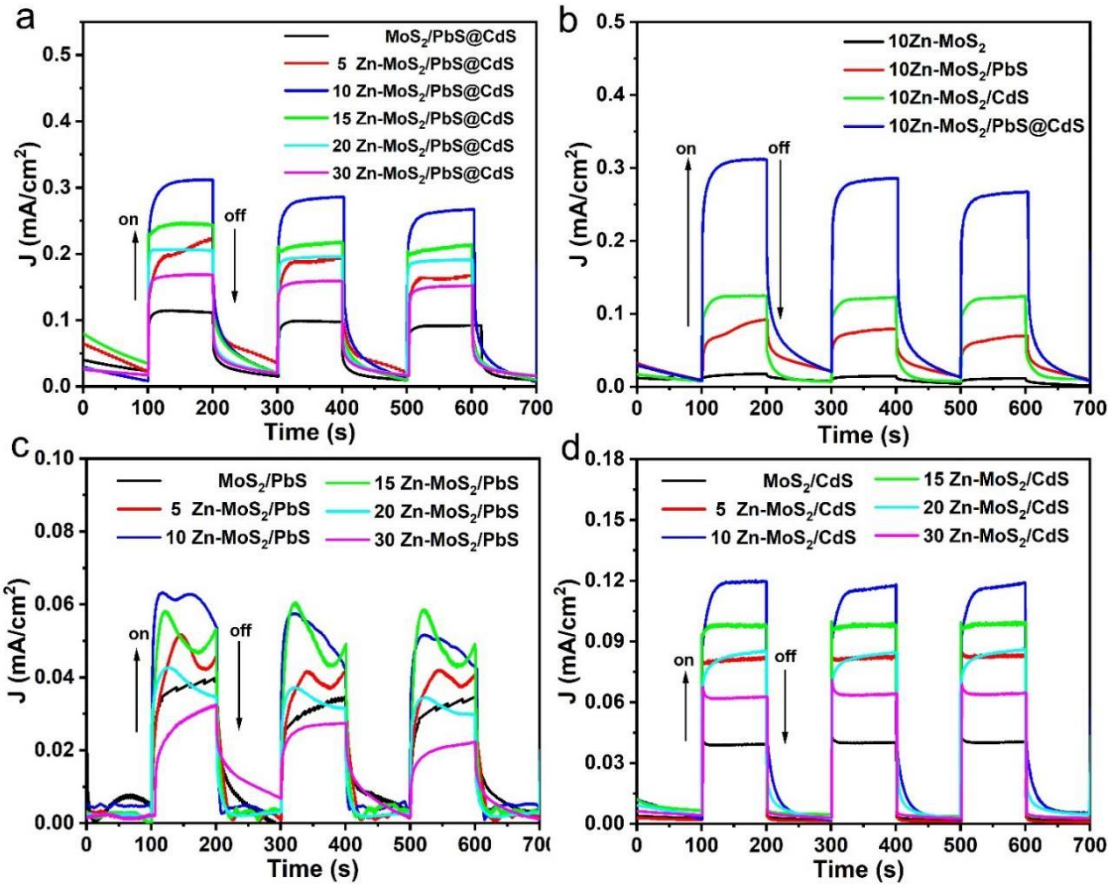

Figure 3.12. Amperometric J-t cycles at 0.9 V vs RHE for PECs with QDs sensitized photo-anodes based on different Zn doped into MoS_2.

The results showed that the photoanodes based on 10 Zn-MoS_2 present the highest values of photocurrent. An overview of the J_{ph} of representative samples of Zn-MoS_2 photo-anode based on a single core or core-shell QDs is reported in Table 3.1. The photoanode based on 10 Zn-MoS_2/PbS@CdS heterostructures exhibits the maximum photocurrent density compared to any other combination. These results demonstrate that the design of an appropriate band alignment can significantly increase PEC performance.

Table 3.1. Photocurrent density of the PEC based on different QDs.

Sample	Without QDs (μA/cm^2)	PbS QDs (μA/cm^2)	CdS QDs (μA/cm^2)	PbS/CdS QDs(μA/cm^2)
MoS_2	3	30	40	80
5 Zn-MoS_2	2	40	75	165
10 Zn-MoS_2	10	60	110	250
15 Zn-MoS_2	6	60	90	210
20 Zn-MoS_2	10	35	80	180
30 Zn-MoS_2	7	25	60	135

EIS was used to investigate the charge transfer properties of the different photoanodes. Figure 3.11d displays the Nyquist plots recorded at 0 V versus Ag/AgCl under 1 Sun (100 mW cm^{-2}) of representative samples of Zn-MoS_2/PbS@CdS, 5 Zn-MoS_2/PbS@CdS, 10 Zn-MoS_2/PbS@CdS, 15 Zn-MoS_2/PbS@CdS, 20 Zn-MoS_2/PbS@CdS and 30 Zn-MoS_2/PbS@CdS QDs photoanodes. All samples present similar Nyquist plots, with a single semicircle followed by a “tail”. The main focus of the analysis is on the diameter of the semicircle as it correlates with the charge transfer resistance (R_{CT}). In particular, a smaller radius of the semicircle means a lower R_{CT} indicating an improved charge transfer.[202] The EIS data were fitted with an equivalent electrical model shown in Figure 3.13: a Randles equivalent circuit consisting of a solution resistance (R_S), double layer capacitance (C_{dl}), charge transfer resistance (R_{CT}) and a Warburg element (W). The values of the Randles equivalent circuit were simulated with ZSimWin software and the relevant data were

shown in Table 3.2. As shown in Figure 3.11 d and Table 3.2, the R_{CT} follows the inverse trend of the photocurrent, with the 10 Zn-MoS_2/PbS@CdS QDs sample presenting the smallest R_{CT} value, indicating a lower charge transfer resistance and superior charge transfer kinetics at the electrolyte/catalyst interface.[181] As the photoanodes are constructed in a similar way, the improved charge transfer can be assigned to the favorable band alignment for charge separation of photoexcited charges between QDs and 10 Zn-MoS_2, confirming that the recombination of electron/hole pairs is strongly reduced in this kind of architecture.

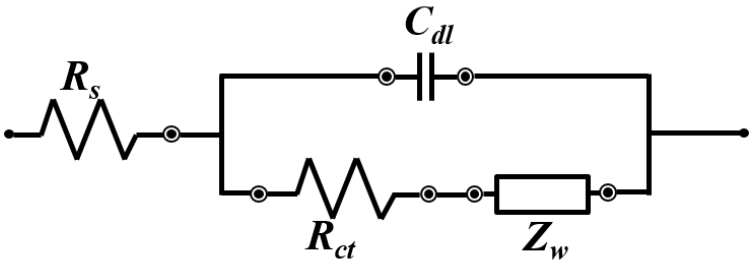

Figure 3.13. The fitting model for EIS.

Table 3.2. Simulation parameters of the equivalent circuit components

Photoanode	R_s (Ω)	R_{et} (Ω)	C_{dl} (F)	Z_W
FTO/ MoS_2/PbS@CdS/ZnS	18.03	1260	5.96×10^{-6}	0.00114
FTO/ 5 Zn-MoS_2/PbS@CdS/ZnS	15.18	749.2	1.27×10^{-5}	0.00133
FTO/ 10 Zn-MoS_2/PbS@CdS/ZnS	12.13	394.8	1.16×10^{-5}	0.00299
FTO/ 15 Zn-MoS_2/PbS@CdS/ZnS	13.05	531.1	6.94×10^{-6}	0.00190
FTO/ 20 Zn-MoS_2/PbS@CdS/ZnS	12.92	667.5	7.84×10^{-6}	0.00177
FTO/ 30 Zn-MoS_2/PbS@CdS/ZnS	17.33	975.9	6.27×10^{-6}	0.00092

The electrochemical effective surface area (EESA) of the prepared photo-anode can be estimated from the electrochemical double-layer capacitance (C_{dl}) of the catalytic surface due to the direct proportion between the EESA and C_{dl}.[203, 204] The electrochemical C_{dl} was obtained by a simple

CV method (Figure 3.14a and b). Then, a linear relationship between the scan rate and the current density is obtained from the CV cycles of the non-faradaic processes. As shown in Figure 3.14c, the 10 Zn-MoS_2/PbS@CdS sensitized photo-anode presents a larger C_{dl} of 3.3 mF/cm^2 than MoS_2/PbS@CdS sensitized photo-anode of 1.3 mF/cm^2, indicating a larger electrode-electrolyte contact area maximum active sites, which is beneficial towards improving the PEC efficiency. The result of electrode-electrolyte contact area is consistent with the intrinsic surface area measured by BET (Figure 3.1c). Both the EIS and EESA confirm the superior charge transport kinetics and the presence of electrochemically active sites of the 10 Zn-MoS_2/PbS@CdS sample.

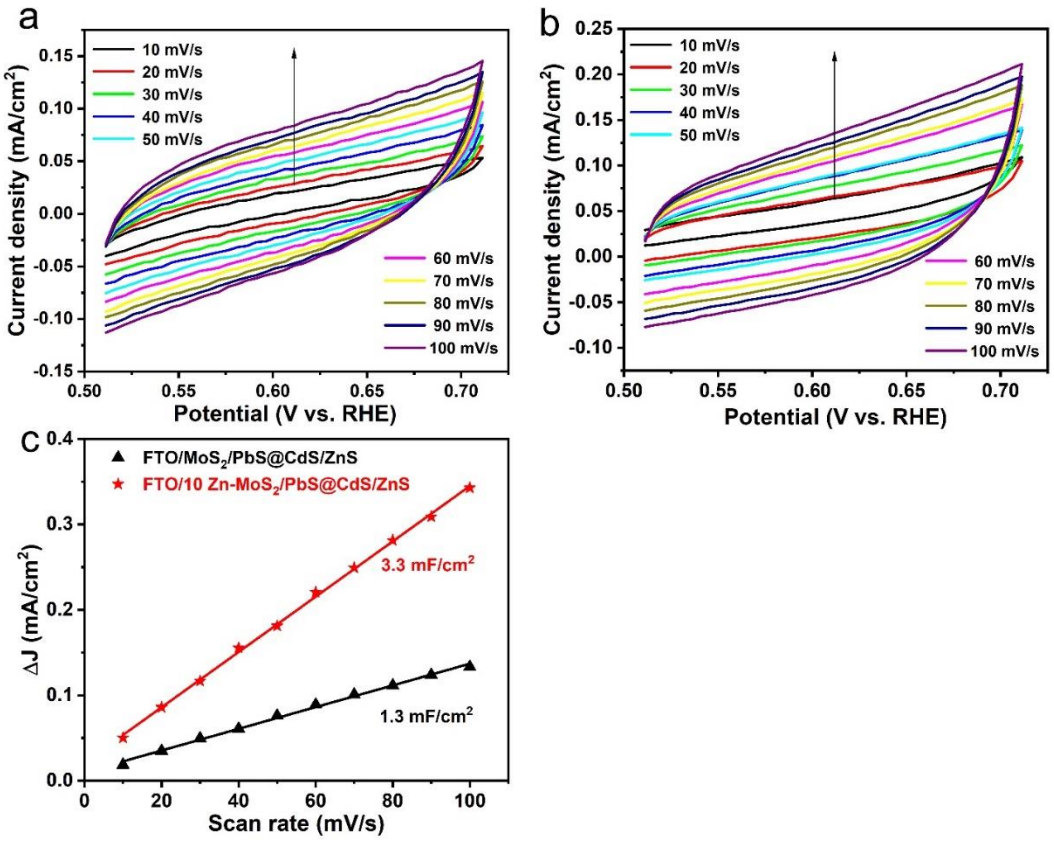

Figure 3.14. Electrochemical cyclic voltammetry (CV) curves at different potential scanning rates (10-100 mV/s) for FTO/MoS_2/PbS@CdS (a) and FTO/10 Zn-MoS_2/PbS@CdS photo-anode (b), respectively; (c) the fitting plots showing C_{dl} for FTO/MoS_2/PbS@CdS and FTO/10 Zn-MoS_2/PbS@CdS photo-anode, respectively. The current density difference at the intermediate value of the voltage window is calculated by the formula (Δj=ja-jc), where the ja and jc are the positive and the negative current density, respectively.

In addition, to quantitatively compare the charge recombination behavior, a normalized parameter (D) was introduced:[205]

$$D = \frac{I_t - I_{st}}{I_{in} - I_{st}}$$

where I_t, I_{st} *and* I_{in} are the time-dependent, steady-state and initial photocurrent, respectively, as shown in Figure 3.15a.[206] In particular, the transient time constant (τ) is defined when lnD = -1 in the normalized plots of lnD~t. As shown in Figure 3.15b, τ of 10 Zn-MoS_2/PbS@CdS was estimated to be 3.35 s, which is much larger than 2.02 s for MoS_2/PbS@CdS, 1.35 s for 20 Zn-MoS_2/PbS@CdS and 1.0 s for 30 Zn-MoS_2/PbS@CdS, respectively, indicating a suppressed charge recombination. Therefore, all of these results confirm that the 10 Zn-MoS_2/PbS@CdS heterojunction presents a faster charge transfer and lower charge recombination at the 0D/2D interface. The real-time detection of H_2 evolution for the best sample (10 Zn-MoS_2/PbS@CdS/ZnS) was further measured.

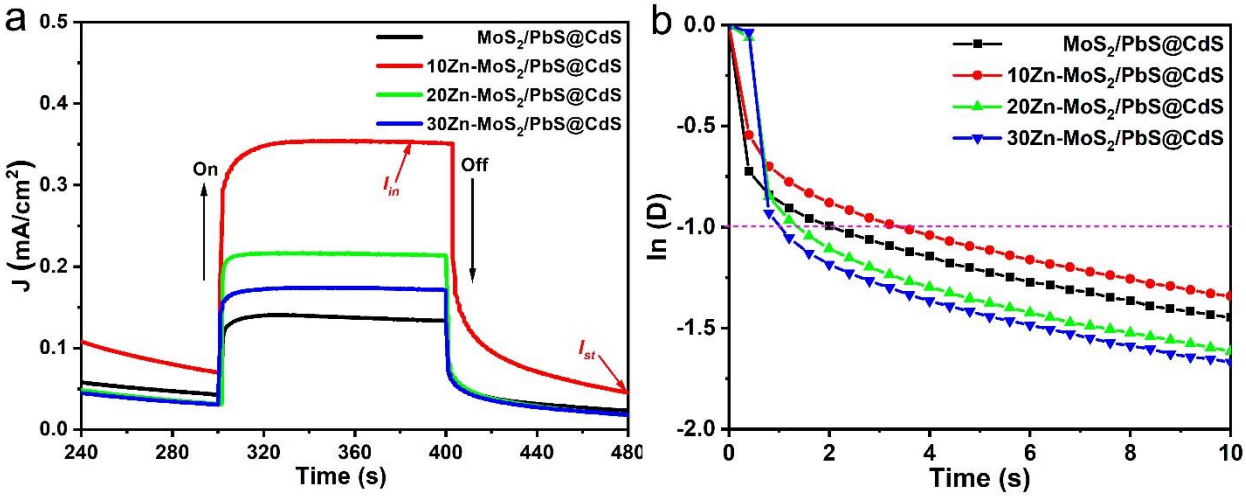

Figure 3.15. (a) The transient photocurrent utilized for the calculation of the transient dynamics; (b) Normalized ln D plot vs time to calculate the transient time constant.

The photo-stability of the PEC device is also an essential aspect of practical applications. The photo-stability of representative PEC devices was measured under one sun illumination at 0.93 V vs. RHE. To compare the photocurrent decay, the initial photocurrent density is normalized to its maximum. As shown in Figure 3.16, the J_{ph} for 10 Zn-MoS_2/PbS QDs device decreases quickly, dropping to only ~38 % after 1 h illumination (black curve). With the addition of the CdS shell, the photocurrent density of 10 Zn-MoS_2/PbS@CdS maintains ~70 % of the initial value (red curve) even after 1 h illumination. The noticeable improvement is ascribed to the superior interfacial interaction, band alignment and protection offered by the CdS shell. In general, the performance of QDs-based PEC devices is sensitive to surface defects under illumination that act as charge

traps, limiting stability. The surface-related traps and defects will form fast non-radiative de-excitation channels for photo-generated charge carriers, reducing the overall performance.[94, 207] However, the superior heterostructure can optimize the interface and accelerate the electron transfer, reducing the photooxidation of the QDs and overall improving the stability.

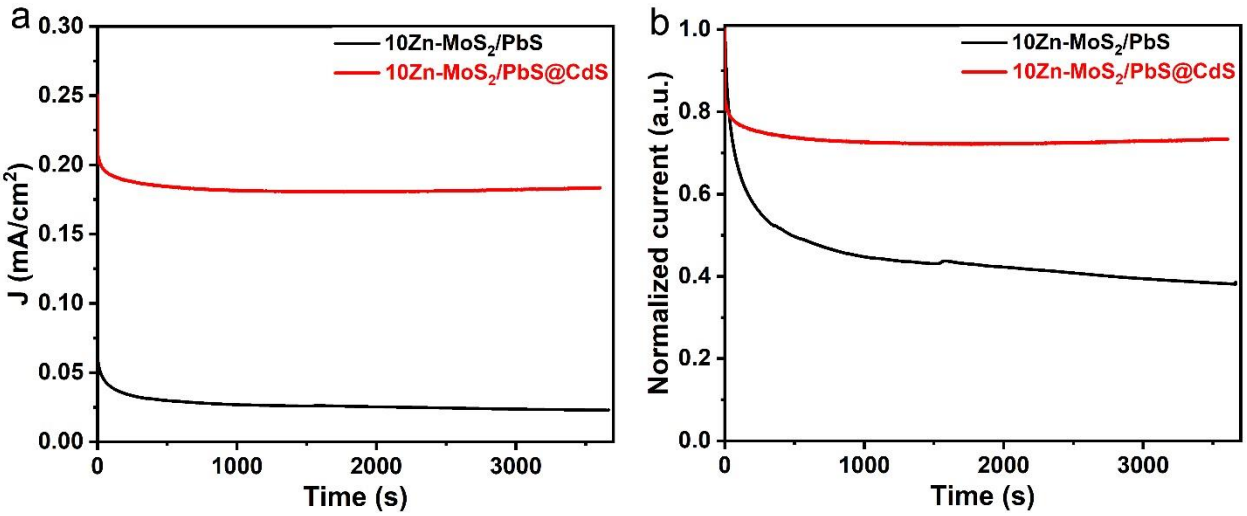

Figure 3.16. Stability of PbS and PbS@CdS sensitized 10Zn-MoS_2 photo-anode before and after normalization.

3.4 Online gas chromatography to measure the H_2 evolution.

The real-time detection of H_2 evolution for the best sample (10 Zn-MoS_2/PbS@CdS/ZnS) was further measured. A gas chromatography (GC) system equipped with a thermal conductivity detector was used to detect the generated H_2 gas. Argon gas was used as the carrier gas for GC analysis. A sealed electrochemical cell (total volume: 100 mL) was used for online gas chromatography (GC). The cell was filled with 20 mL electrolyte in a three-electrode system configuration, using an FTO/10 Zn-MoS_2/PbS@CdS/ZnS as a working electrode, an Ag/AgCl with saturated KCl as a reference electrode and a platinum sheet counter electrode as the auxiliary electrode. Argon gas was used as carrier gas at a flow rate of 20 mL/min, and the electrolyte was constantly stirred. Before the measurements, the electrolyte was degassed with Argon gas for 1.5 h. The gas outlet was connected to a gas chromatograph (PerkinElmer Clarus 580 GC) for periodic sampling, using a thermal conductivity detector (TCD) for H_2 detection. A gas aliquot was automatically injected into the GC every 2.5 min. During online GC, chronoamperometry was performed by applying a 0.93 V *vs.* RHE potential for 1.5 h. Figure 3.17 shows the H_2 evolution curves (theoretical and experimental) linearly increasing with time.

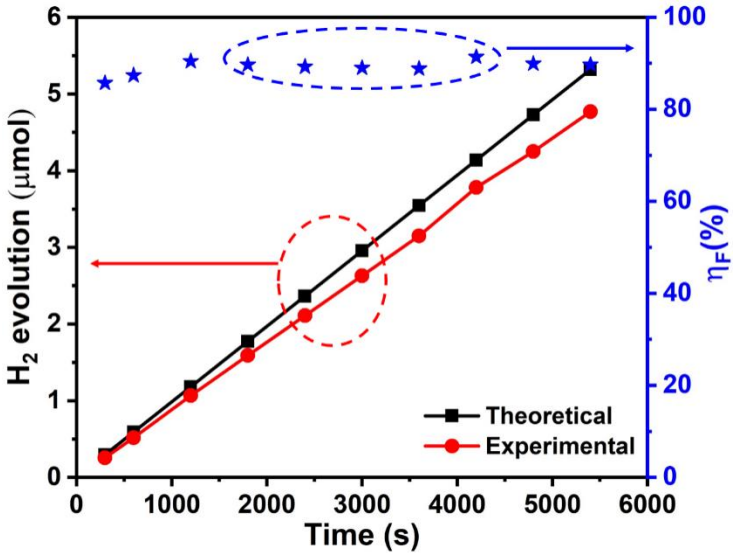

Figure 3.17. H_2 evolution of FTO/Zn-MoS_2/PbS@CdS/ZnS photoanode as a function of time at 0.93 V vs RHE under 100 mW/cm^2 illumination with AM 1.5 G filter. The theoretical amount of H_2 was calculated using the measured photocurrent, whereas the experimental value was determined by GC measurements.

The theoretical curve is calculated based on the actual photocurrent versus time. By comparing the amount of gas generated experimentally with the theoretically calculated value, the relevant Faradaic efficiency (η_F) can be determined.

The Faradaic efficiency was calculated as follows:

$$\eta_{Faradaic} = \frac{n_{H_2}(experimental)}{n_{H_2}(theoretical)} \times 100\%$$

The theoretical number of moles of hydrogen was calculated based on the measured photo-current:

$$n_{H_2}(\text{theoretical}) = \frac{1}{z}\frac{Q}{F} = \frac{1}{2}\frac{I \times t}{F} = \frac{1}{2F}\int_0^t Idt$$

In the above equation, n represents the number of moles of hydrogen produced, while z represents the number of transferred electrons per mole of water (i.e. z=2), Q represents the quantity of charge in coulomb (C) and equals to $I \times t$, F represents the Faraday constant (the quantity of charge in coulomb carried by one mole of electrons, i.e. 96484.34 C/mole), I represents the photocurrent in amperes (A), and t represents time in seconds (s), respectively.

According to GC record after 5400 s, the H_2 gas evolved was 4.77 × 10^{-6} mol, whereas the current density obtained by chronoamperometry is 0.19 mA/cm^2.

$$n_{H_2}(theoretical) = \frac{0.00019\ (A)\times 5400\ (s)}{2\times 96485.33\ C\cdot mol^{-1}} = 5.32\times 10^{-6}\ mol$$

Therefore,

$$\eta_{Faradaic} = \frac{4.77 \times 10^{-6}\ mol}{5.32 \times 10^{-6}\ mol} = 89.6\ \%$$

In the case of the 10 Zn-MoS_2/PbS@CdS/ZnS sample, the calculated ηF is around 89.6 %. The difference between the measured and calculated value of H_2 might be due to gas leakage in our homemade prototype experimental system.

Subsequently, XRD characterization was applied to assess the stability of the proposed photo-anode after long-term run (Figure 3.18). As it was necessary to first perform a chronoamperometric test, the samples were deposited on FTO, thus its signal is visible in the XRD pattern. The increase in the signal of FTO peaks is due to the removal of insulating epoxy resin, which exposes more FTO surfaces. The characteristic peak of Zn-MoS_2 and PbS@CdS did not significantly change after the chronoamperometric test, thus suggesting that the stability of the prepared photoanodes is acceptable.

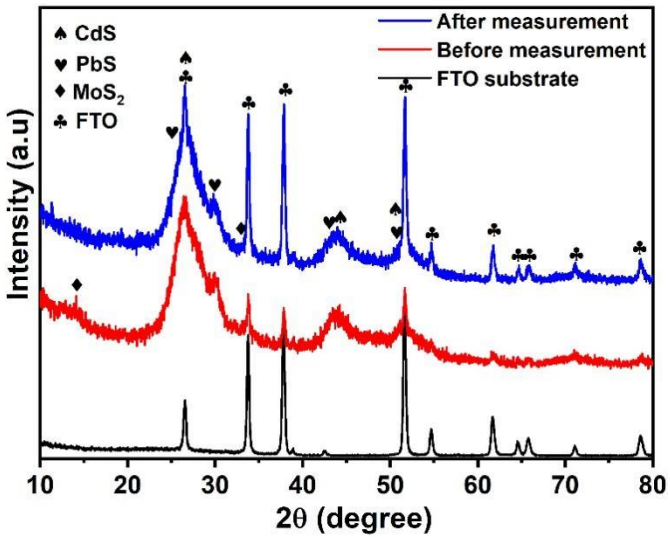

Figure 3.18. XRD patterns of 10 Zn-MoS_2/PbS@CdS photo-anode before and after long term run, the different symbols represent the constituent.

To investigate the possible reasons for the decrease in photocurrent density of the proposed PEC devices, we further conducted XPS measurements to the FTO/10 Zn-MoS_2/PbS@CdS/ZnS photo-anode before and after the long-term PEC measurement. As shown in Figure 3.19, the XPS survey spectrum of the sample before and after measurement presents the same elements: Mo, S, Zn, Pb, Cd and Na elements. The presence of Na is due to the residue of S precursor solution and the electrolyte (Na_2S or Na_2SO_3). Figure 3.19 b-f displays high-resolution spectra of Mo 3d, S 2p, Cd 3d, Pb 4f and Zn 2p chemical states before and after long-term run test, respectively. The binding energy peak of Mo 3d (Figure 3.19b) presents a 0.1 eV shift towards lower energies, which could indicate partial oxidation of Mo. A similar shift is also observed for the S 2s peaks (Figure 3.19c) indicating a partial oxidation of S^{2-} or residue of S precursor of Na_2SO_3 electrolyte. Regarding Pb element (Figure 3.19 d), the binding energy of Pb $4f_{5/2}$ and Pb $4f_{7/2}$ are located at 143.15 eV and 138.19 eV before the long-term stability test, respectively, with a characteristic of 4.94 eV difference of the Pb^{2+} states. The peak located at 139.80 eV, between Pb $4f_{5/2}$ and Pb $4f_{7/2}$ (Figure 3.19d) is assigned to Zn 3s and it is due to the presence of the ZnS protection shell. After the long-term stability test, the binding energy position of Pb $4f_{5/2}$ and Pb $4f_{7/2}$ peaks do not present any obvious shift, whereas the Zn 3S peak presents a 0.15 eV shift towards lower binding energy, indicating partial oxidation of Zn. Regarding the Cd spectra (Figure 3.19 e), before the stability test the characteristic peaks of the Cd $3d_{3/2}$ and Cd $3d_{5/2}$ of CdS can be located at 411.26 eV and 404.51 eV, respectively. The 6.75 eV difference between them is characteristic of Cd^{2+} states. In the used sample, the Cd 3d peaks kept the same position. Figure 3.19 f shows the spectrum of Zn 2p before measurement with a pair of peaks at 1044.4 eV and 1021.4 eV, corresponding to Zn $2p_{1/2}$ and $2p_{3/2}$, respectively. A typical splitting energy of 23.0 eV can be observed, consistent with previously reported values for ZnS.[208] The two Zn 2p peaks had a shift to lower binding energy of about 0.1 eV after PEC measurement. (N.B. The difference of the intensity of the Zn signal between Figure 3.19 and 3.7 is due to the presence of the ZnS shell in the former case). Thus, after long-term PEC measurement, the observed shifts of the Mo 3d, S 2p and Zn 2p peaks could probably be assigned to partial oxidation of Zn-MoS_2 and ZnS shell. Thus, the decreased PEC stability observed in the PEC measurement could be ascribed to the hole-induced self-oxidation decomposition of the metal chalcogenide of the photo-anode.

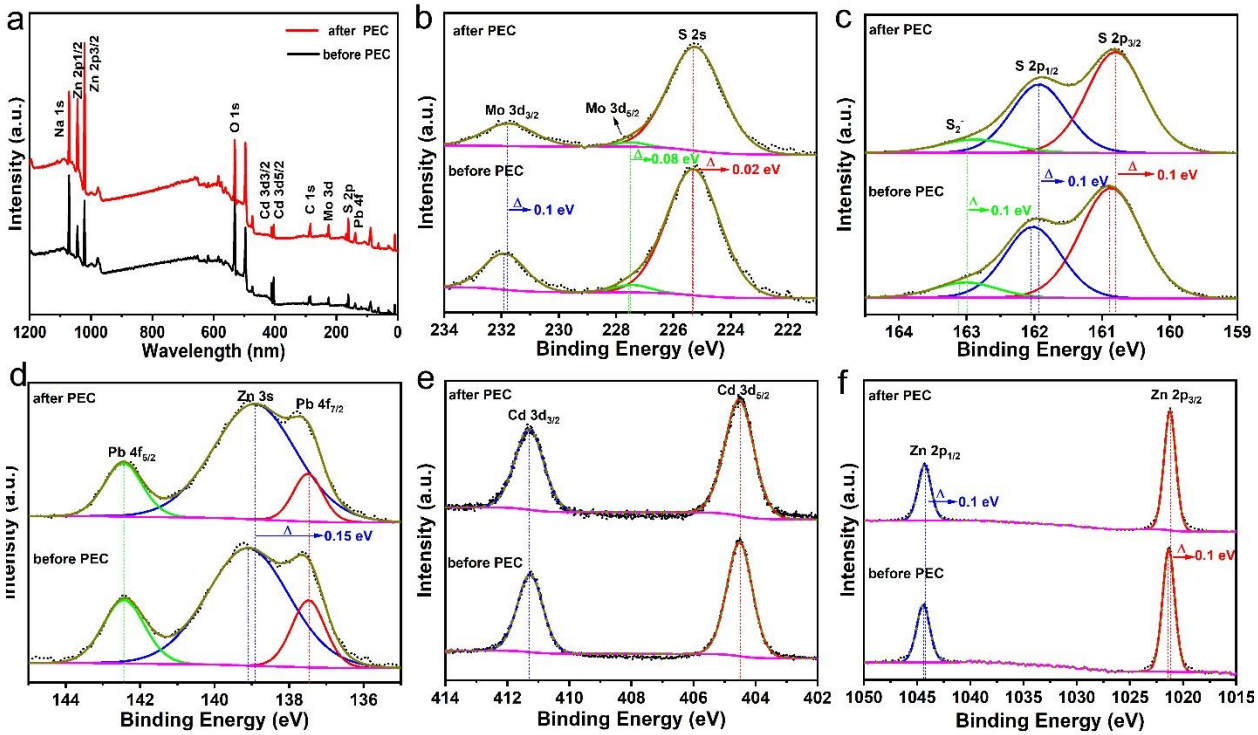

Figure 3.19. The high-resolution XPS spectra of FTO/10 Zn-MoS_2/PbS@CdS/ZnS photo-anode before and after the PEC measurement (Δ represents the peak shift).

3.5 Possible mechanism of PEC based on different Zn dopant and QDs compositions

We investigated the band alignment and charge transfer mechanism, to elucidate the influence of heterostructure nanomaterials on the overall PEC performances of the devices. Figure 3.20a reports the UV-vis DRS absorption spectra of the proposed MoS_2 with different amounts of Zn dopant. An apparent blue shift appears when the MoS_2 is doped with Zn, indicating that the band gap of Zn-MoS_2 is adjustable, and increases with the Zn dopant, which will facilitate matching the band gap between 0D QDs and 2D Zn-MoS_2, similarly to previous reports.[176] Simultaneously, the absorption spectra were also applied to investigate the influence of different QDs SILAR to 10Zn-MoS_2. After the different QDs SILAR process to the 10Zn-MoS_2 photo-anode, the UV-vis absorption spectra exhibit obvious differences. As shown in Figure 3.20 b, the absorption spectra of 10Zn-MoS_2/PbS showed an obvious red-shift compared to pure 10Zn-MoS_2 because of the relatively small band gap of PbS. On the contrary, the absorption spectra of 10Zn-MoS_2/CdS showed a blue-shift compared to pure 10Zn-MoS_2 because of the relatively large band gap of CdS.[4] And, the absorption spectra of 10Zn-MoS_2/PbS@CdS is located between the 10Zn-MoS_2/CdS and 10Zn-MoS_2/PbS, which also confirmed the successful SILAR approach.

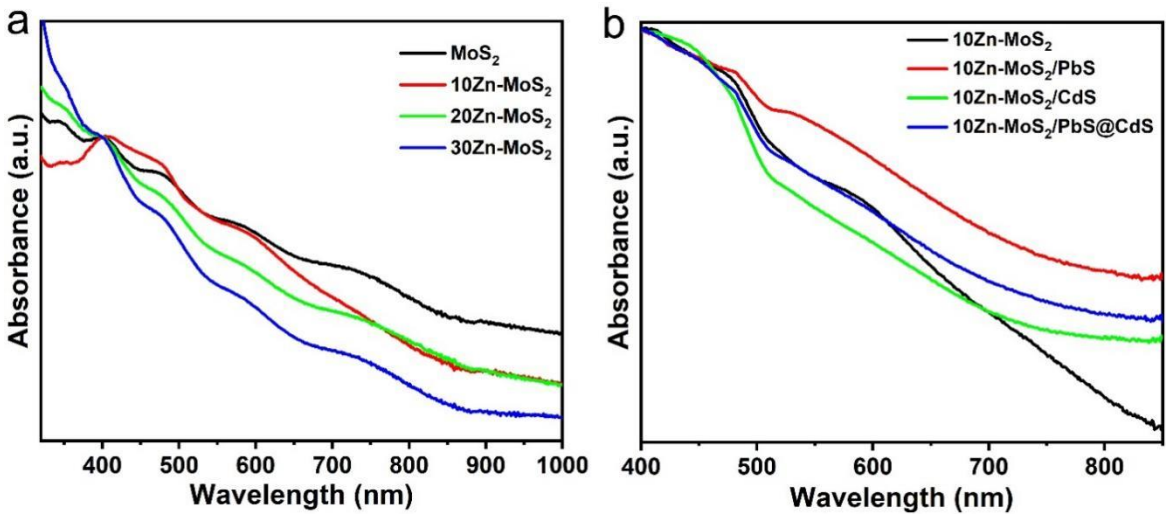

Figure 3.20 UV-vis DRS spectra: different amount of Zn doped to MoS_2 (a), different QDs SILAR approach to 10Zn-MoS_2 (b).

The bandgap of Zn-MoS_2 nanocomposites can be estimated using Tauc's equation, considering MoS_2 as a direct band gap material.[165, 209] In detail, the bandgap energies were estimated by Tauc's equation $(ahv)^n = A(hv - Eg)$, where a, h, v, and Eg referred to absorption coefficient, Planck constant, light frequency, and band gap energy, respectively; $n = 1/2$ for indirect-gap semiconductors and $n = 2$ for direct gap semiconductors.[210] After calculation, the corresponding band-gap energies of as-synthesized Zn-MoS_2 were estimated to shift from 1.65 eV to 1.95 eV with Zn dopant increases (Figure 3.21).

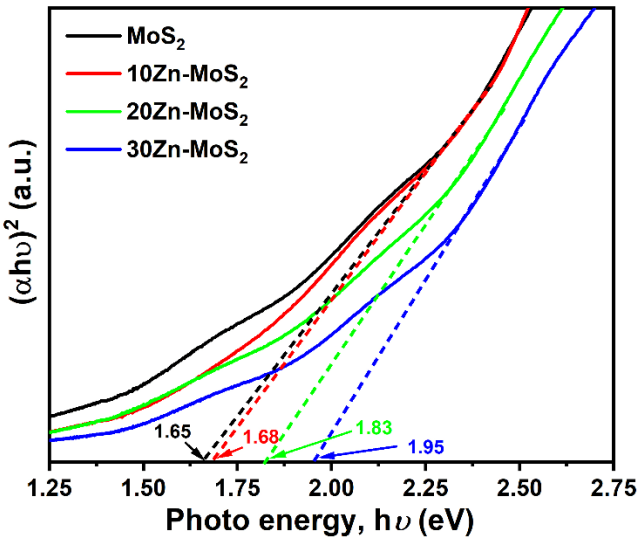

Figure 3.21. Tauc plots of $(\alpha hv)^2$ versus band-gap energy (*hv*) of different amounts of Zn doped MoS_2 composite samples.

In addition, Ultraviolet photoelectron spectroscopy (UPS) measurements using He I radiation (21.22 eV) were carried out to determine the maximum valance band energy level (VBM) of the different MoS_2 samples. Figure 3.22 shows the high and low binding energy cut-off of Zn-MoS_2 samples, obtained by the intersection of the linear extrapolation of the high and low binding energies with the baseline. The difference between high binding energies and low binding energies gives the UPS widths of Zn-MoS_2 samples. As shown in Figure 3.22, the UPS widths were determined to be 14.37 eV, 15.42 eV, 15.47 eV and 15.47 eV corresponding to 0%, 10%, 20% and 30% Zn-MoS_2, respectively. The VBM values of Zn-MoS_2 can be estimated to be 5.85 eV, 5.8 eV, 5.75 eV and 5.75 eV corresponding to 0%, 10%, 20% and 30% Zn-MoS_2, respectively, by subtracting the width of the UPS spectra from the excitation energy (21.22 eV). Then, based on the equation $E_{CB} = E_{VB}-E_g$, the CBM can be calculated. By using the obtained value, we calculated CB values of 4.2 eV for MoS_2, 4.12 eV for 10Zn-MoS_2, 3.92 eV for 20Zn-MoS_2, and 3.8 eV for 30Zn-MoS_2 with respect to the vacuum level, respectively. The detailed values of the band structures of Zn-MoS_2 are reported in Table S3. The modulation of the band energies due to the Zn doping will significantly influence the band alignment between 0D QDs and 2D Zn-MoS_2.

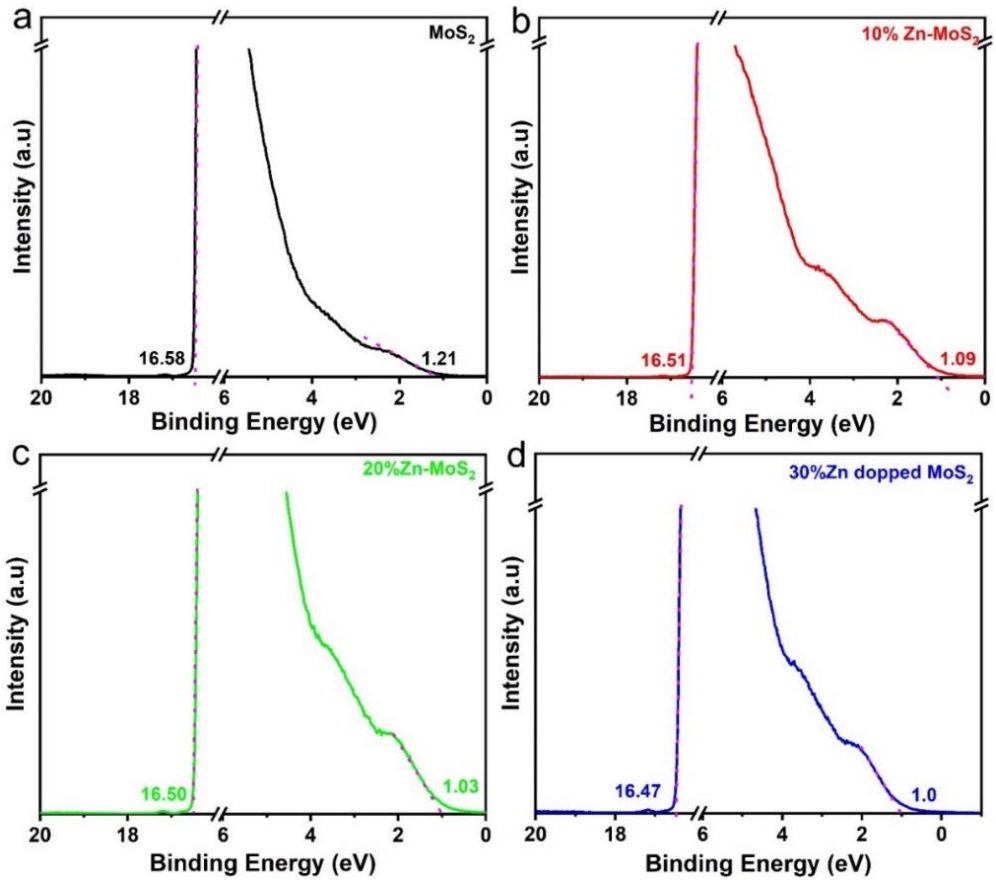

Figure 3.22. UPS cut off spectra of (a) MoS_2, (b) 10Zn-MoS_2, (c) 20Zn-MoS_2 and (d) 30 Zn-MoS_2, respectively.

Table 3.3. Band gap of these proposed Zn-MoS_2.

samples	Band-gap (eV)	VBM (eV)	CBM (eV)
MoS_2	1.65	-5.85	-4.20
10Zn-MoS_2	1.68	-5.80	-4.12
20Zn-MoS_2	1.83	-5.75	-3.92
30Zn-MoS_2	1.95	-5.75	-3.80

Based on the reconstructed band alignment obtained from UV-Vis DRS, UPS and the PEC performance, we propose a mechanism for the Zn-MoS_2 photoanodes sensitized with QDs. The band alignment and schematic diagram of PbS@CdS QDs-sensitized Zn-MoS_2 photoanode for PEC cells are illustrated in Figure 3.23. The accurate band gap of QDs was obtained from the reported literature (PbS[211] and CdS[212], respectively). As shown in Figure 3.23a, the Zn-MoS_2/PbS@CdS heterostructure forms a type II band alignment, which is favourable for the separation and transfer of photoexcited electrons at the QDs/Zn-MoS_2 interface. Based on the type II band alignment, the electrons will be injected from QDs into Zn-MoS_2 and are subsequently collected by the FTO electrode, while the photogenerated holes are oxidized by the sacrificial agent ($Na_2S{\cdot}9H_2O$ and Na_2SO_3) present in the electrolyte. Finally, these electrons will migrate to the Pt counter electrode for water reduction.

Figure 3.23b shows that the modulation of the band alignment in the different QDs also affects the charge injection and thus the final J_{ph}. Independently of the doping of MoS_2, the sensitization with the composite PbS@CdS generates the highest photocurrents. On the other hand, the use of 10% doping increases the photocurrents for each type of QDs. Thus, to enhance the PEC performance it is advisable to combine both the modulation of Zn doping and the choice of the QDs sensitizer. We also observe that PbS QDs, even if they possess a smaller band gap than CdS QDs, generate lower J_{ph} due to a reduced driving force to inject charges into Zn-MoS_2. Overall, there is an optimum condition, namely 10% Zn doping in MoS_2 and PbS@CdS QDs, that creates favourable conditions (fast charge injections and wide absorption range) that allow to maximize performance (Figure 3.23c). Thus, the improved PEC performance of the 10% Zn-doped sample can be attributed to a synergistic effect. The doping can not only modulate the CB to achieve better band alignment, but it can also increase the EESA (Figure 3.14) to achieve

better PEC performance. In contrast, undoped MoS_2, although having a favourable CB for charge injection, suffers from rapid recombination due to the less conductive and small band bending.

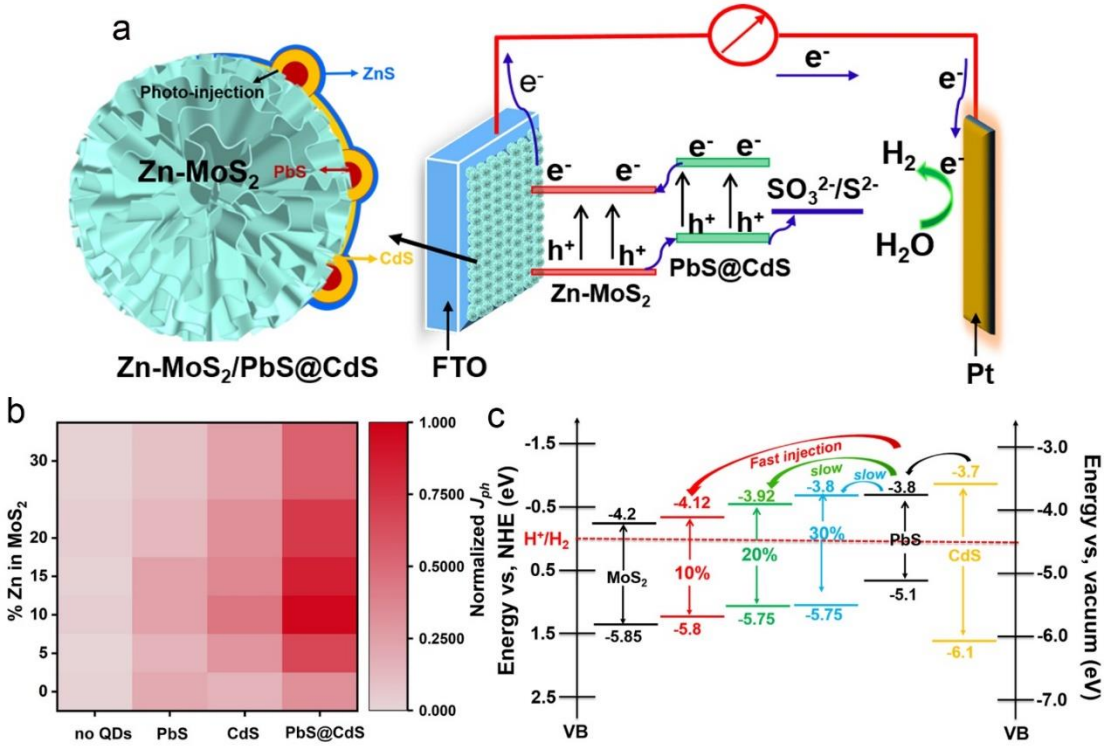

Figure 3.23. Schematic diagrams of (a) formation of anodic photocurrent, (b) Photocurrent density based on different Zn doping and different QDs sensitizer; (c) band energy position of Zn-MoS_2, QDs and the charge transfer mechanism.

Under light irradiation, the electrons in the valence band (VB) of QDs are excited to their conduction band (CB), leaving behind positively charged holes. Thanks to the presence of a favourable driving force, the excited electrons are injected into the CB of adjacent Zn-MoS_2, largely suppressing the recombination of charge carriers and promoting charge transfer. The charge transfer process can also be promoted by the presence of certain Zn trap sites.[7] At the same time, the holes in the VB are immediately captured due the high driving force of hole-sacrificial agent S^{2-}/SO_3^{2-}. The possible mechanism for the hole reaction at the electrode-electrolyte interface could be summarized as follow:

$$Zn\text{-}MoS_2/QDs + hu \rightarrow e^-(CB) + h^+(VB) \qquad (i)$$

$$2H_2O + 2e^-(CB) \rightarrow H_2 + 2OH^- \qquad (ii)$$

$$SO_3^{2-} + 2OH^- + 2h^+(VB) \rightarrow SO_4^{2-} + H_2O \qquad (iii)$$

$$2S^{2-} + 2h^{+} (VB) \rightarrow S_2^{2-} \quad \text{(iv)}$$

$$S_2^{2-} + SO_3^{2-} \rightarrow S_2O_3^{2-} + S^{2-} \quad \text{(v)}$$

$$SO_3^{2-} + S^{2-} + 2h^{+} (VB) \rightarrow S_2O_3^{2-} \quad \text{(vi)}$$

Compared to pure MoS_2, Zn-MoS_2 significantly increases the surface area and electron density due to Zn doping. Therefore, more QDs will adhere to the Zn-MoS_2 surface, increasing absorption and leading to better PEC performance. Further, appropriate Zn doping can adjust the band structure of Zn-MoS_2 allowing the formation of a favorable band alignment for the charge injection. However, doping should be limited below a certain threshold (in this specific case 10%) to avoid unfavorable band alignment for charge injection and the creation of impurities, such as ZnS, that would limit the electron transfer. Overall, an appropriate modulation of the band energy of both, the QDs with the formation of a composite, and an optimum amount of Zn dopant in MoS_2 can increase the final PEC performance.

3.6 Conclusions and Perspectives

An unusual 0D/2D heterojunction based on 0D PbS@CdS QDs and 2D Zn-MoS_2 NSs was rationally designed. The 0D PbS@CdS QDs were deposited *in situ* on both sides of Zn-MoS_2 NSs by SILAR. Due to the synergistic effect of the broad absorption of QDs and superior band alignment between the optimized Zn-MoS_2 and the QDs, the 0D/2D heterojunction presents a remarkable enhancement of PEC performance. In particular, we showed the modulation of the band alignment directly leads to an improved steady-state photocurrent. This work suggests that in order to achieve better PEC performance, it is important to control the complete design of the photoanodes, simultaneously considering both the modulation of the band alignment with the doping and carefully choosing the composition of the QDs. The initial results of the band engineering and the cost-effective preparation of the photoelectrodes showed in this work can pave a new way for the preparation of functional nonoxide photoelectrodes combined with QDs that can be widely used in the PEC field. Further, this approach can be applied to other types of QDs, such as “green” QDs (core-shell and alloyed QDs) and other transition metal chalcogenides, exploring also different optoelectronic applications such as solar cells and photodetectors.

4 "GREEN", GRADIENT MULTI-SHELL $CuInSe_2/(CuInSe_xS_{1-x})_5/CuInS_2$ QUANTUM DOTS FOR PEC H_2 GENERATION

Links between projects:

In chapter 3, we construct a 0D/2D hetero-structure by modulating the band position of 2D hierarchical NSs by different amounts of Zn doping. Meanwhile, core-shell PbS@CdS QDs were used as sensitizers to extend the light-harvesting range. The role of different QDs and the band alignments between 0D QDs and 2D NSs to enhance PEC performance is investigated in detail. Whereas, although direct contact between host semiconductors and QDs is achieved by in-situ growth, also faces challenges such as uncontrolled QDs coverage and high charge recombination due to possible interfacial traps. The above drawbacks can be avoided if QDs are synthesized in the form of colloids with controllable size, crystal phase, and chemical composition, and then grafted onto wide-bandgap semiconductor surfaces. Up to now, the majority of PEC systems based on QDs typically use heavy metal elements, such as Pb and Cd, which are toxic. The development of heavy metal-free QDs for PEC applications is a major unresolved challenge in this field. For the second project, a sequential cation exchange approach was used to synthesize heavy metal-free, gradient multi-shell architecture $CuInSe_2/(CuInSe_xS_{1-x})_5/CuInS_2$ QDs and investigate the PEC performances.

In the 1970s, TiO_2 semiconductors were first developed to use in PEC cells for H_2 generation. To address the problem of short absorption range, QDs were considered as one of the most promising photosensitizers to sensitize TiO_2, thanks to their unique and scalable optical properties where absorption and photoluminescence of the QDs are composition and size-tunable, extending the absorption range from UV to VIS-NIR range. In this chapter, a NIR, graded, "green" $CuInSe_2/(CuInSe_xS_{1-x})_5/CuInS_2$ QDs were used as sensitizers for TiO_2 photo-anodes. The QDs are synthesized by a successive cation exchange approach based on a template, in this case of $CdSe/(CdSe_xS_{1-x})_5/CdS$. A series of characterization techniques were applied to confirm the successful preparation of QDs after cation exchange. The graded multi-shell architecture exhibits tunable Near Infra-Red (NIR) optical absorption and photoluminescence (PL) properties. The resultant QDs were then deposited into a mesoporous TiO_2 film by electrophoretic deposition (EPD) and further coated with two ZnS layers by successive ionic layer adsorption and reaction (SILAR) approach to prevent photo-corrosion. As a proof-of-concept, a comparative study of the PEC performance was performed between the pure core $CuInSe_2$, core/shell $CuInSe_2/(CuInS_2)_6$

and graded $CuInSe_2/(CuInSe_xS_{1-x})_5/CuInS_2$. The $CuInSe_2$ and $CuInSe_2/(CuInS_2)_6$ QDs sensitized photo-anode exhibited a saturated photocurrent density ~1.5 mA/cm^2 and 2.6 mA/cm^2, respectively. When the gradient alloyed shell was introduced, the QDs-based photoanode showed a boost of more than 200% and 73 % in photocurrent respectively, reaching an impressive value (for heavy-metal-free NIR QDs) of photocurrent density of 4.5 mA/cm^2. The photocurrent was stable for a long time, showing a drop of only 17% after 2 h with irradiation at one Sun intensity (AM 1.5 G, 100 mW/cm^2). These remarkable results indicate that NIR, graded, heavy-metal-free QDs are a promising material for not only PEC devices but in general QDs based optoelectronic devices. We analyzed in detail the mechanisms that underpin this significant enhancement and are ascribed to a favorable stepwise electronic band alignment, which improves the electron transfer rate and reduces charge recombination, due to the incorporation of interfacial gradient layers. The experimental data on exciton kinetics are supported also by the theoretical analysis of the electron/hole (e/h) wave function.

4.1 Experiment section

4.1.1 Synthesis of $CdSe/(CdSe_xS_{1-x})_5/CdS$ graded QDs

The CdSe core QDs were synthesized according to a protocol described previously with a hot injection approach.[132] Basically, the Cd-oleate precursor was prepared as follows: 0.38 mmol of CdO was dissolved in the mixture of OA (CdO: OA=1:4) and ODE (1.52 mL) at 240 °C for 30 min under N_2 until the formation of a transparent colloidal solution was observed. Subsequently, the mixture of as-synthesized Cd-oleate (0.38 mmol), TOPO (1 g) and ODE (8 mL) was purged by N_2 for 30 min at room temperature. The temperature was then raised to 100 °C, and further degassed for 30 min before the temperature was raised to 300 °C. After that, a mixture of ODE (1 mL), OLA (3 mL), and TOP-Se (4 mmol, 4 mL) was swiftly injected into the Cd-oleate suspension under vigorous stirring. After two min, the reaction was quenched by cold water. Finally, the resultant was precipitated and washed by ethanol and toluene to eliminate unreacted precursors and the precipitate was re-dispersed in toluene.

The synthesis of core-shell CdSe/CdS QDs and graded $CdSe/(CdSe_xS_{1-x})_5/CdS$ QDs followed a Successive Ionic Layer Adsorption and Reaction (SILAR) approach. Normally, in a 50 mL round bottom flask, CdSe QDs (~2×10^{-7} M in Toluene), OLA (5 ml) and ODE (5 mL) were degassed at 110 °C for 30 min. Then, the reaction was re-stored with N_2 and the temperature was further raised to 240 °C with stirring. According to the volume increment of each monolayer shell, the quantity of precursors for growing each monolayer of shell was calculated, considering the

changing total QDs size with each successive monolayer grown. The Cd-oleate (0.25 mL, 0.2 M) was added dropwise to the reaction and the mixture was allowed to react for 1.5 h, followed by dropwise addition of sulfur in ODE (0.25 mL, 0.2 M). Subsequently, the shell was further annealed for 10 min. Typically, all subsequent shells were annealed at 240 °C for ~1.5 h following dropwise injection of the Cd-oleate and ~10 min following injection of sulfur. The calculation of volume of QDs, Cd-oleate/sulfur addition volumes for shell addition cycles 1-6 are reported in Table 4.1. The reaction was then quenched by cold water. The resultant was precipitated and washed by ethanol and toluene, respectively, and re-dispersed in toluene.

Table 4.1 Injection volumes of sulfur and Cd-oleate for SILAR cycles.

SILAR cycles	1	2	3	4	5	6
Injection volumes (mL)	0.25	0.36	0.48	0.62	0.78	0.96

In particular, the graded shells were synthesized by adjusting the molar ratio of Se:S (with total concentration of 0.2 M) during *in situ* growth of five layers $CdSe_xS_{1-x}$ (the detailed ratio are presented in Table 4.2) on CdSe core QDs. Subsequently, another CdS layer was coated on the graded shell. After that, the reaction was also quenched by cold water. The resultant was precipitated and washed by ethanol and toluene, respectively, and re-dispersed in toluene.

Table 4.2 Injection volumes ratio of Se/S for SILAR cycles.

SILAR cycles	1	2	3	4	5	6
$CdSe/(CdS)_6$	0/10	0/10	0/10	0/10	0/10	0/10
$CdSe/(CdSe_xS_{1-x})_5/CdS$	8/2	6/4	5/5	4/6	2/8	0/10

4.1.2 Cation Exchange Procedure

The cation exchange approach was performed according to a protocol reported by van der Stam et al [138, 213]. Typically, $[Cu(CH_3CN)_4]PF_6$ (150 mg, 0.4 mmol) was dissolved into 5 mL of methanol and diluted with 5 mL of toluene under sonication. Then, the mixture was dropped into QDs in a

flask (~2*10^{-8} M) under vigorous stirring at room temperature for 10 min. To ensure full exchange, the atomic ratio of Cu to Cd was fixed to ~10. Subsequently, the as-synthesized $Cu_2Se/(Cu_2Se_xS_{1-x})_5/Cu_2S$ QDs were centrifuged and washed with methanol and toluene, respectively, and re-dispersed in ~5 mL of toluene. The same process was applied for the core and core-shell QDs cation exchange.

For In^{3+} cation exchange [214], 5 mL of $Cu_2Se/(Cu_2Se_xS_{1-x})_5/Cu_2S$ QDs (~2*10^{-8} M) stock solution was degassed by N_2 to remove toluene and then dispersed into 5 mL of ODE and 2 mL of DDT. Then, the reaction was heated to 100 °C under N_2 flow. Subsequently, 1.75 mL of 2 M TOP-$In(Ac)_3$ precursor in ODE (1 mmol of $In(Ac)_3$ in 0.5 mL of TOP, diluted with 3 mL of ODE) was drop-wised into above reaction when the temperature was stable at 100 °C. The mixture was maintained at 100 °C for 4 h with stirring and then cooled down to room temperature. Finally, the as-synthesized $CuInSe_2/(CuInS_2)_6$ QDs were precipitated and washed with ethanol and toluene to eliminate unreacted precursors, respectively, and re-dispersed in toluene.

4.1.3 Preparation of TiO_2 photoanode

The FTO glass substrate was cleaned with a mixture of methanol, acetone and isopropanol (1:1:2), rinsed with deionized water, and dried in an N_2 flow. Then, the cleaned FTO glass substrates were treated in a UV-ozone cleaner for 15 min to further eliminate surface organic contaminants. Subsequently, a compact TiO_2 blocking layer was deposited on FTO substrates by hydrolysis of 0.05 M $TiCl_4$ solution at 70 °C for 30 min, followed by annealing in air at 500 °C for 30 min and then cooling to room temperature. After that, a commercial TiO_2 paste (18 NR-T) was deposited on FTO substrates by tape-casting and kept in air for 15 min to completely spread out. The electrodes were then dried on a hot plate at 120 °C for 6 min. A blend of small anatase particles (~20 nm) and larger anatase scatter particles (~450 nm) paste (18 NR-AO) was subsequently deposited on top of 18 NR-T, following the same procedure. The electrodes were later sintered at 500 °C for 30 min in a furnace and cooled down to room temperature to obtain the mesoporous TiO_2 films. The total thickness (~16.5 μm) was obtained by Scanning Electron Microscopy (SEM) cross-sectional imaging.

4.1.4 Fabrication of QDs-sensitized photoanode and further ZnS coating.

The QDs-sensitized photoanodes were fabricated by deposition of QDs into a mesoporous TiO_2 film by electrophoretic deposition (EPD). Two as-prepared TiO_2 films on FTO substrates were vertically immersed in the QDs toluene solution. The distance between them was adjusted at 1 cm and a direct

current bias of 200 V was applied for 2 h [24]. To wash off unabsorbed QDs after the EPD process, the electrodes were rinsed several times with toluene and dried with N_2 flow at room temperature. Subsequently, two SILAR cycles of CTAB/methanol solution (10 mg/mL) were applied for the ligand exchange with a dipping time of about 1 min. For each SILAR cycle, after CTAB treating, to remove the chemical residuals from the surface, the films were dipped for 1 min in methanol then dried in N_2 flow, then dipped for one min dipping in toluene and dried with N_2 for each SILAR cycle. Successively, the ZnS capping layer was grown using a similar SILAR process. In detail, the Zn^{2+} were deposited from a methanolic $Zn(OAc)_2$ solution (0.1 M, 20 mL). The sulfide precursor was 0.1 M of Na_2S dissolved in the 20 mL mixture of methanol/water (1/1 v/v). A single SILAR cycle consisted of 1 min of dip-coating the TiO_2/QDs electrode into the Zn^{2+} precursors, and subsequently into S^{2-} solution. After each precursor dipping, the TiO_2/QDs electrode was thoroughly rinsed with the corresponding solvent, respectively, to remove the chemical residuals and then dried with an N_2 flow. Two SILAR cycles were applied to form the capping ZnS layer. To fairly compare the samples, the ZnS layer is applied to all the photoanodes (bare TiO_2 and QDs sensitized).

4.1.5 Characterization

Device characterization: All electrochemical measurements were performed by employing a Gamry 1000E electrochemical workstation with a sweep rate of 20 mV/s. A traditional three-electrode system was used to evaluate the PEC performance of the QDs-sensitized photo-anode, including a platinum sheet counter electrode as an auxiliary electrode, a Ag/AgCl with saturated KCl as a reference electrode, and the fabricated TiO_2/QDs thick film as the working electrode. The surface of the photoanode was covered with an insulating epoxy resin, except for the active area (~0.15 cm^2), to avoid any direct contact between the electrolyte and the conductive back contact and/or the connecting wire. The electrolyte (pH=12.5) was composed of 0.25 M Na_2S and 0.35 M Na_2SO_3, which serves as sacrificial hole scavenger to prevent the photo-corrosion of QDs. Before measurements, the electrolyte was deoxygenated with highly pure N_2 for 30 min. The measured potential (vs Ag/AgCl) was converted into a reversible hydrogen electrode (RHE) according to the following formula:

$$V_{RHE} = V_{Ag/AgCl} + 0.1976 + pH * (0.059)$$

In particular, the photocurrent density-voltage (J-V) curve was measured using a Compact Solar Simulator AAA (Sciencetech SLB-300A) under simulated sunlight (1 Sun = AM 1.5G, 100 mW cm^{-2}). To verify the standard 1 solar illumination (100 mW cm^{-2}) on the as-fabricated photoanode

(working electrode) in the three-electrode system, a Si reference diode (Sciencetech) was used to adjust the distance between solar simulator and photo anode before each measurement. In this case, the distance between the Sun Simulator and PEC cell was fixed at about ~30 cm. Electrochemical impedance spectroscopy (EIS) was carried out under light (1 Sun) conditions by using a Gamry 1000E station with zero bias voltage vs Reference and a sweep in frequency from 300 kHz to 0.1 kHz. All impedance measurements were analysed using an appropriate equivalent circuit model with Z-View software (v3.5, Scribner Associate, Inc.).

4.1.6 Theoretical calculations

The stationary Schrödinger equation was applied to calculate the theoretical wave functions of the electron and hole in spherical geometry, in which the bulk parameters were used for the effective masses of electrons (m_e*) and holes (m_h*), namely, m_e* = 0.09 m_e and m_h* = 0.73 m_e for $CuInSe_2$, and m_e* = 0.16 m_e and m_h* = 0.85 m_e for $CuInS_2$, where m_e is the free electron rest mass. The effective masses for the $CuInSe_xS_{1-x}$ interfacial layers were obtained through the weighted average of the values for the core ($CuInSe_2$) and shell layer ($CuInS_2$). The potentials for electrons and holes as a function of position were approximated to the CBM and VBM, respectively, of the bulk materials. For $CuInSe_2$, these levels are -4.60 eV and -5.64 eV, respectively, while for $CuInS_2$, these levels are -4.39 eV and -5.92 eV, respectively.[215] As for the effective masses, for the alloyed $CuInSe_xS_{1-x}$ interfacial layers we used weighted averages (x for Se and 1-x for S, x = 0.8, 0,6, 0.5, 0.4, 0.2, respectively) of the above quantities. The parameters are summarized in Table 4.3. Outside the QDs, the potentials for electrons and holes were set as 0 and -9.8 eV, respectively, and the interaction between electrons and holes was neglected in the calculations.

Table 4.3 Physical parameters of $CuInSe_2$ and $CuInS_2$. [215]

Type	bulk	*Ec* (eV)	*Ev* (eV)	*Eg* (eV)	m_e/m_0	m_h/m_0
Core	$CuInSe_2$	-4.6	-5.64	1.04	0.09	0.73
Alloyed shell	$CuInSe_xS_{1-x}$	-4.5	-5.78	1.28	0.13	0.79
Shell	$CuInS_2$	-4.39	-5.92	1.53	0.16	0.85

4.2 Result and Discussion

4.2.1 Structure characterization of QDs

A sequential cation exchange approach based on a template was applied to prepare NIR, heavy metal-free colloidal graded QDs. First, CdSe QDs with a uniform radius size of 1.55 nm were synthesized according to a hot injection approach [132]. Subsequently, six layers of CdS shell were overgrown by SILAR method on the surface of CdSe core QDs to form giant CdSe/$(CdS)_6$ core-shell QDs. To further extend the absorption region of CdSe/$(CdS)_6$ QDs, a second kind of gradient multi-shell QDs was also prepared: five gradient alloyed monolayers of $CdSe_xS_{1-x}$ shell were grown over the CdSe core QDs and then one monolayer of CdS were grown on the alloyed shell to form CdSe/$(CdSe_xS_{1-x})_5$/CdS QDs. Successively, the Cd^{2+} based QDs were used as templates for sequential cation exchange to obtain the final heavy metal-free QDs. As shown in Figure 4.1a, the schematic illustrates the detailed exchange approach: Cd^{2+} in CdSe/$(CdSe_xS_{1-x})_5$ /CdS QDs was fully exchanged by Cu^+ and as-synthesized Cu_2Se/$(CuSe_xS_{1-x})_5$/Cu_2S QDs were partially exchanged by In^{3+} to form $CuInSe_2$/$(CuInSe_xS_{1-x})_5$/$CuInS_2$ QDs. With a similar approach, by employing CdSe and CdSe/$(CdS)_6$, respectively, the $CuInSe_2$ and $CuInSe_2$/$(CuInS_2)_6$ QDs were prepared and used as a comparison.

Before proceeding with the cation exchange procedure, it was necessary to verify the successful preparation of the Cd-QDs template. For this reason, TEM, HRTEM and XRD characterization methods were used to confirm the successful preparation of $CdSe_xS_{1-x}$ and CdS shell overgrown on the CdSe core template. Figure 4.1b shows the TEM image of pure CdSe core QDs, confirming the uniform size of the QDs with a diameter of around (3.1±0.3 nm). Figure 4.1c and 1d present the TEM images of the CdSe/$(CdS)_6$ and CdSe/$(CdSe_xS_{1-x})_5$/CdS QDs, respectively. As visible, the CdSe/$(CdS)_6$ QDs possess a basic spheroid morphology with uniform sizes of (7.2±0.6) nm, while the CdSe/$(CdSe_xS_{1-x})_5$/CdS QDs show a size distribution of (7.4±0.6) nm. The thickness of the shell was calculated using the single core size found in the TEM image in Figure 4.1b. In this case, the thickness of CdS shell in CdSe/$(CdS)_6$ QDs (Figure 4.1c) was found to be ~ 2.01 nm. By tuning the feeding ratio of Se and S precursors, five $CdSe_xS_{1-x}$ and additional one CdS layer were also overgrown on the CdSe core, with shell thickness of ~2.11 nm. The thicker shell for CdSe/$(CdSe_xS_{1-x})_5$/CdS QDs compared to CdSe/$(CdS)_6$ is due to the relatively large lattice space compared CdSe to CdS corresponded to as-synthesized hexagonal crystallize [111]. The HRTEM images (inset images in Figure 4.1c and 1d) reveal a lattice space ~ 0.335 nm, which can be indexed to the (002) plane of hexagonal Wurtzite (WZ) phase of CdS (JCPDS No. 01-077-2306).

The detailed average size of core radius and shell thickness are presented in Table 4.4, as well as the size distribution in Figure 4.2.

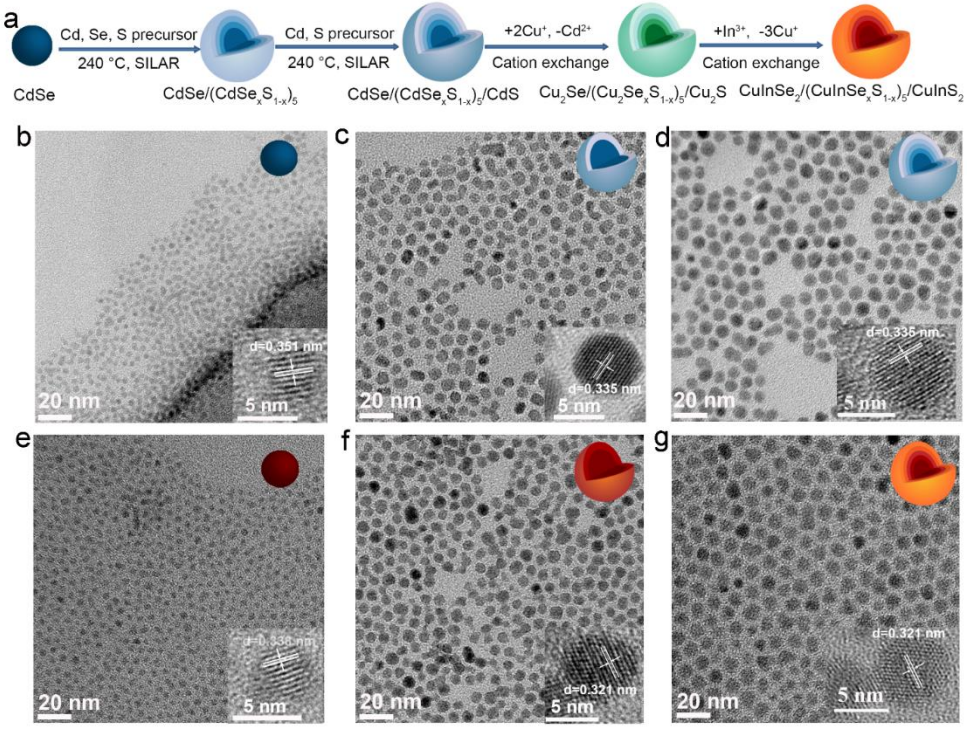

Figure 4.1 (a) Schematic diagram of sequential cation exchange procedures for synthesis of $CuInSe_2/(CuInSe_xS_{1-x})_5/CuInS_2$ QDs. Representative TEM images of: (b) CdSe, the insets is the HR-TEM image displaying the (111) plane of ZB CdSe; (c) $CdSe/(CdS)_6$ and (d) $CdSe/(CdSe_xS_{1-x})_5/CdS$ QDs before cation exchange, the insets are the HR-TEM images showing the (002) plane of WZ CdS. TEM images of (e) $CuInSe_2$, the insets is the HR-TEM image exhibiting the (111) plane of ZB $CuInSe_2$; (f) $CuInSe_2/(CuInS_2)_6$ and (g) $CuInSe_2/(CuInSe_xS_{1-x})_5/CuInS_2$ QDs, the insets are the HR-TEM image showing the (002) plane of hexagonal WZ $CuInS_2$ after cation exchange. The cartoons in the inset of the TEM images show the schematic QD.

Table 4.4 Particles size and optical parameters for the as-synthesized QDs in toluene.

samples	R^a (nm)	H^b (nm)	Oversize (nm)	Abs (nm)	PL (nm)
CdSe	1.55 nm	0	3.1 ± 0.3	552	574
$CdSe/(CdS)_6$	1.55 nm	2.01	7.2 ± 0.6	594	612
$CdSe/(CdSe_xS_{1-x})_5/CdS$	1.55 nm	2.11	7.4 ± 0.6	627	649

R^a is the CdSe core radius and H^b is the shell thickness.

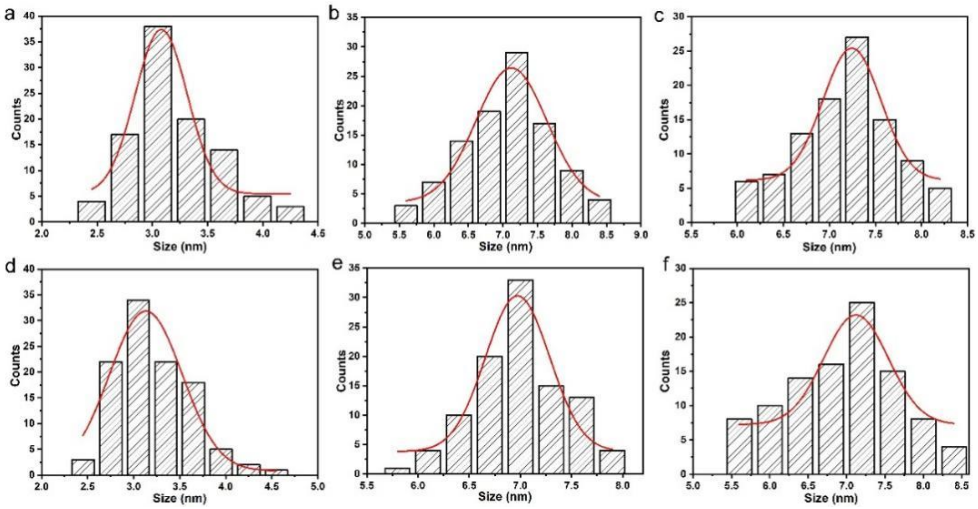

Figure 4.2. Size distribution of as-synthesized QDs corresponded to TEM imagine (Figure 4.1). The QDs before cation exchange: (a) CdSe, (b) CdSe/$(CdS)_6$ and (c) CdSe/$(CdSe_xS_{1-x})_5$@CdS QDs. After cation exchange: (d) $CuInSe_2$; (e) $CuInSe_2$/$(CuInS_2)_6$ and (f) $CuInSe_2$/$(CuInSe_xS_{1-x})_5$/$CuInS_2$ QDs.

Especially, it was hard to distinguish the core-shell structure by TEM characterization due to the small lattice mismatch between CdSe core and CdS shell around ~3.9% [216]. However, to verify the core-shell structures, XRD characterization can be applied [111]. The XRD pattern was carried out to further analyze the crystal structure of the QDs. As shown in Figure 4.3a, the black curve corresponding to CdSe QDs, shows that the nanocrystals have a zinc blende (ZB) crystal structure, which is consistent with the literature [96]. After growing six monolayers of CdS shells over the CdSe core via SILAR, the diffraction pattern of CdSe/$(CdS)_6$ core-shell QDs (red curve in Figure 4.3a) is dominated by the WZ crystal structure of CdS while the ZB crystal structure of the CdSe core is less visible, due to large volume of the CdS shell compared to the CdSe core [132]. On the other hand, the diffraction pattern of the CdSe/$(CdSe_xS_{1-x})_5$/CdS QDs (blue curve in Figure 4.3a) exhibits mixed reflections between WZ structure of CdS and WZ of CdSe, indicating the formation of the alloyed WZ $CdSe_xS_{1-x}$. These data fully confirm the successful preparation of the gradient multi-shell template CdSe/$(CdSe_xS_{1-x})_5$/CdS QDs.

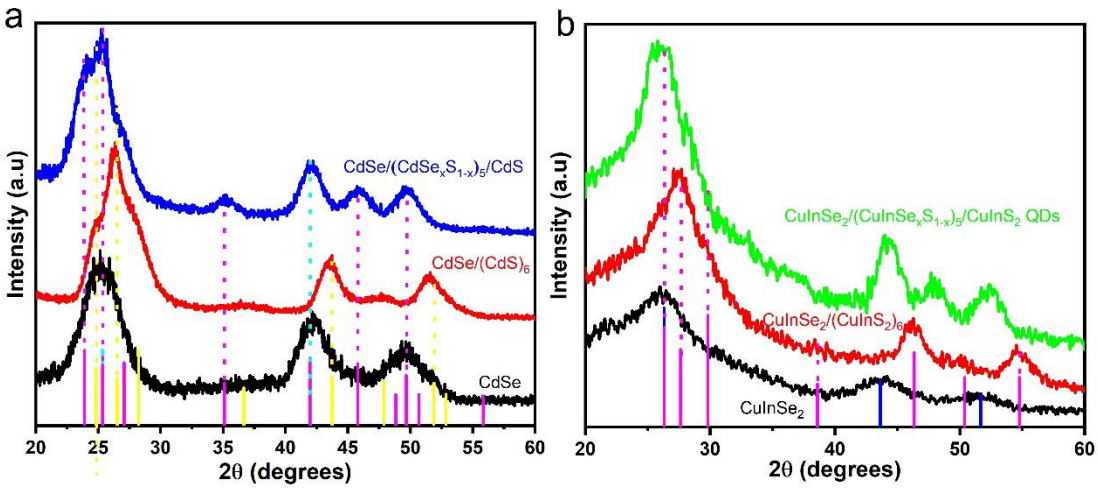

Figure 4.3 (a) XRD patterns of CdSe QDs before SILAR and after SILAR treatment with six layer CdS shell or five alloyed shell with $CdSe_xS_{1-x}$ interfacial layer and another CdS layer. TheJoint Committee on Powder Diffraction Standards (JCPDS) card files for CdSe (00190191, cyan for ZB and 08-459, pink dashed for WZ) and CdS (01-077-2306, yellow for WZ) are shown for identification; (b) XRD patterns of QDs after sequential cation exchange: $CuInSe_2$ QDs (black curve), $CuInSe_2/(CuInS_2)_6$ QDs (red curve), $CuInSe_2/(CuInSe_xS_{1-x})_5/CuInS_2$ QDs (green curve); The Joint Committee on Powder Diffraction Standards (JCPDS) card files for cubic ZB phase of $CuInSe_2$ (blue curve, JCPDS card no. 01-074-9867) and hexagonal WZ phase of $CuInS_2$ (pink curve, JCPDS card no. 01-077-9459).

After sequential cation exchange, the TEM images of as-synthesized $CuInSe_2$ (Figure 4.1e), $CuInSe_2/(CuInS_2)_6$ (Figure 4.1f) and $CuInSe_2/(CuInSe_xS_{1-x})_5/CuInS_2$ QDs (Figure 4.1g) show no obvious change of shapes compared to the samples before cation exchange, suggesting that the QDs morphology are preserved even after the cation exchange procedure [217]. Therefore, the morphology of QDs after sequential cation exchange depends on the initial QD templates. The size distribution of QDs after cation exchange is reported in Figure 4.2 d-f. While $CuInSe_2$ QDs show no obvious change in size, $CuInSe_2/(CuInS_2)_6$ and $CuInSe_2/(CuInSe_xS_{1-x})_5/CuInS_2$ QDs present a small shrinkage. In this case, the thickness of $(CuInSe_xS_{1-x})_5$ and $CuInS_2$ shells is around 1.675 nm and 0.335 nm, respectively. The HRTEM images (inset images in Figure 4.1f and 4.1g) reveal a lattice space ~ 0.321 nm, which is indexed to the (002) plane of hexagonal phase $CuInS_2$ (JCPDS No. 01-077-9459). To support this data, the lattice space was also measured by selected area electron diffraction (SAED) pattern of QDs after cation exchange. As shown in Figure 4.4 a, the SAED of $CuInSe_2$ can be well indexed into the (111), (220) and (311) planes of cubic ZB phase of $CuInSe_2$, data consistent with XRD patterns reported in Figure 4.3b (black curve, JCPDS No. 01-074-9867). Similarly, the SAED of $CuInSe_2/(CuInS_2)_6$ (Figure 4.4 b)

can be also indexed into the (002), (110), and (112) planes of hexagonal WZ phase of $CuInS_2$, consistent with diffraction peaks in the XRD pattern in Figure 4.3 b (red curve, JCPDS No. 01-077-9459). The diffraction patterns of $CuInSe_2/(CuInS_2)_6$ core-shell QDs (red curve) are dominated by the hexagonal crystal structure of $CuInS_2$ that hide the signal of the cubic crystal structure of $CuInSe_2$, due to large volume of the $CuInS_2$ shell compared to the $CuInSe_2$ core. Similarly, the lattice spacing in SAED patterns of $CuInSe_2/(CuInSe_xS_{1-x})_5/CuInS_2$ (Figure 4.4 c) can be indexed into the (111), (220) and (311) planes of ZB phase of $CuInSe_2$ as well as the (002), (110), and (112) planes of WZ phase of $CuInS_2$. In this case, an obvious overlap for the planes of $CuInSe_2$ and $CuInS_2$ is present. The corresponding XRD diffraction patterns (green curve in Figure 4.3 b) also exhibit a mix between the $CuInSe_2$ and $CuInS_2$, confirming the formation of the alloyed $CuInSe_xS_{1-x}$.

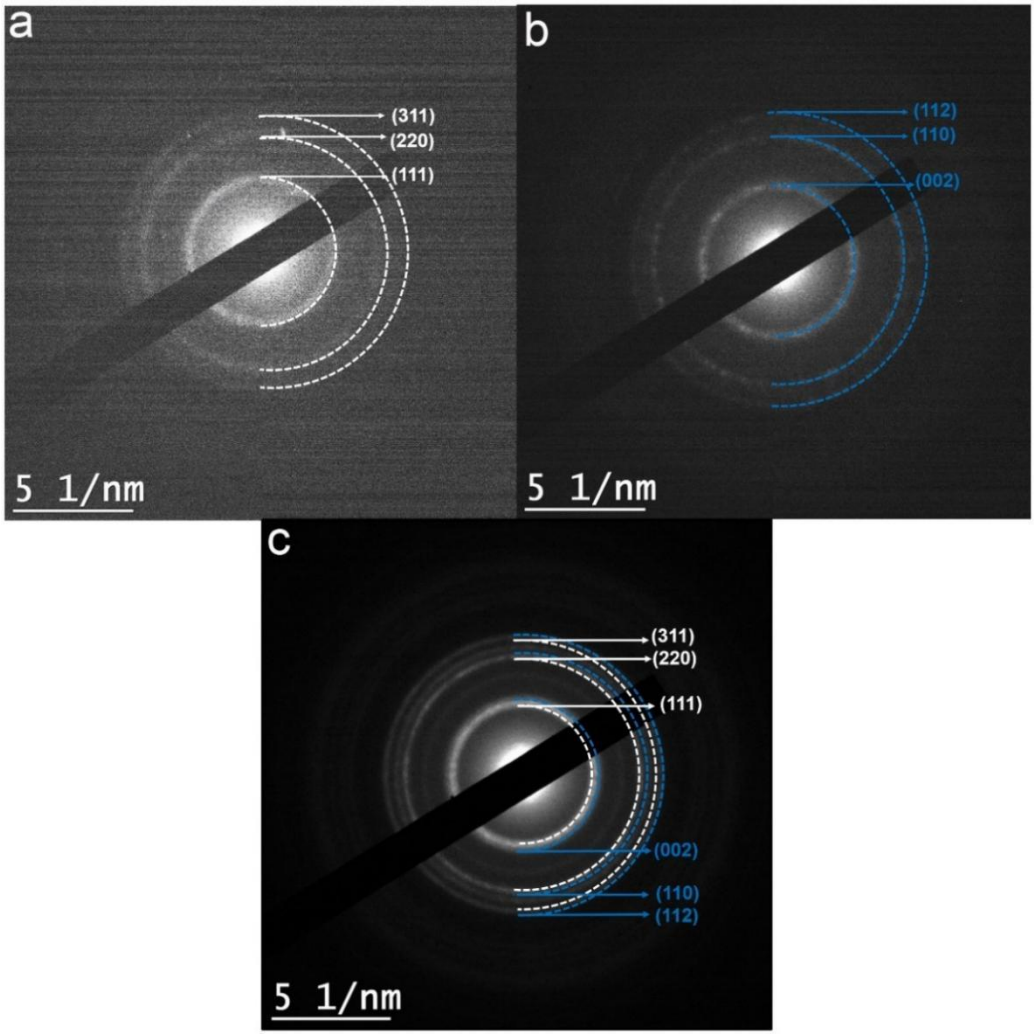

Figure 4.4. SAED patterns of (a) $CuInSe_2$, (b) $CuInSe_2/(CuInS_2)_6$ QDs and (c) $CuInSe_2/(CuInSe_xS_{1-x})_5/CuInS_2$ QDs, which are consistent with the XRD patterns in Fig. 4.3b.

To verify the exchange process, energy-dispersive X-ray spectroscopy (EDS) spectrum of QDs after cation exchange was performed. As shown in Figure 4.5 a, Cu and Se element was detected in $CuInSe_2$ QDs but absent the Cd element, which confirms the successful cation exchange. Then, Cu, In, Se and S elements was detected in Figure 4.5 b, the stronger S peak ascribes to the thick shell of $CuInS_2$, while the Se was weak because the smaller core size. After that, the Cu, In, Se and S elements were detected in $CuInSe_2/(CuInSe_xS_{1-x})_5/CuInS_2$ QDs (Figure 4.5 c), which confirm the succeed cation exchange. Compared to the core-shell QDs, the Se peak is relative much strong because of the presence of five interfacial layer $CuInSe_xS_{1-x}$. Especially, the relatively strong Cu element peak was ascribing the Cu substrate for TEM measurement. Furthermore, inductively coupled plasma-optical emission spectrometry (ICP-OES) was carried out to investigate the residual Cd^{2+} after Cu^+ cation exchange. As shown in Table 4.5, the molar ratio of residual Cd^{2+} to Cu^+ is ~ 0.9 %. Therefore, we can safely assume that full cation exchange took place.

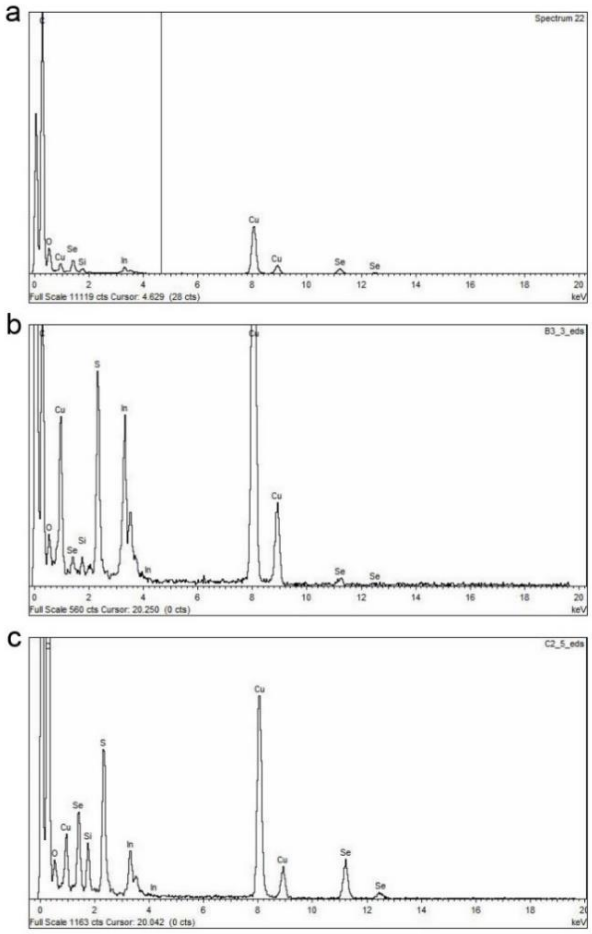

Figure 4.5 EDS spectra of (a) $CuInSe_2$ QDs, (b) $CuInSe_2/(CuInS_2)_6$ QDs and (c) $CuInSe_2/(CuInSe_xS_{1-x})_5/CuInS_2$ QDs.

Table 4.5 The ICP-OES analysis results of $Cu_2Se/(Cu_2Se_xS_{1-x})_5/Cu_2S$ QDs, showing the concentration of residual Cd and Cu as well as the molar ratio.

Element (Wavelength)	Correlation coefficient	Concentration (ppm)	Molar ratio (Cd: Cu)
Cd (214.439)	0.99982	0.09	0.009:1
Cu (324.754)	0.99998	5.56	

Subsequently, the as-synthesized $Cu_2Se/(Cu_2Se_xS_{1-x})_5/Cu_2S$ was further used for In^{3+} exchange. As shown in Table 4.6, the molar ratio of Cu:In:Se:S is around 1:0.95:0.57:1.3. After the sequential cation exchange, the Cd^{2+} was fully exchanged by Cu^+ and In^{3+}, consistent with the EDS results (Fig. 4.5 c).

Table 4.6 The ICP-OES analysis results of $CuInSe_2/(CuInSe_xS_{1-x})_5/CuInS_2$ QDs, showing the concentration of Cu, In, and Se as well as the molar ratio.

Element (Wavelength)	Correlation coefficient	Concentration (ppm)	Molar ratio (Cu: In:Se:S)
Cu (324.754)	0.99998	0.35	1:0.95:0.57:1.3
In (303.936 nm)	0.99997	0.60	
Se (203.985 nm)	0.99945	0.25	
S (181.972nm)	0.99966	0.23	

The chemical state and composition of the as-synthesized $CuInSe_2/(CuInSe_xS_{1-x})_5/CuInS_2$ was confirmed by X-ray photoelectron spectroscopy (XPS). The XPS survey spectrum of $CuInSe_2/(CuInSe_xS_{1-x})_5/CuInS_2$ (Figure 4.6 a), indicates the presence of Cu, In, Se and S elements. No signal for Cd element was detected. As shown in Figure 4.6b, the binding energy of Cu 2p splits into Cu $2p_{3/2}$ (933.2 eV) and Cu $2p_{1/2}$ (953.1 eV) with a peak separation of 19.9 eV, which is consistent with the presence of Cu^+.[218] The peaks at 444.9 eV and 452.4 eV (Figure 4.6c),

separated by 7.5 eV, can be ascribed to In $3d_{5/2}$ and In $3d_{3/2}$, respectively, confirming the presence of In^{3+}.[219] As shown in Figure 4.6d, the peak of Se 3d at 54.8 eV can be assigned to Se^{2-}.[218] The binding energy of S 2p (Figure 4.6e) splits into S $2p_{3/2}$ (161.5 eV) and S $2p_{1/2}$ (162.7 eV) with a peak splitting of 1.1 eV, due to the spin-orbit coupling, which can be assigned to S^{2-}.[219] No significant impurities were detected in the sample.

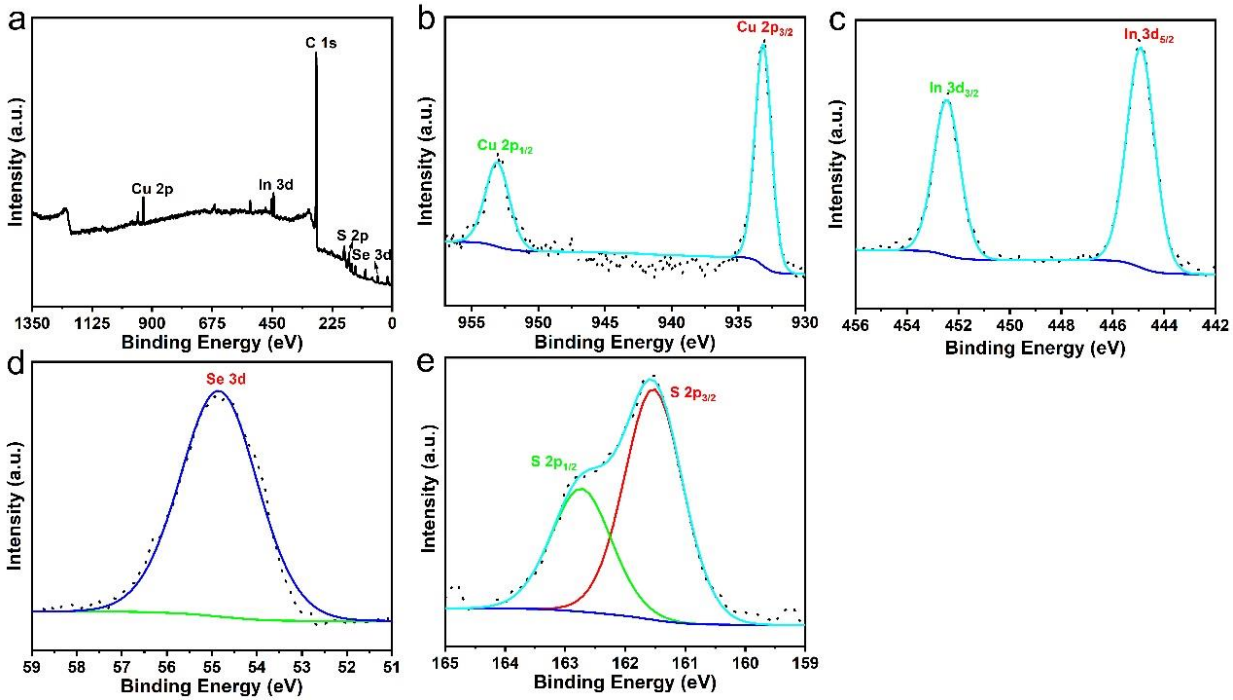

Figure 4.6 High-resolution XPS spectra of a $CuInSe_2/(CuInSe_xS_{1-x})_5/CuInS_2$: (a) Survey, (b) Cu, (c) In, (d) Se, and (e) S.

4.2.2 Optical Properties of QDs

The optical properties of the CdSe-based templates and the heavy-metal free QDs in toluene are reported in Figure 4.7. The corresponding values are also reported in Table 4.4. Before sequential cation exchange, the absorption spectra of the initial QDs spans from UV to VIS region. As shown in Figure 4.7a, the first-excitonic peak for pure CdSe QDs and $CdSe/(CdS)_6$ QDs are centered at ~552 nm (black curve) and 594 nm (red curve), respectively. By adding the interfacial alloy layers, the first-excitonic absorption peak of $CdSe/(CdSe_xS_{1-x})_5/CdS$ QDs red-shifts to longer wavelengths, and it is centered at 626 nm (blue curve). The bathochromic shift is due to the relatively narrow band gap of CdSe compared to CdS, and the influence from quantum size effect with size increase [220]. Simultaneously, a similar red shift was observed for the PL peak, due to increased leakage of electrons from the core to the shell region [221]. In fact, in general, in a core-

shell system, electron leakage from the core to the shell region causes a red shift in the PL peak, which has been confirmed in many core-shell structured QDs [96, 222]. As aforementioned, the Cd-based QDs were used as templates for the sequential cation exchange approach to prepare the NIR, green multi-shell QDs. After this procedure (Figure 4.7b), the absorption spectra of $CuInSe_2$ QDs (green curve), $CuInSe_2/(CuInS_2)_6$ (cyan curve), and $CuInSe_2/(CuInSe_xS_{1-x})_5/CuInS_2$ (magenta curve) have shifted to the NIR region up to 1000 nm, respectively, with the disappearance of first-excitonic peaks, indicating the fully cation exchange. The poorly resolved excitonic peak is a typical feature for ternary alloyed QDs [223, 224]. In addition, the PL peak of $CuInSe_2$ QDs, $CuInSe_2/(CuInS_2)_6$, and $CuInSe_2/(CuInSe_xS_{1-x})_5/CuInS_2$ also exhibit significant red shift to ~930 nm, 1040 nm, and 1140 nm (Figure 4.7b), respectively. In particular, both the absorption and PL of graded QDs exhibit a considerable red shift after the cation exchange.

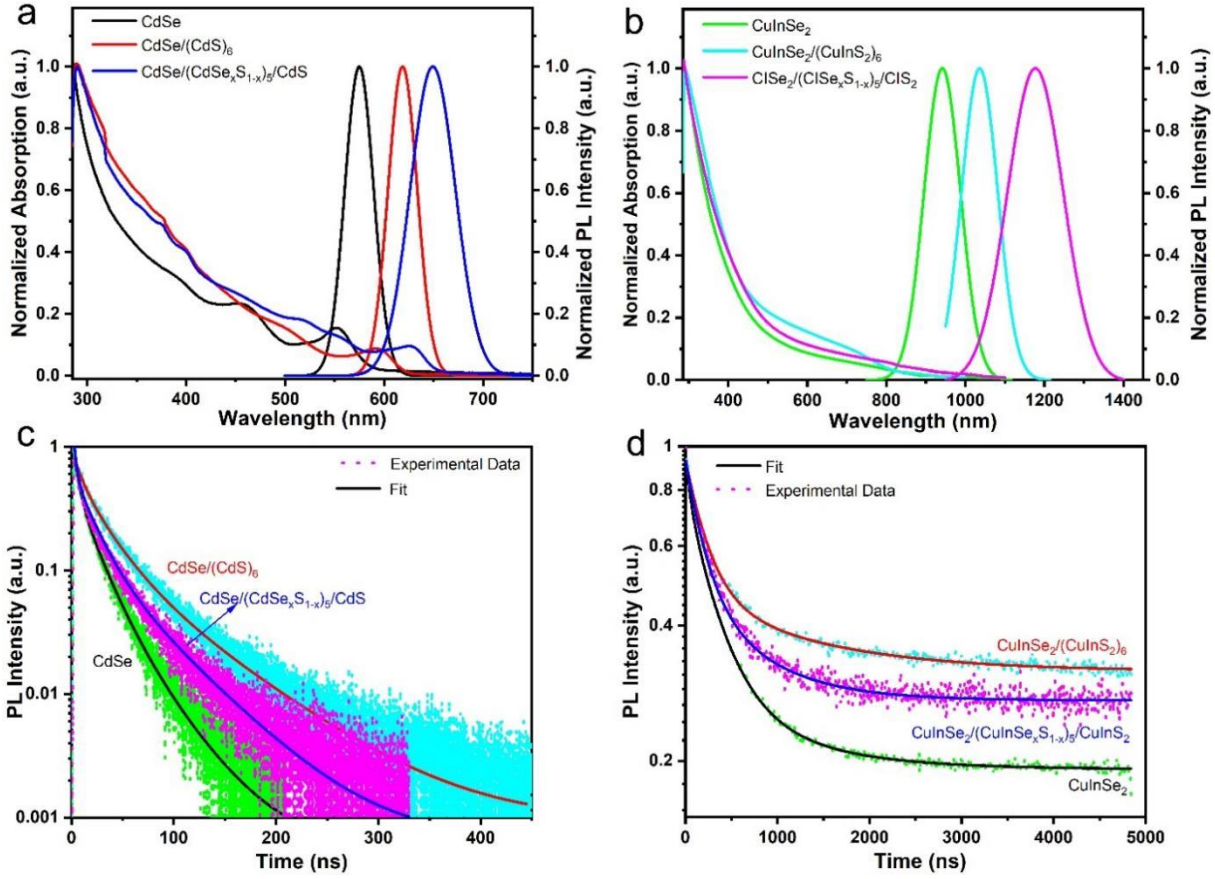

Figure 4.7 (a) Absorption and PL spectra of CdSe (black curve), $CdSe/(CdS)_6$ (red curve), and $CdSe/(CdSe_xS_{1-x})_5/CdS$ (blue curve). (b) Absorption and PL spectra of $CuInSe_2$ (green curve), $CuInSe_2/(CuInS_2)_6$ (cyan curve), and $CuInSe_2/(CuInSe_xS_{1-x})_5/CuInS_2$ (magenta curve). (c) Transient PL spectra of CdSe (black curve), $CdSe/(CdS)_6$ (red curve) and $CdSe/(CdSe_xS_{1-x})_5/CdS$ (blue curve) in toluene; (d) Transient PL spectra of $CuInSe_2CuInSe_2/(CuInS_2)_6$ and $CuInSe_2/(CuInSe_xS_{1-x})_5/CuInS_2$ QDs in toluene, respectively.

The TEM characterization of $CuInSe_2$ core QDs confirmed that, after cation exchange, the core size does not exhibit obvious changes. Thus, the red shift of $CuInSe_2/(CuInSe_xS_{1-x})_5/CuInS_2$ compared to $CuInSe_2$ QDs and $CuInSe_2/(CuInS_2)_6$ can be ascribed to an improved electron leakage from core to shell, due to the formation of an appropriate gradient in the band alignment. To further investigate the exciton dynamics of the as-synthesized QDs before and after cation exchange, transient fluorescence spectroscopy was applied to study their PL lifetime in toluene. The PL lifetime of QDs in solution was measured using a time-correlated single-photon counting mode with an excitation of 375 nm. The average lifetime "τ" can be calculated as follow [24]:

$$< \tau >= \frac{a_1{\tau_1}^2 + a_2{\tau_2}^2 + a_3{\tau_3}^2}{a_1\tau_1 + a_2\tau_2 + a_3\tau_3}$$

where α_x (x=1, 2, 3) represents the fitting coefficients of PL decay, while the τ_x (x=1, 2, 3) represent the characteristic lifetimes. The PL lifetime of QDs before cation exchange are presented in Figure 4.7c. After fitting with tri-exponential decay function, the templates of CdSe, $CdSe/(CdS)_6$ and $CdSe/(CdSe_xS_{1-x})_5/CdS$ QDs exhibit average lifetime of ~29, 54, and 43 ns, respectively. The detailed fitting parameter and results are also presented in Table 4.7.

Table 4.7 Optical parameters of QDs before cation exchange including parameters of fitted lifetime.

samples	PL peak (nm)	τ_1 (ns)	τ_2 (ns)	τ_3 (ns)	α_1 (%)	α_2 (%)	α_3 (%)	τ_{ave} (ns)
CdSe	574	17.7	39.1	5.2	54.8	29.7	15.5	28.5
$CdSe/(CdS)_6$	612	2.6	7.81	72.8	47	7.3	45.7	58.6
$CdSe/(CdSe_xS_{1-x})_5/CdS$	649	148	28.3	12	2.1	76.3	21.6	41

The PL lifetime spectra of QDs after cation exchange are presented in Figure 4.7d. After fitting with bi- and tri-exponential decay functions, the $CuInSe_2$ QDs exhibit an average lifetime ~370 ± 5 ns, while the $CuInSe_2/(CuInS_2)_6$ core-shell QDs, and $CuInSe_2/(CuInSe_xS_{1-x})_5/CuInS_2$ graded QDs exhibit longer average lifetimes ~ 1180 ± 10 and 630 ± 5 ns, respectively. The detailed fitting

parameter and results for these NIR QDs are reported in Table 4.8. Compared to the single core structure, as the thickness of the shell increases, the electronic band structure of the core-shell QDs changes, leading a quasi-type II core-shell structure formed. The special quasi-type II core-shell structure will accelerate the leakage of the electrons from the core to the shell region when the holes are still mainly confined in the core region, effectively decreasing the spatial overlap between electron and hole wave functions, inhibiting recombination and leading to a prolonged lifetime. However, when the graded shell was added between the interface of core and shell, the delocalization effect will be reduced because the graded layer simultaneously increases the leakage of electrons and holes to the surface. Therefore, the average lifetime of graded QDs will decrease relative to the core-shell QDs. In conclusion, both the redshift of the PL peak and longer lifetime confirm the formation of quasi type-II band alignment between the core and shell of $CuInSe_2/(CuInSe_xS_{1-x})_5/CuInS_2$ QDs after sequential cation exchange [225].

Table 4.8 Optical parameters of QDs after cation exchange including parameters of fitted lifetime.

samples	PL peak (nm)	τ_1 (ns)	τ_2 (ns)	τ_3 (ns)	α_1 (%)	α_2 (%)	α_3 (%)	τ_{ave} (ns)
$CuInSe_2$	940	54.3	157.3	492.1	3.4	61	35.6	370
$CuInSe_2/(CuInS_2)_6$	1040	224.4	1271.5	---	34.5	65.5	---	1180
$CuInSe_2/(CuInSe_xS_{1-x})_5/CuInS_2$	1160	192.7	690.8	---	35.6	64.4	---	620

To better understand the exciton kinetics of these as-synthesized NIR QDs, we calculated the theoretical electron/hole (e/h) wave function of $CuInSe_2$, $CuInSe_2/(CuInS_2)_6$ and $CuInSe_2/(CuInSe_xS_{1-x})_5/CuInS_2$ QDs based on their bulk band alignment using the effective mass of e/h in bulk $CuInSe_2$ and $CuInS_2$ [226, 227]. The electron [$\psi_e(r)$] and hole [$\psi_h(r)$] wave functions for these three QDs were calculated by solving the stationary Schrödinger equation in a spherical geometry with the bulk band alignment (Figure 4.8). The details of the calculations are described in the Experimental Section.

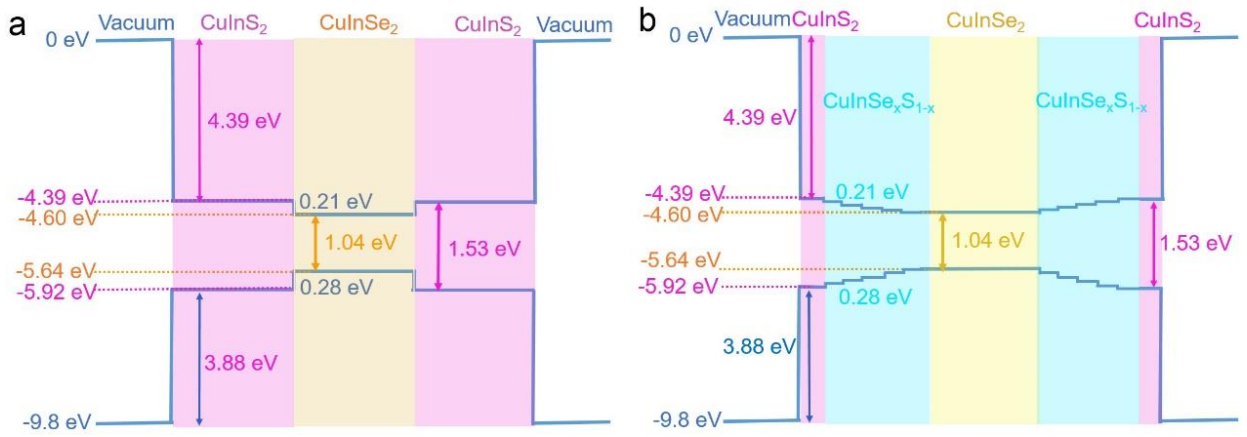

Figure 4.8 The band structure used in the simulation for (a) $CuInSe_2/(CuInS_2)_6$ and (b) $CuInSe_2/(CuInSe_xS_{1-x})_5/CuInS_2$ QDs.

The norms of the calculated $\psi_e(r)$ and $\psi_h(r)$ as a function of radius (nm) are shown in Figure 4.9. Figure 4.9a and 4.9b show the wave function of electrons and holes along a line beginning at the center of the structure, in the three different NIR QDs structures. The core-shell structure exhibits a typical quasi-type II band alignment, in which electrons can leak in the $CuInS_2$ layer while the holes are still mainly confined in the core region [228]. When a shell or an alloyed graded $CuInSe_xS_{1-x}$ interfacial layer are introduced, both $\psi_e(r)$ and $\psi_h(r)$ show an increased leakage into the shell region as a consequence of favorable band alignment. To qualitatively evaluate the lifetime of the photoexcited carriers in the QDs, we calculated the overlap integral (OI) of the photoexcited carriers in the three different QDs:

$$OI = \left| \int \psi_e(\mathbf{r}) \psi_h(\mathbf{r}) \, d\mathbf{r}^3 \right|^2$$

This magnitude provides an estimate of the probability of carrier recombination occurring in the QD. The model assumed that the recombination occurs from conduction band minimum (CBM) to valence band maximum (VBM) without any impurities in the core. The PL lifetime should be proportional to the inverse overlap integral, 1/OI. As depicted in Figure 4.9c, 1/OI increases moving from a core to a core-shell structure while the gradient structure presents an intermediate value between the other two. This trend qualitatively agrees with the measured lifetime, indicating that the shorter lifetime and the slight broadening of the PL peak of the $CuInSe_2/(CuInSe_xS_{1-x})_5/CuInS_2$ QDs compared to $CuInSe_2/(CuInS_2)_6$ QDs can be understood as arising from a larger overlap of the e/h in the shell region of the gradient alloyed structure compared to core-shell QDs. However, the larger degree of e/h leaking in alloy-shelled QDs compared to $CuInSe_2/(CuInS_2)_6$ QDs, can be helpful for e/h transfer from QDs to e/h acceptors and for further improving the efficiency of optoelectronic devices.

In summary, in the $CuInSe_2/(CuInSe_xS_{1-x})_5/CuInS_2$ QDs, the presence of the interfacial layer contributes both to the wider absorption of QDs and to increased leakage of e/h to the shell region compared to $CuInSe_2/(CuInS_2)_6$ QDs with similar shell thickness.

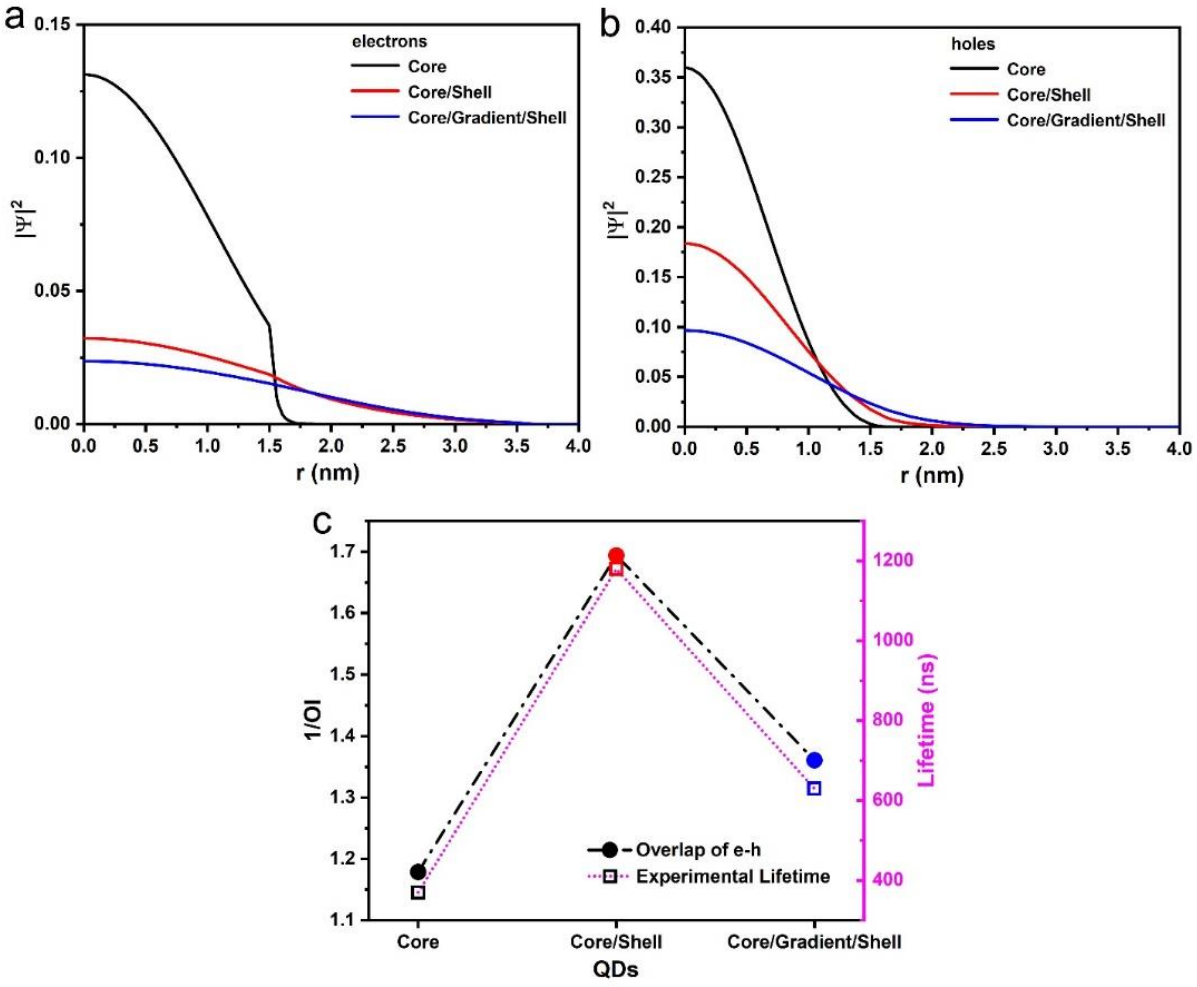

Figure 4.9 Wave function norm along a radial cut beginning at the center of the QD, for (a) 1s electrons, and (b) 1s holes. (c) Inverse of the overlap integral between the electrons and holes of $CuInSe_2$, $CuInSe_2/(CuInS_2)_6$ and $CuInSe_2/(CuInSe_xS_{1-x})_5/CuInS_2$ with R = 1.55 nm and H_{shell} = 2.1 nm, compared with the experimental lifetimes.

4.2.3 PEC performance

To test the PEC performances, the as-synthesized gradient multi-shell green QDs (and the template QDs for comparison) were applied as photo-sensitizers to fabricate PEC photoanode. The detailed fabrication procedure is shown in the Experimental Section. Typically, the QDs are deposited into mesoporous TiO_2 film via EPD approach. Subsequently, two ZnS layers are coated on the surface of TiO_2/QDs photoanode by SILAR approach to reduce photo-corrosion. TEM imaging and corresponding EDS spectra of the QDs sensitized TiO_2 are shown in Figure 4.10 and

Figure 4.11. As shown in Figure 4.10, the CdSe/$(CdSe_xS_{1-x})_5$/CdS QDs were distributed in the TiO_2 film homogenously without noticeable aggregation. The partial enlarged view (Figure 4.10b) shows the lattice of CdSe/$(CdSe_xS_{1-x})_5$@CdS QDs. The EDS spectrum (Figure 4.10c) confirms the presence of CdSe/$(CdSe_xS_{1-x})_5$@CdS QDs on the TiO_2 film.

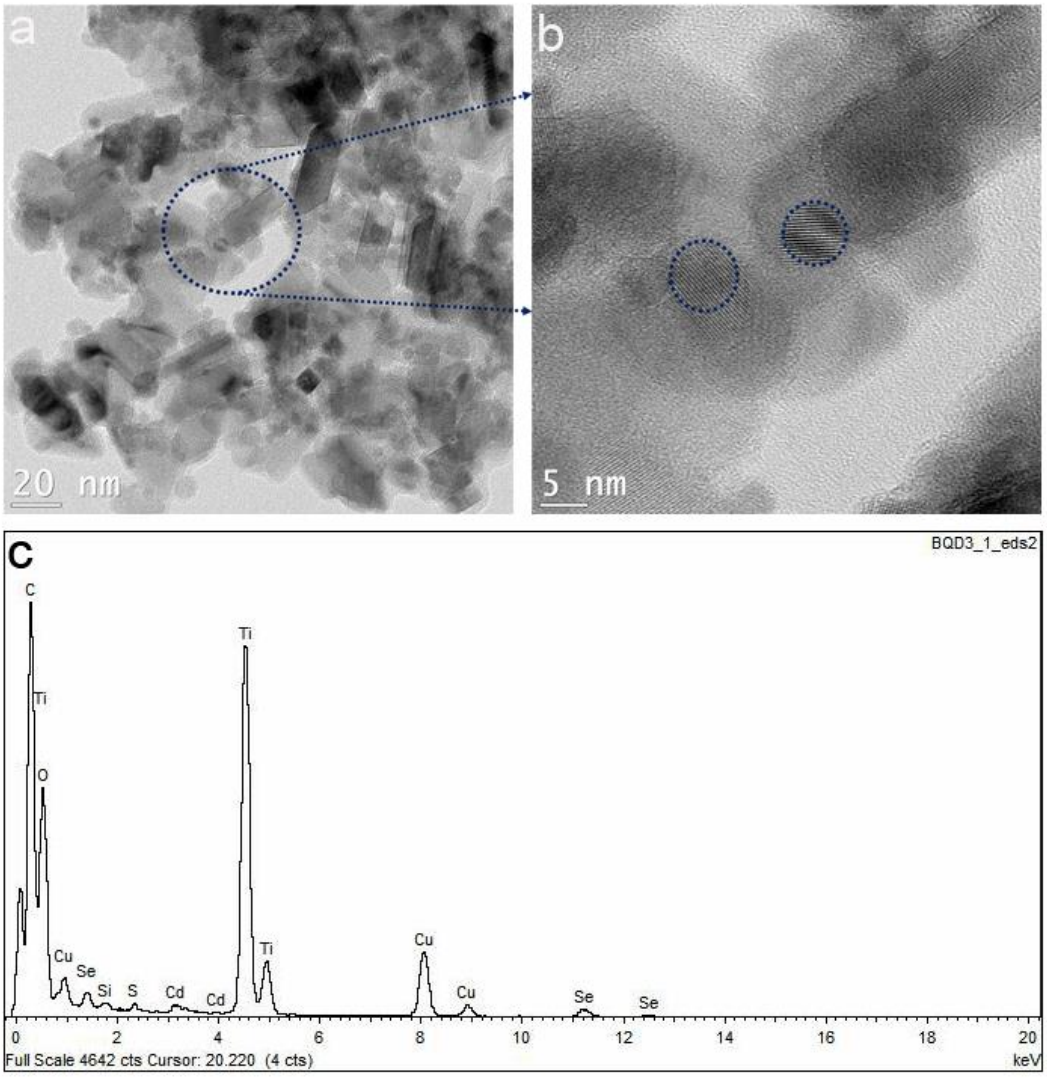

Figure 4.10. (a) Typical TEM image of CdSe/$(CdSe_xS_{1-x})_5$/CdS QDs dispersed on TiO_2 films after EPD process (dotted circles highlight the presence of QDs). (b) The partial enlarged view corresponded to the dotted circles in Fig. a. (c) EDS spectrum of TiO_2/ CdSe/$(CdSe_xS_{1-x})_5$/CdS QDs, confirming the presence of the elements including Ti, O, Cd, Se and S.

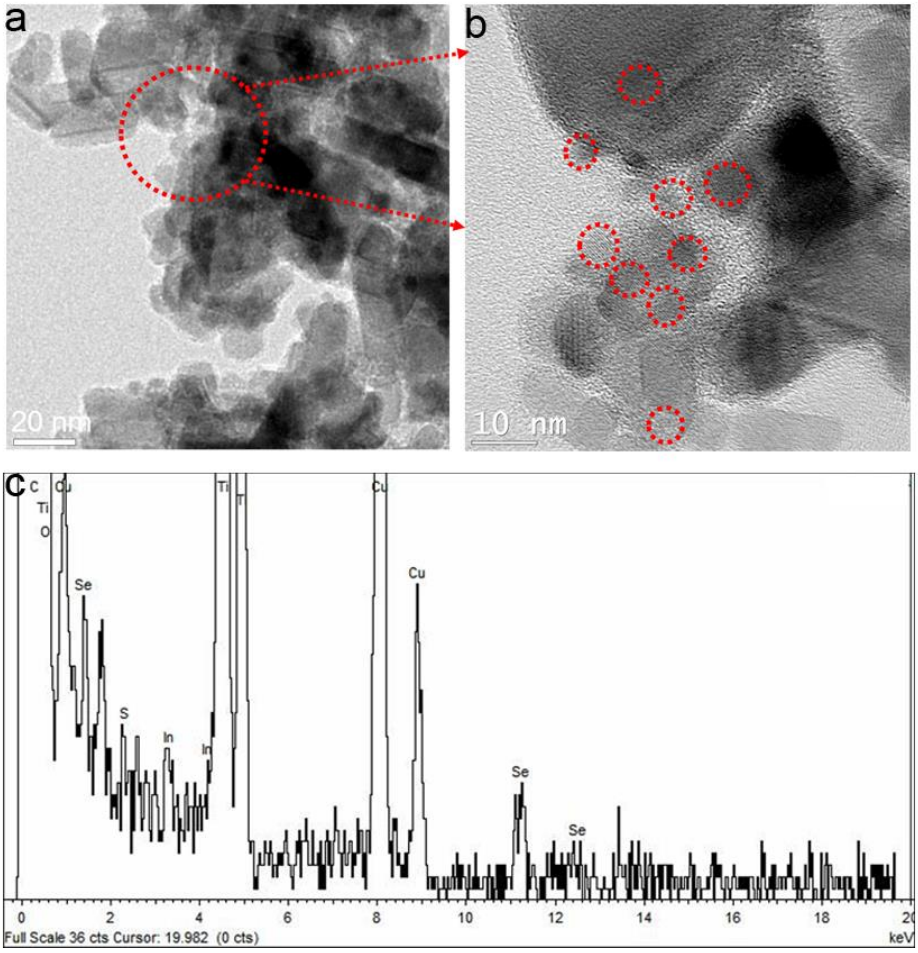

Figure 4.11 (a) Typical TEM image of $CuInSe_2/(CuInSe_xS_{1-x})_5/CuInS_2$ QDs dispersed on TiO_2 films after EPD process (dotted circles highlight the presence of QDs). (b) The partial enlarged view corresponded to the dotted circles in Fig. a: The $CuInSe_2/(CuInSe_xS_{1-x})_5/CuInS_2$ QDs are highlighted in the red circle. (c) EDS spectrum of TiO_2/ $CuInSe_2/(CuInSe_xS_{1-x})_5/CuInS_2$ QDs, confirming the presence of the elements including Ti, O, Cu, In, Se and S.

Similarly, as shown in Figure 4.11a, the $CuInSe_2/(CuInSe_xS_{1-x})_5/CuInS_2$ QDs were also distributed in the TiO_2 film homogenously without noticeable aggregation, suggesting to the efficient electron transfer from QDs to TiO_2. The EDS spectrum (Figure 4.11c) shows the elemental composition of the film confirming the presence of QDs on the TiO_2 film.

The cross-section SEM imaging and corresponding EDS analysis of the graded $CuInSe_2/(CuInSe_xS_{1-x})_5/CuInS_2$ QDs sensitized photo-electrode are shown in Figure 4.12. As shown in Figure 4.12 a, the thickness of the mesoporous TiO_2/QDs/ZnS film is ~16.5 µm. The EDS mapping spectra (Figure 4.12 b) verified the presence of Ti, O, Cu, In, Se, Zn, S, and Si,

respectively, consistent with the chemical composition in the QDs sensitized photoanode. The EDS characterization (Figure 4.12 c) also verified the presence of these elements. The element of In has overlapped EDS signal with Sn, leading to the richer EDS signal of In at the surface. The content of Zn is much higher due to two ZnS layers deposited on the surface of photoanode to prevent the QDs from photocorrosion. In addition, the semi-quantified QD loading amounts in the TiO_2 film are presented in the EDS line scan (Figure 4.12 d), which corresponds to the green line in Figure 4.12 a. All the EDS analysis results confirm the homogeneous distribution of QDs on the mesoporous TiO_2 film, suggesting the successful deposition by EPD process.

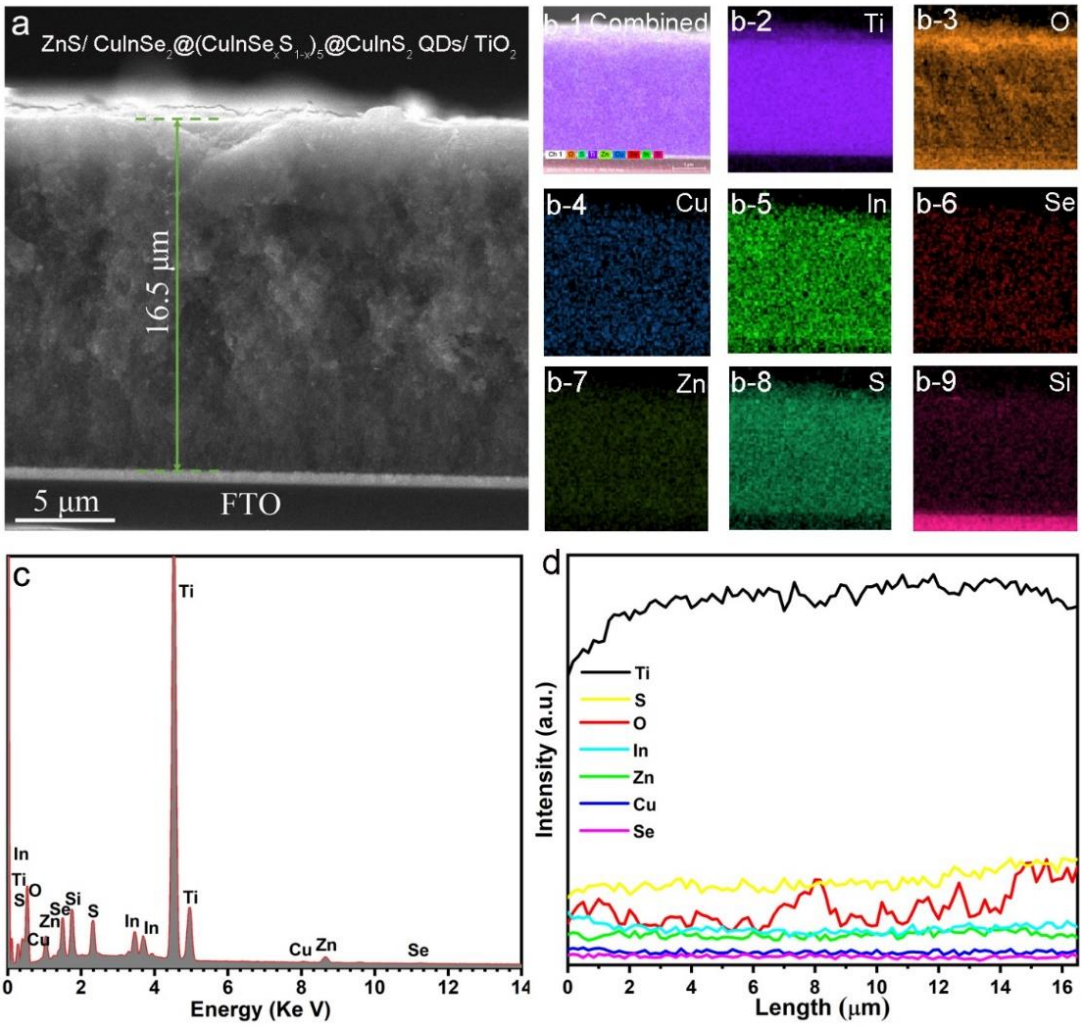

Figure 4.12 (a) Cross-sectional SEM image and of graded $CuInSe_2/(CuInSe_xS_{1-x})_5/CuInS_2$ QDs sensitized photo-anode. (b) EDS mapping and relevant chemical composition, including Ti, O, Cu, In, Se, Zn, S, and Si. (c) EDS spectra of photo-anode after ZnS treatment. (d) EDS line scan illustrating the semi-quantified variation of elements along the green line (highlighted in the SEM image).

PEC analysis was carried out using a traditional three-electrode configuration, with an Ag/AgCl with saturated KCl as the reference electrode, a platinum foil as the auxiliary electrode, and the fabricated TiO_2/QDs/ZnS thick film as the working electrode. The electrolyte contains 0.25 M Na_2S and 0.35 M Na_2SO_3 (pH=12.5), which serve also as sacrificial hole scavengers to prevent the photo-corrosion of QDs. Figure 4.13 shown approximate simplified band alignment and schematic diagram of $CuInSe_2/(CuInSe_xS_{1-x})_5/CuInS_2$ QDs sensitized photo-anode. The energy levels for TiO_2, $CuInSe_2$ and $CuInS_2$ are summarized in Table 4.9.

Table 4.9 The band position of bulk TiO_2, $CuInSe_2$ and $CuInS_2$.

bulk	E_{CB} (eV)	E_{VB} (eV)	E_g (eV)	Ref.
TiO_2	-4.47	-7.67	3.2	[229]
$CuInSe_2$	-4.6	-5.64	1.04	[215]
$CuInS_2$	-4.39	-5.92	1.53	[215]

In general, when QDs are coupled with another metal oxide with favourable energy band alignment, charge separation improves, leading to high photocurrent [195, 230]. Upon irradiation, the photo-generated electrons will leak from the core to the shell region followed by injection into the conduction band of TiO_2 due to the favorable band alignment. Subsequently, the electrons are collected at the FTO interface and transported by the external circuit to the Pt counter electrode for water reduction, to produce H_2 [231]. Even if for the bulk parameter, the conduction band of $CuInS_2$ is higher than $CuInSe_2$ [215], as also confirmed by the theoretical calculations, both core-shell $CuInSe_2/(CuInS_2)_6$ and graded $CuInSe_2/(CuInSe_xS_{1-x})_5/CuInS_2$ QDs belong to quasi type II structures. Therefore, the electrons can effectively transfer from the core to the shell region. Compare to the core/shell structure, the graded layer can serve as a “ladder” for electrons to overcome the original high energy barrier, improving the likelihood of electron transfer from core to shell region. Meanwhile, the dissociated hole can be extracted by Na_2S/Na_2SO_3 electrolyte (pH ~ 12.5), which serves as a hole scavenger. Also in this case, the presence of a gradient structure can increase the hole transfer to the electrolyte. As the driving force of hole extraction in the presence of Na_2SO_3 is high, the augmented leakage of the holes in the shell structure does not increase recombination with electrons. As confirmed in previous works, the ZnS thin layer acts as a passivation layer for the

surface of the QDs, improving their photostability and as an electron blocking barrier to reduce the recombination between the metal oxide and the electrolyte [195, 232, 233].

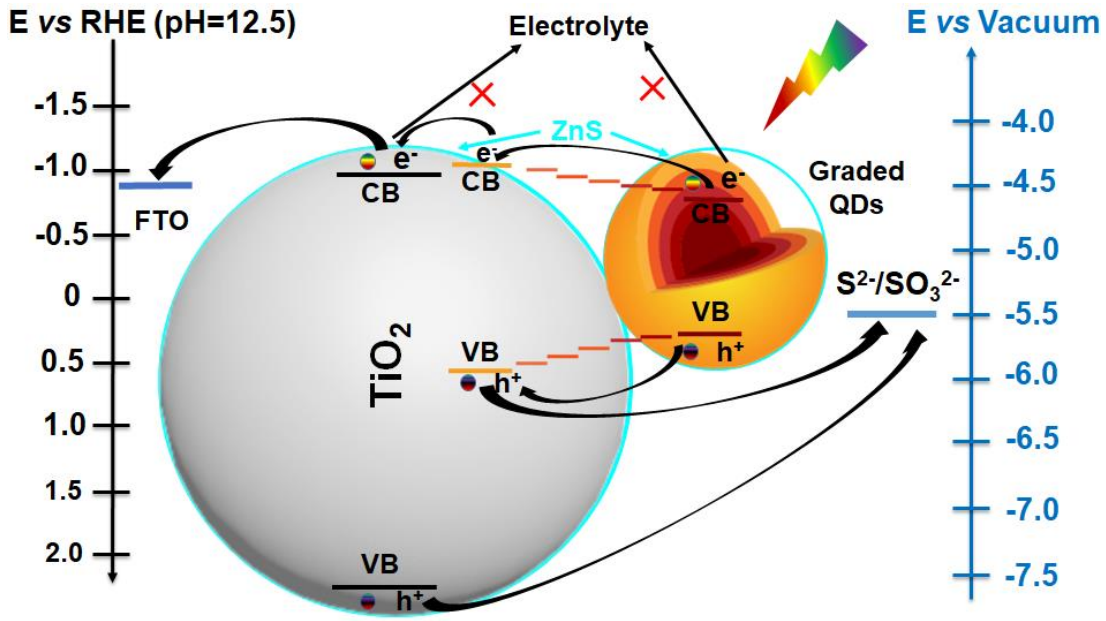

Figure 4.13 The approximate band alignment and schematic diagram of graded $CuInSe_2/(CuInSe_xS_{1-x})_5/CuInS_2$ QDs sensitized TiO_2 photo-anodes. The arrows indicate the electron and hole transfer process.

The possible mechanism for the PEC reaction at the electrode-electrolyte interface could be summarized as follow [234, 235]:

$$TiO_2/QDs + hu \rightarrow e^- (CB) + h^+ (VB) \quad (i)$$

$$2H_2O + 2e^- (CB) \rightarrow H_2 + 2OH^- \quad (ii)$$

$$SO_3^{2-} + 2OH^- + 2h^+ (VB) \rightarrow SO_4^{2-} + H_2O \quad (iii)$$

$$2S^{2-} + 2h^+ (VB) \rightarrow S_2^{2-} \quad (iv)$$

$$S_2^{2-} + SO_3^{2-} \rightarrow S_2O_3^{2-} + S^{2-} \quad (v)$$

$$SO_3^{2-} + S^{2-} + 2h^+ (VB) \rightarrow S_2O_3^{2-} \quad (vi)$$

The three different NIR QDs-based photo-anode (core, core-shell, and core/graded shell-shell) performances are evaluated and compared in Figure 4.14a. To fairly compare the properties of as-synthesized NIR QDs, all of the fabricated PEC devices were measured under identical preparation and measurement condition. The photocurrent densities were measured under dark conditions, chopped light and continuous light illumination conditions (AM 1.5G, 100 mW cm^{-2}).

The results are reported in Figure 4.14 a. For the pure core $CuInSe_2$ QDs sensitized photo-anode (Figure 4.14a), the photocurrent density is almost zero in dark conditions (dashed curve), while a saturated photocurrent of 1.5 mA cm^{-2} is measured at 0.9 V versus the reversible hydrogen electrode (RHE). The saturated photocurrent density of $CuInSe_2/(CuInS_2)_6$ and $CuInSe_2/(CuInSe_xS_{1-x})_5/CuInS_2$ sensitized photo-anode can reach ~2.6 mA cm^{-2} (0.9V vs RHE, green solid curve) and 4.5 mA cm^{-2} (0.9V vs RHE, blue solid curve), respectively. In particular, the gradient core-shell structure shows an increment of +200% compared to the single core structure and +73% compared to the core-shell architecture. In addition, the pure TiO_2/ZnS photo-anode without any QDs sensitized only displays a saturated photocurrent density ~0.32 mA cm^{-2} (Figure 4.15). This relatively low background current suggests that the increased photocurrent density of the QDs sensitized mesoporous TiO_2/ZnS photoanode should be mainly ascribed to the contribution from the QDs.

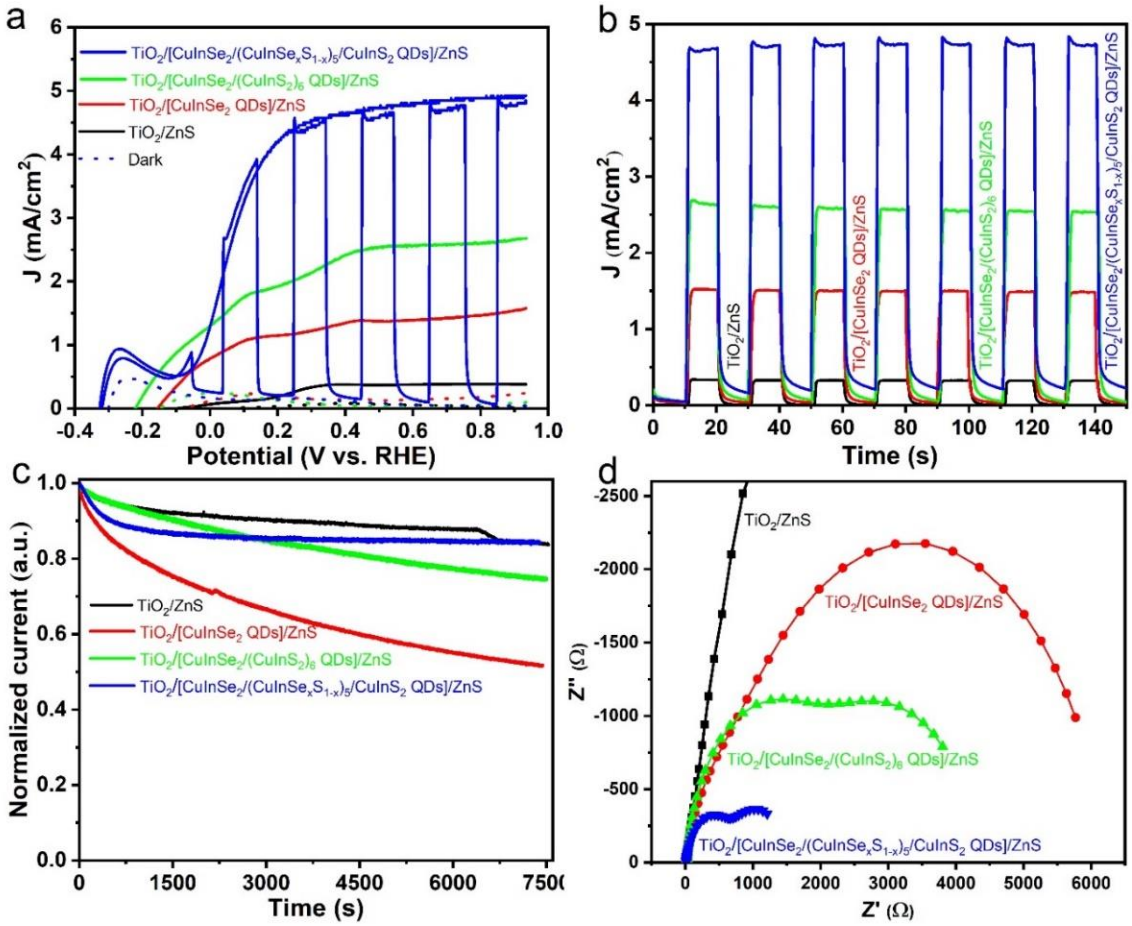

Figure 4.14 (a) J-V curves of TiO_2/ZnS and TiO_2 sensitized with $CuInSe_2$ QDs, $CuInSe_2/(CuInS_2)_6$ QDs, and $CuInSe_2/(CuInSe_xS_{1-x})_5/CuInS_2$ QDs, respectively, under the dark (dashed curve), chopped and continuous (solid curve) illumination (AM 1.5 G, 100 mW cm^{-2}). (b) Photocurrent density versus time for the as-synthesized

photoanodes (c) Photostability and (d) Nyquist plots of representative photoanodes under illumination (100 mW/cm^2) at 0V vs Ag/AgCl.

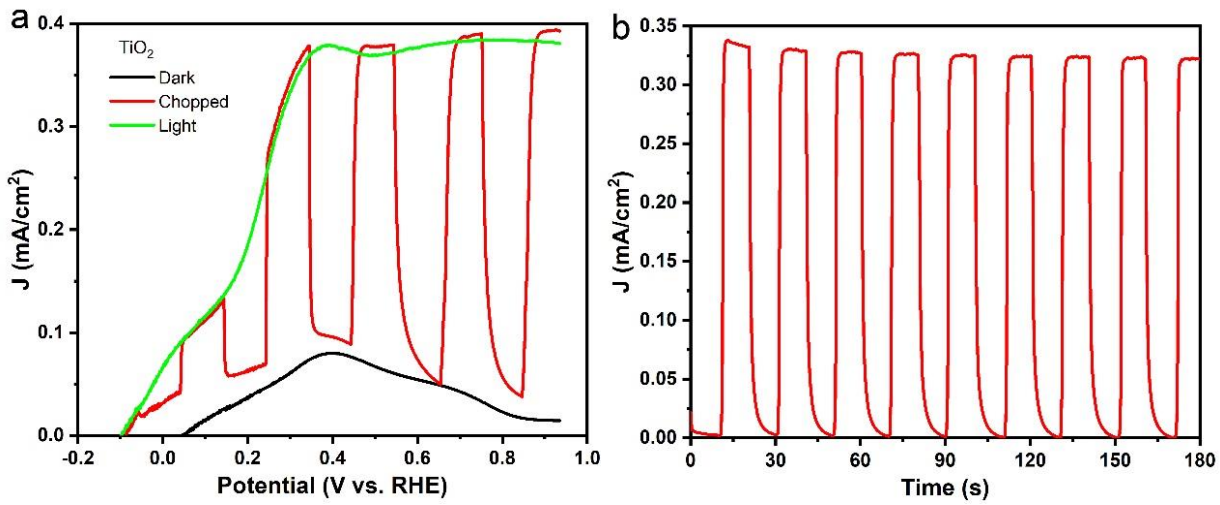

Figure 4.15. (a) J-V dependence of bare mesoporous-TiO_2/ZnS modified photoanode in dark, chopped, and continuous light under 1 sun illumination (AM 1.5G, 100 mW/cm^{-2}). (b) The photocurrent density versus times for bare mesoporous-TiO_2/ZnS modified photoanode displayed about ~0.32 mA/cm^2.

To demonstrate the superior performance of the gradient core-shell, a chronoamperometry test of the fabricated PEC devices was measured at 0.9 V versus the RHE. As shown in Figure 4.14 b, the $CuInSe_2/(CuInSe_xS_{1-x})_5/CuInS_2$ QDs with gradient layer exhibit a saturated photocurrent which is 1.7 times higher than the PEC devices based on $CuInSe_2/(CuInS_2)_6$. The higher photocurrent density can be ascribed to several synergistic effects: (i) the appropriate band bending accelerates the electron transfer from the QDs to TiO_2, suppressing electron-hole recombination. (ii) with the formation of a graded layer, the electron transfer is relatively high compared to core-shell QDs based on the dynamic analysis. (iii) ZnS protective layer effectively inhibits photo-corrosion of QDs.

We also measured the photocurrent density of the Cd-based QDs before sequential cation exchange under identical conditions. The photocurrent density is shown in Figure 4.16, with photocurrent density about ~4.5 mA cm^{-2}, 6 mA cm^{-2}, and 9.8 mA cm^{-2} for CdSe, $CdSe/(CdS)_6$, and $CdSe/(CdSe_xS_{1-x})_5/CdS$ QDs sensitized photo-anode, respectively. These values are higher compared to the ones obtained with heavy-metal-free QDs, however, considering the environment and sustainable development, the application of toxic heavy metals will seriously limit their practical application.

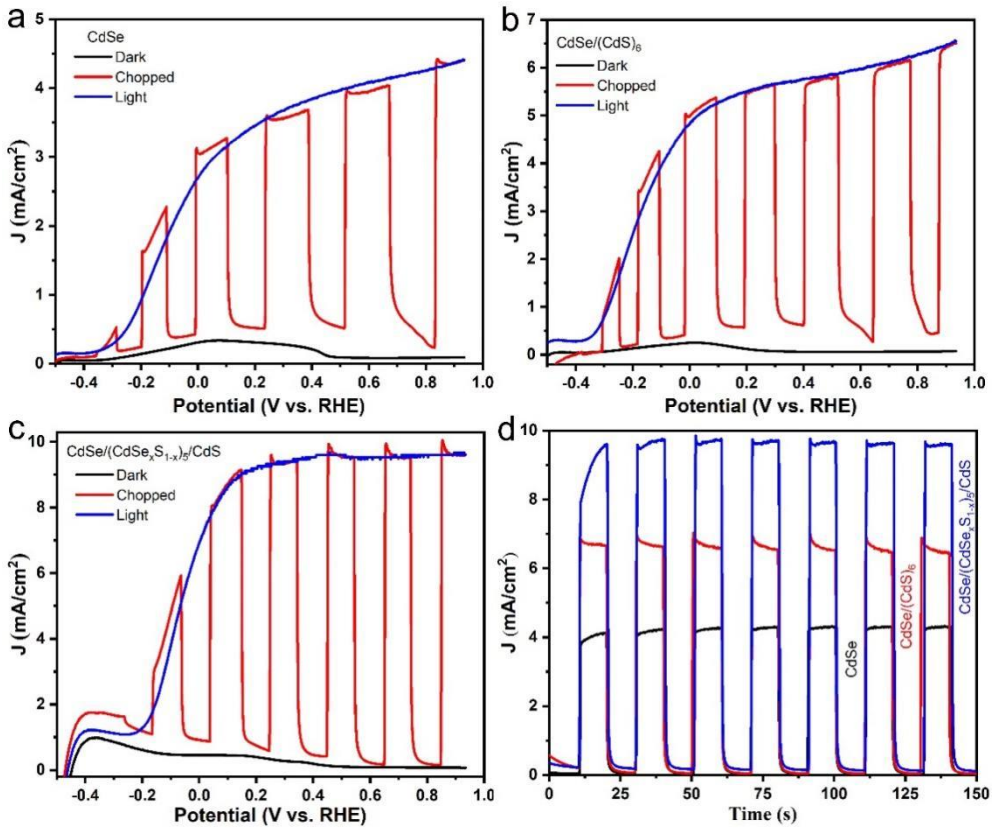

Figure 4.16 Photocurrent density-potential dependence of TiO_2 sensitized with (a) CdSe QDs; (b) $CdSe/(CdS)_6$ QDs; (c) $CdSe/(CdSe_xS_{1-x})_5/CdS$ QDs in the dark (black curve), chopped (red curve) and under continuous (blue curve) illumination (AM 1.5 G, 100 mW cm^{-2}). (d) Photocurrent density versus time for the as-synthesized photo-anode by: CdSe QDs (black curve), $CdSe/(CdS)_6$ QDs (red curve), $CdSe/(CdSe_xS_{1-x})_5/CdS$ QDs (blue curve) at 0.9 V versus the RHE.

The photo-stability of the PEC device is also an essential factor for H_2 generation. In general, the performance of QDs sensitized PEC devices is sensitive to the surface defects under illumination that act as charge traps, limiting stability [236, 237]. The surface-related traps and defects will form fast non-radiative de-excitation channels for photo-generated charge carriers, reducing the overall performance. However, the inorganic shell can reduce the surface traps to strengthen the PEC performance. The photo-stability of the PEC devices was measured under one sun illumination at 0.9 V vs. RHE. To compare the photocurrent decay, the initial photocurrent density was normalized to its maximum. As shown in Figure 4.14c, the pure TiO_2/ZnS photoanode exhibits a good photo-stability, maintaining about ~83 % of the initial value after 2 h illumination (black curve) due to the inert stability of TiO_2 to corrosion. The photocurrent density for bare $CuInSe_2$ QDs sensitized PEC devices gradually decreases with time, dropping to ~53 % of the initial value after

2 h illumination (red curve). With the presence of the $CuInS_2$ shell protection, the photocurrent density maintains more than ~74 % of the initial value (green curve), while much higher stability, about ~83% of the initial value, was observed for the $CuInSe_2/(CuInSe_xS_{1-x})_5/CuInS_2$ QDs (blue curve) after 2 h illumination. The noticeable improvement is ascribed to the shell protection and interfacial interaction. In fact, by increasing the amounts of charges leaked from the QDs, photo-oxidation can be further delayed.

To further confirm that the observed improved performances are due to a better charge transfer mechanism in the gradient core-shell structure, the charge transfers characteristics of the photoelectrodes were investigated using electrochemical impedance spectroscopy (EIS). Figure 4.14 d displays the Nyquist plots recorded at 0 V versus Ag/AgCl under 1 Sun (100 mW/cm^2) of representative samples of core, core-shell and core/gradient shell QDs deposited on similar TiO_2 photoanodes. The data have been fitted with the following model (Figure 4.17): a Randles equivalent circuit consisting of a series of resistance (R_S), space charge capacitance and resistance (C_{SC} and R_{SC}), double layer capacitance (C_{DL}), charge transfer resistance (R_{CT}) and a Warburg element (W). Analogous models have been already developed for similar heterostructured materials [238-240].

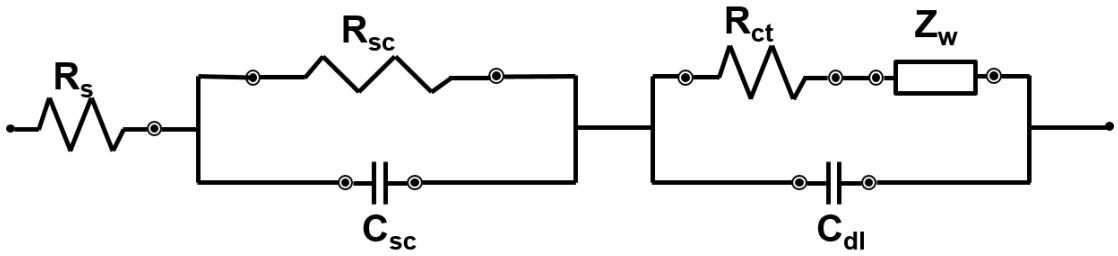

Figure 4.17 The fitting model for EIS.

In this case, the main focus of the analysis is on the diameter of the semicircle at mid-frequency (rightmost semicircle) as it correlates with the charge transfer resistance. In particular, a smaller radius of the semicircle means a lower R_{CT} indicating an improved charge transfer. As shown in Figure 4.14d, the R_{CT} follows the inverse trend of the photocurrent, with values of 8.8 kΩ, 5.7 kΩ, 2.53 kΩ and 0.87 kΩ for TiO_2/ZnS, TiO_2/[$CuInSe_2$ QDs]/ZnS, TiO_2/[$CuInSe_2/(CuInS_2)_6$ QDs]/ZnS, and TiO_2 /[$CuInSe_2/(CuInSe_xS_{1-x})_5/CuInS_2$ QDs]/ZnS, respectively. As the photoanodes are constructed in a similar way with the same materials, the improved charge transfer can be assigned to the better charge separation in the gradient structure, confirming that the recombination of electron/hole pairs is reduced in this kind of architecture.

Faraday's law was applied to calculate theoretically the hydrogen generation from the measured photocurrent based on the $CuInSe_2/(CuInSe_xS_{1-x})_5/CuInS_2$ QDs sensitized photo-anode. In this work, H_2 evolution was further estimated based on the CdSe/CdS g-QDs in our previous work,[24] which serves as a reference to calculate the H_2 evolution of PEC cells based on $CuInSe_2/(CuInSe_xS_{1-x})_5/CuInS_2$ QDs-sensitized photoanodes. This approach is quite reliable because the only difference in our QDs-based PEC system is the types of QDs, all other components including electrolyte, a Pt counter electrode and reference electrode (Ag/AgCl) are the same. In our previous work, the H_2 evolution increases approximately linearly with time, which fits well with the theoretical curve. Based on the reference curve calculated with CdSe/CdS QDs, a faradic efficiency of ~80% can be estimated. [24] We then integrated the current density (Figure 4.14 b), and on this basis, the calculated hydrogen generation rate of the PEC device based on graded $CuInSe_2/(CuInSe_xS_{1-x})_5/CuInS_2$ QDs is around 30 $mL \cdot cm^{-2} \cdot d^{-1}$ (Figure 4.18).

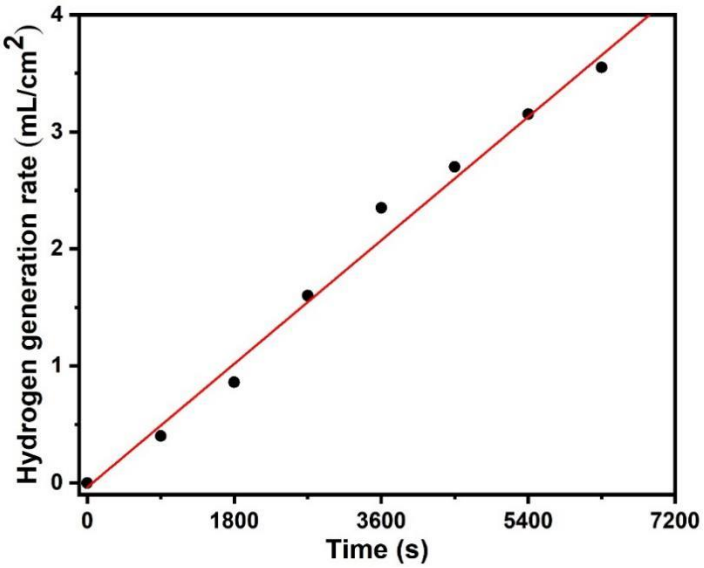

Figure 4.18 H_2 evolution based CdSe/CdS QDs as a function of time under 100 mW/cm² illumination with AM 1.5 G filter. The H_2 evolution increases approximately linearly with time. In this project, the photocurrent density is ~6.5 mA/cm² at 0.2 V vs. RHE under 100 mW/cm² illumination with AM 1.5 G filter. The preparation of CdSe/CdS sensitized TiO_2 anode followed reference [24].

Theoretical Calculation of H_2 Evolution:

The theoretical number of moles of hydrogen was calculated according to Faraday's law based on the measured photo-current:

$$\mathrm{n} = \frac{1}{\mathrm{z}}\frac{Q}{F} = \frac{1}{2}\frac{I \times t}{F} = \frac{1}{2F}\int_0^t I dt$$

In the above equation, z is the number of transferred electrons per mole of water (i.e. z=2), Q is the quantity of charge in coulomb (C) and equals to I×t, F is the Faraday constant (the quantity of charge in coulomb carried by one mole of electrons, i.e. 96484.34 C/mole), the I represent the photocurrent in amperes (A), and t is time in seconds (s).

$$n_{H_2}(\text{theoretical}) = \frac{0.0045\ (A)\times 7200\ (s)}{2\times 96485.33\ C\cdot mol^{-1}} = 1.68\times 10^{-4}\ mol$$

$$V_{H_2} = 1.68\times 10^{-4}\ mol \times 22.4\ L\cdot mol^{-1} = 3.77\ mL$$

Therefore, the H_2 generation was: 3.77 mL×12×83%×80%=30 mL

4.3 Conclusion and Perspectives

In summary, near-infrared, heavy-metal-free, gradient multi-shell colloidal $CuInSe_2/(CuInSe_xS_{1-x})_5/CuInS_2$ QDs were successfully synthesized by a sequential cation exchange approach based on $CdSe/(CdSe_xS_{1-x})_5/CdS$ template. ICP-OES characterization confirmed the full cation exchange of heavy metal composition, indicating that Cd^{2+} was fully replaced by Cu^{+} and In^{3+}. After the cation replacement, the giant QDs with gradient shell exhibit an extended absorption up to NIR region and a strong red shift of the PL. The QDs were efficiently deposited into the mesoporous TiO_2 film by EPD, showing an intimate connection between the QDs and the TiO_2 nanoparticles. To reduce surface traps of resulting QDs, two layers of inorganic ZnS surface passivation were added by SILAR approach. The proposed PEC devices based on $CuInSe_2@(CuInSe_xS_{1-x})_5@CuInS_2$ QDs showed a saturated photocurrent density as high as ~ 4.5 mA cm^{-2}, with an improvement of more than 200% compared to single core QDs and of more than 70% compared to core-shell structure. Furthermore, the PEC devices based on the gradient QDs exhibit excellent stability, retaining more than 80% of their current after 2 h of full illumination. The stability performance of the as-synthesized QDs sensitized photo-anode is comparable to that of heavy-metal QDs based PEC devices. The superior PEC performances can be ascribed to the graded interfacial layer that optimizes the charge transfer between the QDs and the metal oxide/electrolyte interfaces. This proposed green gradient multi-shell QDs with absorption and PL extended to the NIR region, expand the practical application not only for the PEC system but also could present new opportunities to develop more efficient optoelectronic devices that require NIR absorption capabilities.

5 0D/2D/2D NANOCOMPOSITE BASED ON GREEN Zn-DOPED $CuInS_2$ AND MoS_2/REDUCED GRAPHENE AS PHOTOELECTRODES FOR SOLAR H_2 GENERATION

Links between projects:

In chapter 3, to investigate the charge separation and transmission influenced by band alignment, an effective heterojunction composed of 0D PbS@CdS core-shell QDs and 2D Zn doped MoS_2 NSs was rationally constructed and demonstrated. The PbS@CdS QDs were in-situ growth on the Zn-MoS_2 surface. However, the PbS@CdS QDs present a large size distribution and also contain heavy metal elements, such as Cd and Pb, which constitute a big concern in the application of environmental purification. In Chapter 4, we synthesize a heavy-metal-free, eco-friendly gradient $CuInSe_2$/$(CuInSe_xS_{1-x})_5$/$CuInS_2$ QDs by sequential cation exchange approach. Combined with these aforementioned strategies, to accelerate the charge transfer and utilize solar energy more environmentally friendly, without introducing heavy-metal-containing materials, and more cost-effectively, a completely metal-free 0D/2D/2D heterojunction $ZnCuInS_2$/MoS_2/rGO was rationally designed and synthesized. Moreover, the band alignment was adjusted by modulating the Zn doping amounts to $CuInS_2$ QDs. Furthermore, the introduction of graphene is supposed to promote charge separation, make QDs stable and make 0D/2D/2D possess high activity and long-term stability in H_2 evolution.

In this chapter, a photoelectrode based on a 0D/2D/2D heterojunction is constructed by 0D heavy metal free Zn doped $CuInS_2$ QDs and hierarchical 2D/2D MoS_2/rGO (MG) NSs ternary nano-junctions for PEC water splitting. The interfacial structure and band alignment between the proposed 0D QDs and 2D/2D MG NSs is engineered by modulating the Zn molar ratio during the QDs synthesis. In particular, the doped QDs with tunable band position allow the formation of an optimum band alignment of the ternary-heterojunction. In addition, the 2D hierarchical MG NS structure, with a large surface area and good permeability, can increase the light utilization rate through multiple scattering of incidence light. Overall, this hybrid hierarchical architecture used as a photoanode provides a broad optical window for effective light harvesting, a short diffusion distance for excellent charge transport, as well as a large contact area for rapid interfacial charge separation and PEC reactions.[71] Therefore, the proposed heterostructure system is expected to exhibit good PEC performance.

5.1 Experiment section

5.1.1 Synthesis of Zn doped $CuInS_2$ QDs

In a typical synthesis of $ZnCuInS_2$ QDs,[121] $Zn(Ac)_2$ (0.0183 g, 0.1 mmol), $Cu(Ac)_2$ (0.0199 g, 0.1 mmol) and $In(Ac)_3$ (0.0292 g, 0.1 mmol) were mixed with DDT (0.48 mL), OA (0.6 mmol) and ODE (4 mL) in a three-necked flask. The reaction mixture was purged with N_2 for 30 min at room temperature. The temperature was then raised to 100 °C and further degassed for 30 min. Subsequently, the reaction was heated to 210 °C until a clear solution was formed, and then the sulfur solution (0.3 mmol) dissolved in OLA (0.5 mL) was swiftly injected into the reaction solution under vigorous stirring. After 15 min, the reaction was quenched using cold water. Finally, the resultant product was precipitated and washed by successive ethanol and toluene extraction to eliminate unreacted precursors, and the precipitate was re-dispersed in dichloromethane (10 mL). For the synthesis of the Zn doped $CuInS_2$ QDs with various compositions, only the $Zn(Ac)_2$ precursor used was different while keeping the other reaction conditions unchanged.

5.1.2 Aqueous Phase Transfer of Zn-$CuInS_2$ QDs

The aqueous phase transfer was achieved by replacing the initial hydrophobic ligands using MPA as ligands.[241] Briefly, the pH value of MPA in methanol solution (2.0 M, 1.0 mL) was first adjusted to around 10. The MPA solution was mixed with the as-synthesized oil-soluble Zn-$CuInS_2$ QDs dispersion under stirring. After 5 min, deionized water (10 mL) was added to the mixture, and the QDs were extracted into the water phase gradually. The water-soluble QDs were purified through precipitation with acetone and subsequent centrifugation. The purified MPA capped Zn-$CuInS_2$ QDs were finally re-dissolved in deionized water for further use.

5.1.3 Synthesis of layered amino functionalized MoS_2/rGO hybrids

Graphene oxide (GO) was prepared from natural graphite powder by an improved Hummer's method.[242] The 2D/2D layered MoS_2/rGO (MG) hybrids were synthesized by a hydrothermal approach. Briefly, $Na_2MoO_4 \cdot 2H_2O$ (1.5 mmol, 0.36 g) and thiourea (7.5 mmol, 0.57g) were dissolved in water (60 mL) under sonication, and then the prepared GO (0.018 g) dispersed in water (15 mL) were added into the above solution. After that, the homogeneous solution was further sonicated for 10 min before being transferred into a 100 mL Teflon-lined autoclave. Subsequently, the reaction was kept at 200 °C for 20 h before being cooled down to room temperature. After the reaction, the black precipitates were collected by several rinse-centrifugation cycles with water and ethanol to remove impurities. Finally, the MG NSs were dried

at 80 °C for 12 h. Similarly, the synthesis of purely MoS_2 was similar to that of MG hybrids but without the addition of GO. The amount of the rGO loaded onto MoS_2 was calculated by assuming that the $Na_2MoO_4 \cdot 2H_2O$ was converted entirely to MoS_2.

The amino-functionalized MG composites (MG-NH_2) were prepared as follows: in detail, 0.1 g MG were dispersed in 10 mL of anhydrous ethanol under ultrasonication to obtain symmetrical dispersions. Then, 3-aminopropyl triethoxysilane (0.1 mL) was added to the solution and kept reflux at 70 °C for 1.5 h in an oil bath. Subsequently, the solid product was collected by several rinse-centrifugation cycles with anhydrous ethanol to remove the impurities. Finally, the prepared MG-NH_2 was dried under vacuum at room temperature.

Preparation of the 0D/2D/2D $ZnCuInS_2$/MG nanocomposite: specifically, 0.1 g of MG-NH_2 dispersed in 100 mL water and ultrasonicated for 8 h. Then, 0.1 mmol of MPA capped Zn-$CuInS_2$ QDs were dropped into the MG solution under violent stirring, ultrasonicated for 3 h, and kept shaking for 9 h to obtain the QDs/MG nanocomposite. After centrifugation, the prepared $ZnCuInS_2$/MG was dispersed in ethanol for later use.

5.1.4 Photoanode preparation

The FTO glass substrate was cleaned with triton, then cleaned with a mixture of methanol, acetone, and isopropanol (1:1:2), rinsed with deionized water, and dried in an N_2 flow. Then, the cleaned FTO glass substrates were treated in a UV-ozone cleaner for 15 min to further eliminate surface organic contaminants. Subsequently, a commercial solution Ti-Nanoxide BL/SC was spin coated on the FTO substrate at a speed of 6000 rpm for 30 s to form a TiO_2 blocking layer. After a brief drying in air, the deposited TiO_2 films were annealed at 500 °C for 30 min and cooled to room temperature. The QDs/MG NSs were deposited onto the working electrode by a modified space-confined self-assembly approach.[179, 243] Typically, the modified FTO substrates are placed in two immiscible solvent filled frit funnels to form a liquid-liquid interface, and the bottom phase was composed of water: acetonitrile (85:15, v/v, ~15 mL), when using hexane (~10 mL) as the top phase. The 0D/2D/2D MG/QDs ethanol solution (~1.0 mg/mL) was continuously injected into the interface until a dense film was formed at the interface. After the 2D self-assembly process, the top liquid phase was removed by a pipette, and then the bottom phase was removed by low vacuum (~50 mbar) auxiliary filtration so that the thin film at the interface is deposited on the substrate. Subsequently, the thin films deposited on the FTO substrates were dried at 80 °C. In particular, several 2D self-assembly process repetition to optimize the film thickness to obtain the optimum PEC performance. Previous works have shown that a passivating ZnS capping layer on

the surface of the FTO/TiO_2/MG-QDs photoanode can inhibit the photo-corrosion and further improve the stability.[244] Thus, two passivating ZnS capping layers were deposited on the surface of FTO/MG-QDs photoanodes by successive ionic layer adsorption and reaction (SILAR) approach to reduce the photo-corrosion. In a conventional SILAR process, 0.1 M $Zn(OAc)_2$ methanol solution and 0.1 M Na_2S methanol/water mixture (1/1 v/v) were used as the source of Zn^{2+} and S^{2-}, respectively. Typically, a single SILAR cycle consisted of 1 min dipping of the working electrode in the Zn^{2+} precursors, followed by 1 min dipping in the S^{2-} precursors. After each bath, the photoanode was thoroughly rinsed with the corresponding solvent to remove the chemical residuals on the surface, respectively, and then dried with N_2.

5.1.5 PEC activity measurements

A conventional three-electrode system was used to assess the PEC performance of the 0D/2D/2D heterostructure sensitized photoanode consisting of a platinum sheet as the counter electrode, an Ag/AgCl reference electrode (saturated with KCl) as the reference electrode, and the heterostructure modified FTO photoanode as the working electrode, respectively. The surface of the photoanode was covered with a layer of insulating epoxy resin, except for the active area (~0.2 cm^2), to avoid any direct contact between the electrolyte and the conductive back contacts or connecting wires. In particular, the photocurrent density-voltage (J-V) curve was measured using a Compact Solar Simulator AAA (Sciencetech SLB-300A) under simulated sunlight (1 Sun = AM 1.5G, 100 mW cm^{-2}) using a Gamry 1000E electrochemical workstation with a sweep rate of 20 mV/s. In general, the electrolyte containing 0.25 M $Na_2S{\cdot}9H_2O$ and 0.35 M Na_2SO_3, deoxidized with high-purity N_2 for 30 min, which served as a sacrificial hole scavenger. Subsequently, the measured potential (vs Ag/AgCl) was converted to the RHE according to the following equation:

$$V_{RHE} = V_{Ag/Agcl} + 0.197 + 0.059 * \mathrm{pH}$$

In addition, 0.6 M Na_2SO_4 solution served as an electrolyte without a scavenger. And, EIS was performed in the presence of 0.25 M $Na_2S{\cdot}9H_2O$ and 0.35 M Na_2SO_3 mixture under light by using a Gamry 1000E station with zero bias voltage vs reference and a sweep in frequency from a range of 0.1 Hz to 100 kHz. The EIS data were fitted with Zview software. The incident photon-to-electron conversion efficiencies (IPCE) of doped QDs-sensitized MG photoanodes can be estimated according to the following equation:

$$\mathrm{IPCE} = \frac{1240 \times J[\mu A \cdot cm^{-2}]}{\lambda[nm] \times P[\mu W \cdot cm^{-2}]} \times 100\%$$

where J [μA·cm^{-2}] represents the photocurrent density under monochromatic incident light provided by the solar simulator equipped with band-pass filters, and λ [nm] and P [μw·cm^{-2}] represent the wavelength and optical power density of incident monochromatic light, respectively.

5.2 Results and Discussion

5.2.1 Morphological, structural, and compositional information

To synthesize the proposed 0D/2D/2D hybrid, first, Zn-$CuInS_2$ QDs and MG NSs were prepared separately, and then bound together by electrostatic self-assembly method under the assistance of ultrasounds and shaking.[48] As shown in Figure 5.1, Zn-$CuInS_2$ QDs and MG exhibit opposite (negatively and positively) charged surfaces in deionized water (pH=7), with a corresponding zeta potential of -73.76 and 32.4 mV, respectively. Therefore, they have a great tendency to spontaneous assembly into composites due to strong electrostatic interaction.

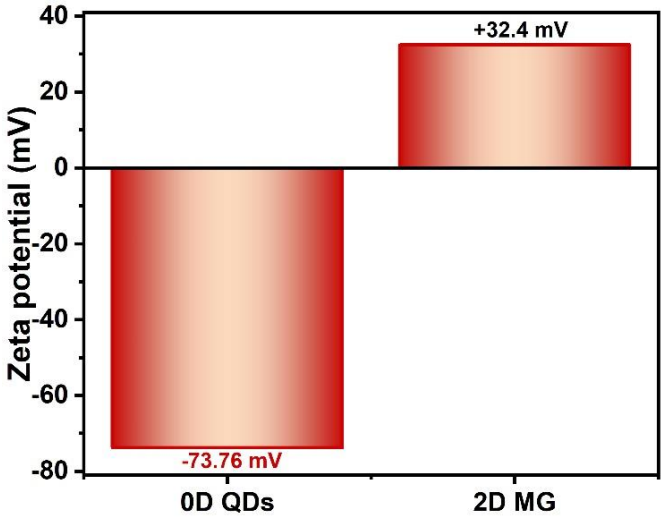

Figure 5.1 The zeta potentials of 0D Zn-$CuInS_3$ QDs and 2D/2D MG in water at pH around 7.

A series of characterization approaches were used to investigate the morphology and microstructure of the as-prepared 0D/2D/2D heterostructure composites. As shown in the TEM (Figure 5.2 a) and SEM (Figure 5.3 a) image of GO, the as-prepared GO exhibits a wrinkled, paper-like structure. Instead, pure MoS_2 forms dense aggregates due to Van der Waals interactions, exhibiting an irregular shape with an average aggregate size of more than 2 μm (Figure 5.2b and 5.3d). However, when GO is introduced (and reduced to rGO) in the synthesis process of MoS_2, the obtained 2D/2D heterostructure, MG, exhibits a regular nano-flower morphology with an average size of 450 nm, consisting of a hierarchical structure of 2D petal-like

NSs (Figure 5.2c, 5.3b and 5.3c). The difference in structure between pure MoS_2 and the MG composite is attributed to the fact that during the synthetic process of the MG composite, MoS_2 is reduced *in situ* on the surface of reduced graphene layers, thus the restacking of MoS_2 layers is inhibited.[245] Further, the TEM (Figure 5.2 c) and HRTEM images (Figure 5.2d) of MG show ripples and wrinkles, suggesting the ultrathin structure of the hierarchical NSs. In particular, the appearance of small NSs with sharp edges indicates a high degree of crystallinity. The SAED (Figure 5.4a) pattern of the synthesized MG NSs proves the hexagonal structure with (002), (100), (103) and (110) planes and corresponding diffraction intensity. The HRTEM image shows MoS_2 layers with an interlayer distance of 0.62 nm which can be assigned to the (002) crystalline plane of MoS_2, which are grown on the surface of rGO (Fig. 5.2d).

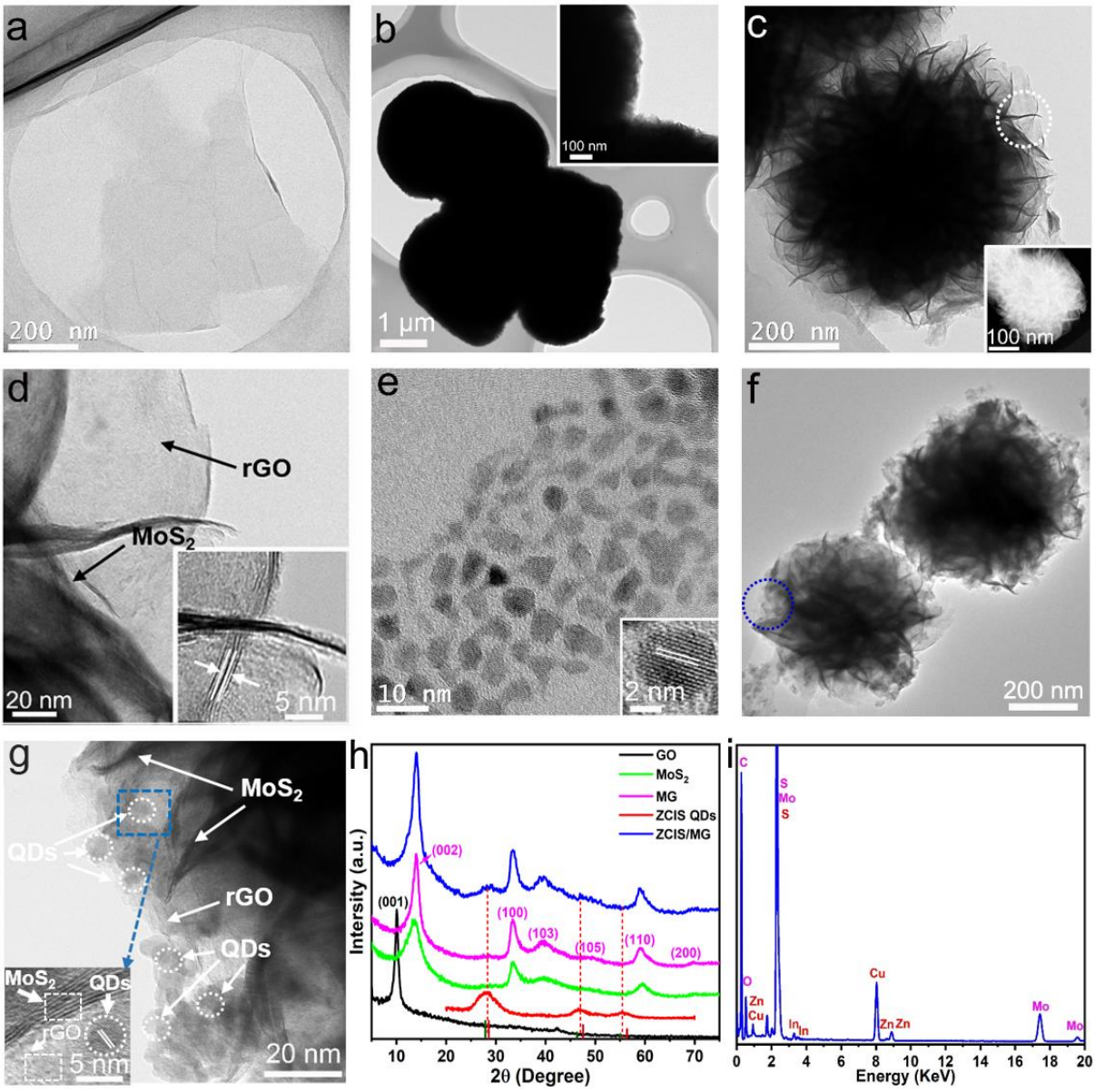

Figure 5.2 Morphological characterizations of the proposed 0D/2D/2D photocatalysts: TEM image of (a) GO, (b) MoS_2, (c-d) MG with different magnifications, (e) ZCIS QDs, (f-g) ZCIS QDs/MG heterostructure with different magnifications; The inset in (b) and (d) are HRTEM image of MoS2 and MoS2/rGO respectively. The insets in (e) and (g) are HRTEM images of ZCIS QDs; (h) XRD patterns and (i) EDX spectra of 0D/2D/2D ZCIS/MG NSs.

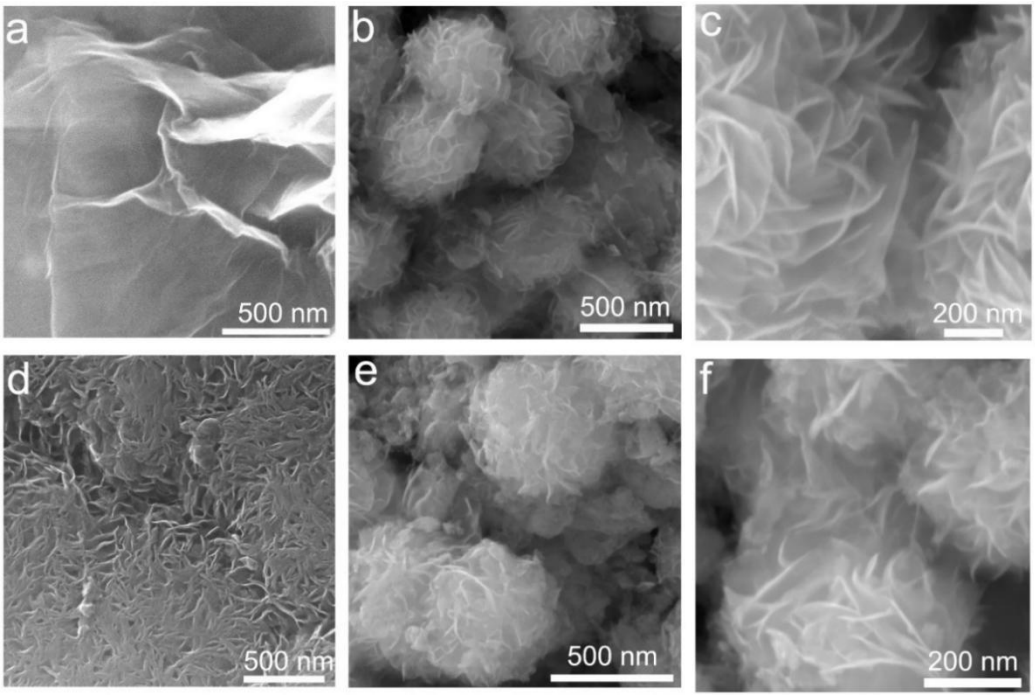

Figure 5.3 SEM image: (a) graphene (a), (b-c) MG with different magnifications, (d) MoS_2, (e-f) ZCIS QDs/MG with different magnifications.

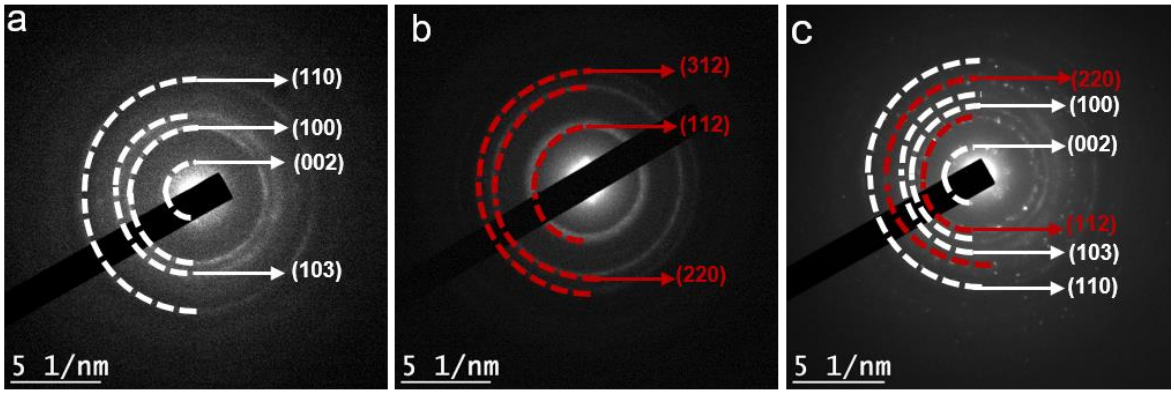

Figure 5.4 SAED patterns of (a) MG, (b) ZCIS QDs and (c) MG-ZCIS are consistent with the XRD patterns in Figure 5.2h.

Raman characterization was used to confirm the successful introduction of GO to MG. Figure 5.5a shows the Raman spectra related to GO, MoS_2 and MG nanocomposites. The Raman spectrum of MoS_2 displays two peaks at 378.7 and 404.5 cm^{-1}, corresponding to the E^1_{2g} and A_{1g} mode of the hexagonal MoS_2 crystal, respectively, indicating the typical 2H phase of MoS_2.[246] In general, the E^1_{2g} mode is caused by the opposite vibrations of the two S atoms relative to the Mo atom, while the A_{1g} mode is caused by the out-of-plane vibrations of only S atoms in the opposite direction.[247] It has been reported that as the number of layers decreases, the A_{1g} peak of the few-layer MoS_2 crystal decreases.[248] As shown in the Raman spectrum of GO, two distinct peaks at 1355.4 and 1596.2 cm^{-1} correspond to D and G bands of graphene, respectively.[249] Normally, the D band represents the defect properties of graphene, while the G band represents the structural sequence of graphene combined with the sp^2 carbon atom E_{2g} vibration mode. After incorporating GO into MG, the Raman spectrum shows four peaks corresponding to MoS_2 and graphene. In particular, the A_{1g} peak shifts from 404.5 cm^{-1} of the pure MoS_2 to 403.5 cm^{-1} of the MG hybrid, resulting from the decreased number of layers of MoS_2 NSs, as confirmed by SEM and TEM images. Furthermore, as shown in Figure 5.5a, the value of I_D/I_G peak intensity is 0.96 for GO and 1.08 for MG, indicating the successful reduction of GO to rGO, with mass defects being introduced into the structure during the reduction process.[250, 251] Based on the Raman result, we can confirm that the rGO was successfully incorporated into MoS_2, forming MG composites. In addition, the BET surface area results shown in Figure 5.5b reveal that the MG sample has a larger BET surface area (53.2 m^2/g) compared to the original MoS_2 (27.6 m^2/g), which could provide more contact areas for 0D QDs and the electrolyte redox reaction.

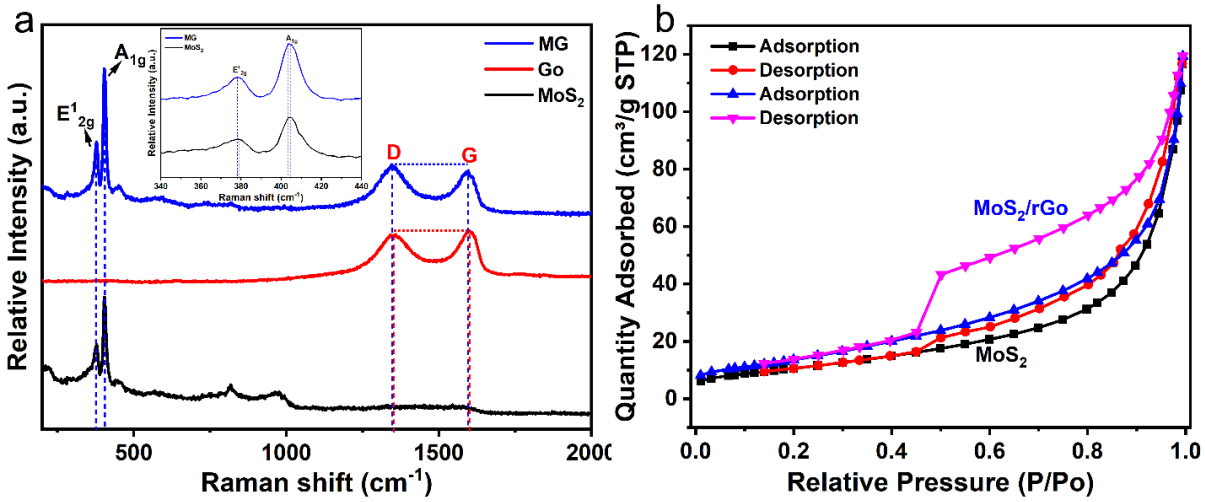

Figure 5.5 (a) Raman spectra of GO, MoS_2 and MG composite. (b) BET spectra of MoS_2 and MG composite.

A hot injection approach was used to prepare 0D Zn doped $CuInS_2$ QDs. For simplicity, the optimized $Zn_xCu_1InS_2$ QDs with a precursor ratio of 1:1 between Zn/Cu were denoted as ZCIS. Figure 5.2e shows the TEM image of the obtained 0D ZCIS QDs. The QDs present a basic spheroid morphology with uniform sizes of (4.5 ± 0.6) nm. Their crystal structure was investigated by XRD. As shown in Figure 5.6, the $CuInS_2$ QDs show a typical chalcopyrite structure (JCPDS: no. 75-0106). With the increase of the Zn/Cu-In ratio from 0 to 3, the diffraction peak positions shifted regularly to higher angles, and the crystalline structure changed from chalcopyrite structure of $CuInS_2$ to zinc blend of ZnS (JCPDS: no. 03-0570), indicating the formation of alloyed QDs. Furthermore, this peak shift of the QDs reveals that no phase separation or separated nucleation happened during the QD synthesis, indicating the successful formation of Zn-$CuInS_2$ QDs.[252, 253] The SAED pattern of the synthesized ZCIS QDs (Figure 5.4b) proves the chalcopyrite structure with (112), (220), and (312) planes and corresponding diffraction intensity, consistent with the XRD results. In addition, the HRTEM images (inset in Figure 5.2e) reveal a lattice space ~0.32 nm, which can be indexed to the (112) plane of chalcopyrite of CIS.

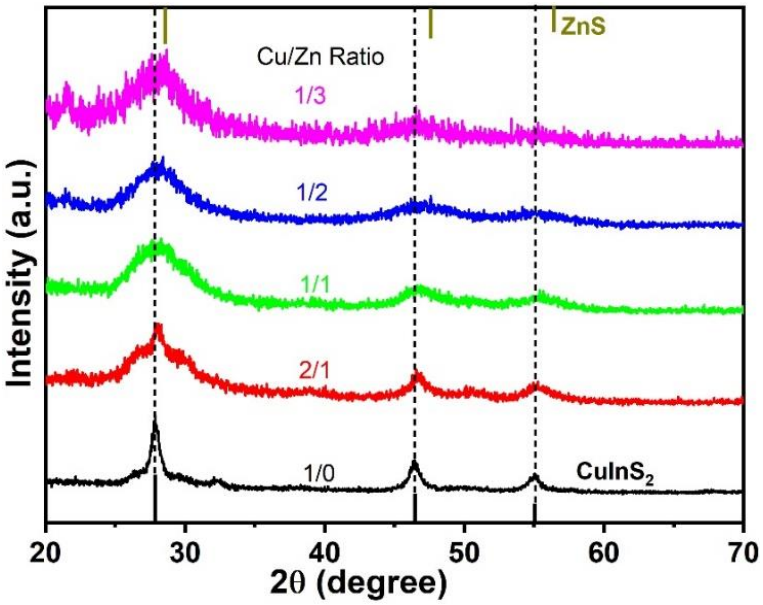

Figure 5.6 XRD patterns of the Zn doped $CuInS_2$ QDs with different compositions.

Furthermore, to allow the electrostatic self-assembly between 0D QDs and 2D NSs, the colloidal Z_xC_1IS QDs were transferred to the aqueous phase by replacing the initial hydrophobic ligands using hydrophilic carboxyl as ligands. Fourier transform infrared spectroscopy (FTIR) spectra (Figure 5.7) were collected to confirm the successful ligand exchange from OLA to MPA. As shown in Figure 5.7a, the ZCIS QDs dissolved in Toluene (top phase) before ligand exchange. After ligand exchange, the MPA-capped ZCIS QDs can dissolve in water (bottom phase). FTIR

characterization was applied to verify the successful surface ligand exchange process. Figure 5.7b shows the FTIR spectra of QDs before and after ligand exchange, respectively. After ligand exchange, it was found that the QDs exhibit an additional distinct bands at 1651 cm^{-1}, which can be assigned to the C=O bond stretching vibration of MPA.[254] In contrast, before the ligand exchange, the OLA-capped QDs do not show any carboxyl signal from MPA. Efficient ligand exchange is furthermore evident from the almost complete disappearance of the ligand C-H stretching FTIR bands at 2853 and 2923 cm^{-1}. Therefore, the FITR spectra confirm the successful ligand exchange of the QDs.

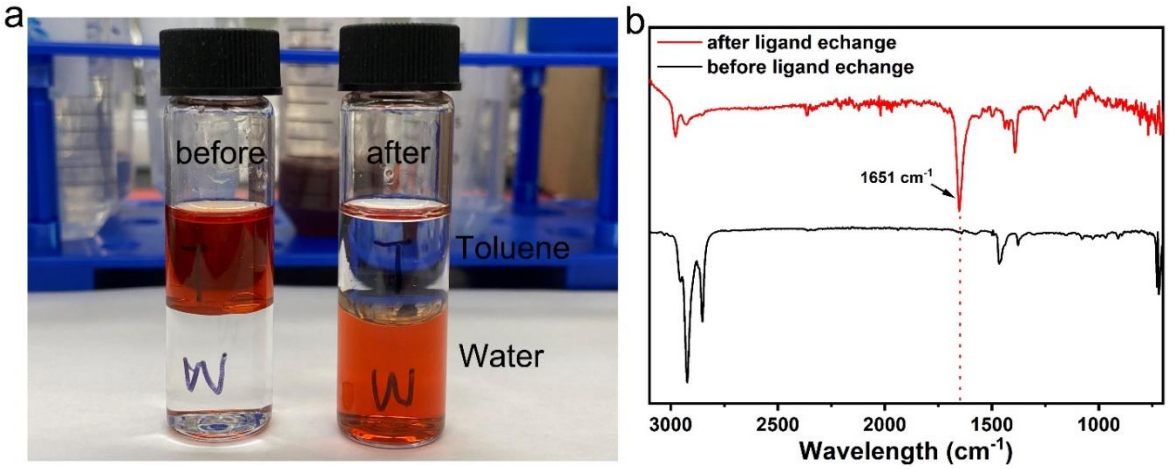

Figure 5.7. (a) Photographs of ZCIS QDs before and after ligand exchange. (b) FTIR spectra of OLA capped ZCIS QDs before ligand exchange (black line), and the sample after ligand exchange using MPA (red line).

Through the electrostatic self-assembly method, the ZCIS QDs were made to adhere to the MG surface. However, during this process, QDs had a tendency to aggregate. This may be due to the high surface energy generated by the presence of a large number of chemically unsaturated atoms on the surface of the QDs.[255] TEM characterization was used to analyze the morphology of the as-produced 0D/2D/2D nanocomposite. Figure 5.2f shows the TEM image of the proposed 0D/2D/2D ZCIS/MG heterostructure, where the ZCIS QDs (4.5 nm) were uniformly distributed on the surface of the MG film surface. The HRTEM image (Figure 5.2g) obtained from the partially enlarged view of the blue-circled area (Figure 5.2f) shows the 0D/2D/2D assembly; the QDs are highlighted by superimposed circles, while the MG exhibits a different lattice. The HRTEM image of ZCIS QD shows lattice fringes with 0.32 nm spacing (Figure 5.2g), corresponding to the chalcopyrite (112) plane, while the HRTEM image of the 2D hierarchical NSs shows the expected hexagonal MG nanostructure, with a lattice spacing of 0.62 nm, belonging to the (002) plane of MoS_2.

XRD characterization were acquired to investigate the crystal structure and synthesis process of the 0D/2D/2D heterostructure (Figure 5.2h). As shown in the XRD patterns of MoS_2, the diffraction peaks located at 13.9°, 33.5°, 39.8°, and 59.5° can be assigned to the (002), (100), (103), and (110) planes, respectively, which can be indexed to the hexagonal-phase MoS_2 (JCPDS no. 37-1492). The (002) reflection at 13.9° is indicative of the layered structure of MoS_2.[256] The intense and sharp diffraction peak of GO at 10.0° corresponding to the (001) crystal plane, disappears in the MG nanocomposite, revealing the reduction of GO during the hydrothermal process. However, the peak corresponding to rGO (usually present at 24°~30°) is not visible, probably due to the relatively small amount of rGO (less than 5%) present in MG. As expected, the spectrum of MG/ZCIS is composed of of a combination of MG and ZCIS diffraction peaks. The lattice spacing in the SAED patterns of the proposed MG/ZCIS (Figure 5.4c) can be indexed into the (002), (100), (103) and (110) planes of hexagonal phase of MG as well as the (112) and (220) planes of the ZB phase of ZnS. In this case, an overlap between the planes of MG and ZCIS is present. EDS analysis performed on MG/ZCIS confirms the coexistence of C, O, Mo, S, Cu, In and Zn elements (Figure 5.2i) (N.B. the strong Cu signal is due to the Cu grid used for TEM imaging). In addition, Figure 5.8 shows the EDS mapping of as-synthesized 0D/2D/2D hetero-structure composites, wherein Mo and S signals originate from the MoS_2, C and O arise from the rGO (and possible ambient contamination), and Zn, Cu, In and S elements come from the ZCIS QDs. The presence of these elements confirms that the 0D ZICS QDs are successfully loaded on the 2D/2D MG NSs. The content of Cu is much higher due to the grid used for TEM imaging.

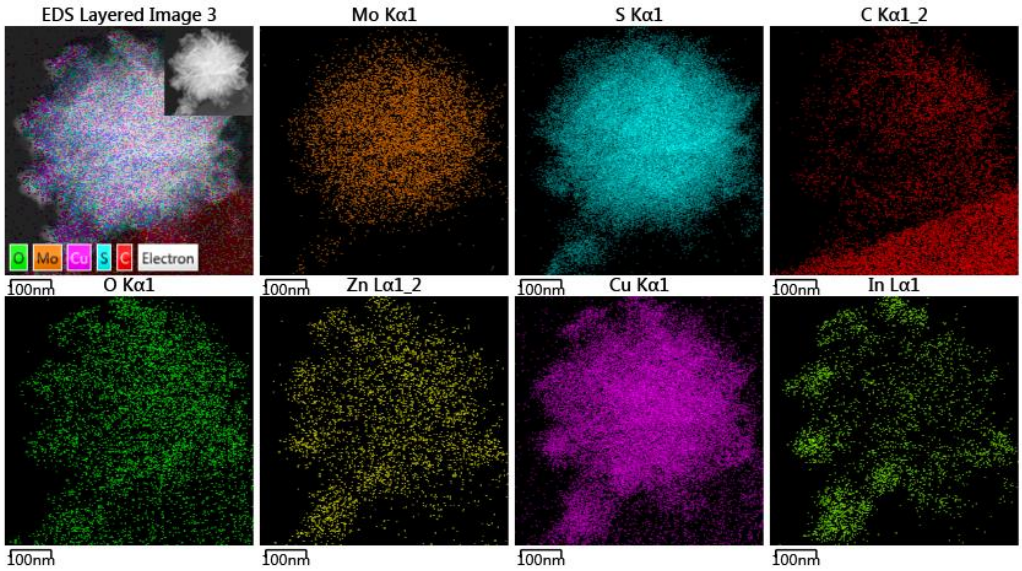

Figure 5.8. EDS mapping of 0D/2D/2D ZCIS/MG heterojunction element mapping images: Mo, S, C, O, Zn, Cu and In, respectively. The scale bar is 100 nm.

The chemical states of the proposed 0D/2D/2D heterostructure were investigated by XPS analysis. Figure 5.9a shows the XPS survey spectra of pure 2D/2D MG, 0D ZCIS QDs, and 0D/2D/2D ZCIS/MG heterostructure. In the latter, the coexistence of Mo, S, C, O and Zn, Cu, In elements, indicates the successful synthesis of the MG/ZCIS hybrid. No significant impurities were detected in these samples. Figures 5.9b-h show the HR-XPS spectra of C1s, O1s, Mo 3d, S 2p, Cu2p, In3d and Zn 2p of ZCIS/MG, respectively. The HR-XPS of C1s spectrum can be deconvoluted into three peaks (Figure 5.9a), with the peak located at 284.6 eV can be attributed to C-C/C=C sp^2 carbon species, the peak located at 286.2 eV can be attributed to hydroxyl carbon C-O, and the peak at 288.2 eV can be attributed to carboxylate carbon O-C=O.[257] The O 1s spectrum (Figure 5.9c) can be deconvoluted into four peaks: the peaks located at 532, 533.2, and 534.5 eV are assigned to absorbed water, while the peak located at 530.7 eV is assigned to the Mo-O groups.[258]

As shown in Figure 5.9d, there are two distinct peaks around 232.4 and 229.3 eV with a 3.1 eV difference, which can be attributed to Mo $3d_{5/2}$ and Mo $3d_{3/2}$, respectively, confirming the existence of Mo^{4+}.[186] The weak peaks at higher binding energies at 233.5 and 235.9 eV are attributed to the oxidation state of Mo^{6+}, suggesting that the Mo edges are slightly oxidized, which may be caused by the sample being oxidized in air.[187] In addition, the peak located at 226.5 eV can be indexed to S 2s. Sulfur oxidation states were determined by the HR-XPS spectrum of S 2p. As shown in Figure 5.9e, the S 2p can split into doublet peaks of S $2p_{3/2}$ (162.0 eV) and S $2p_{1/2}$ (163.25 eV) due to the spin-orbit coupling, indicating the existence of S^{2-}.[219] Meanwhile, the weak peak present at a binding energy of 164.6 eV suggests the existence of bridging disulfides S_2^{2-} and/or apical S^{2-} ligands. Furthermore, the Cu 2p is split into Cu $2p_{3/2}$ (932.5 eV) and Cu $2p_{1/2}$ (952.3 eV) with a peak separation of 19.8 eV, which matched well with that of Cu^{+} (Figure 5.9f).

In the spectrum (Figure 5.9g), the two distinct peaks around 445.0 eV and 452.6 eV with a 7.6 eV difference can be assigned to In $3d_{5/2}$ and In $3d_{3/2}$, respectively, confirming the presence of In^{3+}.[219] The Zn spectrum shows peaks located at 1022.1 eV and 1045.2 eV (Figure 5.9h), with a 23.1 eV difference which can be ascribed to Zn $2p_{3/2}$ and Zn $2p_{1/2}$, respectively, confirming the presence of Zn^{2+}.[259] The S 2p peaks can be also used to investigate the inner structure of MoS_2 and MG. After the introduction of GO to MoS_2, the binding energy of Mo and S in MG (Figure 5.10) is slightly shifted to lower energy, indicating a strong interaction between MoS_2 and Rgo, confirming the GO incorporation in the nanohybrid. The negative shifts of the binding energies of S 2p indicates an increase in electronic density in MG NSs.[190, 260] As shown in Figure 5.9i, the S2p of ZCIS/MG displays an intermediate value between the MG and ZCIS after the electrostatic self-

assembly of MG and ZCIS, further implying the successful hybrid formation. The chemical composition confirmed by XPS is also in agreement with EDS spectra in Figure 5.2i.

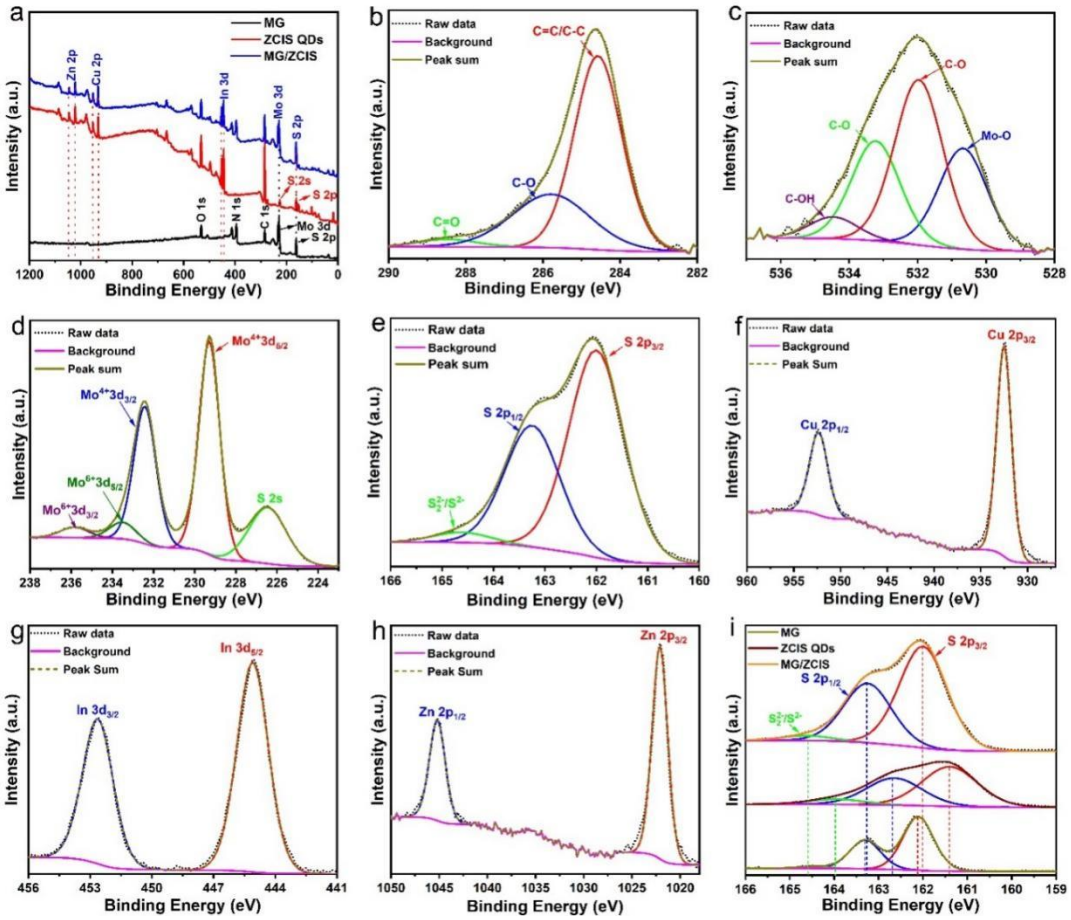

Figure 5.9. (a) XPS survey spectra; (b-h) C1s, O1s, Mo 3d, S 2p, Zn 2p, Cu2p and In3d HR-XPS spectra of MG/ZCIS QDs, respectively; (i) S 2p XPS spectra of MG, ZCIS and MG/ZCIS.

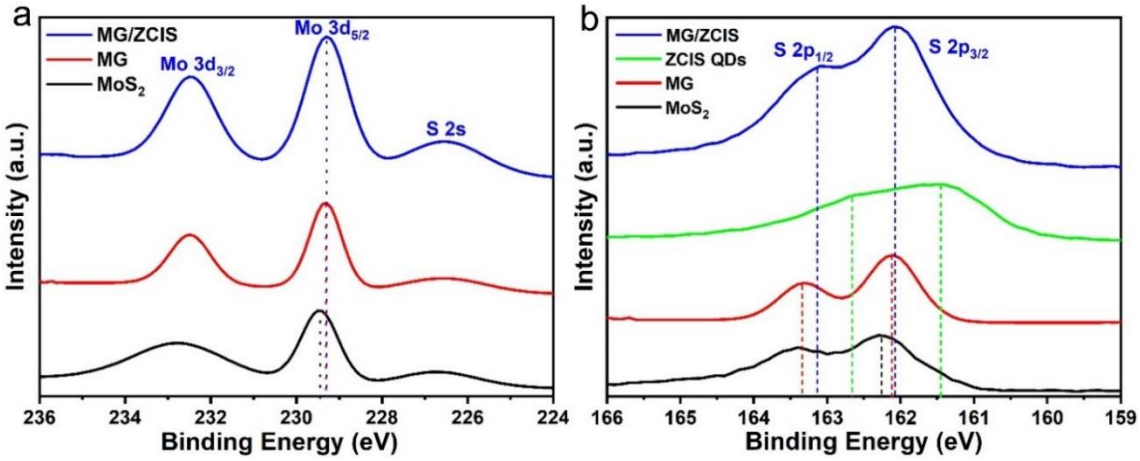

Figure 5.10 Comparison of high-resolution XPS spectra for (a) Mo 3d and (b) S 2p.

5.2.2 Optical properties of ZCIS QDs

The optoelectronic properties of the ZCIS QDs with different amounts of Zn were investigated to find the best ratio for their successive integration with the 2D/2D NSs hybrid. Figure 5.11 shows the absorption and emission spectra of Zn doped $CuInS_2$ QDs in which the Cu/Zn molar ratio is modulated while the other reaction conditions have been kept constant. As shown in Figure 5.11a, the absorption spectrum of pure $CuInS_2$ QD ranges from the UV-vis region up to the NIR region. With the increase of the Zn/Cu-In ratio from 0/1 to 3/1, the absorption onset blue shifted from 900 nm up to 560 nm. Furthermore, Figure 5.12 also shows the TEM images and size distribution of different amounts of Zn doped $CuInS_2$ QDs. When the Zn amount increases, the QDs size slightly shrink. Overall, the tuned optical properties of the ZCIS QDs originate from the quantum confinement as well as the formed intra Zn state above the lowest unoccupied molecular orbital or below the highest occupied molecular orbital of $CuInS_2$. Pure $CuInS_2$ QDs did not possess well-defined excitonic absorption peaks. Generally, a poorly resolved excitonic absorption peak is a typical feature for some ternary and quaternary semiconductor QDs. Previous research has shown that the broad absorption peaks observed in ternary and quaternary nanocrystals are due to the irregular elemental distribution of elements and/or intra bandgap states in a single particle, which results in different crystal structures with various bandgaps.[121, 261] Especially, compared to the poor resolution of exciton absorption peaks of Cu/Zn precursors with other ratios, it can be observed that when the ratio of Cu/Zn precursors is 1:1, the prepared ZCIS QDs have a relatively sharp exciton absorption peak at 517 nm. This suggests that the composition, size and shape of ZCIS QDs are uniformly distributed.[59] The bandgap of these QDs can be estimated using Tauc's equation based on the corresponding absorption edges, and the detailed results are shown in Figure 5.13. It is worth noting that due to the existence of the extended absorption tail arising from the intraband states, the bandgap energy obtained in wavelength units is significantly shorter than the corresponding absorption onset.[262] The PL emissions peaks of the as-prepared QDs exhibit a similar blue shift (Figure 5.11b), from 835 nm to 564 nm with the increase of the Zn/Cu-In ratio. These data further confirm the successful incorporation of Zn inside the chalcopyrite $CuInS_2$ crystal lattice to form alloyed ZCIS QDs.

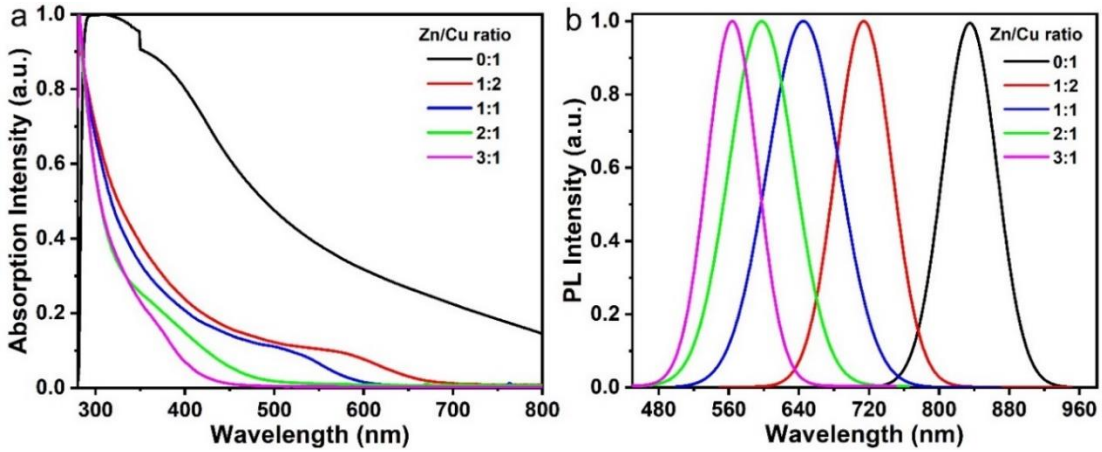

Figure 5.11 The Normalized (a) UV-vis absorption and (b) steady PL emission spectra of different amounts of Zn doped $CuInS_2$ QDs.

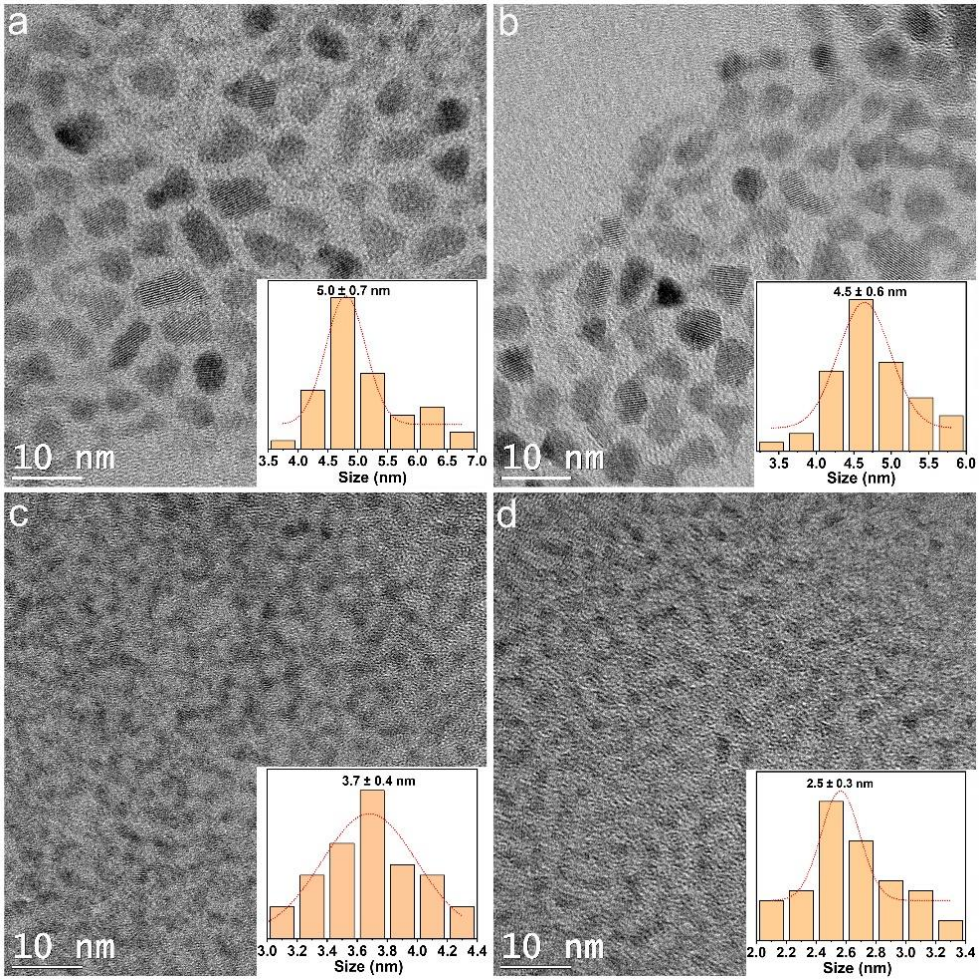

Figure 5.12 TEM images of CIS QDs with different Zn doping molar ratios (Zn/Cu–In): (a) 0.5/1, (b) 1/1, (c) 2/1, and (d) 3/1; The inset is the size distribution.

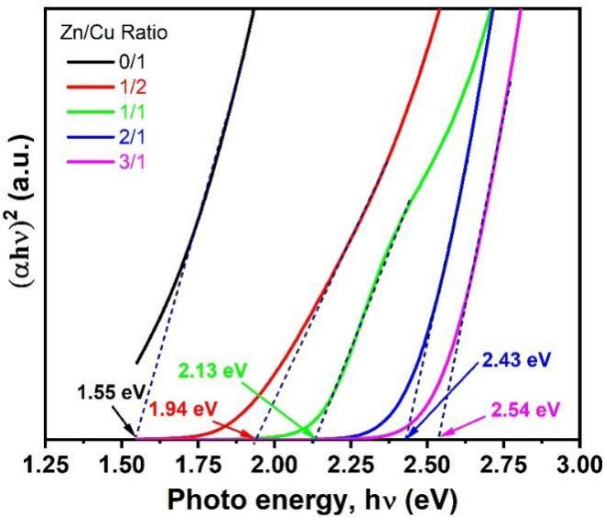

Figure 5.13 Tauc plots of $(\alpha h\nu)^2$ versus band-gap energy (hv) of different amounts of Zn doped $CuInS_2$ QDs.

5.3 PEC performances

A modified space-confined self-assembly approach was used to prepare the thin film photoanode.[179, 243] Figure 5.14 shows the detailed preparation process of FTO/TiO_2/MG-ZCIS photoanode. It mainly contains five steps: (1) injection of MG-ZCIS dispersion; (2) flake confinement and self-assembly; (3) hexane removal; (4) acetonitrile removal and film deposition; (5) drying at 80 °C.

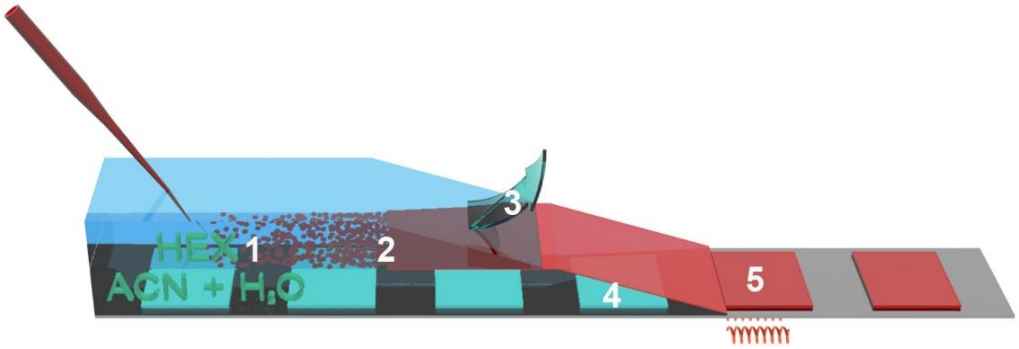

Figure 5.14. The space-confined self-assembly approach for MG-ZCIS thin-film deposition; the red solution represents MG-ZCIS.

Cross-sectional SEM imaging and the corresponding EDS analysis of the FTO/TiO_2/MG-ZCIS/ZnS photo-anode are shown in Figure 5.15. As shown in Figure 5.15 a, the thickness of the mesoporous TiO_2/MG-ZCIS/ZnS film is ~2.5 µm. The EDS spectra (Figure 5.15 b) confirmed the presence of elemental Ti, O, Mo, S, C, Zn, Cu, and In, respectively, consistent with the chemical

composition in the QDs sensitized photoanode. The content of Zn is much higher due to two ZnS layer deposited on the surface of photoanode to prevent photocorrosion of the QDs. In addition, the EDS mapping characterization (Figure 5.15 c-k) also confirmed the homogeneously distribution of Sn, Ti, O, Mo, S, C, Zn, Cu, and In elements, respectively, suggesting the successful preparation of photoanode. In particular, the Si and Sn signal originates from the FTO glasses substrate.

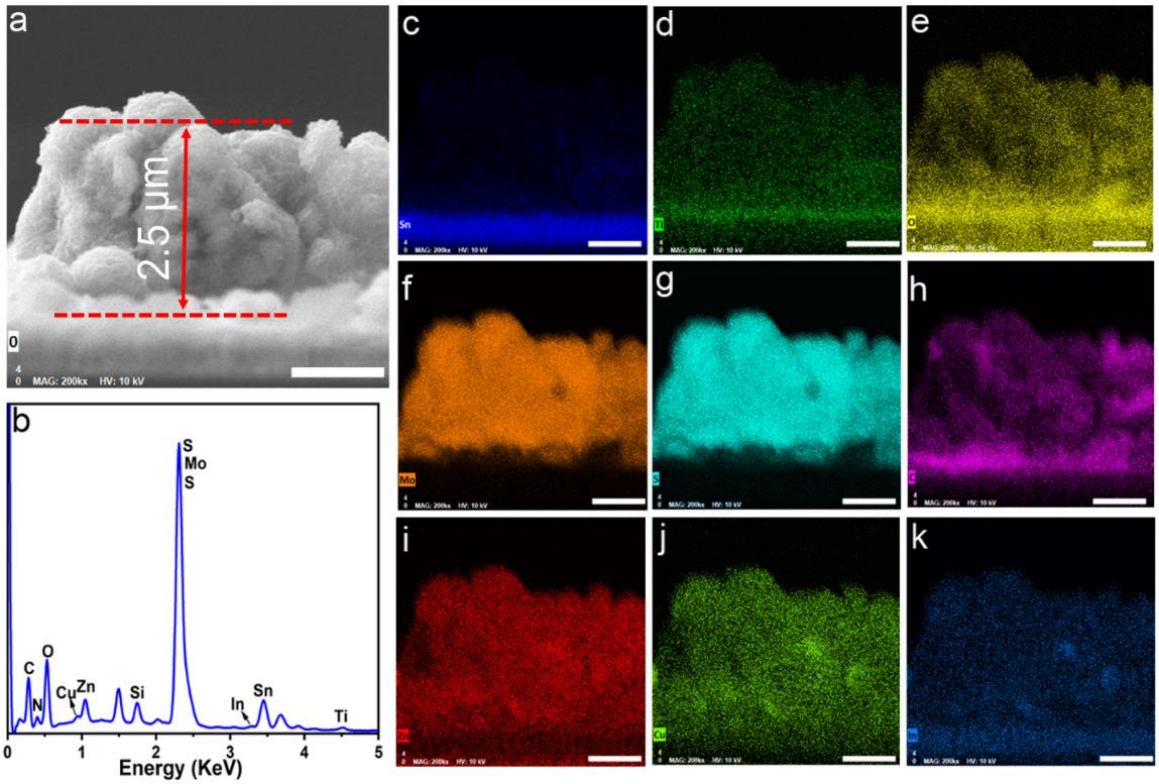

Figure 5.15 (a) Cross-sectional SEM image; (b) EDS spectra of FTO/TiO_2/MG-ZCIS/ZnS photo-anode; (c-k) EDS mapping and relevant chemical composition.

Photoanodes sensitized with different QDs and based on a different number of layers of MG were investigated in an electrolyte (0.25 M $Na_2S{\cdot}9H_2O$ and 0.35 M Na_2SO_3), by using a typical three-electrode setup under dark and light conditions, including LSV, chronoamperometry, and EIS. OCP transient analysis was also used to investigate the charge injection direction of the prepared photoelectrodes (Figure 5.16). The prepared photoanodes exhibit a negative voltage under light irradiation, implying that the photogenerated electrons are injected from the film into the FTO substrate, generating an anodic current. In particular, the photovoltage (i.e., the difference between the voltages in light on and off) of the MG-ZCIS sample (0.49 V vs Ag/AgCl) is four times

larger than the MG-CIS film sample (0.12 V vs Ag/AgCl). This suggests that the proposed MG-ZCIS photoanode possesses remarkable photoelectric conversion ability.

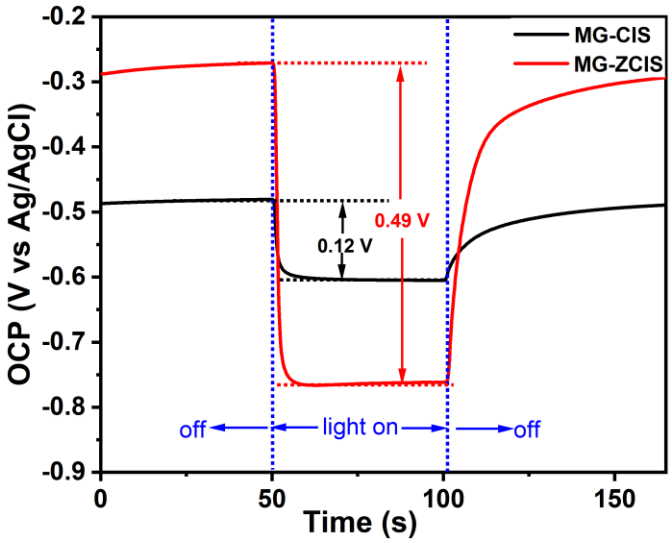

Figure 5.16 Transient OCP of MG-CIS and MG-ZCIS film samples under dark and light illumination.

In order to obtain the optimal PEC performance, we have optimized the thickness of the ZCIS/MG film deposited on the FTO/TiO_2 substrate. As shown in Figure 5.17, the photoanodes with three layers exhibited the highest photocurrent density. For film formed with more layers, the photocurrent performance decreased. Increasing the thickness of the MG film over a certain value could lead to an increase in the charge transfer resistance of the interface. As shown in Figure 5.17, a film formed with more than three layers exhibited a decrease in the photocurrent. Therefore, in this study, three MG layers are selected as the optimal condition for the substrate.

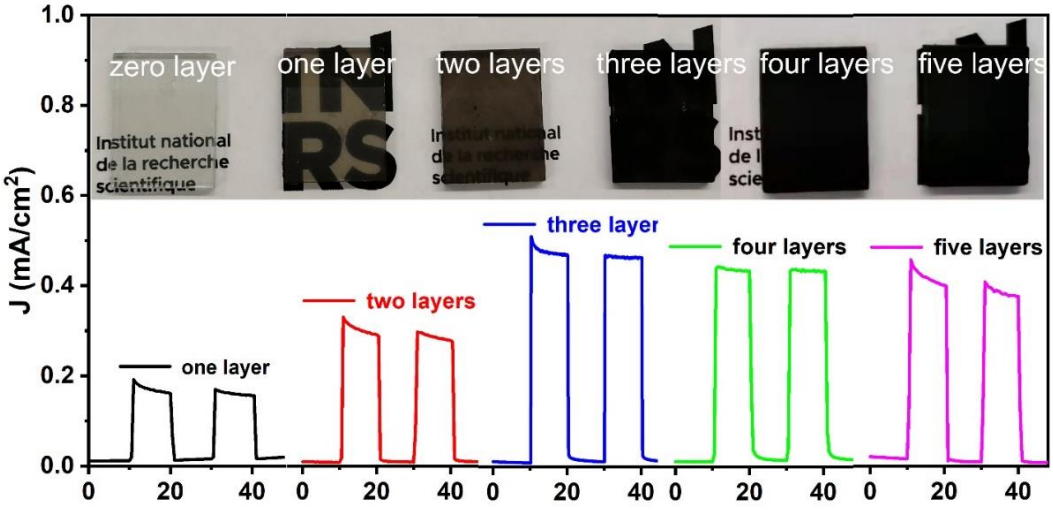

Figure 5.17 The corresponding amperometric i-t cycles for different layers. The inset is the photographs of FTO/TiO_2 coated with different MG-ZCIS layers, the FTO is 1.5 cm*2cm.

To study the effect of Zn dopants on the band alignment of the proposed heterojunction and how it can influence the PEC performance, representative samples of pure MG/CIS, and Zn-doped CIS/MG (Zn:Cu = 1:2, 1:1, 2:1, 3:1) have been tested. As shown in Figure 5.18a and Figure 5.19, the photocurrent density (J_{ph}) strongly depends on the type of QDs used. Compared to the undoped MG/$CuInS_2$ QDs (J_{ph}≈0.09 mA cm^{-2} at 0.93V vs RHE), all the Zn-doped QDs show higher photocurrent, indicating a stronger ability to generate charge carriers. The highest photocurrent is obtained for the photoanode sensitized with a 1:1 ratio of Zn/Cu, with a saturated photocurrent of 0.44 mA/cm^2 at 0.93 V (vs. RHE) which is almost five times higher compared to the pure CIS QDs. The sample with 1:2 ratio of Zn/Cu, presents a photocurrent density of 0.23 mA cm^{-2}, an intermediate value between the one obtained for 0:1 and 1:1 Zn doping. Instead, the PEC performance decreases gradually with a higher amount of Zn doping, with values of photocurrent equal to 0.3 and 0.18 mA cm^{-2}, for 2:1 and 3:1 Zn/Cu ratios, respectively.

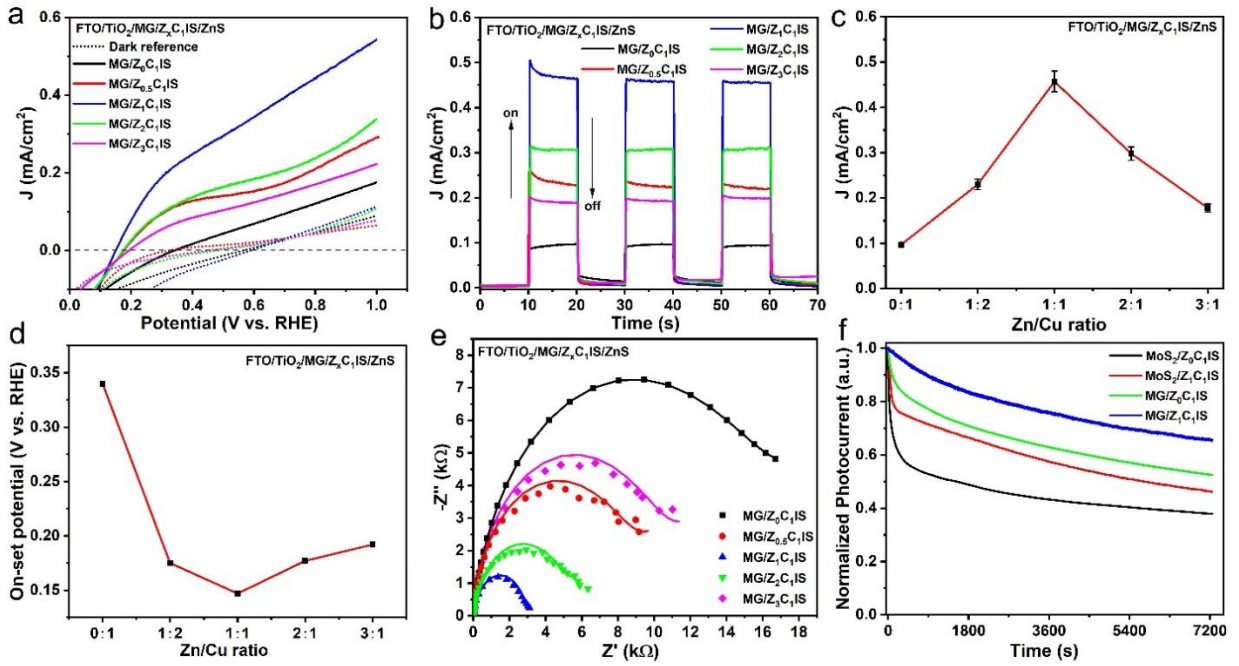

Figure 5.18 (a) J-V curves and (b) chronoamperometric J-t cycles of different amounts of the Zn doped $CuInS_2$ QDs sensitized photoanode in the dark (dashed curve) and under continuous (solid curve) illumination (AM 1.5 G, 100 mW cm^{-2}); (c) The trends of photocurrent density and onset potential (d) of MG/Z_XC_1IS photo-anodes based on different amount of Zn doping. The red line is a guide for the eyes; (e) Nyquist plots of EIS and (f) photostability of representative photoanodes under illumination (100 mW/cm^{-2}) at 0 V vs Ag/AgCl. The fitting results are plotted as solid traces in EIS.

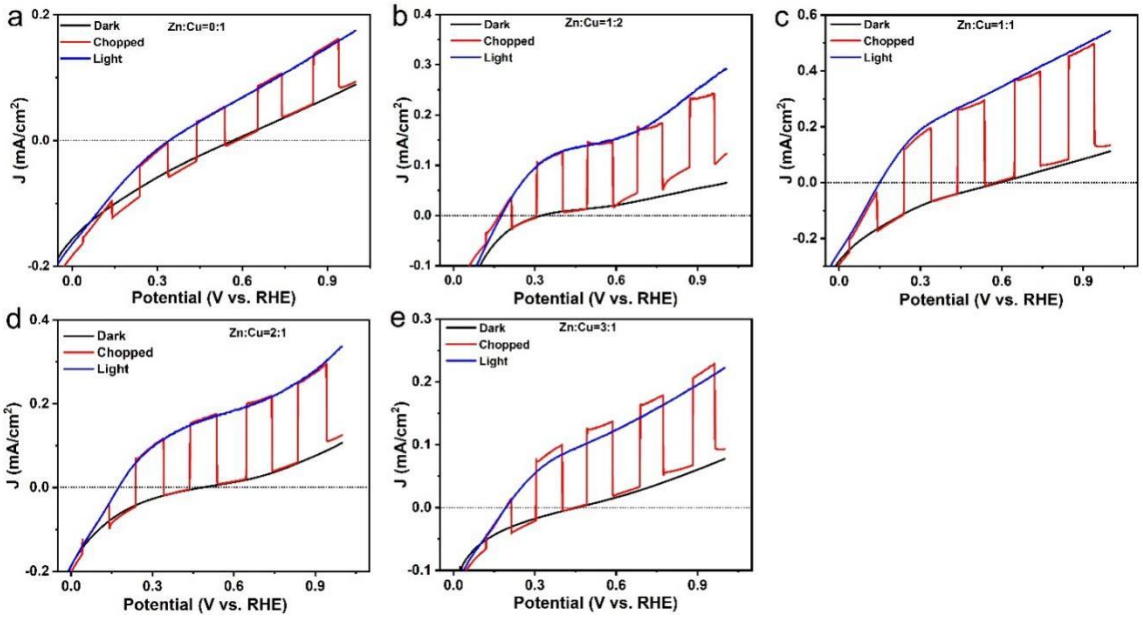

Figure 5.19 Photocurrent density-potential dependence of the different amounts of Zn doped $CuInS_2$ QDs sensitized photo-anode in the dark (black curve), chopped (red curve) and under continuous (blue curve) illumination (AM 1.5 G, 100 mW cm^{-2}).

For comparison, the pure FTO/TiO_2/MG/ZnS photoanode without any QDs displays a saturated photocurrent density of only ~0.05 mA cm^{-2} (Figure 5.20). The relatively low background current suggests that the increased photocurrent density of the QDs sensitized FTO/TiO_2/MG/ZnS photoanode can be mainly ascribed to the QDs contribution.

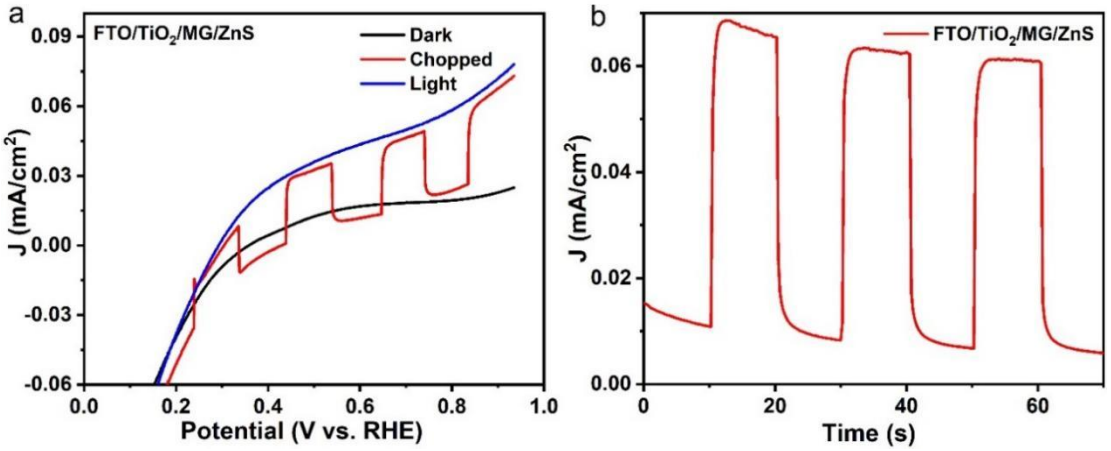

Figure 5.20 (a) J-V dependence of FTO/TiO_2/MG/ZnS photoanode in dark, chopped and continuous light under 1 sun illumination (AM 1.5G, 100 mW/cm^{-2}). (b) The photocurrent density versus times for FTO/TiO_2/MG/ZnS photoanode displayed about ~0.05 mA/cm^2.

Figure 5.18b shows the on/off transient amperometric *j-t* characteristics of these photoanodes, measured at 0.93 V vs. RHE (0 V vs. Ag/AgCl). Compared to the dark current (OFF state), for all samples, the J_{ph} is significantly increased under light illumination (ON state). The instantaneous increase in photocurrent indicates that the photoanodes can effectively generate and separate electron-hole pairs and transfer electrons to the counter electrode. In particular, the J_{ph} of photoanodes based on MG/ZCIS QDs sensitizer shows a maximum 400% increment compared to the MG/CIS QDs sensitized photoanode. The addition of Zn can in fact modulate the photocurrent density by changing the light absorption range and energy band arrangement of the QDs. To highlight the function that rGO plays in improving the photocurrent, the photocurrent density of MoS_2/ZCIS QDs based photoanodes was also measured (Figure 5.21). The LSV curve demonstrates that the Jph of MoS_2/ZCIS is significantly lower than that of MG/ZCIS. This difference can be attributed to the higher conductivity of rGO, which helps to expedite electron transport and prevent carrier recombination.

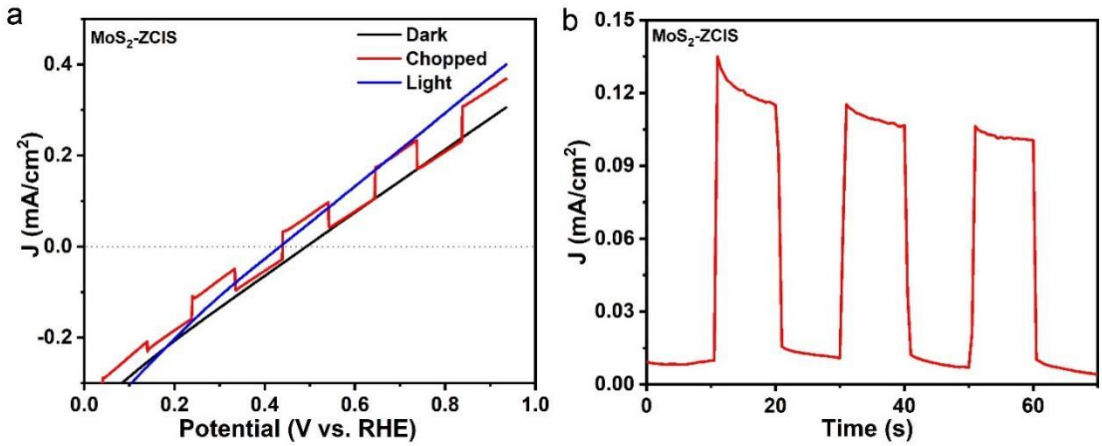

Figure 5.21 (a) J-V dependence of FTO/TiO_2/MoS_2-ZCIS/ZnS photoanode in dark, chopped and continuous light under 1 sun illumination (AM 1.5G, 100 mW/cm^{-2}). (b) The photocurrent density versus times for FTO/TiO_2/MoS_2-ZCIS/ZnS photoanode displaying about ~0.1 mA/cm^2.

The general trend of photocurrent versus the amount of Zn doped is reported in Figure 5.18c: 1:1 Zn doped $CuInS_2$ QDs is the optimum condition that yields the highest photocurrent. In addition, the onset potential shift negatively compared to the pure MG/$CuInS_2$ QDs (Figure 5.18d), indicating that more electrons are released and accumulated in the heterostructure.[263] The significantly increased photocurrent density of MG/ZCIS QDs-based photoanode, can also be attributed to the faster electron transport and higher separation efficiency of the photogenerated electron-hole pairs due to the introduction of graphene.

Furthermore, a test without a sacrificial agent was carried out for MG-ZCIS based photoanode. Figure 5.22 displays the J-V curves of FTO/TiO_2/MG-ZCIS/ZnS photo-anodes in Na_2SO_4 (0.6 M) electrolyte, under dark, continuous and chopped illumination (AM 1.5 G, 100 mW/cm^2). The photocurrent density is about ~0.14 mA cm^{-2}. Compared to the photocurrent density (Figure 5.19 c) with a sacrificial agent (0.25 M Na_2S and 0.35 M Na_2SO_3), the photocurrent density without any sacrificial agent is obviously reduced, due to increased charge recombination caused by the accumulation of holes on the surface of the QDs. This behavior is typical for the majority of QDs-based PEC devices.[264]

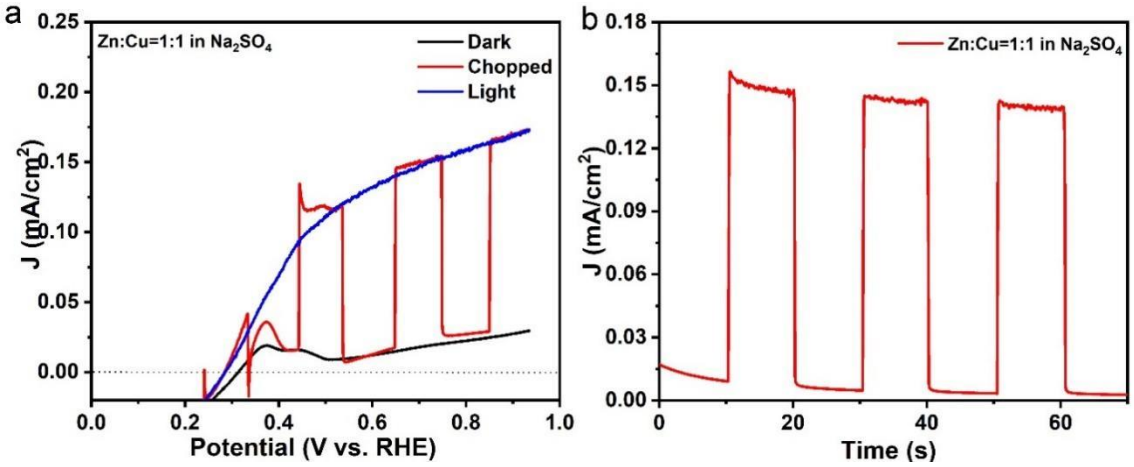

Figure 5.22 J-V dependence of MG/ZCIS photo-anodes in Na_2SO_4 (0.6 M) electrolyte. A SILAR ZnS layer is present on all the films.

EIS was employed to investigate the charge transfer mechanism. Figure 5.18e shows the Nyquist plots of the representative photoanode based on the MG/Z_xC_1IS heterostructure at 0.93 V (vs. RHE) under 1 Sun (100 mW/cm^2). As shown in Figure 5.18e, all the Nyquist plots obtained show a similar semicircle shape. In this case, the main focus of the analysis is the diameter of the intermediate frequency semicircle because it correlates with the charge transfer resistance (R_{ct}). In general, a smaller radius of the semicircle indicates a lower R_{ct}, which suggests a better charge transfer. The raw EIS data were fitted with an equivalent electrical model similar to Figure 4.17 (in Chapter 4): Randles equivalent circuit composed of series resistance (R_s), space charge capacitance and resistance (C_{SC} and R_{SC}), double layer capacitance (C_{dl}), charge transfer resistance (R_{ct}) and Warburg element (W). The values of the Randles equivalent circuit were simulated with ZSimWin software and the relevant data are shown in Table 5.1. As shown in Figure 5.18e, the photoanode based on MG/ZCIS QDs (ratio 1:1) exhibits the smallest charge transfer resistance compared to other composite photoanodes. As the photoelectrodes are

constructed in a similar way, the improved charge transfer can be assigned to a better charge separation and transport at the interfaces thanks to the excellent band alignment and to the presence of graphene, confirming that the charge carrier recombination is reduced in the MG/ZCIS architecture.

Table 5.1 Simulation parameters of the equivalent circuit components

Photoanode	R_s (Ω)	R_{ct} (Ω)	C_{dl} (F)	Z_W
FTO/ TiO_2/MG/$CuInS_2$/ZnS	11.94	18966	8.375×10^{-6}	1.496×10^{-4}
FTO/ TiO_2/ MG/$Zn_{0.5}Cu_1InS_2$/ZnS	14.40	10622	4.715×10^{-6}	1.955×10^{-4}
FTO/ TiO_2/ MG/$Zn_1Cu_1InS_2$/ZnS	15.70	3155	6.004×10^{-6}	1.581×10^{-3}
FTO/ TiO_2/ MG/$Zn_2Cu_1InS_2$/ZnS	12.31	6917	7.708×10^{-6}	4.874×10^{-4}
FTO/ TiO_2/ MG/$Zn_3Cu_1InS_2$/ZnS	16.06	11761	4.232×10^{-6}	1.727×10^{-4}

We measured the IPCE of several representative photoanodes. The values are reported in Figure Figure 5.23. The integrated photocurrent obtained from the IPCE is in good agreement with the LSV data (Figure 5.18). Similar to the LSV data, the MG/Z_1C_1IS sample exhibits the highest IPCE, indicating higher ability to convert photons into charges. Interestingly, even if the photoanodes based on MG/$Z_{0.5}C_1$IS and MG/CIS present a wider absorption range compared to MG/Z_1C_1IS, they present lower IPCE, which is also in agreement with the photocurrent trend. This clearly shows that a wider absorption range is not a sufficient feature to obtain higher efficiencies.[265, 266] Even though these samples have a wider absorption spectrum than the Z_1C_1IS samples, they have poor band alignment and surface traps, which lower the final efficiency of the devices.[265] In addition, the IPCE of the MG/Z_2C_1IS and MG/Z_3C_1IS-based photoanodes decreased in a sequential manner. This is mainly due to a narrow absorption range and higher charge recombination. All of these findings indicate that an optimized composition and acceptable absorption range, (Zn:Cu = 1:1) are necessary for improving PEC performance, as shown by the MG/Z_1C_1IS photoanode (Zn:Cu = 1:1). These results are in agreement with the EIS data, confirming better charge transfers.

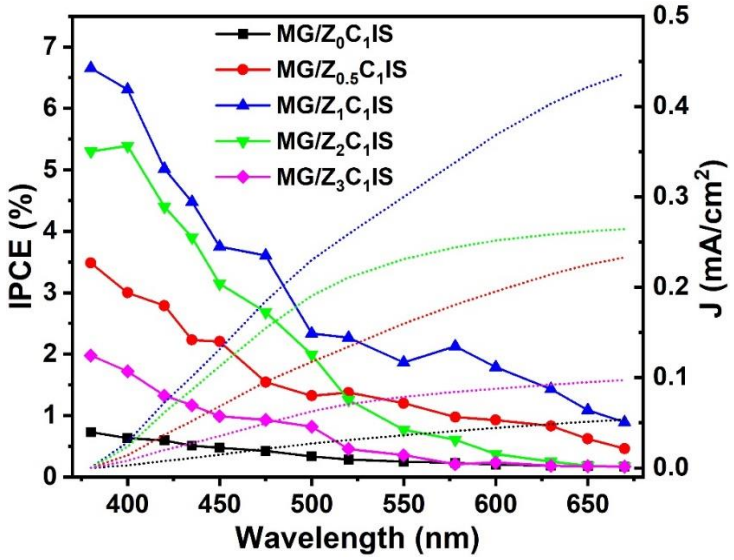

Figure 5.23. IPCE spectra of Zn-doped CIS/MG (Zn:Cu = 0:1, 0.5:1, 1:1, 2:1, 3:1) based photoanodes and integrated photocurrent density.

Stability is one of the main unresolved challenges that hinders the commercialization of PEC devices. In this work, the stability is measured under sunlight at 0.93 V vs. RHE. To clearly compare the photocurrent decay rate, the initial photocurrent density was normalized to its maximum value. The J_{ph} of the MoS_2/CIS QDs device experiences a quick decrease, as shown in Figure 5.18f. After 2 h of illumination, the J_{ph} reaches a value that is just 38% of its initial value. Similarly, the photocurrent density of MoS_2/ZCIS QDs (1:1) maintains 46% of the initial value. The Zn doping might be responsible for the reduction in the amount of charge traps on the surface of the QDs, which led to a minor improvement in the material's stability. On contrary, the photocurrent density of MG/CIS and MG/ZCIS QD remains about 53 and 68% of the initial value, respectively. Previous studies have shown that graphene and other nanocarbon allotropes can be used to improve the performance of several optoelectronic devices.[267] In particular the introduction of graphene can also significantly improve the long-term stability of photovoltaics devices.[268] Overall, the significant stability improvement compared to MoS_2/ZCIS QDs based PEC can be attributed to excellent interfacial interaction, appropriate band alignment and reduced charge recombination. In general, the QDs-based PEC devices are sensitive to photo-oxidation due to surface defects, which act as charge traps. Surface-related traps and defects will form fast non-radiative de-excitation channels for photo-generated charge carriers, thereby reducing overall performance. Therefore, an appropriate amount of dopant can optimize the interface and accelerate electron transfer, reduce photooxidation of QDs and improve overall stability.

Simultaneously, the MoS_2/rGO 2D hybrid can also significantly improve the PEC performances and long-term stability thanks to the improved carrier mobility. Overall the higher performance of MG/ZCIS (1:1) can be attributed to the synergistic effect of: (i) an appropriate band alignment between MG and QDs, accelerating the charge injection from QDs to MG and inhibiting electron-hole recombination; (ii) an optimum thickness of the thin film, offering high loading of QDs while keeping at minimum the charge travel path, reducing charge recombination thanks to the presence of graphene; (iii) ZnS protective layer effectively inhibits photocorrosion of QDs.

To further investigate the mechanisms that underpin the decreased stability of the proposed PEC devices, we acquired XPS spectra from FTO/TiO_2/MG/ZCIS/ZnS photoanode samples before and after long-term PEC measurements. As shown in Figure 5.24, the XPS survey spectrum of the sample before and after measurement presents the same elements: Ti, Mo, S, C, O, Zn, Cu, In, S and Na elements. Especially, the presence of Na is due to the residue of S precursor solution utilized for ZnS SILAR (Na_2S) and/or from the electrolyte (Na_2S or Na_2SO_3). Figure 5.24 b-f displays high resolution spectra of Mo 3d, S 2p, Cu 2p, In 3d and Zn 2p chemical states before and after long-term run tests, respectively. As shown in Figure 5.24b, the binding energy peak of Mo 3d peaks does not present any obvious shift after the long-term stability test. (N.B. The difference in the intensity of the Mo 3d and S2s signal between Figure 5.24 and Figure 5.10 is due to the residue of S precursor of Na_2S and Na_2SO_3 electrolyte in the former case). However, the S 2p presents a 0.4 eV shift towards lower energies (Figure 5.24c), indicating probably a partial oxidation of S^{2-} or residue of S precursor of Na_2SO_3 electrolyte. Similarly, the binding energy of Cu 2p, In 3d and Zn 2p also present an obvious shift by 0.35, 0.15 and 0.33 eV towards lower binding energy after PEC measurement, respectively. These shifts could probably be assigned to the partial oxidation of metal chalcogenide QDs and ZnS shell, providing a possible reason for decreased performance over time (photostability). Therefore, after a long-term stability test, the sample present some decomposition of the metal chalcogenide QDs thus showing hole-induced self-oxidative phenomena that reduce the photocurrent. Therefore, we can speculate that the activity degradation is induced by partial oxidation of metal chalcogenide QDs and ZnS shell while the morphology is retained.

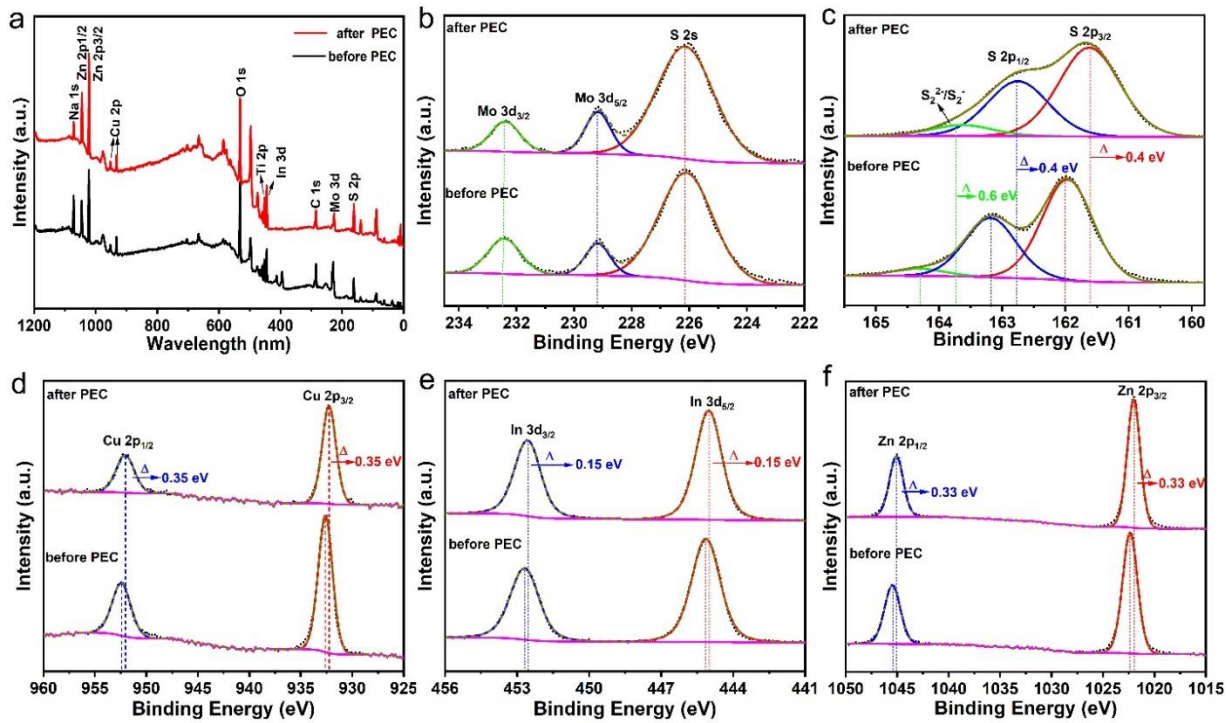

Figure 5.24 High-resolution XPS spectra of FTO/TiO_2/MG-ZCIS/ZnS photo-anode before and after the PEC measurement (Δ represents the peak shift).

The real-time detection of H_2 evolution of the photoanode based on the best sample (MoS_2/rGo/$ZnCuInS_2$) was further measured. A GC system equipped with a thermal conductivity detector is used to detect the generated H_2 gas. A sealed electrochemical cell (total volume: 100 mL) was used for online GC, which was filled with 20 mL of electrolyte. A conventional three-electrode system was used to record the H_2 generation process, consisting of a platinum sheet as the counter electrode, an Ag/AgCl with saturated KCl as a reference electrode, and the FTO/TiO_2/MG/ZCIS/ZnS sensitized photo-anode as working electrode, respectively. Argon gas was used as carrier gas at a flow rate of 20 mL/min, and the electrolyte was constantly stirred. Before the measurements, the electrolyte was degassed with Argon gas for 2 h. The gas outlet was connected to a gas chromatograph (PerkinElmer Clarus 580 GC) for regular sampling, using a thermal conductivity detector (TCD) for H_2 detection. A gas aliquot was automatically injected into the GC every 2.5 min. During online GC, chronoamperometry was performed by applying a 0.93 V *vs.* RHE potential for 1.5 h.

The Faradaic efficiency was calculated as follows:

$$\eta_{Faradaic} = \frac{n_{H_2}(experimental)}{n_{H_2}(theoretical)} \times 100\%$$

The theoretical number of moles of hydrogen was calculated based on the measured photo-current:

$$n_{H_2}(\text{theoretical}) = \frac{1}{z}\frac{Q}{F} = \frac{1}{2}\frac{I \times t}{F} = \frac{1}{2F}\int_0^t Idt$$

In the above formula, *n* represents the number of moles of hydrogen produced, while *z* represents the number of transferred electrons per mole of water (i.e. z=2), Q represents the quantity of charge in coulomb (C) and equals to $I \times t$, F represents the Faraday constant (the quantity of charge in coulomb carried by one mole of electrons, i.e. 96484.34 C/mole), I represents the photocurrent in amperes (A), and t represents time in seconds (s), respectively.

According to GC record after 5400 s, the H_2 gas evolved was 7.41×10^{-6} mol, whereas the current density obtained by chronoamperometry is 0.32 mA/cm^2.

$$n_{H_2}(theoretical) = \frac{0.00032\ (A) \times 5400\ (s)}{2 \times 96485.33\ C \cdot mol^{-1}} = 9.0 \times 10^{-6}\ mol$$

Therefore,

$$\eta_{Faradaic} = \frac{7.41 \times 10^{-6}\ mol}{9.0 \times 10^{-6}\ mol} = 82.3\ \%$$

Figure 5.25 shows the H_2 evolution curve (theoretical and experimental) that increases linearly with time. The theoretical curve is calculated based on the actual photocurrent versus time. The relative Faraday efficiency (η_F) can be determined by comparing the amount of gas generated in the experiment with the theoretical calculation value. For the MoS_2/rGo/Zn-$CuInS_2$ sample based photoanode, the calculated η_F is about 82.3%. The difference between the measured value and the calculated value of H_2 may be caused by a gas leak in our homemade prototype experimental system.

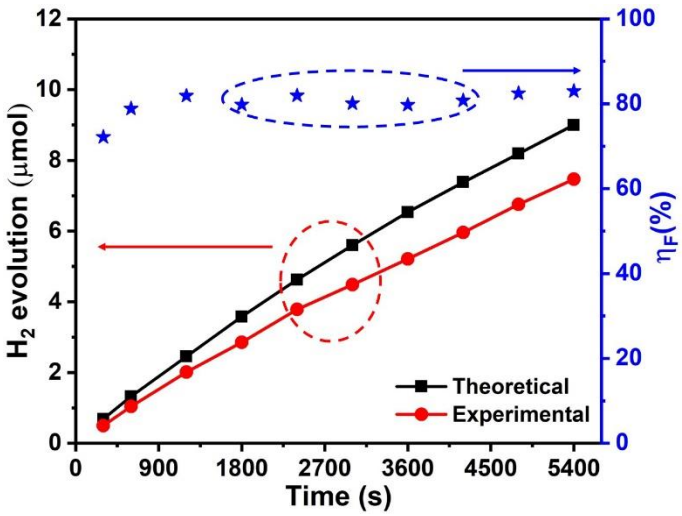

Figure 5.25. H_2 evolution of FTO/TiO_2/MG/ZCIS/ZnS photoanode as a function of time at 0.93 V vs RHE under 100 mW/cm^2 illumination with AM 1.5 G filter. The theoretical amount of H_2 was calculated using the measured photocurrent, whereas the experimental value was determined by GC measurements.

5.4 Mechanism of PEC H_2 generation

To further clarify the influence of the Zn doping and the presence of graphene on the overall PEC performance of the device, we studied the band alignment and charge separation and migration mechanism of the different heterostructures. Figure 5.26 a shows the UV-VIS DRS absorption spectra of the representative MoS_2, MG, ZCIS QDs and ZCIS/MG nanocomposites. The bandgap of MG and ZCIS QDs can be estimated using Tauc's equation, considering them as direct bandgap materials.[269, 270] The corresponding bandgap energies of a monomer of the proposed heterostructure nanocomposites were estimated by the Tauc's equation $(\alpha h\upsilon)^n = A(h\upsilon - E_g)$, where α, h, υ, and E_g referred to absorption coefficient, Planck constant, light frequency, and band gap energy, respectively; $n = 1/2$ for indirect-gap semiconductors and $n = 2$ for direct gap semiconductors. After calculation, the corresponding band-gap energies of the as-synthesized monomer were reported in Table 5.2. The corresponding bandgap energies of as-synthesized MoS_2 and MG are estimated to be 1.97 eV and 1.69 eV, respectively (Figure 5.26b).

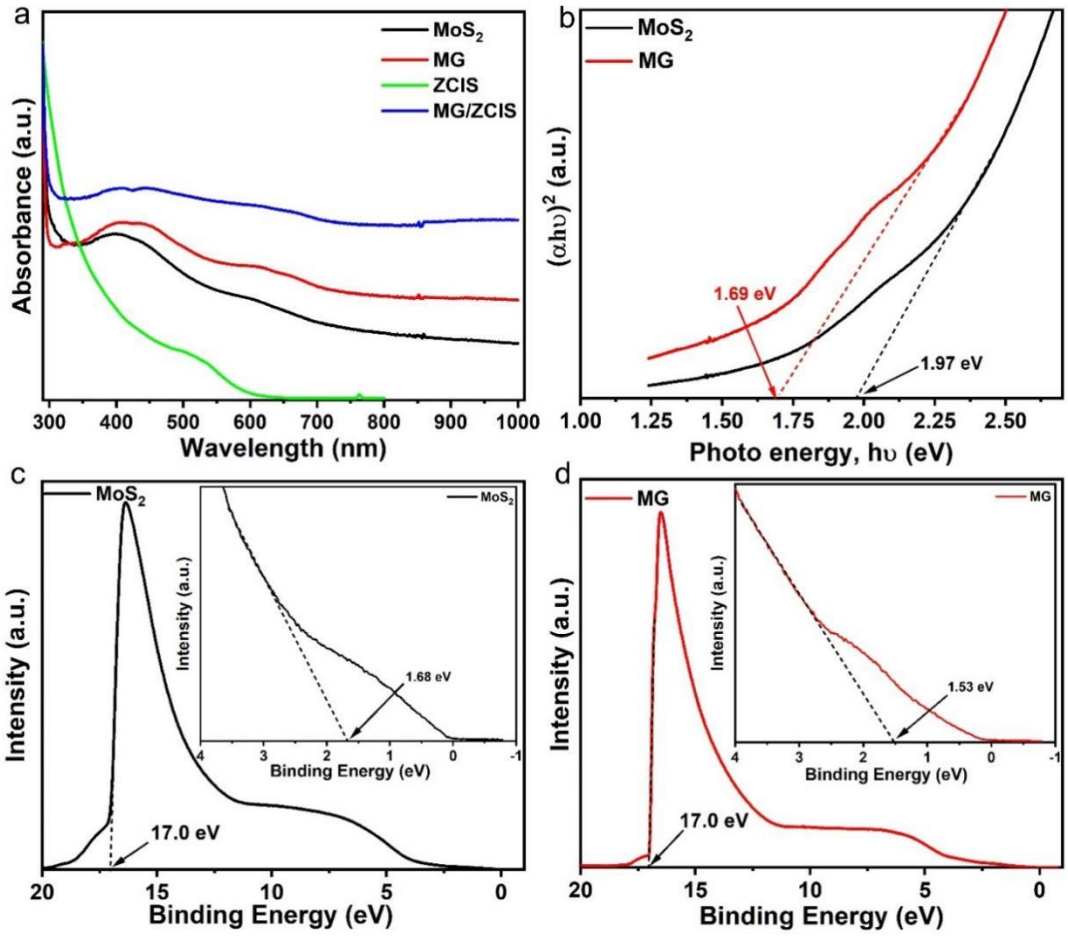

Figure 5.26 (a) UV-vis absorption spectra; (b) Tauc plots of $(\alpha hu)^2$ versus band-gap energy (hv) of MoS_2 and MG. UPS cut off spectra of (c) MoS_2 and (d) MG.

The band gap of Zn doped $CuInS_2$ QDs shifts from 1.55 eV up to 2.54 eV with Zn dopant increments (Figure 5.13). Furthermore, to determine the VBM, UPS measurements using He I radiation (21.22 eV) were carried out (Figure 5.26 and 5.27). The detailed values of the band structures of MoS_2, MG and Z_xC_1IS QDs are reported in Table 5.2. E_{cutoff} is the energy where the secondary photoemission begins; W_F is the work function; VB_{UPS} is the difference value of VBM with the Fermi; E_g represents optical bandgap energy; E_f is the Fermi level (equal to 0). The following equations were used in the band structure calculation according to the UPS data and band gaps:

$$WF = 21.22 - E_{Cutoff} + E_f = 21.22 - E_{Cut\ off} \quad (1)$$

$$VBM = W_F + VB_{UPS} \quad (2)$$

$$CBM = VBM - E_g \quad (3)$$

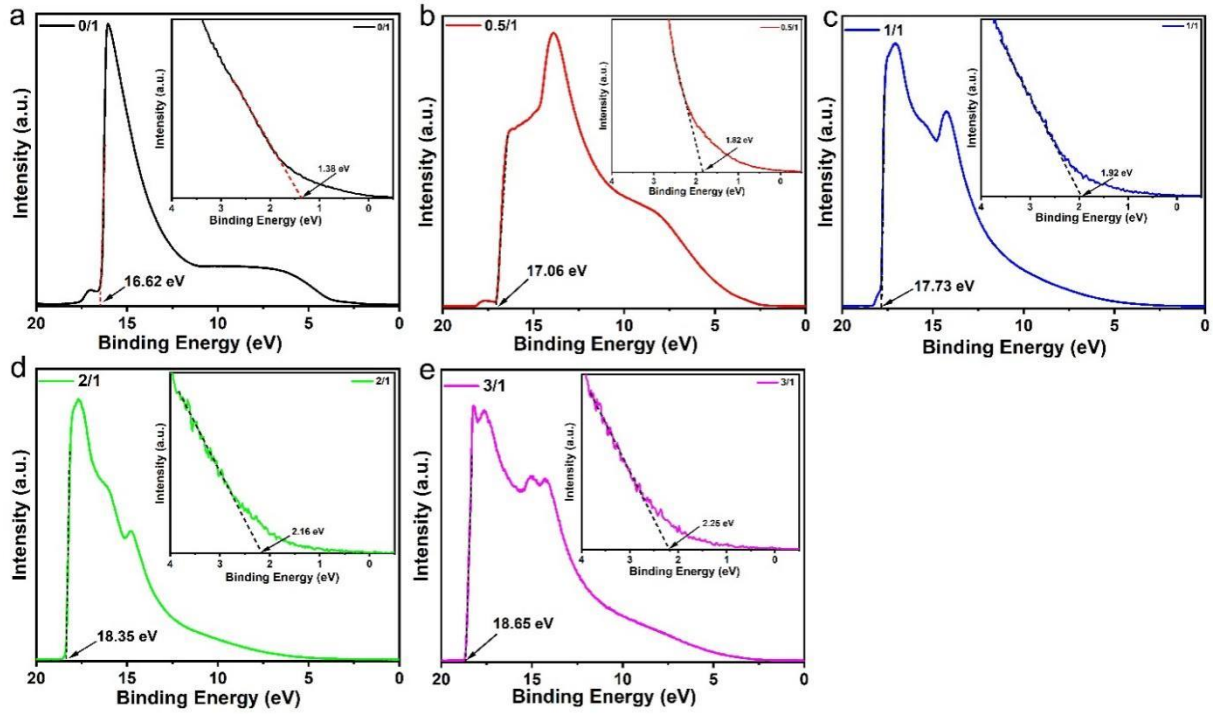

Figure 5.27. UPS cut off spectra of Zn doped $CuInS_2$ QDs based on different Zn/Cu ratio: (a) 0/1, (b) 1/2, (c) 1/1, (d) 2/1 and (e) 3/1, respectively.

Table 5.2 Band energy information (vs. Vacuum) of proposed MoS_2, MG and Z_xC_1IS QDs.

Samples	$E_{Cut\ off}$ (eV)	W_F (eV)	VB_{UPS} (eV)	VBM (eV)	E_g (eV)	CBM (eV)
MoS_2	17.0	4.22	1.68	5.9	1.97	3.93
MG	17.0	4.22	1.53	5.75	1.69	4.06
CIS	16.62	4.6	1.38	5.98	1.55	4.43
$Zn_{0.5}$-$Cu_{1.0}InS_2$	17.06	4.16	1.82	5.98	1.94	4.04
$Zn_{1.0}$-$Cu_{1.0}InS_2$	17.73	3.49	1.92	5.41	2.13	3.28
$Zn_{2.0}$-$Cu_{1.0}InS_2$	18.35	2.87	2.16	5.03	2.43	2.60
$Zn_{3.0}$-$Cu_{1.0}InS_2$	18.65	2.57	2.25	4.82	2.54	2.28

Based on the DRS and UPS data, a possible mechanism for the PEC activity of MG/ZnCuInS$_2$ photoanodes can be proposed (Figure 5.28). The schematic diagram illustrates the band energy structure of the MG/Z$_x$C$_1$IS heterostructure and the charge carriers separation and migration. These properly positioned bands are suitable for the efficient charge separation and migration, confirming the ability of MG/ZnCuInS$_2$ as a friendly photocatalyst for PEC devices.

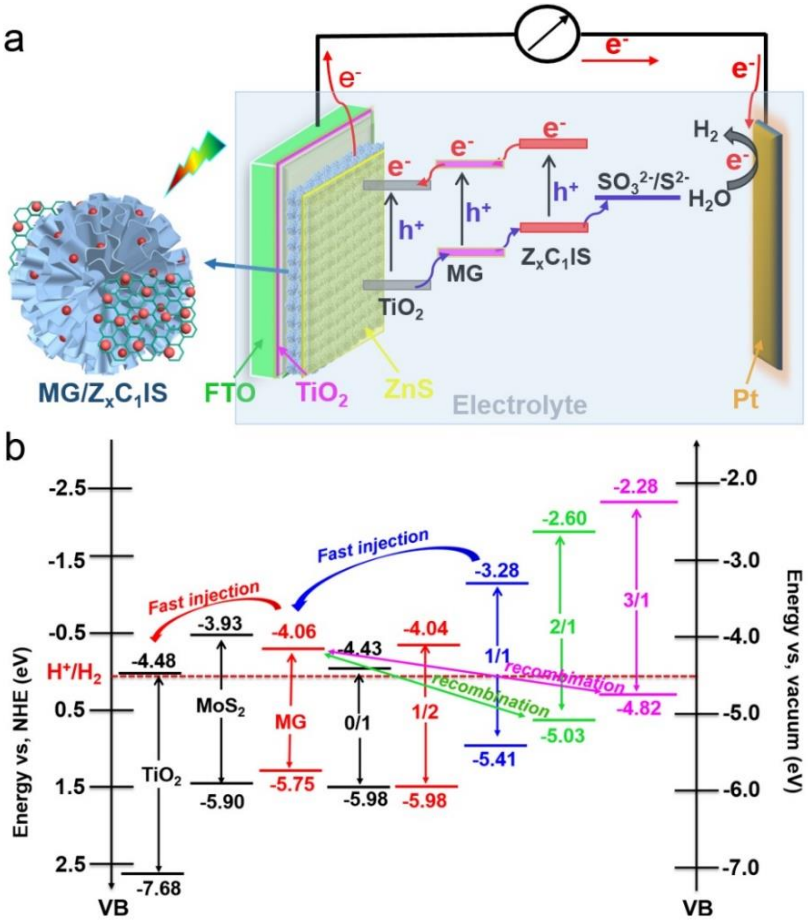

Figure 5.28 (a) Schematic diagrams of formation of anodic photocurrent; (b) Band energy position of MG and different amount of Z$_x$C$_1$IS and the charge transfer mechanism.

Upon light irradiation, the photogenerated electrons are rapidly excited from the VB of ZCIS QDs to CB, leaving the holes behind. Two cases can occur: if the CB of the QDs is more negative than the CB of the MG, no electron transfer can take place, and recombination phenomena come into play. Conversely, if the CB of the QD is more positive than the CB of the MG, electrons in the CB of the QD can be rapidly transferred to the CB of the adjacent MG. In this latter case, the recombination of charge carriers is reduced and the reduction of H_2O to H_2 is promoted. The

introduction of graphene also effectively promotes charge transfer. Afterward, the electrons can be further transferred into the CB of TiO_2 and collected by FTO. The additional TiO_2 blocking layer inhibits the electrons back transfer from FTO to the electrolyte. On the other side, the holes are immediately captured by the hole scavenger. In this process, graphene mainly plays a role as the charge acceptor to inhibit the charge carrier recombination and leads to efficient PEC performances.

As a result of rapid charge carrier recombination, the MoS_2-based photoanode that does not contain rGO presents the poorest performance, as confirmed by EIS (Figure 5.29). After rGO introduction, the charge transfers resistance is significantly reduced. This can be attributed to the improved charge transfer capacity and highlights the role of rGO in enabling charge transfer. Furthermore, we observe that when increasing Zn-doping, the position of the CB of the QDs becomes more positive, moving from -4.43 eV up to -2.28 eV. In particular, for no doping, the CB of the QDs is positioned below the CB of MG, thus poor charge transfer can occur between the two materials. Instead for values of Zn doping from 1:1, 2:1 and 3:1, the CB of the QDs is in favorable position for an efficient charge transfer between QDs and MG. Instead, for the 1:2 ratio of Zn/Cu, we speculate that the smaller driving force can lead to lower PEC performances compared to 1:1 ratio. On the other hand, the photoanodes with 2:1 and 3:1 ratio present lower photocurrent compared to 1:1 ratio sample, because electrons on the CB of MG have higher chance to recombine with the holes in the VB of ZCIS QDs. This result further demonstrates that the construction of Zn-doped $CuInS_2$ QDs can improve the charge separation and transfer efficiency by appropriate controling the dopant concentration.[271, 272] Thus, due to the appropriate band energy level, the high interface charge transfer and separation capabilities inhibit charge carrier recombination, which explains the enhanced photoactivity and improved photocurrent response of the MG/Z_1C_1IS composite.

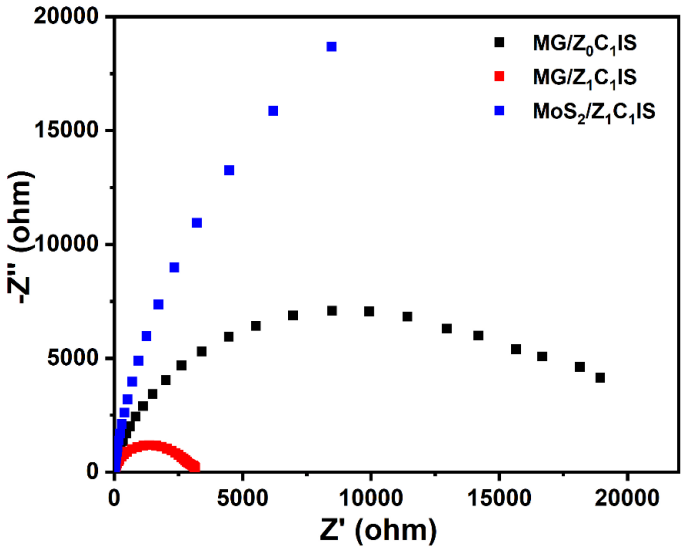

Figure 5.29 Nyquist plots of EIS of photoelectrodes with and without graphene.

5.5 Conclusions and perspectives

In this work, Zn doped $CuInS_2$ 0D QDs are deposited into 2D/2D rGO/MoS_2 hierarchical NSs, forming a 0D/2D/2D heterostructure. Thanks to the optimization of the Zn doping amount and number of deposited layers, the bandgap alignment between ZCIS QDs and 2D/2D substrate can be adjusted to favor charge transfer and reduce recombination phenomena. The results confirm that doping can effectively decrease the surface traps on the surface of QDs. Furthermore, the introduction of rGO to the system improves the electrons transfer and the photo-stability. Therefore, we have shown that an effective approach to optimizing the PEC performance of the MoS_2-based PEC devices is to actively optimize the interface between the nanomaterials and modulation of the band alignment, improving the charge generation, separation and transport. This work suggests that to construct efficient PEC devices, the photoelectrode and its materials should be appropriately engineered. In particular, by appropriate doping of the QDs sensitizer, it is possible to modulate the band alignment between the heterostructure, and by employing a better conductive substrate, the charge separation and transport can be improved. These initial results point to a new way for the development of highly efficient PEC devices based on the 0D/2D/2D heterostructure nanocomposite. In future work, heterojunctions constructed from other types of “green” core-shell or gradient QDs combined with the novel 2D substrate (e.g. tungsten selenide and graphitic carbon nitride) can be used simultaneously explore PEC and the photocatalytic mechanism (e.g. photodegradation).

6 CONCLUSION AND PERSPECTIVES

6.1 Conclusions

The PEC water splitting process directly converts solar energy into chemical energy in the form of H_2 using semiconductor materials. In this thesis, QDs semiconductors are utilized as sensitizer for wide-band semiconductors, such as TiO_2, and for 2D metal chalcogenide materials. By exploiting the size effect, it is possible to broad the light absorption range by regulating the composition or size of QDs. Several devices has been prepared, showing enanched performance when the appropriate combination of QDs and 2D materials was utilized. In particular, based on the presence of the heterojunction, accelerated separation and transport of charge carriers lead to improved PEC performance.

In chapter 3, a 0D/2D heterojunction based on 0D PbS@CdS QDs and 2D Zn-MoS_2 NSs was rationally designed. The 0D PbS@CdS QDs were deposited *in-situ* on Zn-MoS_2 NSs by SILAR method. Due to the synergistic effect of the broad absorption of QDs and superior band alignment between the optimized Zn-MoS_2 and the QDs, the 0D/2D heterojunction presents a remarkable enhancement of PEC performance. In particular, we showed the modulation of the band alignment directly leads to an improved steady-state photocurrent. This work suggests that in order to achieve better PEC performance, it is important to control the complete design of the photoanodes, simultaneously considering both the modulation of the band alignment with the doping and carefully choosing the composition of the QDs. The initial results of the band engineering and the cost-effective preparation of the photoelectrodes shown in this work can pave a new way for the preparation of functional nonoxide photoelectrodes combined with QDs that can be widely used in the PEC field. Further, this approach can be applied to other types of QDs, such as “green” QDs (core-shell and alloyed QDs) and other transition metal chalcogenides, exploring also different optoelectronic applications, such as solar cells and photodetectors.

In chapter 4, NIR, heavy-metal-free, gradient multi-shell colloidal $CuInSe_2/(CuInSe_xS_{1-x})_5/CuInS_2$ QDs were successfully synthesized by a sequential cation exchange approach based on $CdSe/(CdSe_xS_{1-x})_5/CdS$ template. ICP-OES characterization confirmed the full cation exchange of heavy metal composition, indicating that Cd^{2+} was fully replaced by Cu^{+} and In^{3+}. After the cation replacement, the giant QDs with gradient shells exhibit an extended absorption up to the NIR region and a strong red shift of the PL. The QDs were efficiently deposited into the mesoporous TiO_2 film by EPD, showing an intimate connection between the QDs and the TiO_2 nanoparticles. To reduce surface traps of resulting QDs, two layers of inorganic ZnS surface

passivation were added by the SILAR approach. The proposed PEC devices based on $CuInSe_2$@($CuInSe_xS_{1-x}$)$_5$@$CuInS_2$ QDs show a saturated photocurrent density as high as ~ 4.5 mA cm^{-2}, with an improvement of more than 200 % compared to single core QDs and of more than 70 % compared to the core-shell structure. Furthermore, the PEC devices based on the gradient QDs exhibit excellent stability, retaining more than 80 % of their current after 2 h of full illumination. The stability performance of the as-synthesized QDs sensitized photo-anode is comparable to that of heavy-metal QDs-based PEC devices. The superior PEC performances can be ascribed to the graded interfacial layer that optimizes the charge transfer between the QDs and the metal oxide/electrolyte interfaces. This proposed green gradient multi-shell QDs with absorption and PL extended to the NIR region, expand the practical application not only for the PEC system but also could present new opportunities to develop more efficient optoelectronic devices that require NIR absorption capabilities.

In chapter 5, Zn doped $CuInS_2$ 0D QDs are deposited into 2D/2D rGO/MoS_2 hierarchical NSs, forming a 0D/2D/2D heterostructure. Thanks to the optimization of the Zn doping amount and number of deposited layers, the bandgap alignment between ZCIS QDs and 2D/2D substrate can be adjusted to favor charge transfer and reduce recombination phenomena. The results confirm that doping can effectively decrease the surface traps on the surface of QDs. Furthermore, the introduction of rGO to the system improves the electrons transfer rate and photo-stability. Therefore, we have shown that an effective approach to optimizing the PEC performance of MoS_2-based PEC devices is to actively optimize the interface between the nanomaterials and modulation of the band alignment, improving the charge generation, separation and transport. This work suggests that to construct efficient PEC devices, the photoelectrode and its materials should be appropriately engineered. In particular, by appropriate doping of the QDs sensitizer, it is possible to modulate the band alignment between the heterostructure, and by employing a better conductive substrate the charge separation and transport can be improved. These initial results point to a new way for the development of highly efficient PEC devices based on the 0D/2D/2D heterostructure nanocomposite. In future work, heterojunctions constructed from other types of “green” core-shell or gradient QDs combined with a novel 2D substrate (e.g. tungsten selenide and graphitic carbon nitride) can be used to simultaneously explore PEC and the photocatalytic mechanism (e.g. photodegradation).

6.2 Perspectives

In this thesis we have synthesized a series of heterojunctions based on QDs to improve optoelectronic performance, such as doped alloyed QDs, core-shell QDs, gradient layers QDs, and investigated their composition, optical properties and their application in solar-driven PEC H_2 production. Although these devices have shown promising results, there are still several issues that need further optimization and improvement for achieving better PEC performances. The future development of these QDs-based heterojunctions can focus on the following aspects:

(1) In addition to type II heterostructure, Z-scheme photocatalysts hold great promise for solar energy conversion due to their effectiveness in spatially separating photogenerated electron-hole pairs and optimizing the reduction and oxidation capabilities of photocatalytic systems.[273-275] We will design new Z-scheme photocatalysts based on mixed-dimensional semiconductors and investigate their PEC performances.

(2) In general, the 2H-phase of MoS_2 is a typical narrow bandgap semiconductor, which can extend the light absorption range of other wide bandgap semiconductor. The 1T-phase MoS_2 possesses excellent electrical conductivity, ascribe to its metallic properties, which is beneficial to electron transfer. However, the 1T and 2H mixed-phase of MoS_2 are also of great research value. Previous works have confirmed that the mixed phase of MoS_2 can effectively promote charge carrier separation. In future works, we will focus on different phases of MoS_2 in the design process of the MoS_2-based photoanode to optimize its PEC performance.

(3) Other types of 2D NSs, such as the $MoSe_2$, a typical transition metal chalcogenide with graphite-like Se-Mo-Se layers, with higher electrical conductivity as Se brings its intrinsic metallic nature (1×10^{-3} S m^{-1} for Se vs. 5×10^{-28} S m^{-1} for S)[276-278] also used as a 2D substrate to investigate the PEC performances.

(4) Compared with MoS_2 ($MoSe_2$) NSs, MoS_2 ($MoSe_2$) QDs can provide more catalytically active sites, especially its quantum size effect is beneficial to the separation of photogenerated carriers. The quantum confinement effect of MoS_2 ($MoSe_2$) QDs increases the energy band and narrows the absorption range. However, the research of photoanode based on MoS_2 quantum dots is still at the beginning. At present, there are few studies on the preparation of MoS_2 ($MoSe_2$) QDs photoelectrodes, which deserve further research, especially the revealing of the mechanism of MoS_2 ($MoSe_2$) QDs photoanode.

(5) In addition, designing and synthesizing other types of new, heavy metal free core-shell and/or gradient shell QDs (such as Zn-$AgInSe_2$/$AgInS_2$ QDs). By modulating the core size, shell

thickness, morphology, and element ratio of QDs, the optical properties and electronic energy band alignment of QDs are optimized. Ideal carrier spatial separation can be achieved by manipulating the energy band alignment, thereby reducing carrier recombination, which is applied to the generation of H_2 in QDs-based PEC devices. The light absorption, carrier dynamics and charge transfer rate of PEC should investigate in depth by combining theoretical calculations and experiments.

(6) The current commonly used electrolytes are strong alkaline and corrosive electrolytes as hole scavengers (Na_2S and Na_2SO_3 solution). In future work, we will explore how to improve the PEC performances and long-term stability in other type of electrolyte, with and without charge scavenger (i.e. Na_2SO_4 solution).

BIBLIOGRAPHY

1. Poizot, P.; Dolhem, F., Clean energy new deal for a sustainable world: from non-CO_2 generating energy sources to greener electrochemical storage devices. *Energy Environ. Sci.* **2011,** *4* (6), 2003-2019.
2. Shafiee, S.; Topal, E., When will fossil fuel reserves be diminished? *Energy policy* **2009,** *37* (1), 181-189.
3. Roger, I.; Shipman, M. A.; Symes, M. D., Earth-abundant catalysts for electrochemical and photoelectrochemical water splitting. *Nature Reviews Chemistry* **2017,** *1* (1), 1-13.
4. Li, C.; Cao, Q.; Wang, F.; Xiao, Y.; Li, Y.; Delaunay, J.-J.; Zhu, H., Engineering graphene and TMDs based van der Waals heterostructures for photovoltaic and photoelectrochemical solar energy conversion. *Chem. Soc. Rev.* **2018,** *47* (13), 4981-5037.
5. Hisatomi, T.; Kubota, J.; Domen, K., Recent advances in semiconductors for photocatalytic and photoelectrochemical water splitting. *Chem. Soc. Rev.* **2014,** *43* (22), 7520-7535.
6. Yang, W.; Prabhakar, R. R.; Tan, J.; Tilley, S. D.; Moon, J., Strategies for enhancing the photocurrent, photovoltage, and stability of photoelectrodes for photoelectrochemical water splitting. *Chem. Soc. Rev.* **2019,** *48* (19), 4979-5015.
7. Jiang, C.; Moniz, S. J.; Wang, A.; Zhang, T.; Tang, J., Photoelectrochemical devices for solar water splitting–materials and challenges. *Chem. Soc. Rev.* **2017,** *46* (15), 4645-4660.
8. Wang, Z.; Hisatomi, T.; Li, R.; Sayama, K.; Liu, G.; Domen, K.; Li, C.; Wang, L., Efficiency accreditation and testing protocols for particulate photocatalysts toward solar fuel production. *Joule* **2021,** *5* (2), 344-359.
9. Zhao, Y.; Ding, C.; Zhu, J.; Qin, W.; Tao, X.; Fan, F.; Li, R.; Li, C., A hydrogen farm strategy for scalable solar hydrogen production with particulate photocatalysts. *Angew. Chem., Int. Ed.* **2020,** *59* (24), 9653-9658.
10. Cheng, W.-H.; Richter, M. H.; May, M. M.; Ohlmann, J.; Lackner, D.; Dimroth, F.; Hannappel, T.; Atwater, H. A.; Lewerenz, H.-J., Monolithic photoelectrochemical device for direct water splitting with 19% efficiency. *ACS Energy Letters* **2018,** *3* (8), 1795-1800.
11. Kang, D.; Young, J. L.; Lim, H.; Klein, W. E.; Chen, H.; Xi, Y.; Gai, B.; Deutsch, T. G.; Yoon, J., Printed assemblies of GaAs photoelectrodes with decoupled optical and reactive interfaces for unassisted solar water splitting. *Nature Energy* **2017,** *2* (5), 1-5.
12. Song, H.; Luo, S.; Huang, H.; Deng, B.; Ye, J., Solar-Driven Hydrogen Production: Recent Advances, Challenges, and Future Perspectives. *ACS Energy Letters* **2022,** *7* (3), 1043-1065.
13. Jia, J.; Seitz, L. C.; Benck, J. D.; Huo, Y.; Chen, Y.; Ng, J. W. D.; Bilir, T.; Harris, J. S.; Jaramillo, T. F., Solar water splitting by photovoltaic-electrolysis with a solar-to-hydrogen efficiency over 30%. *Nat. Commun.* **2016,** *7* (1), 1-6.
14. Grätzel, M., Photoelectrochemical cells. *Nature* **2001,** *414* (6861), 338.
15. Chen, X.; Zhang, Z.; Chi, L.; Nair, A. K.; Shangguan, W.; Jiang, Z., Recent advances in visible-light-driven photoelectrochemical water splitting: catalyst nanostructures and reaction systems. *Nano-micro letters* **2016,** *8* (1), 1-12.
16. Osterloh, F. E.; Parkinson, B. A., Recent developments in solar water-splitting photocatalysis. *MRS bulletin* **2011,** *36* (1), 17-22.
17. Boddy, P., Oxygen evolution on semiconducting TiO_2. *Journal of The Electrochemical Society* **1968,** *115* (2), 199.
18. Fujishima, A.; Honda, K., Electrochemical photolysis of water at a semiconductor electrode. *Nature* **1972,** *238* (5358), 37-38.

19. Su, T.; Shao, Q.; Qin, Z.; Guo, Z.; Wu, Z., Role of interfaces in two-dimensional photocatalyst for water splitting. *ACS Catalysis* **2018,** *8* (3), 2253-2276.
20. Abe, R., Recent progress on photocatalytic and photoelectrochemical water splitting under visible light irradiation. *Journal of Photochemistry and Photobiology C: Photochemistry Reviews* **2010,** *11* (4), 179-209.
21. Peng, K.; Wang, X.; Lee, S.-T., Silicon nanowire array photoelectrochemical solar cells. *Appl. Phys. Lett.* **2008,** *92* (16), 163103.
22. Kudo, A.; Miseki, Y., Heterogeneous photocatalyst materials for water splitting. *Chem. Soc. Rev.* **2009,** *38* (1), 253-278.
23. Hensel, J.; Wang, G.; Li, Y.; Zhang, J. Z., Synergistic effect of CdSe quantum dot sensitization and nitrogen doping of TiO_2 nanostructures for photoelectrochemical solar hydrogen generation. *Nano Lett.* **2010,** *10* (2), 478-483.
24. Adhikari, R.; Jin, L.; Navarro-Pardo, F.; Benetti, D.; AlOtaibi, B.; Vanka, S.; Zhao, H.; Mi, Z.; Vomiero, A.; Rosei, F., High efficiency, Pt-free photoelectrochemical cells for solar hydrogen generation based on “giant” quantum dots. *Nano Energy* **2016,** *27*, 265-274.
25. Tachibana, Y.; Vayssieres, L.; Durrant, J. R., Artificial photosynthesis for solar water-splitting. *Nat. Photonics* **2012,** *6* (8), 511-518.
26. Jeong, S. Y.; Song, J.; Lee, S., Photoelectrochemical device designs toward practical solar water splitting: A review on the recent progress of bivo4 and bifeo3 photoanodes. *Applied Sciences* **2018,** *8* (8), 1388.
27. Walter, M. G.; Warren, E. L.; McKone, J. R.; Boettcher, S. W.; Mi, Q.; Santori, E. A.; Lewis, N. S., Solar water splitting cells. *Chem. Rev.* **2010,** *110* (11), 6446-6473.
28. Ding, Q.; Song, B.; Xu, P.; Jin, S., Efficient electrocatalytic and photoelectrochemical hydrogen generation using MoS_2 and related compounds. *Chem* **2016,** *1* (5), 699-726.
29. Meng, L.; Rao, D.; Tian, W.; Cao, F.; Yan, X.; Li, L., Simultaneous manipulation of O-doping and metal vacancy in atomically thin $Zn_{10}In_{16}S_{34}$ nanosheet arrays toward improved photoelectrochemical performance. *Angew. Chem., Int. Ed.* **2018,** *57* (51), 16882-16887.
30. Zhang, Y.; Li, Y.; Ni, D.; Chen, Z.; Wang, X.; Bu, Y.; Ao, J. P., Improvement of $BiVO_4$ photoanode performance during water photo-oxidation using Rh-doped $SrTiO_3$ perovskite as a co-catalyst. *Adv. Funct. Mater.* **2019,** *29* (32), 1902101.
31. Li, Y.; Liu, Z.; Guo, Z.; Ruan, M.; Li, X.; Liu, Y., Efficient WO_3 photoanode modified by Pt layer and plasmonic Ag for enhanced charge separation and transfer to promote photoelectrochemical performances. *ACS Sustainable Chemistry & Engineering* **2019,** *7* (14), 12582-12590.
32. Li, F.; Xu, R.; Nie, C.; Wu, X.; Zhang, P.; Duan, L.; Sun, L., Dye-sensitized $LaFeO_3$ photocathode for solar-driven H_2 generation. *Chemical Communications* **2019,** *55* (86), 12940-12943.
33. Li, S.; Xu, W.; Meng, L.; Tian, W.; Li, L., Recent Progress on Semiconductor Heterojunction-Based Photoanodes for Photoelectrochemical Water Splitting. *Small Science* **2022**, 2100112.
34. Lin, H.; Long, X.; An, Y.; Zhou, D.; Yang, S., Three-dimensional decoupling co-catalyst from a photoabsorbing semiconductor as a new strategy to boost photoelectrochemical water splitting. *Nano Lett.* **2018,** *19* (1), 455-460.
35. Yang, J.; Wang, D.; Han, H.; Li, C., Roles of cocatalysts in photocatalysis and photoelectrocatalysis. *Accounts Chem. Res.* **2013,** *46* (8), 1900-1909.
36. Wang, H.; Zhang, L.; Chen, Z.; Hu, J.; Li, S.; Wang, Z.; Liu, J.; Wang, X., Semiconductor heterojunction photocatalysts: design, construction, and photocatalytic performances. *Chem. Soc. Rev.* **2014,** *43* (15), 5234-5244.
37. Verlage, E.; Hu, S.; Liu, R.; Jones, R. J.; Sun, K.; Xiang, C.; Lewis, N. S.; Atwater, H. A., A monolithically integrated, intrinsically safe, 10% efficient, solar-driven water-splitting system

based on active, stable earth-abundant electrocatalysts in conjunction with tandem III–V light absorbers protected by amorphous TiO_2 films. *Energy Environ. Sci.* **2015,** *8* (11), 3166-3172.
38. Hong, G.; Diao, S.; Antaris, A. L.; Dai, H., Carbon nanomaterials for biological imaging and nanomedicinal therapy. *Chem. Rev.* **2015,** *115* (19), 10816-10906.
39. Zhu, C.; Yang, G.; Li, H.; Du, D.; Lin, Y., Electrochemical sensors and biosensors based on nanomaterials and nanostructures. *Analytical chemistry* **2015,** *87* (1), 230-249.
40. Guo, S.; Wang, E., Noble metal nanomaterials: controllable synthesis and application in fuel cells and analytical sensors. *Nano today* **2011,** *6* (3), 240-264.
41. Li, W.-Y.; Xu, L.-N.; Chen, J., Co_3O_4 nanomaterials in lithium-ion batteries and gas sensors. *Adv. Funct. Mater.* **2005,** *15* (5), 851-857.
42. Meinardi, F.; McDaniel, H.; Carulli, F.; Colombo, A.; Velizhanin, K. A.; Makarov, N. S.; Simonutti, R.; Klimov, V. I.; Brovelli, S., Highly efficient large-area colourless luminescent solar concentrators using heavy-metal-free colloidal quantum dots. *Nat. Nanotechnol.* **2015,** *10* (10), 878-885.
43. Kim, S. Y.; Cho, S. J.; Byeon, S. E.; He, X.; Yoon, H. J., Self-Assembled Monolayers as Interface Engineering Nanomaterials in Perovskite Solar Cells. *Adv. Energy Mater.* **2020,** *10* (44), 2002606.
44. Mino, L.; Agostini, G.; Borfecchia, E.; Gianolio, D.; Piovano, A.; Gallo, E.; Lamberti, C., Low-dimensional systems investigated by x-ray absorption spectroscopy: a selection of 2D, 1D and 0D cases. *Journal of Physics D: Applied Physics* **2013,** *46* (42), 423001.
45. Rossetti, R.; Ellison, J.; Gibson, J.; Brus, L. E., Size effects in the excited electronic states of small colloidal CdS crystallites. *The Journal of chemical physics* **1984,** *80* (9), 4464-4469.
46. Ding, J.-R.; Kim, K.-S., 1-D WO_3@ $BiVO_4$ heterojunctions with highly enhanced photoelectrochemical performance. *Chem. Eng. J.* **2018,** *334*, 1650-1656.
47. Zhao, Y.; Hoivik, N.; Wang, K., Recent advance on engineering titanium dioxide nanotubes for photochemical and photoelectrochemical water splitting. *Nano Energy* **2016,** *30*, 728-744.
48. Liu, X. Y.; Chen, H.; Wang, R.; Shang, Y.; Zhang, Q.; Li, W.; Zhang, G.; Su, J.; Dinh, C. T.; de Arquer, F. P. G., 0D–2D quantum dot: metal dichalcogenide nanocomposite photocatalyst achieves efficient hydrogen generation. *Adv. Mater.* **2017,** *29* (22), 1605646.
49. Shi, L.; Yin, Y.; Zhang, L.-C.; Wang, S.; Sillanpää, M.; Sun, H., Design and engineering heterojunctions for the photoelectrochemical monitoring of environmental pollutants: a review. *Applied Catalysis B: Environmental* **2019,** *248*, 405-422.
50. Kroemer, H., Nobel Lecture: Quasielectric fields and band offsets: teaching electrons new tricks. *Reviews of modern physics* **2001,** *73* (3), 783.
51. Mannhart, J.; Schlom, D. G., Oxide interfaces—an opportunity for electronics. *Science* **2010,** *327* (5973), 1607-1611.
52. Zheng, H.; Li, Y.; Liu, H.; Yin, X.; Li, Y., Construction of heterostructure materials toward functionality. *Chem. Soc. Rev.* **2011,** *40* (9), 4506-4524.
53. Chi, Z.; Zhao, J.; Zhang, Y.; Yu, H.; Yu, H., The fabrication of atomically thin-MoS_2 based photoanodes for photoelectrochemical energy conversion and environment remediation: A review. *Green Energy & Environment* **2021**.
54. Zheng, Z.; Zu, X.; Zhang, Y.; Zhou, W., Rational design of type-II nano-heterojunctions for nanoscale optoelectronics. *Materials Today Physics* **2020,** *15*, 100262.
55. Kumar, S.; Kumar, A.; Kumar, A.; Krishnan, V., Nanoscale zinc oxide based heterojunctions as visible light active photocatalysts for hydrogen energy and environmental remediation. *Catalysis Reviews* **2020,** *62* (3), 346-405.
56. Wang, Q.; Wang, X.; Yu, Z.; Jiang, X.; Chen, J.; Tao, L.; Wang, M.; Shen, Y., Artificial photosynthesis of ethanol using type-II g-C_3N_4/ZnTe heterojunction in photoelectrochemical CO_2 reduction system. *Nano Energy* **2019,** *60*, 827-835.

57. Wang, Y.; Wang, Q.; Zhan, X.; Wang, F.; Safdar, M.; He, J., Visible light driven type II heterostructures and their enhanced photocatalysis properties: a review. *Nanoscale* **2013,** *5* (18), 8326-8339.
58. Ou, Q.; Bao, X.; Zhang, Y.; Shao, H.; Xing, G.; Li, X.; Shao, L.; Bao, Q., Band structure engineering in metal halide perovskite nanostructures for optoelectronic applications. *Nano Materials Science* **2019,** *1* (4), 268-287.
59. Du, J.; Du, Z.; Hu, J.-S.; Pan, Z.; Shen, Q.; Sun, J.; Long, D.; Dong, H.; Sun, L.; Zhong, X., Zn–Cu–In–Se quantum dot solar cells with a certified power conversion efficiency of 11.6%. *J. Am. Chem. Soc.* **2016,** *138* (12), 4201-4209.
60. Jariwala, D.; Marks, T. J.; Hersam, M. C., Mixed-dimensional van der Waals heterostructures. *Nat. Mater.* **2017,** *16* (2), 170-181.
61. Padgaonkar, S.; Olding, J. N.; Lauhon, L. J.; Hersam, M. C.; Weiss, E. A., Emergent optoelectronic properties of mixed-dimensional heterojunctions. *Accounts Chem. Res.* **2020,** *53* (4), 763-772.
62. Carey, G. H.; Abdelhady, A. L.; Ning, Z.; Thon, S. M.; Bakr, O. M.; Sargent, E. H., Colloidal quantum dot solar cells. *Chem. Rev.* **2015,** *115* (23), 12732-12763.
63. Kramer, I. J.; Sargent, E. H., The architecture of colloidal quantum dot solar cells: materials to devices. *Chem. Rev.* **2014,** *114* (1), 863-882.
64. Selinsky, R. S.; Ding, Q.; Faber, M. S.; Wright, J. C.; Jin, S., Quantum dot nanoscale heterostructures for solar energy conversion. *Chem. Soc. Rev.* **2013,** *42* (7), 2963-2985.
65. Yamashita, S. i.; Hamada, M.; Nakanishi, S.; Saito, H.; Nosaka, Y.; Wakida, S. i.; Biju, V., Auger Ionization Beats Photo-Oxidation of Semiconductor Quantum Dots: Extended Stability of Single-Molecule Photoluminescence. *Angew. Chem., Int. Ed.* **2015,** *54* (13), 3892-3896.
66. Guo, C. X.; Yang, H. B.; Sheng, Z. M.; Lu, Z. S.; Song, Q. L.; Li, C. M., Layered graphene/quantum dots for photovoltaic devices. *Angew. Chem., Int. Ed.* **2010,** *49* (17), 3014-3017.
67. Kufer, D.; Nikitskiy, I.; Lasanta, T.; Navickaite, G.; Koppens, F. H.; Konstantatos, G., Hybrid 2D–0D MoS_2–PbS quantum dot photodetectors. *Adv. Mater.* **2015,** *27* (1), 176-180.
68. Li, Q.; Guo, B.; Yu, J.; Ran, J.; Zhang, B.; Yan, H.; Gong, J. R., Highly efficient visible-light-driven photocatalytic hydrogen production of CdS-cluster-decorated graphene nanosheets. *J. Am. Chem. Soc.* **2011,** *133* (28), 10878-10884.
69. Ye, M. Y.; Zhao, Z. H.; Hu, Z. F.; Liu, L. Q.; Ji, H. M.; Shen, Z. R.; Ma, T. Y., 0D/2D heterojunctions of vanadate quantum dots/graphitic carbon nitride nanosheets for enhanced visible-light-driven photocatalysis. *Angew. Chem., Int. Ed.* **2017,** *56* (29), 8407-8411.
70. Boulesbaa, A.; Wang, K.; Mahjouri-Samani, M.; Tian, M.; Puretzky, A. A.; Ivanov, I.; Rouleau, C. M.; Xiao, K.; Sumpter, B. G.; Geohegan, D. B., Ultrafast charge transfer and hybrid exciton formation in 2D/0D heterostructures. *J. Am. Chem. Soc.* **2016,** *138* (44), 14713-14719.
71. Hou, Y.; Wen, Z.; Cui, S.; Guo, X.; Chen, J., Constructing 2D porous graphitic C_3N_4 nanosheets/nitrogen-doped graphene/layered MoS_2 ternary nanojunction with enhanced photoelectrochemical activity. *Adv. Mater.* **2013,** *25* (43), 6291-6297.
72. Yue, S.; Li, L.; McGuire, S. C.; Hurley, N.; Wong, S. S., Metal chalcogenide quantum dot-sensitized 1D-based semiconducting heterostructures for optical-related applications. *Energy Environ. Sci.* **2019,** *12* (5), 1454-1494.
73. Tang, J.; Sargent, E. H., Infrared colloidal quantum dots for photovoltaics: fundamentals and recent progress. *Adv. Mater.* **2011,** *23* (1), 12-29.
74. Tang, J.; Kemp, K. W.; Hoogland, S.; Jeong, K. S.; Liu, H.; Levina, L.; Furukawa, M.; Wang, X.; Debnath, R.; Cha, D., Colloidal-quantum-dot photovoltaics using atomic-ligand passivation. *Nat. Mater.* **2011,** *10* (10), 765-771.
75. Kovalenko, M. V., Opportunities and challenges for quantum dot photovoltaics. *Nat. Nanotechnol.* **2015,** *10* (12), 994-997.

76. Sun, Q.; Wang, Y. A.; Li, L. S.; Wang, D.; Zhu, T.; Xu, J.; Yang, C.; Li, Y., Bright, multicoloured light-emitting diodes based on quantum dots. *Nat. Photonics* **2007,** *1* (12), 717-722.
77. Dai, X.; Zhang, Z.; Jin, Y.; Niu, Y.; Cao, H.; Liang, X.; Chen, L.; Wang, J.; Peng, X., Solution-processed, high-performance light-emitting diodes based on quantum dots. *Nature* **2014,** *515* (7525), 96-99.
78. Shirasaki, Y.; Supran, G. J.; Bawendi, M. G.; Bulović, V., Emergence of colloidal quantum-dot light-emitting technologies. *Nat. Photonics* **2013,** *7* (1), 13-23.
79. Shu, J.; Tang, D., Current advances in quantum-dots-based photoelectrochemical immunoassays. *Chemistry–An Asian Journal* **2017,** *12* (21), 2780-2789.
80. Yue, Z.; Lisdat, F.; Parak, W. J.; Hickey, S. G.; Tu, L.; Sabir, N.; Dorfs, D.; Bigall, N. C., Quantum-dot-based photoelectrochemical sensors for chemical and biological detection. *ACS applied materials & interfaces* **2013,** *5* (8), 2800-2814.
81. Alivisatos, A. P., Semiconductor clusters, nanocrystals, and quantum dots. *Science* **1996,** *271* (5251), 933-937.
82. Moreels, I.; Lambert, K.; Smeets, D.; De Muynck, D.; Nollet, T.; Martins, J. C.; Vanhaecke, F.; Vantomme, A.; Delerue, C.; Allan, G., Size-dependent optical properties of colloidal PbS quantum dots. *ACS Nano* **2009,** *3* (10), 3023-3030.
83. Zhao, H.; Rosei, F., Colloidal quantum dots for solar technologies. *Chem* **2017,** *3* (2), 229-258.
84. Murray, C.; Norris, D. J.; Bawendi, M. G., Synthesis and characterization of nearly monodisperse CdE (E= sulfur, selenium, tellurium) semiconductor nanocrystallites. *J. Am. Chem. Soc.* **1993,** *115* (19), 8706-8715.
85. Brus, L. E., Electron–electron and electron-hole interactions in small semiconductor crystallites: The size dependence of the lowest excited electronic state. *The Journal of chemical physics* **1984,** *80* (9), 4403-4409.
86. Rogach, A.; Katsikas, L.; Kornowski, A.; Su, D.; Eychmüller, A.; Weller, H., Synthesis and characterization of thiol-stabilized CdTe nanocrystals. *Berichte der Bunsengesellschaft für physikalische Chemie* **1996,** *100* (11), 1772-1778.
87. Michalet, X.; Pinaud, F.; Bentolila, L.; Tsay, J.; Doose, S.; Li, J.; Sundaresan, G.; Wu, A.; Gambhir, S.; Weiss, S., Quantum dots for live cells, in vivo imaging, and diagnostics. *science* **2005,** *307* (5709), 538-544.
88. Rühle, S.; Shalom, M.; Zaban, A., Quantum-dot-sensitized solar cells. *Chemphyschem : a European journal of chemical physics and physical chemistry* **2010,** *11* (11), 2290-2304.
89. Chen, H. M.; Chen, C. K.; Chang, Y. C.; Tsai, C. W.; Liu, R. S.; Hu, S. F.; Chang, W. S.; Chen, K. H., Quantum Dot Monolayer Sensitized ZnO Nanowire-Array Photoelectrodes: True Efficiency for Water Splitting. *Angewandte Chemie* **2010,** *122* (34), 6102-6105.
90. Wang, G.; Yang, X.; Qian, F.; Zhang, J. Z.; Li, Y., Double-sided CdS and CdSe quantum dot co-sensitized ZnO nanowire arrays for photoelectrochemical hydrogen generation. *Nano Lett.* **2010,** *10* (3), 1088-1092.
91. Smith, A. M.; Nie, S., Semiconductor nanocrystals: structure, properties, and band gap engineering. *Accounts of chemical research* **2010,** *43* (2), 190.
92. de Mello Donegá, C., Synthesis and properties of colloidal heteronanocrystals. *Chem. Soc. Rev.* **2011,** *40* (3), 1512-1546.
93. Reiss, P.; Protiere, M.; Li, L., Core/shell semiconductor nanocrystals. *Small* **2009,** *5* (2), 154-168.
94. Ghosh Chaudhuri, R.; Paria, S., Core/shell nanoparticles: classes, properties, synthesis mechanisms, characterization, and applications. *Chem. Rev.* **2012,** *112* (4), 2373-2433.
95. Kim, S.; Fisher, B.; Eisler, H.-J.; Bawendi, M., Type-II quantum dots: CdTe/CdSe (core/shell) and CdSe/ZnTe (core/shell) heterostructures. *J. Am. Chem. Soc.* **2003,** *125* (38), 11466-11467.

96. Chen, Y.; Vela, J.; Htoon, H.; Casson, J. L.; Werder, D. J.; Bussian, D. A.; Klimov, V. I.; Hollingsworth, J. A., "Giant" multishell CdSe nanocrystal quantum dots with suppressed blinking. *J. Am. Chem. Soc.* **2008,** *130* (15), 5026-5027.
97. Lim, J.; Jeong, B. G.; Park, M.; Kim, J. K.; Pietryga, J. M.; Park, Y. S.; Klimov, V. I.; Lee, C.; Lee, D. C.; Bae, W. K., Influence of Shell Thickness on the Performance of Light-Emitting Devices Based on CdSe/$Zn_{1-X}Cd_XS$ Core/Shell Heterostructured Quantum Dots. *Adv. Mater.* **2014,** *26* (47), 8034-8040.
98. Jin, L.; Zhao, H.; Wang, Z. M.; Rosei, F., Quantum dots-based photoelectrochemical hydrogen evolution from water splitting. *Adv. Energy Mater.* **2021,** *11* (12), 2003233.
99. De Geyter, B.; Justo, Y.; Moreels, I.; Lambert, K.; Smet, P. F.; Van Thourhout, D.; Houtepen, A. J.; Grodzinska, D.; de Mello Donega, C.; Meijerink, A., The different nature of band edge absorption and emission in colloidal PbSe/CdSe core/shell quantum dots. *ACS nano* **2011,** *5* (1), 58-66.
100. Huang, J.; Mulfort, K. L.; Du, P.; Chen, L. X., Photodriven charge separation dynamics in CdSe/ZnS core/shell quantum dot/cobaloxime hybrid for efficient hydrogen production. *J. Am. Chem. Soc.* **2012,** *134* (40), 16472-16475.
101. Zhang, H.; Besteiro, L. V.; Liu, J.; Wang, C.; Selopal, G. S.; Chen, Z.; Barba, D.; Wang, Z. M.; Zhao, H.; Lopinski, G. P., Efficient and stable photoelectrochemical hydrogen generation using optimized colloidal heterostructured quantum dots. *Nano Energy* **2021,** *79*, 105416.
102. Balet, L.; Ivanov, S.; Piryatinski, A.; Achermann, M.; Klimov, V., Inverted core/shell nanocrystals continuously tunable between type-I and type-II localization regimes. *Nano Lett.* **2004,** *4* (8), 1485-1488.
103. Swafford, L. A.; Weigand, L. A.; Bowers, M. J.; McBride, J. R.; Rapaport, J. L.; Watt, T. L.; Dixit, S. K.; Feldman, L. C.; Rosenthal, S. J., Homogeneously alloyed CdS_xSe_{1-x} nanocrystals: synthesis, characterization, and composition/size-dependent band gap. *J. Am. Chem. Soc.* **2006,** *128* (37), 12299-12306.
104. Pan, Z.; Zhang, H.; Cheng, K.; Hou, Y.; Hua, J.; Zhong, X., Highly efficient inverted type-I CdS/CdSe core/shell structure QD-sensitized solar cells. *ACS Nano* **2012,** *6* (5), 3982-3991.
105. Zhu, H.; Song, N.; Lian, T., Wave function engineering for ultrafast charge separation and slow charge recombination in type II core/shell quantum dots. *J. Am. Chem. Soc.* **2011,** *133* (22), 8762-8771.
106. Zhu, H.; Song, N.; Rodríguez-Córdoba, W.; Lian, T., Wave function engineering for efficient extraction of up to nineteen electrons from one CdSe/CdS quasi-type II quantum dot. *J. Am. Chem. Soc.* **2012,** *134* (9), 4250-4257.
107. García-Santamaría, F.; Chen, Y.; Vela, J.; Schaller, R. D.; Hollingsworth, J. A.; Klimov, V. I., Suppressed auger recombination in "giant" nanocrystals boosts optical gain performance. *Nano Lett.* **2009,** *9* (10), 3482-3488.
108. Selopal, G. S.; Zhao, H.; Liu, G.; Zhang, H.; Tong, X.; Wang, K.; Tang, J.; Sun, X.; Sun, S.; Vidal, F., Interfacial engineering in colloidal "giant" quantum dots for high-performance photovoltaics. *Nano Energy* **2019,** *55*, 377-388.
109. Blackman, B.; Battaglia, D. M.; Mishima, T. D.; Johnson, M. B.; Peng, X., Control of the morphology of complex semiconductor nanocrystals with a type II heterojunction, dots vs peanuts, by thermal cycling. *Chem. Mater.* **2007,** *19* (15), 3815-3821.
110. Sitt, A.; Sala, F. D.; Menagen, G.; Banin, U., Multiexciton engineering in seeded core/shell nanorods: transfer from type-I to quasi-type-II regimes. *Nano Lett.* **2009,** *9* (10), 3470-3476.
111. Zhang, J.; Tang, Y.; Lee, K.; Ouyang, M., Nonepitaxial growth of hybrid core-shell nanostructures with large lattice mismatches. *Science* **2010,** *327* (5973), 1634-1638.
112. Smith, A. M.; Mohs, A. M.; Nie, S., Tuning the optical and electronic properties of colloidal nanocrystals by lattice strain. *Nat. Nanotechnol.* **2009,** *4* (1), 56-63.

113. Jiao, S.; Wang, J.; Shen, Q.; Li, Y.; Zhong, X., Surface engineering of PbS quantum dot sensitized solar cells with a conversion efficiency exceeding 7%. *Journal of Materials Chemistry A* **2016,** *4* (19), 7214-7221.
114. Park, Y.-S.; Lim, J.; Makarov, N. S.; Klimov, V. I., Effect of interfacial alloying versus "volume scaling" on Auger recombination in compositionally graded semiconductor quantum dots. *Nano Lett.* **2017,** *17* (9), 5607-5613.
115. Ma, W.; Luther, J. M.; Zheng, H.; Wu, Y.; Alivisatos, A. P., Photovoltaic devices employing ternary PbS_xSe_{1-x} nanocrystals. *Nano Lett.* **2009,** *9* (4), 1699-1703.
116. Beaulac, R.; Archer, P. I.; Ochsenbein, S. T.; Gamelin, D. R., Mn^{2+}-doped CdSe quantum dots: new inorganic materials for spin-electronics and spin-photonics. *Adv. Funct. Mater.* **2008,** *18* (24), 3873-3891.
117. Luo, B.; Liu, J.; Guo, H.; Liu, X.; Song, R.; Shen, K.; Wang, Z. M.; Jing, D.; Selopal, G. S.; Rosei, F., High efficiency photoelectrochemical hydrogen generation using eco-friendly Cu doped Zn-In-Se colloidal quantum dots. *Nano Energy* **2021,** *88*, 106220.
118. Santra, P. K.; Kamat, P. V., Mn-doped quantum dot sensitized solar cells: a strategy to boost efficiency over 5%. *J. Am. Chem. Soc.* **2012,** *134* (5), 2508-2511.
119. Guria, A. K.; Dutta, S. K.; Adhikari, S. D.; Pradhan, N., Doping Mn2+ in lead halide perovskite nanocrystals: successes and challenges. *ACS Energy Letters* **2017,** *2* (5), 1014-1021.
120. Bang, J.; Das, S.; Yu, E.-J.; Kim, K.; Lim, H.; Kim, S.; Hong, J. W., Controlled photoinduced electron transfer from InP/ZnS quantum dots through Cu doping: a new prototype for the visible-light photocatalytic hydrogen evolution reaction. *Nano Lett.* **2020,** *20* (9), 6263-6271.
121. Zhang, J.; Xie, R.; Yang, W., A simple route for highly luminescent quaternary Cu-Zn-In-S nanocrystal emitters. *Chem. Mater.* **2011,** *23* (14), 3357-3361.
122. Erickson, C. S.; Bradshaw, L. R.; McDowall, S.; Gilbertson, J. D.; Gamelin, D. R.; Patrick, D. L., Zero-reabsorption doped-nanocrystal luminescent solar concentrators. *ACS Nano* **2014,** *8* (4), 3461-3467.
123. Sarkar, S.; Karan, N. S.; Pradhan, N., Ultrasmall Color-Tunable Copper-Doped Ternary Semiconductor Nanocrystal Emitters. *Angewandte Chemie* **2011,** *123* (27), 6189-6193.
124. Tan, L.; Liu, Y.; Mao, B.; Luo, B.; Gong, G.; Hong, Y.; Chen, B.; Shi, W., Effective bandgap narrowing of Cu–In–Zn–S quantum dots for photocatalytic H_2 production via cocatalyst-alleviated charge recombination. *Inorganic Chemistry Frontiers* **2018,** *5* (1), 258-265.
125. Yue, L.; Rao, H.; Du, J.; Pan, Z.; Yu, J.; Zhong, X., Comparative advantages of Zn–Cu–In–S alloy QDs in the construction of quantum dot-sensitized solar cells. *RSC advances* **2018,** *8* (7), 3637-3645.
126. Jose Varghese, R.; Oluwafemi, O. S., The photoluminescence and biocompatibility of $CuInS_2$-based ternary quantum dots and their biological applications. *Chemosensors* **2020,** *8* (4), 101.
127. Kim, J.-Y.; Jang, Y. J.; Park, J.; Kim, J.; Kang, J. S.; Chung, D. Y.; Sung, Y.-E.; Lee, C.; Lee, J. S.; Ko, M. J., Highly loaded PbS/Mn-doped CdS quantum dots for dual application in solar-to-electrical and solar-to-chemical energy conversion. *Applied Catalysis B: Environmental* **2018,** *227*, 409-417.
128. Hodes, G., Semiconductor and ceramic nanoparticle films deposited by chemical bath deposition. *Physical Chemistry Chemical Physics* **2007,** *9* (18), 2181-2196.
129. Roy, P.; Ota, J. R.; Srivastava, S. K., Crystalline ZnS thin films by chemical bath deposition method and its characterization. *Thin Solid Films* **2006,** *515* (4), 1912-1917.
130. Hachiya, S.; Shen, Q.; Toyoda, T., Effect of ZnS coatings on the enhancement of the photovoltaic properties of PbS quantum dot-sensitized solar cells. *J. Appl. Phys.* **2012,** *111* (10), 104315.
131. Nicolau, Y., Solution deposition of thin solid compound films by a successive ionic-layer adsorption and reaction process. *Applications of Surface Science* **1985,** *22*, 1061-1074.

132. Ghosh, Y.; Mangum, B. D.; Casson, J. L.; Williams, D. J.; Htoon, H.; Hollingsworth, J. A., New insights into the complexities of shell growth and the strong influence of particle volume in nonblinking “giant” core/shell nanocrystal quantum dots. *J. Am. Chem. Soc.* **2012,** *134* (23), 9634-9643.
133. Zhao, H.; Fan, Z.; Liang, H.; Selopal, G.; Gonfa, B.; Jin, L.; Soudi, A.; Cui, D.; Enrichi, F.; Natile, M., Controlling photoinduced electron transfer from PbS@ CdS core@ shell quantum dots to metal oxide nanostructured thin films. *Nanoscale* **2014,** *6* (12), 7004-7011.
134. Yin, Y.; Alivisatos, A. P., Colloidal nanocrystal synthesis and the organic–inorganic interface. *Nature* **2005,** *437* (7059), 664-670.
135. Hines, M. A.; Scholes, G. D., Colloidal PbS nanocrystals with size-tunable near-infrared emission: observation of post-synthesis self-narrowing of the particle size distribution. *Adv. Mater.* **2003,** *15* (21), 1844-1849.
136. Son, D. H.; Hughes, S. M.; Yin, Y.; Paul Alivisatos, A., Cation exchange reactions in ionic nanocrystals. *Science* **2004,** *306* (5698), 1009-1012.
137. De Trizio, L.; Manna, L., Forging colloidal nanostructures via cation exchange reactions. *Chem. Rev.* **2016,** *116* (18), 10852-10887.
138. Sadtler, B.; Demchenko, D. O.; Zheng, H.; Hughes, S. M.; Merkle, M. G.; Dahmen, U.; Wang, L.-W.; Alivisatos, A. P., Selective facet reactivity during cation exchange in cadmium sulfide nanorods. *J. Am. Chem. Soc.* **2009,** *131* (14), 5285-5293.
139. Moon, G. D.; Ko, S.; Min, Y.; Zeng, J.; Xia, Y.; Jeong, U., Chemical transformations of nanostructured materials. *Nano Today* **2011,** *6* (2), 186-203.
140. Fenton, J. L.; Steimle, B. C.; Schaak, R. E., Tunable intraparticle frameworks for creating complex heterostructured nanoparticle libraries. *Science* **2018,** *360* (6388), 513-517.
141. Lambert, K.; Geyter, B. D.; Moreels, I.; Hens, Z., PbTe| CdTe core| shell particles by cation exchange, a HR-TEM study. *Chem. Mater.* **2009,** *21* (5), 778-780.
142. Binetti, E.; Striccoli, M.; Sibillano, T.; Giannini, C.; Brescia, R.; Falqui, A.; Comparelli, R.; Corricelli, M.; Tommasi, R.; Agostiano, A., Tuning light emission of PbS nanocrystals from infrared to visible range by cation exchange. *Science and Technology of Advanced Materials* **2015,** *16* (5), 055007.
143. Izquierdo, E.; Robin, A.; Keuleyan, S.; Lequeux, N.; Lhuillier, E.; Ithurria, S., Strongly confined HgTe 2D nanoplatelets as narrow near-infrared emitters. *J. Am. Chem. Soc.* **2016,** *138* (33), 10496-10501.
144. Li, J. J.; Wang, Y. A.; Guo, W.; Keay, J. C.; Mishima, T. D.; Johnson, M. B.; Peng, X., Large-scale synthesis of nearly monodisperse CdSe/CdS core/shell nanocrystals using air-stable reagents via successive ion layer adsorption and reaction. *J. Am. Chem. Soc.* **2003,** *125* (41), 12567-12575.
145. Niu, P.; Zhang, L.; Liu, G.; Cheng, H. M., Graphene-like carbon nitride nanosheets for improved photocatalytic activities. *Adv. Funct. Mater.* **2012,** *22* (22), 4763-4770.
146. Xiang, Q.; Yu, J.; Jaroniec, M., Graphene-based semiconductor photocatalysts. *Chem. Soc. Rev.* **2012,** *41* (2), 782-796.
147. Chen, D.; Zhang, H.; Liu, Y.; Li, J., Graphene and its derivatives for the development of solar cells, photoelectrochemical, and photocatalytic applications. *Energy & Environmental Science* **2013,** *6* (5), 1362-1387.
148. Low, J.; Cao, S.; Yu, J.; Wageh, S., Two-dimensional layered composite photocatalysts. *Chemical communications* **2014,** *50* (74), 10768-10777.
149. Novoselov, K. S.; Geim, A. K.; Morozov, S. V.; Jiang, D.-e.; Zhang, Y.; Dubonos, S. V.; Grigorieva, I. V.; Firsov, A. A., Electric field effect in atomically thin carbon films. *science* **2004,** *306* (5696), 666-669.
150. Miró, P.; Audiffred, M.; Heine, T., An atlas of two-dimensional materials. *Chem. Soc. Rev.* **2014,** *43* (18), 6537-6554.

151. Lin, Y.; Zhang, K.; Chen, W.; Liu, Y.; Geng, Z.; Zeng, J.; Pan, N.; Yan, L.; Wang, X.; Hou, J., Dramatically enhanced photoresponse of reduced graphene oxide with linker-free anchored CdSe nanoparticles. *ACS Nano* **2010,** *4* (6), 3033-3038.
152. Cao, A.; Liu, Z.; Chu, S.; Wu, M.; Ye, Z.; Cai, Z.; Chang, Y.; Wang, S.; Gong, Q.; Liu, Y., A facile one-step method to produce graphene–CdS quantum dot nanocomposites as promising optoelectronic materials. *Adv. Mater.* **2010,** *22* (1), 103-106.
153. Novoselov, K. S.; Geim, A. K.; Morozov, S. V.; Jiang, D.; Zhang, Y.; Dubonos, S. V.; Grigorieva, I. V.; Firsov, A. A., Electric field effect in atomically thin carbon films. *Science* **2004,** *306* (5696), 666-669.
154. Xie, G.; Zhang, K.; Guo, B.; Liu, Q.; Fang, L.; Gong, J. R., Graphene-based materials for hydrogen generation from light-driven water splitting. *Adv. Mater.* **2013,** *25* (28), 3820-3839.
155. Liang, Y. T.; Vijayan, B. K.; Gray, K. A.; Hersam, M. C., Minimizing graphene defects enhances titania nanocomposite-based photocatalytic reduction of CO_2 for improved solar fuel production. *Nano Lett.* **2011,** *11* (7), 2865-2870.
156. Hou, Y.; Qiu, M.; Zhang, T.; Ma, J.; Liu, S.; Zhuang, X.; Yuan, C.; Feng, X., Efficient electrochemical and photoelectrochemical water splitting by a 3D nanostructured carbon supported on flexible exfoliated graphene foil. *Adv. Mater.* **2017,** *29* (3), 1604480.
157. Xiao, F.-X.; Miao, J.; Liu, B., Layer-by-layer self-assembly of CdS quantum dots/graphene nanosheets hybrid films for photoelectrochemical and photocatalytic applications. *J. Am. Chem. Soc.* **2014,** *136* (4), 1559-1569.
158. Jia, L.; Wang, D.-H.; Huang, Y.-X.; Xu, A.-W.; Yu, H.-Q., Highly durable N-doped graphene/CdS nanocomposites with enhanced photocatalytic hydrogen evolution from water under visible light irradiation. *The Journal of Physical Chemistry C* **2011,** *115* (23), 11466-11473.
159. Ning, F.; Shao, M.; Xu, S.; Fu, Y.; Zhang, R.; Wei, M.; Evans, D. G.; Duan, X., TiO_2/graphene/NiFe-layered double hydroxide nanorod array photoanodes for efficient photoelectrochemical water splitting. *Energy Environ. Sci.* **2016,** *9* (8), 2633-2643.
160. Wang, Q. H.; Kalantar-Zadeh, K.; Kis, A.; Coleman, J. N.; Strano, M. S., Electronics and optoelectronics of two-dimensional transition metal dichalcogenides. *Nature nanotechnology* **2012,** *7* (11), 699-712.
161. Zhang, W.; Chuu, C.-P.; Huang, J.-K.; Chen, C.-H.; Tsai, M.-L.; Chang, Y.-H.; Liang, C.-T.; Chen, Y.-Z.; Chueh, Y.-L.; He, J.-H., Ultrahigh-gain photodetectors based on atomically thin graphene-MoS_2 heterostructures. *Scientific reports* **2014,** *4* (1), 1-8.
162. Tang, R.; Yin, R.; Zhou, S.; Ge, T.; Yuan, Z.; Zhang, L.; Yin, L., Layered MoS_2 coupled MOFs-derived dual-phase TiO_2 for enhanced photoelectrochemical performance. *Journal of Materials Chemistry A* **2017,** *5* (10), 4962-4971.
163. Carvalho, A.; Ribeiro, R.; Neto, A. C., Band nesting and the optical response of two-dimensional semiconducting transition metal dichalcogenides. *Phys. Rev. B* **2013,** *88* (11), 115205.
164. Xu, X.; Hu, J.; Yin, Z.; Xu, C., Photoanode current of large–area MoS_2 ultrathin nanosheets with vertically mesh–shaped structure on indium tin oxide. *ACS Applied Materials & Interfaces* **2014,** *6* (8), 5983-5987.
165. Mak, K. F.; Lee, C.; Hone, J.; Shan, J.; Heinz, T. F., Atomically thin MoS_2: a new direct-gap semiconductor. *Physical review letters* **2010,** *105* (13), 136805.
166. Splendiani, A.; Sun, L.; Zhang, Y.; Li, T.; Kim, J.; Chim, C.-Y.; Galli, G.; Wang, F., Emerging photoluminescence in monolayer MoS_2. *Nano Lett.* **2010,** *10* (4), 1271-1275.
167. Pesci, F. M.; Sokolikova, M. S.; Grotta, C.; Sherrell, P. C.; Reale, F.; Sharda, K.; Ni, N.; Palczynski, P.; Mattevi, C., MoS_2/WS_2 heterojunction for photoelectrochemical water oxidation. *ACS Catalysis* **2017,** *7* (8), 4990-4998.
168. Chang, K.; Mei, Z.; Wang, T.; Kang, Q.; Ouyang, S.; Ye, J., MoS_2/graphene cocatalyst for efficient photocatalytic H_2 evolution under visible light irradiation. *ACS Nano* **2014,** *8* (7), 7078-7087.

169. Liu, Y.; Yu, Y.-X.; Zhang, W.-D., MoS_2/CdS heterojunction with high photoelectrochemical activity for H_2 evolution under visible light: the role of MoS_2. *The Journal of Physical Chemistry C* **2013,** *117* (25), 12949-12957.
170. Zheng, L.; Han, S.; Liu, H.; Yu, P.; Fang, X., Hierarchical MoS_2 nanosheet@ TiO_2 nanotube array composites with enhanced photocatalytic and photocurrent performances. *Small* **2016,** *12* (11), 1527-1536.
171. Singh, A. K.; Mathew, K.; Zhuang, H. L.; Hennig, R. G., Computational screening of 2D materials for photocatalysis. *The journal of physical chemistry letters* **2015,** *6* (6), 1087-1098.
172. Wu, M.-h.; Li, L.; Xue, Y.-c.; Xu, G.; Tang, L.; Liu, N.; Huang, W.-y., Fabrication of ternary GO/g-C_3N_4/MoS_2 flower-like heterojunctions with enhanced photocatalytic activity for water remediation. *Applied Catalysis B: Environmental* **2018,** *228*, 103-112.
173. Choudhary, N.; Islam, M. A.; Kim, J. H.; Ko, T.-J.; Schropp, A.; Hurtado, L.; Weitzman, D.; Zhai, L.; Jung, Y., Two-dimensional transition metal dichalcogenide hybrid materials for energy applications. *Nano Today* **2018,** *19*, 16-40.
174. In, S. I.; Vaughn, D. D.; Schaak, R. E., Hybrid CuO-TiO_2−xN_x Hollow Nanocubes for Photocatalytic Conversion of CO_2 into Methane under Solar Irradiation. *Angew. Chem., Int. Ed.* **2012,** *51* (16), 3915-3918.
175. Yu, X.; Du, R.; Li, B.; Zhang, Y.; Liu, H.; Qu, J.; An, X., Biomolecule-assisted self-assembly of CdS/MoS_2/graphene hollow spheres as high-efficiency photocatalysts for hydrogen evolution without noble metals. *Applied Catalysis B: Environmental* **2016,** *182*, 504-512.
176. Shi, Y.; Zhou, Y.; Yang, D.-R.; Xu, W.-X.; Wang, C.; Wang, F.-B.; Xu, J.-J.; Xia, X.-H.; Chen, H.-Y., Energy level engineering of MoS_2 by transition-metal doping for accelerating hydrogen evolution reaction. *J. Am. Chem. Soc.* **2017,** *139* (43), 15479-15485.
177. Huang, Z.; Han, W.; Tang, H.; Ren, L.; Chander, D. S.; Qi, X.; Zhang, H., Photoelectrochemical-type sunlight photodetector based on MoS_2/graphene heterostructure. *2D Materials* **2015,** *2* (3), 035011.
178. Zhang, P.; Lu, X.; Huang, Y.; Deng, J.; Zhang, L.; Ding, F.; Su, Z.; Wei, G.; Schmidt, O. G., MoS_2 nanosheets decorated with gold nanoparticles for rechargeable Li–O_2 batteries. *Journal of Materials Chemistry A* **2015,** *3* (28), 14562-14566.
179. Yu, X.; Prévot, M. S.; Guijarro, N.; Sivula, K., Self-assembled 2D WSe_2 thin films for photoelectrochemical hydrogen production. *Nature communications* **2015,** *6* (1), 1-8.
180. Benetti, D.; Cui, D.; Zhao, H.; Rosei, F.; Vomiero, A., Direct measurement of electronic band structure in single quantum dots of metal chalcogenide composites. *Small* **2018,** *14* (51), 1801668.
181. Li, F.; Zhang, M.; Benetti, D.; Shi, L.; Besteiro, L. V.; Zhang, H.; Liu, J.; Selopal, G. S.; Sun, S.; Wang, Z., “Green”, gradient multi-shell CuInSe2/(CuInSexS1-x) 5/CuInS2 quantum dots for photo-electrochemical hydrogen generation. *Applied Catalysis B: Environmental* **2021,** *280*, 119402.
182. Zhang, M.; Li, F.; Benetti, D.; Nechache, R.; Wei, Q.; Qi, X.; Rosei, F., Ferroelectric Polarization-enhanced Charge Separation in Quantum Dots Sensitized Semiconductor Hybrid for Photoelectrochemical Hydrogen Production. *Nano Energy* **2020**, 105626.
183. Deng, J.; Li, H.; Xiao, J.; Tu, Y.; Deng, D.; Yang, H.; Tian, H.; Li, J.; Ren, P.; Bao, X., Triggering the electrocatalytic hydrogen evolution activity of the inert two-dimensional MoS_2 surface via single-atom metal doping. *Energy Environ. Sci.* **2015,** *8* (5), 1594-1601.
184. McDonnell, S.; Addou, R.; Buie, C.; Wallace, R. M.; Hinkle, C. L., Defect-dominated doping and contact resistance in MoS_2. *ACS Nano* **2014,** *8* (3), 2880-2888.
185. Holder, C. F.; Schaak, R. E., Tutorial on powder X-ray diffraction for characterizing nanoscale materials. ACS Publications: 2019.
186. Chang, Y. H.; Lin, C. T.; Chen, T. Y.; Hsu, C. L.; Lee, Y. H.; Zhang, W.; Wei, K. H.; Li, L. J., Highly efficient electrocatalytic hydrogen production by MoS_x grown on graphene-protected 3D Ni foams. *Adv. Mater.* **2013,** *25* (5), 756-760.

187. Zheng, X.; Xu, J.; Yan, K.; Wang, H.; Wang, Z.; Yang, S., Space-confined growth of MoS_2 nanosheets within graphite: the layered hybrid of MoS_2 and graphene as an active catalyst for hydrogen evolution reaction. *Chem. Mater.* **2014,** *26* (7), 2344-2353.
188. Zhao, L.; Jia, J.; Yang, Z.; Yu, J.; Wang, A.; Sang, Y.; Zhou, W.; Liu, H., One-step synthesis of CdS nanoparticles/MoS_2 nanosheets heterostructure on porous molybdenum sheet for enhanced photocatalytic H_2 evolution. *Applied Catalysis B: Environmental* **2017,** *210*, 290-296.
189. Vrubel, H.; Merki, D.; Hu, X., Hydrogen evolution catalyzed by MoS_3 and MoS_2 particles. *Energy Environ. Sci.* **2012,** *5* (3), 6136-6144.
190. Wu, W.; Niu, C.; Wei, C.; Jia, Y.; Li, C.; Xu, Q., Activation of MoS_2 basal planes for hydrogen evolution by zinc. *Angew. Chem., Int. Ed.* **2019,** *58* (7), 2029-2033.
191. Luo, Y.; Li, X.; Cai, X.; Zou, X.; Kang, F.; Cheng, H.-M.; Liu, B., Two-dimensional MoS_2 confined $Co(OH)_2$ electrocatalysts for hydrogen evolution in alkaline electrolytes. *ACS Nano* **2018,** *12* (5), 4565-4573.
192. Liu, H.; Chen, X.; Deng, L.; Ding, M.; Li, J.; He, X., Perpendicular growth of few-layered MoS_2 nanosheets on MoO_3 nanowires fabricated by direct anion exchange reactions for high-performance lithium-ion batteries. *Journal of Materials Chemistry A* **2016,** *4* (45), 17764-17772.
193. Liu, P.; Zhu, J.; Zhang, J.; Tao, K.; Gao, D.; Xi, P., Active basal plane catalytic activity and conductivity in Zn doped MoS_2 nanosheets for efficient hydrogen evolution. *Electrochimica Acta* **2018,** *260*, 24-30.
194. Zhou, M.; Liu, Z.; Song, Q.; Li, X.; Chen, B.; Liu, Z., Hybrid 0D/2D edamame shaped $ZnIn_2S_4$ photoanode modified by Co-Pi and Pt for charge management towards efficient photoelectrochemical water splitting. *Applied Catalysis B: Environmental* **2019,** *244*, 188-196.
195. Yang, H. B.; Miao, J.; Hung, S.-F.; Huo, F.; Chen, H. M.; Liu, B., Stable quantum dot photoelectrolysis cell for unassisted visible light solar water splitting. *ACS Nano* **2014,** *8* (10), 10403-10413.
196. Braga, A.; Giménez, S.; Concina, I.; Vomiero, A.; Mora-Seró, I., Panchromatic sensitized solar cells based on metal sulfide quantum dots grown directly on nanostructured TiO_2 electrodes. *The Journal of Physical Chemistry Letters* **2011,** *2* (5), 454-460.
197. Li, F.; Feng, J.; Gao, Z.; Shi, L.; Wu, D.; Du, B.; Wei, Q., Facile synthesis of Cu_2O@TiO_2-PtCu nanocomposites as a signal amplification strategy for the insulin detection. *ACS Applied Materials & interfaces* **2019,** *11* (9), 8945-8953.
198. Ye, L.; Wang, D.; Chen, S., Fabrication and enhanced photoelectrochemical performance of MoS2/S-doped g-C3N4 heterojunction film. *ACS. Appl. mater. inter.* **2016,** *8* (8), 5280-5289.
199. Le Formal, F.; Tetreault, N.; Cornuz, M.; Moehl, T.; Grätzel, M.; Sivula, K., Passivating surface states on water splitting hematite photoanodes with alumina overlayers. *Chem. Sci.* **2011,** *2* (4), 737-743.
200. Liu, B.; Li, X.-B.; Gao, Y.-J.; Li, Z.-J.; Meng, Q.-Y.; Tung, C.-H.; Wu, L.-Z., A solution-processed, mercaptoacetic acid-engineered CdSe quantum dot photocathode for efficient hydrogen production under visible light irradiation. *Energy Environ. Sci.* **2015,** *8* (5), 1443-1449.
201. Wu, S.; Yin, Z.; He, Q.; Lu, G.; Zhou, X.; Zhang, H., Electrochemical deposition of Cl-doped n-type Cu_2O on reduced graphene oxide electrodes. *J. Mater. Chem.* **2011,** *21* (10), 3467-3470.
202. Benetti, D.; Dembele, K. T.; Benavides, J.; Zhao, H.; Cloutier, S.; Concina, I.; Vomiero, A.; Rosei, F., Functionalized multi-wall carbon nanotubes/TiO_2 composites as efficient photoanodes for dye sensitized solar cells. *Journal of Materials Chemistry C* **2016,** *4* (16), 3555-3562.
203. Chang, B.; Deng, L.; Wang, S.; Shi, D.; Ai, Z.; Jiang, H.; Shao, Y.; Zhang, L.; Shen, J.; Wu, Y., A vanadium–nickel oxynitride layer for enhanced electrocatalytic nitrogen fixation in neutral media. *Journal of Materials Chemistry A* **2020,** *8* (1), 91-96.

204. Chang, B.; Ai, Z.; Shi, D.; Zhong, Y.; Zhang, K.; Shao, Y.; Zhang, L.; Shen, J.; Wu, Y.; Hao, X., p–n tungsten oxide homojunctions for Vis-NIR light-enhanced electrocatalytic hydrogen evolution. *Journal of Materials Chemistry A* **2019,** *7* (33), 19573-19580.
205. Li, J.; Cushing, S. K.; Zheng, P.; Meng, F.; Chu, D.; Wu, N., Plasmon-induced photonic and energy-transfer enhancement of solar water splitting by a hematite nanorod array. *Nat. Commun.* **2013,** *4* (1), 1-8.
206. Tafalla, D.; Salvador, P.; Benito, R., Kinetic approach to the photocurrent transients in water photoelectrolysis at n-TiO_2 electrodes II. Analysis of the photocurrent-time dependence. *Journal of The Electrochemical Society* **1990,** *137* (6), 1810-1815.
207. Pietryga, J. M.; Werder, D. J.; Williams, D. J.; Casson, J. L.; Schaller, R. D.; Klimov, V. I.; Hollingsworth, J. A., Utilizing the lability of lead selenide to produce heterostructured nanocrystals with bright, stable infrared emission. *J. Am. Chem. Soc.* **2008,** *130* (14), 4879-4885.
208. Acharya, S. A.; Maheshwari, N.; Tatikondewar, L.; Kshirsagar, A.; Kulkarni, S. K., Ethylenediamine-Mediated Wurtzite Phase Formation in ZnS. *Crystal Growth & Design* **2013,** *13* (4), 1369-1376.
209. Sun, H.; Zhou, G.; Wang, Y.; Suvorova, A.; Wang, S., A new metal-free carbon hybrid for enhanced photocatalysis. *ACS applied materials & interfaces* **2014,** *6* (19), 16745-16754.
210. Ke, J.; Liu, J.; Sun, H.; Zhang, H.; Duan, X.; Liang, P.; Li, X.; Tade, M. O.; Liu, S.; Wang, S., Facile assembly of Bi_2O_3/Bi_2S_3/MoS_2 np heterojunction with layered n-Bi_2O_3 and p-MoS_2 for enhanced photocatalytic water oxidation and pollutant degradation. *Applied Catalysis B: Environmental* **2017,** *200*, 47-55.
211. Hyun, B.-R.; Zhong, Y.-W.; Bartnik, A. C.; Sun, L.; Abruna, H. D.; Wise, F. W.; Goodreau, J. D.; Matthews, J. R.; Leslie, T. M.; Borrelli, N. F., Electron injection from colloidal PbS quantum dots into titanium dioxide nanoparticles. *ACS Nano* **2008,** *2* (11), 2206-2212.
212. Yuan, C.-T.; Wang, Y.-G.; Huang, K.-Y.; Chen, T.-Y.; Yu, P.; Tang, J.; Sitt, A.; Banin, U.; Millo, O., Single-particle studies of band alignment effects on electron transfer dynamics from semiconductor hetero-nanostructures to single-walled carbon nanotubes. *ACS Nano* **2012,** *6* (1), 176-182.
213. van der Stam, W.; Bladt, E.; Rabouw, F. T.; Bals, S.; de Mello Donega, C., Near-infrared emitting $CuInSe_2$/$CuInS_2$ dot core/rod shell heteronanorods by sequential cation exchange. *ACS Nano* **2015,** *9* (11), 11430-11438.
214. Van Der Stam, W.; Berends, A. C.; Rabouw, F. T.; Willhammar, T.; Ke, X.; Meeldijk, J. D.; Bals, S.; de Mello Donega, C., Luminescent $CuInS_2$ Quantum Dots by Partial Cation Exchange in Cu_{2-x} S Nanocrystals. *Chem. Mater.* **2015,** *27* (2), 621-628.
215. Wei, S. H.; Zunger, A., Band offsets and optical bowings of chalcopyrites and Zn-based II-VI alloys. *J. Appl. Phys.* **1995,** *78* (6), 3846-3856.
216. Peng, X.; Schlamp, M. C.; Kadavanich, A. V.; Alivisatos, A. P., Epitaxial growth of highly luminescent CdSe/CdS core/shell nanocrystals with photostability and electronic accessibility. *J. Am. Chem. Soc.* **1997,** *119* (30), 7019-7029.
217. Stam, W. V. D.; Bladt, E.; Rabouw, F. T.; Bals, S.; Donega, C. D. M., Near-Infrared Emitting $CuInSe_2$/$CuInS_2$ Dot Core/Rod Shell Heteronanorods by Sequential Cation Exchange. *ACS Nano* **2015,** *9* (11), 11430.
218. Wang, J.-J.; Wang, Y.-Q.; Cao, F.-F.; Guo, Y.-G.; Wan, L.-J., Synthesis of monodispersed wurtzite structure $CuInSe_2$ nanocrystals and their application in high-performance organic− inorganic hybrid photodetectors. *J. Am. Chem. Soc.* **2010,** *132* (35), 12218-12221.
219. Zhong, H.; Zhou, Y.; Ye, M.; He, Y.; Ye, J.; He, C.; Yang, C.; Li, Y., Controlled synthesis and optical properties of colloidal ternary chalcogenide $CuInS_2$ nanocrystals. *Chem. Mater.* **2008,** *20* (20), 6434-6443.
220. Zhao, H.; Benetti, D.; Jin, L.; Zhou, Y.; Rosei, F.; Vomiero, A., Absorption Enhancement in “Giant” Core/Alloyed-Shell Quantum Dots for Luminescent Solar Concentrator. *Small* **2016,** *12* (38), 5354-5365.

221. Bae, W. K.; Padilha, L. A.; Park, Y.-S.; McDaniel, H.; Robel, I.; Pietryga, J. M.; Klimov, V. I., Controlled alloying of the core–shell interface in CdSe/CdS quantum dots for suppression of Auger recombination. *ACS Nano* **2013,** *7* (4), 3411-3419.
222. Dennis, A. M.; Mangum, B. D.; Piryatinski, A.; Park, Y.-S.; Hannah, D. C.; Casson, J. L.; Williams, D. J.; Schaller, R. D.; Htoon, H.; Hollingsworth, J. A., Suppressed blinking and Auger recombination in near-infrared type-II InP/CdS nanocrystal quantum dots. *Nano Lett.* **2012,** *12* (11), 5545-5551.
223. McDaniel, H.; Fuke, N.; Makarov, N. S.; Pietryga, J. M.; Klimov, V. I., An integrated approach to realizing high-performance liquid-junction quantum dot sensitized solar cells. *Nat. Commun.* **2013,** *4*, 2887.
224. Xie, R.; Rutherford, M.; Peng, X., Formation of high-quality I− III− VI semiconductor nanocrystals by tuning relative reactivity of cationic precursors. *J. Am. Chem. Soc.* **2009,** *131* (15), 5691-5697.
225. Park, Y.-S.; Bae, W. K.; Pietryga, J. M.; Klimov, V. I., Auger recombination of biexcitons and negative and positive trions in individual quantum dots. *ACS Nano* **2014,** *8* (7), 7288-7296.
226. Shabaev, A.; Mehl, M.; Efros, A. L., Energy band structure of $CuInS_2$ and optical spectra of $CuInS_2$ nanocrystals. *Phys. Rev. B* **2015,** *92* (3), 035431.
227. Neumann, H., Optical properties and electronic band structure of $CuInSe_2$. *Sol. Cells* **1986,** *16*, 317-333.
228. Cirloganu, C. M.; Padilha, L. A.; Lin, Q.; Makarov, N. S.; Velizhanin, K. A.; Luo, H.; Robel, I.; Pietryga, J. M.; Klimov, V. I., Enhanced carrier multiplication in engineered quasi-type-II quantum dots. *Nat. Commun.* **2014,** *5*, 4148.
229. Shi, L.; Benetti, D.; Li, F.; Wei, Q.; Rosei, F., Phase-junction design of MOF-derived TiO_2 photoanodes sensitized with quantum dots for efficient hydrogen generation. *Applied Catalysis B: Environmental* **2020,** *263*, 118317.
230. Tvrdy, K.; Frantsuzov, P. A.; Kamat, P. V., Photoinduced electron transfer from semiconductor quantum dots to metal oxide nanoparticles. *PNAS* **2011,** *108* (1), 29-34.
231. Jin, L.; AlOtaibi, B.; Benetti, D.; Li, S.; Zhao, H.; Mi, Z.; Vomiero, A.; Rosei, F., Near-Infrared Colloidal Quantum Dots for Efficient and Durable Photoelectrochemical Solar-Driven Hydrogen Production. *Adv. Sci.* **2016,** *3* (3), 1500345.
232. Zhao, K.; Pan, Z.; Zhong, X., Charge recombination control for high efficiency quantum dot sensitized solar cells. *The journal of physical chemistry letters* **2016,** *7* (3), 406-417.
233. Tong, X.; Channa, A. I.; You, Y.; Wei, P.; Li, X.; Lin, F.; Wu, J.; Vomiero, A.; Wang, Z. M., Boosting the performance of eco-friendly quantum dots-based photoelectrochemical cells via effective surface passivation. *Nano Energy* **2020**, 105062.
234. Tsuji, I.; Kato, H.; Kobayashi, H.; Kudo, A., Photocatalytic H_2 evolution reaction from aqueous solutions over band structure-controlled $(AgIn)_x Zn_{2(1-x)}S_2$ solid solution photocatalysts with visible-light response and their surface nanostructures. *J. Am. Chem. Soc.* **2004,** *126* (41), 13406-13413.
235. Zhang, J.; Yu, J.; Jaroniec, M.; Gong, J. R., Noble metal-free reduced graphene oxide-$Zn_xCd_{1-x}S$ nanocomposite with enhanced solar photocatalytic H_2-production performance. *Nano Lett.* **2012,** *12* (9), 4584-4589.
236. Tang, J.; Kemp, K. W.; Hoogland, S.; Jeong, K. S.; Liu, H.; Levina, L.; Furukawa, M.; Wang, X.; Debnath, R.; Cha, D., Colloidal-quantum-dot photovoltaics using atomic-ligand passivation. *Nat. Mater.* **2011,** *10* (10), 765.
237. Ip, A. H.; Thon, S. M.; Hoogland, S.; Voznyy, O.; Zhitomirsky, D.; Debnath, R.; Levina, L.; Rollny, L. R.; Carey, G. H.; Fischer, A., Hybrid passivated colloidal quantum dot solids. *Nat. Nanotechnol.* **2012,** *7* (9), 577.
238. Trevisan, R.; Rodenas, P.; Gonzalez-Pedro, V.; Sima, C.; Sanchez, R. S.; Barea, E. M.; Mora-Sero, I.; Fabregat-Santiago, F.; Gimenez, S., Harnessing infrared photons for

photoelectrochemical hydrogen generation. A PbS quantum dot based “quasi-artificial leaf”. *J. Phys. Chem. Lett.* **2012,** *4* (1), 141-146.
239. Hernández, S.; Hidalgo, D.; Sacco, A.; Chiodoni, A.; Lamberti, A.; Cauda, V.; Tresso, E.; Saracco, G., Comparison of photocatalytic and transport properties of TiO 2 and ZnO nanostructures for solar-driven water splitting. *Phys. Chem. Chem. Phys.* **2015,** *17* (12), 7775-7786.
240. Lopes, T.; Andrade, L.; Ribeiro, H. A.; Mendes, A., Characterization of photoelectrochemical cells for water splitting by electrochemical impedance spectroscopy. *Int. J. Hydrogen Energy* **2010,** *35* (20), 11601-11608.
241. Wang, W.; Feng, W.; Du, J.; Xue, W.; Zhang, L.; Zhao, L.; Li, Y.; Zhong, X., Cosensitized quantum dot solar cells with conversion efficiency over 12%. *Adv. Mater.* **2018,** *30* (11), 1705746.
242. Marcano, D. C.; Kosynkin, D. V.; Berlin, J. M.; Sinitskii, A.; Sun, Z.; Slesarev, A.; Alemany, L. B.; Lu, W.; Tour, J. M., Improved synthesis of graphene oxide. *ACS Nano* **2010,** *4* (8), 4806-4814.
243. Li, F.; Benetti, D.; Zhang, M.; Feng, J.; Wei, Q.; Rosei, F., Modulating the 0D/2D Interface of Hybrid Semiconductors for Enhanced Photoelectrochemical Performances. *Small Methods* **2021,** *5* (8), 2100109.
244. Tong, X.; Channa, A. I.; You, Y.; Wei, P.; Li, X.; Lin, F.; Wu, J.; Vomiero, A.; Wang, Z. M., Boosting the performance of eco-friendly quantum dots-based photoelectrochemical cells via effective surface passivation. *Nano Energy* **2020,** *76*, 105062.
245. Chang, K.; Chen, W., In situ synthesis of MoS_2/graphene nanosheet composites with extraordinarily high electrochemical performance for lithium ion batteries. *Chem. Commun.* **2011,** *47* (14), 4252-4254.
246. Acerce, M.; Voiry, D.; Chhowalla, M., Metallic 1T phase MoS_2 nanosheets as supercapacitor electrode materials. *Nature nanotechnology* **2015,** *10* (4), 313-318.
247. Li, H.; Zhang, Q.; Yap, C. C. R.; Tay, B. K.; Edwin, T. H. T.; Olivier, A.; Baillargeat, D., From bulk to monolayer MoS_2: evolution of Raman scattering. *Adv. Funct. Mater.* **2012,** *22* (7), 1385-1390.
248. Chakraborty, B.; Matte, H. R.; Sood, A.; Rao, C., Layer-dependent resonant Raman scattering of a few layer MoS_2. *Journal of Raman Spectroscopy* **2013,** *44* (1), 92-96.
249. Xiang, Q.; Yu, J.; Jaroniec, M., Synergetic effect of MoS_2 and graphene as cocatalysts for enhanced photocatalytic H_2 production activity of TiO_2 nanoparticles. *J. Am. Chem. Soc.* **2012,** *134* (15), 6575-6578.
250. Cançado, L. G.; Jorio, A.; Ferreira, E. M.; Stavale, F.; Achete, C. A.; Capaz, R. B.; Moutinho, M. V. d. O.; Lombardo, A.; Kulmala, T.; Ferrari, A. C., Quantifying defects in graphene via Raman spectroscopy at different excitation energies. *Nano Lett.* **2011,** *11* (8), 3190-3196.
251. Bao, J.; Zeng, X.-F.; Huang, X.-J.; Chen, R.-K.; Wang, J.-X.; Zhang, L.-L.; Chen, J.-F., Three-dimensional MoS_2/rGO nanocomposites with homogeneous network structure for supercapacitor electrodes. *Journal of Materials Science* **2019,** *54* (24), 14845-14858.
252. Zhong, X.; Han, M.; Dong, Z.; White, T. J.; Knoll, W., Composition-Tunable $Zn_xCd_{1-x}Se$ Nanocrystals with High Luminescence and Stability. *J. Am. Chem. Soc.* **2003,** *125* (28), 8589-8594.
253. Torimoto, T.; Adachi, T.; Okazaki, K.-i.; Sakuraoka, M.; Shibayama, T.; Ohtani, B.; Kudo, A.; Kuwabata, S., Facile synthesis of ZnS-$AgInS_2$ solid solution nanoparticles for a color-adjustable luminophore. *J. Am. Chem. Soc.* **2007,** *129* (41), 12388-12389.
254. Susumu, K.; Uyeda, H. T.; Medintz, I. L.; Pons, T.; Delehanty, J. B.; Mattoussi, H., Enhancing the stability and biological functionalities of quantum dots via compact multifunctional ligands. *J. Am. Chem. Soc.* **2007,** *129* (45), 13987-13996.
255. Luo, B.; Song, R.; Geng, J.; Liu, X.; Jing, D.; Wang, M.; Cheng, C., Towards the prominent cocatalytic effect of ultra-small CoP particles anchored on g-C_3N_4 nanosheets for

visible light driven photocatalytic H_2 production. *Applied Catalysis B: Environmental* **2019,** *256*, 117819.
256. Zhu, Z.; Tang, Y.; Leow, W. R.; Xia, H.; Lv, Z.; Wei, J.; Ge, X.; Cao, S.; Zhang, Y.; Zhang, W., Approaching the lithiation limit of MoS_2 while maintaining its layered crystalline structure to improve lithium storage. *Angew. Chem.* **2019,** *131* (11), 3559-3564.
257. Stankovich, S.; Dikin, D. A.; Piner, R. D.; Kohlhaas, K. A.; Kleinhammes, A.; Jia, Y.; Wu, Y.; Nguyen, S. T.; Ruoff, R. S., Synthesis of graphene-based nanosheets via chemical reduction of exfoliated graphite oxide. *carbon* **2007,** *45* (7), 1558-1565.
258. Zhou, K.; Zhou, W.; Liu, X.; Sang, Y.; Ji, S.; Li, W.; Lu, J.; Li, L.; Niu, W.; Liu, H., Ultrathin MoO_3 nanocrystalsself-assembled on graphene nanosheets via oxygen bonding as supercapacitor electrodes of high capacitance and long cycle life. *Nano Energy* **2015,** *12*, 510-520.
259. Wang, T.; Jin, B.; Jiao, Z.; Lu, G.; Ye, J.; Bi, Y., Photo-directed growth of Au nanowires on ZnO arrays for enhancing photoelectrochemical performances. *Journal of Materials Chemistry A* **2014,** *2* (37), 15553-15559.
260. Wu, Y.; Li, F.; Chen, W.; Xiang, Q.; Ma, Y.; Zhu, H.; Tao, P.; Song, C.; Shang, W.; Deng, T., Coupling interface constructions of $MoS_2/Fe_5Ni_4S_8$ heterostructures for efficient electrochemical water splitting. *Adv. Mater.* **2018,** *30* (38), 1803151.
261. Chen, S.; Gong, X.; Walsh, A.; Wei, S.-H., Electronic structure and stability of quaternary chalcogenide semiconductors derived from cation cross-substitution of II-VI and I-III-VI_2 compounds. *Physical Review B* **2009,** *79* (16), 165211.
262. Leach, A. D.; Macdonald, J. E., Optoelectronic properties of $CuInS_2$ nanocrystals and their origin. *The journal of physical chemistry letters* **2016,** *7* (3), 572-583.
263. Zheng, L.; Han, S.; Liu, H.; Yu, P.; Fang, X., Hierarchical MoS_2 nanosheet@TiO_2 nanotube array composites with enhanced photocatalytic and photocurrent performances. *Small* **2016,** *12* (11), 1527-1536.
264. Dotan, H.; Sivula, K.; Grätzel, M.; Rothschild, A.; Warren, S. C., Probing the photoelectrochemical properties of hematite (α-Fe_2O_3) electrodes using hydrogen peroxide as a hole scavenger. *Energy Environ. Sci.* **2011,** *4* (3), 958-964.
265. Fu, Y.; Cao, F.; Wu, F.; Diao, Z.; Chen, J.; Shen, S.; Li, L., Phase-Modulated Band Alignment in CdS Nanorod/SnS_x Nanosheet Hierarchical Heterojunctions toward Efficient Water Splitting. *Adv. Funct. Mater.* **2018,** *28* (16), 1706785.
266. Li, C.; Hisatomi, T.; Watanabe, O.; Nakabayashi, M.; Shibata, N.; Domen, K.; Delaunay, J.-J., Positive onset potential and stability of Cu_2O-based photocathodes in water splitting by atomic layer deposition of a Ga_2O_3 buffer layer. *Energy Environ. Sci.* **2015,** *8* (5), 1493-1500.
267. Yin, Z.; Zhu, J.; He, Q.; Cao, X.; Tan, C.; Chen, H.; Yan, Q.; Zhang, H., Graphene-based materials for solar cell applications. *Advanced energy materials* **2014,** *4* (1), 1300574.
268. Wang, Q.; Jin, Z.; Chen, D.; Bai, D.; Bian, H.; Sun, J.; Zhu, G.; Wang, G.; Liu, S., μ-Graphene Crosslinked $CsPbI_3$ Quantum Dots for High Efficiency Solar Cells with Much Improved Stability. *Adv. Energy Mater.* **2018,** *8* (22), 1800007.
269. Liu, P.; Liu, Y.; Ye, W.; Ma, J.; Gao, D., Flower-like N-doped MoS_2 for photocatalytic degradation of RhB by visible light irradiation. *Nanotechnology* **2016,** *27* (22), 225403.
270. Zhong, H.; Lo, S. S.; Mirkovic, T.; Li, Y.; Ding, Y.; Li, Y.; Scholes, G. D., Noninjection gram-scale synthesis of monodisperse pyramidal $CuInS_2$ nanocrystals and their size-dependent properties. *ACS Nano* **2010,** *4* (9), 5253-5262.
271. Gong, G.; Liu, Y.; Mao, B.; Tan, L.; Yang, Y.; Shi, W., Ag doping of Zn-In-S quantum dots for photocatalytic hydrogen evolution: Simultaneous bandgap narrowing and carrier lifetime elongation. *Applied Catalysis B: Environmental* **2017,** *216*, 11-19.
272. Benetti, D.; Rosei, F., The Role of Carbon Allotrope-Based Charge Transport Layers in Enhancing the Performance of Perovskite Solar Cells. **2021**.

273. Safaei, J.; Ullah, H.; Mohamed, N. A.; Noh, M. F. M.; Soh, M. F.; Tahir, A. A.; Ludin, N. A.; Ibrahim, M. A.; Isahak, W. N. R. W.; Teridi, M. A. M., Enhanced photoelectrochemical performance of Z-scheme g-C_3N_4/$BiVO_4$ photocatalyst. *Applied Catalysis B: Environmental* **2018,** *234*, 296-310.
274. Xu, Q.; Zhang, L.; Yu, J.; Wageh, S.; Al-Ghamdi, A. A.; Jaroniec, M., Direct Z-scheme photocatalysts: Principles, synthesis, and applications. *Materials Today* **2018,** *21* (10), 1042-1063.
275. Low, J.; Jiang, C.; Cheng, B.; Wageh, S.; Al-Ghamdi, A. A.; Yu, J., A review of direct Z-scheme photocatalysts. *Small Methods* **2017,** *1* (5), 1700080.
276. Kong, D.; Wang, H.; Cha, J. J.; Pasta, M.; Koski, K. J.; Yao, J.; Cui, Y., Synthesis of MoS_2 and $MoSe_2$ films with vertically aligned layers. *Nano Lett.* **2013,** *13* (3), 1341-1347.
277. Yang, C. P.; Xin, S.; Yin, Y. X.; Ye, H.; Zhang, J.; Guo, Y. G., An advanced selenium–carbon cathode for rechargeable lithium–selenium batteries. *Angew. Chem., Int. Ed.* **2013,** *52* (32), 8363-8367.
278. Eftekhari, A., Molybdenum diselenide ($MoSe_2$) for energy storage, catalysis, and optoelectronics. *Applied Materials Today* **2017,** *8*, 1-17.

LIST OF PUBLICATIONS, CONFERENCE PRESENTATIONS, AND AWARDS

Articles published in peer-review journals

1. **Faying Li**, Daniele Benetti*, Min Zhang, Jinhui Feng, Qin Wei*, and Federico Rosei*. "Modulating the 0D/2D Interface of Hybrid Semiconductors for Enhanced Photoelectrochemical Performances." Small Methods 5, no. 8 (2021): 2100109.

2. **Faying Li**, Min Zhang, Daniele Benetti*, Li Shi, Lucas V. Besteiro, Hui Zhang, Jiabin Liu, Shuhui Sun, Qin Wei*, and Federico Rosei*. "“Green”, gradient multi-shell $CuInSe_2$/$(CuInSe_xS_{1-x})_5$/$CuInS_2$ quantum dots for photo-electrochemical hydrogen generation." Applied Catalysis B: Environmental 280 (2021): 119402.

3. **Faying Li**, Daniele Benetti*, Min Zhang, Li Shi, Jinhui Feng, Qin Wei*, and Federico Rosei*. "Tunable 0D/2D/2D nanocomposite based on green Zn-doped $CuInS_2$ Quantum Dots and MoS_2/rGO as photoelectrodes for solar hydrogen production." ACS Applied Materials & Interfaces, 2022, 14(49), 54790–54802.

4. Min Zhang[#], **Faying Li**[#], Daniele Benetti*, Riad Nechache, Qin Wei, Xiwei Qi*, and Federico Rosei*. "Ferroelectric polarization-enhanced charge separation in quantum dots sensitized semiconductor hybrid for photoelectrochemical hydrogen production." Nano Energy 81 (2021): 105626. (Co-first author; [#]: Contributed equally to this work)

5. Tingting Wu, Yu Du, Zhongfeng Gao, Kun Xu, Li Dai, Lei Liu, **Faying Li***, Qin Wei*, Huangxian Ju. Dual Direct Z-scheme Heterojunction with Stable Electrons Supply to Au/PANI Photocathode for Ultrasensitive Photoelectrochemical and Electrochromic Visualization Detection of Ofloxacin in Microfluidic Sensing Platform. Analytical Chemistry, 2023, 95, 2, 1627–1634. Accepted on 15 December 2022. https://doi.org/10.1021/acs.analchem.2c04740. (*: Corresponding author)

6. **Faying Li**, Jinhui Feng, Zengqiang Gao, Li Shi, Dan Wu, Bin Du, and Qin Wei*. "Facile synthesis of Cu_2O@TiO_2-PtCu nanocomposites as a signal amplification strategy for the insulin detection." ACS Applied Materials & Interfaces, 2019. 11(9): 8945-8953.

7. **Faying Li**, Yueyun Li, Jinhui Feng, Zengqiang Gao, Hui Lv, Xiang Ren, and Qin Wei*. "Facile synthesis of MoS_2@Cu_2O-Pt nanohybrid as enzyme-mimetic label for the detection of the Hepatitis B surface antigen." Biosensors and Bioelectronics, 2018, 100: 512-518.

8. Li Shi, Daniele Benetti*, **Faying Li**, Qin Wei*, and Federico Rosei*. "Phase-junction design of MOF-derived TiO_2 photoanodes sensitized with quantum dots for efficient hydrogen generation." Applied Catalysis B: Environmental 263 (2020): 118317.

9. Li Shi, Daniele Benetti*, **Faying Li**, Qin Wei*, and Federico Rosei*. Design of MOF-Derived NiO-Carbon Nanohybrids Photocathodes Sensitized with Quantum Dots for Solar Hydrogen Production. Small, (2022): 2201815.

10. Xuejing Liu, Xiaolong Xu, **Faying Li**, Jingyi Xu, Hongmin Ma, Xu Sun, Dan Wu, Changwen Zhang, Xiang Ren*, and Qin Wei* Heterostructured Bi_2S_3/MoS_2 Nanoarrays for Efficient Electrocatalytic Nitrate Reduction to Ammonia Under Ambient Conditions[J]. ACS Applied Materials & Interfaces, 2022, 14(34): 38835-38843.

11. Jinhui Feng, **Faying Li**, Lei Liu, Xuejing Liu, Yanrong Qian, Xiang Ren, Xueying Wang, and Qin Wei*. "Ultrasensitive photoelectrochemical immunosensor for procalcitonin detection with porous nanoarray $BiVO_4$/CuxS platform as advanced signal amplification under anodic bias." *Sensors and Actuators B: Chemical* 308 (2020): 127685.

12. Jinhui Feng, **Faying Li**, Yanrong Qian, Xu Sun, Dawei Fan, Huan Wang, Hongmin Ma, and Qin Wei*. "Mo-doped porous $BiVO_4/Bi_2S_3$ nanoarray to enhance photoelectrochemical efficiency for quantitative detection of 17β-estradiol." *Sensors and Actuators B: Chemical* 305 (2020): 127443.

13. Jinhui Feng, **Faying Li**, Xiaojian Li, Xiang Ren, Dawei Fan, Dan Wu, Hongmin Ma, Bin Du, Nuo Zhang, and Qin Wei*. "An amplification label of core-shell CdSe@CdS QD sensitized GO for a signal-on photoelectrochemical immunosensor for amyloid β-protein." *Journal of Materials Chemistry B* 7, no. 7 (2019): 1142-1148.

14. Jinhui Feng, **Faying Li**, Xiaojian Li, Yaoguang Wang, Dawei Fan, Bin Du, Yueyun Li, and Qin Wei*. "Label-free photoelectrochemical immunosensor for NT-proBNP detection based on La-CdS/3D $ZnIn_2S_4$/Au@ZnO sensitization structure." Biosensors and Bioelectronics 117 (2018): 773-780.

Conference Presentations

1. 44th International Conference & Exposition on Advanced Ceramics and Composites (ICACC 2020) in Daytona Beach, USA. January 22-27, 2020, **Oral presentation**.
2. CQMF Annual Student Symposium (2019), November 18, Montreal, Canada.
3. IEEE Conference, (2019), October, Montreal, Canada.

Awards and Honors

1. Doctoral Scholarship (2020-2022) provided by Fonds de recherche du Québec - Nature et technologies (FRQNT)
2. Quebec Merit scholarship program for foreign students (PBEEE) (2018-2020) provided by Fonds de recherche du Québec - Nature et technologies (FRQNT)
3. CSC Scholarship (2018-2021) provided by China Scholarship Council.

APPENDIX B RÉSUMÉ

Des Nanomatériaux à hétérostructure pour des dispositifs photoélectrochimiques efficaces

Introduction et context:

Les combustibles fossiles sont confrontés à un épuisement accéléré et posent de graves problèmes environnementaux et menacent le climat mondial. La production de PEC H_2 est largement considérée comme une approche prometteuse pour produire des carburants solaires propres qui pourraient partiellement relever les défis posés par la demande énergétique mondiale croissante et le changement climatique. Le processus de fractionnement de l'eau PEC est la conversion directe de l'énergie solaire en énergie chimique sous forme d'hydrogène à l'aide de matériaux semi-conducteurs.[10]

Le processus de fractionnement de l'eau PEC se compose principalement de trois processus principaux. Le premier est le processus de récupération de la lumière. Le second est le processus de séparation et de transfert de charge. Le troisième est le processus de réaction de surface.Dans les applications pratiques, la performance de la récolte d'hydrogène solaire pour la production d'hydrogène à l'aide de photocatalyseurs à semi-conducteurs détermine la performance des systèmes de séparation d'eau PEC. L'aspect le plus important de la séparation de l'eau PEC est la sélection d'un matériau de photoélectrode approprié. Une photoélectrode idéale nécessite des matériaux semi-conducteurs qui possèdent les caractéristiques suivantes :

(1) Une énergie de bande interdite et une position de bande appropriées peuvent étendre la plage d'absorption.

(2) Séparation et transport efficaces des porteurs de charge. Une stratégie efficace pour accélérer la séparation et le transport des porteurs de charge est nécessaire, qui dépend des propriétés intrinsèques (mobilité des porteurs) et des propriétés extrinsèques (cristallinité et nanostructure). Les photocatalyseurs avec des tailles plus petites dans certaines dimensions, tels que les QD 0D, les nanofils 1D[25,26] ou les nanofeuilles 2D[27], peuvent minimiser la distance de diffusion des électrons et des trous générés par l'excitation dans le transport, réduisant ainsi le taux de recombinaison.

(3) Forte activité catalytique et stabilité. Une cinétique de réaction de surface rapide et appropriée peut éviter l'accumulation de charges de surface, qui pourraient autrement conduire à une recombinaison électron-trou et à une photo-corrosion.

De plus, d'un point de vue applicatif, un alignement de bande favorable doit pouvoir équilibrer la séparation des porteurs, le confinement, ainsi que la recombinaison. Pour réduire la recombinaison électron-trou photogénérée, la construction d'hétéro-structure est une stratégie prometteuse grâce à l'alignement de bande approprié. Simultanément, les positions non idéales des bandes de la plupart des matériaux par rapport aux potentiels thermodynamiques de séparation de l'eau sont l'une des raisons pour lesquelles il est avantageux d'utiliser deux photo-absorbeurs en série. De cette façon, chaque semi-conducteur n'a besoin d'avoir qu'une seule bande (soit la bande de conduction, soit la bande de valence) qui convient à la réaction respective.[5]

"L'interface est le dispositif", comme l'a dit Herbert Kroemer dans sa conférence Nobel, l'interface semi-conducteur joue un rôle crucial dans les dispositifs électroniques et optoélectroniques modernes.[29,30] contrairement aux semi-conducteurs à un seul composant, dont le réglage de la bande interdite est limité par leurs propriétés inhérentes.31 Par conséquent, coupler des semi-conducteurs à large bande interdite avec des semi-conducteurs à bande interdite étroite et construire des hétérostructures avec des alignements de bande adaptés est une stratégie prometteuse pour améliorer les performances du PEC en accélérant la séparation des porteurs de charge et transférer. De manière générale, selon des décalages de bande interdite distincts, les hétérojonctions formées par deux semi-conducteurs peuvent être classées en trois modèles : les hétérostructures à gap chevauchant (type I), à gap décalé (Type II) et à gap cassé (Type III).

En particulier, pour une hétérojonction de type II, les bandes interdites des deux semi-conducteurs forment un alignement de bande échelonné, à savoir que les énergies à la fois du CB et du VB d'un semi-conducteur sont relativement supérieures à celles de l'autre semi-conducteur. Par conséquent, après la génération initiale de porteurs de charge sous le rayonnement, les électrons et/ou les trous photogénérés ont tendance à se transférer dans des directions opposées à travers l'interface, ce qui entraîne une séparation spatiale efficace des porteurs de charge et la formation ultérieure du champ électrique intégré.[32] Dans ce cas, l'hétérostructure de type II s'est avérée une stratégie prometteuse pour améliorer les performances du PEC grâce à la séparation spatiale efficace des paires électron-trou photogénérées et à la réduction de la recombinaison de charge.[35] De plus, les transitions interfaciales peuvent étendre la gamme spectrale à des longueurs d'onde plus longues. que celles

définies par la bande interdite de tout composant. Par conséquent, des stratégies de conception rationnelles pour les hétérojonctions de type II sont essentielles pour obtenir les propriétés souhaitées requises pour les applications PEC.

L'alignement de la bande d'énergie à l'interface joue un rôle crucial dans les propriétés de transfert de porteur et les performances optoélectroniques de l'hétérojonction de type II. Une fois que la jonction atteint l'équilibre thermique, le potentiel intégré implique une structure de bande et provoque une courbure de bande due aux décalages de bande.[33] La conception de l'alignement de bande favorable est d'une grande importance pour faciliter l'extraction de la séparation des porteurs de charge pour les dispositifs PEC.36 D'un point d'application De vue, un alignement de bande favorable doit pouvoir équilibrer la séparation des porteurs, le confinement, ainsi que la recombinaison. En particulier, l'ingénierie d'alignement de bande repose généralement sur le réglage intrinsèque de la composition d'un ou deux matériaux semi-conducteurs qui forment l'interface. Avec le développement rapide de diverses techniques de synthèse, un réglage précis de la composition chimique, comme le dopage et l'alliage, peut fournir une stratégie puissante pour le contrôle de l'alignement de bande souhaité.[37]

Bien que chaque classe de structures de faible dimension possède des propriétés optiques et électroniques supérieures, il existe également certaines limitations inhérentes. En combinant des nanomatériaux de différentes dimensions, les hétérojonctions à dimensions mixtes présentent des propriétés uniques, offrant une option pour contourner les limitations intrinsèques d'un matériau de faible dimension.[38] Simultanément, les hétérojonctions de type II de différentes dimensions peuvent générer des niveaux d'énergie discrets en raison de leurs différences quantiques. effets de confinement, ce qui fait que les structures de bandes s'écartent les unes des autres.[33]

L'hétérostructure à base d'interfaces 0D/2D est particulièrement intéressante du fait de la possibilité de construire facilement des interfaces proches. Généralement, dans l'hétérostructure mixte 0D-2D, les matériaux 0D fonctionnent généralement comme des couches d'absorption de la lumière en raison de leur efficacité quantique élevée. Par conséquent, le revêtement de matériaux 0D à la surface de matériaux 2D est une stratégie courante pour former des hétérostructures 0D/2D. L'hybride 0D/2D peut combiner la forte capacité de collecte de lumière des QD avec les performances catalytiques de la plate-forme 2D.

Pour résoudre le problème de la plage d'absorption courte, les hétérostructures à base de QD représentent un excellent système de modèle pertinent pour comprendre et régler le comportement optoélectronique des cellules solaires de 3e génération, et fournissent une analyse

d'interface nanométrique bien définie des opportunités de dissociation des excitons et de séparation des charges.[50] De plus, pour réduire les pièges de surface à la surface des QD nus, la construction d'un noyau-coque, d'une coque à gradient et du dopage sont des stratégies prometteuses pour améliorer les performances du PEC basé sur les QD.

Objectifs de la thèse

Depuis les travaux pionniers de Fujishima et Honda en 1972, des variétés de semi-conducteurs ont été utilisées pour construire des photoélectrodes pour les dispositifs PEC. Malgré des progrès majeurs, ces matériaux font encore face à plusieurs défis importants. En particulier : (1) les oxydes métalliques possèdent généralement une large bande interdite qui limite l'absorption de la lumière solaire ; (2) tous les semi-conducteurs n'ont pas un alignement de bande favorable pour réaliser les deux processus redox (réduction de l'eau et oxydation); (3) une faible conductivité électrique et une longueur de diffusion de trou limitée; (4) la recombinaison de charge peut se produire facilement dans la masse et en surface, limitant l'efficacité du système.

Pour relever ces défis mentionnés ci-dessus, les dispositifs PEC à semi-conducteurs à hétérojonction sont des candidats prometteurs. Les hétérojonctions à dimensions mixtes peuvent utiliser l'effet synergique de chaque composant pour améliorer les propriétés optoélectroniques. Pour étendre la plage d'absorption, les QD 0D ont été introduits à l'hétérojonction grâce à la position de bande accordable et à la plage d'absorption due à l'effet de confinement quantique. Cependant, le mécanisme d'amélioration du signal de différents types de QD (QD core-shell, QD à gradient et QD dopés) dans différentes hétérojonctions reste à explorer.

Ainsi, les objectifs de cette thèse sont les suivants :

(1) Le premier projet vise à concevoir et synthétiser des hétéro-structures hybrides 0D/2D pour la production de PEC H_2. Cependant, à ce jour, le rôle des différents QD et les alignements de bande entre les QD 0D et le MoS_2 2D pour améliorer les performances du PEC sont rarement étudiés. Synthétisant MoS_2 dopé au Zn avec une bande interdite réglable, puis les QD cœur-coque PbS@CdS sont chargés par une méthode in situ pour construire une hétérojonction 0D/2D. Les mécanismes PEC de ce projet ont été analysés en détail.

(2) Jusqu'à présent, la majorité des systèmes PEC basés sur des QD utilisent généralement des éléments de métaux lourds, tels que Pb et Cd, qui sont toxiques. Le développement de QD sans métaux lourds pour les applications PEC est un défi majeur non résolu dans ce domaine. Pour le deuxième projet, une approche séquentielle d'échange de cations a été utilisée pour synthétiser des QD d'architecture multicoque à gradient sans métaux lourds $CuInSe_2/(CuInSe_xS_{1-x})_5/CuInS_2$.

Le mécanisme d'amélioration du signal est exposé à travers les résultats expérimentaux combinés au calcul théorique.

(3) Inspirés par les premier et deuxième projets, dans le troisième projet, nous concevons et synthétisons des QD écologiques $CuInS_2$ dopés au Zn et modulons la position de la bande par différentes quantités de dopant. Par la suite, construisez des hétérojonctions 2D/2D MoS_2/rGO pour améliorer la conductivité de MoS_2 pour inhiber la recombinaison de charge. En construisant des hétérojonctions 0D/2D/2D, combinées à leur alignement de bande après différentes quantités de QD écologiques dopés au Zn pour étudier en détail le mécanisme PEC. L'hétérojonction 0D/2D/2D distinctive peut tirer parti des capacités de collecte de lumière des QD avec les performances catalytiques et de conductivité des NS 2D.

Résultats et discussions

Modulation de l'interface 0D/2D des semi-conducteurs hybrides pour des performances photoélectrochimiques améliorées

L'imagerie SEM et TEM a été utilisée pour étudier la morphologie des nanocristaux de MoS_2 et Zn-MoS_2 vierges. Comme le montre la figure R1a, le MoS_2 pur présente une morphologie de nano-fleur. Chaque nanofleur est une structure hiérarchique de NS en forme de pétale 2D avec une longueur moyenne d'environ 130 à 150 nm. Après un dopage à 10 % de Zn (10 % est basé sur le rapport du précurseur, l'échantillon est étiqueté comme 10 Zn-MoS_2), la morphologie (Figure R1b) et la taille n'ont pas montré de changement évident par rapport au MoS_2 pur. Les résultats de la surface de Brunauer-Emmett-Teller (BET) illustrés à la figure R1c révèlent que l'échantillon 10 Zn-MoS_2 possède une plus grande surface BET (47.9 m^2/g) par rapport au MoS_2 vierge (9.72 m^2/g), ce qui pourrait fournir plus de zones de contact pour la nucléation des QD 0D et pour la réaction redox électrolytique lors des tests PEC.

Ensuite, la caractérisation XRD a été appliquée pour surveiller les changements de structure cristalline avec un dopage Zn accru. Comme le montre la figure R1d, le MoS_2 non dopé présente trois pics de diffraction distincts correspondant au MoS_2 vierge (carte JCPDS Card No. 73-1508). A un faible niveau de dopage (jusqu'à 10% de dopage au Zn), les atomes de Zn sont incorporés dans la matrice MoS_2 sans formation de ZnS. En particulier, la faible intensité des pics XRD est due au fait que les échantillons sont polycristallins. De plus, les nanofeuillets minces sont souvent déformés lorsqu'ils sont repositionnés sous forme de poudre, et en raison de cette déformation, leur périodicité d'empilement sera désordonnée, conduisant à des pics XRD moins intenses.[137] En outre, le modèle SAED des échantillons de Zn-MoS_2 tels que synthétisés (Figure R1e)

présente trois anneaux évidents correspondant à (002), (100) et (110), indiquant en outre du Zn-MoS_2 polycristallin dans la structure hexagonale. Alors que pour les quantités de dopage au Zn supérieures à 10 %, le Zn commence à former une phase d'impureté secondaire de ZnS. Par exemple, le spectre DRX des 20 échantillons de Zn-MoS_2 présente trois nouveaux pics de diffraction, correspondant aux pics (111), (220) et (311) de la sphalérite cubique ZnS [JCPDS Card No. 77-2100].

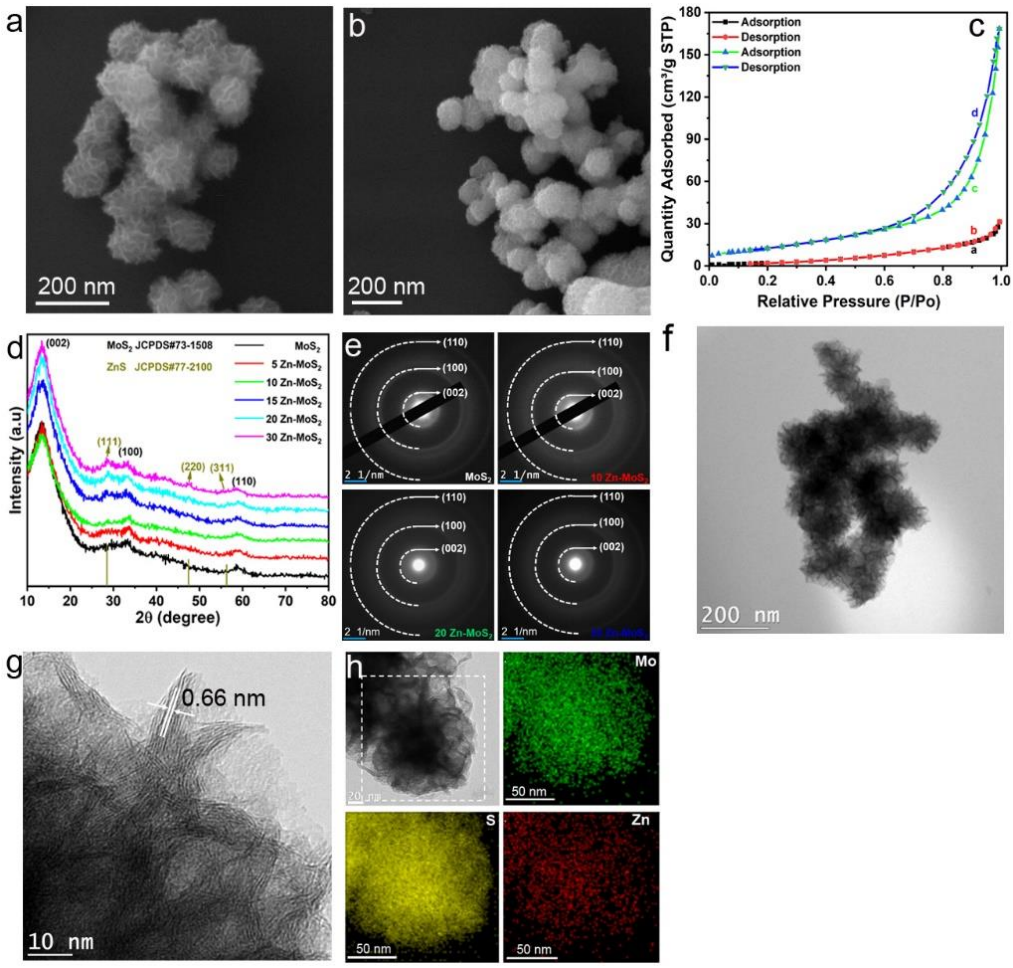

Figure R1. Caractérisations morphologiques par imagerie SEM: (a) nanofleurs de MoS_2 pur et (b) 10 nanofleurs de Zn-MoS_2; (c) XRD de différentes teneurs en zinc dopé MoS_2. (d) Courbes BET de MoS_2 (courbe a, b) et 10Zn-MoS_2 (courbe c, d), respectivement. (e) Modèles SAED de MoS_2, 10 Zn-MoS_2, 20 Zn-MoS_2 et 30 Zn-MoS_2. Images TEM (f) et HRTEM (g) de 10 Zn-MoS_2; (h) Images de cartographie élémentaire de 10 Zn-MoS_2.

Les images TEM (Figure R1f) et HRTEM (Figure R1g) de 10 Zn-MoS_2 montrent des ondulations et des rides importantes, indiquant la présence d'une structure ultra-mince. Les NS en forme de pétale 2D avec un espacement de couches d'environ 0.66 nm peuvent être attribués au plan

cristallin (002) de MoS_2.[134] L'apparition de petites nanofeuilles aux bords tranchants indique un degré élevé de cristallisation. En outre, conformément aux modèles XRD ne montrant aucune autre phase cristalline évidente, 10 Zn-MoS_2 ne montre aucune nanoparticule évidente ou de grands amas apparaissant à sa surface, confirmant qu'aucun composé de sulfure de zinc ne se forme à la surface. L'analyse de cartographie par spectroscopie à rayons X à dispersion d'énergie (EDS) de 10 Zn-MoS_2 (Figure R1h) confirme la coexistence de Mo (indiqué par la couleur verte), S (indiqué par la couleur jaune) et Zn (indiqué par la couleur rouge) éléments de l'échantillon. De toute évidence, les éléments Zn sont uniformément répartis dans les NS, indiquant le dopage Zn réussi de MoS_2.

Pour tester les performances du PEC, les différentes photoanodes ont été étudiées dans un électrolyte avec un piégeur de trous (0.25 M $Na_2S{\cdot}9H_2O$ et 0.35 M Na_2SO_3) en utilisant une configuration typique à trois électrodes dans des conditions d'obscurité et de lumière, y compris la LSV, la EIS. Des échantillons représentatifs de pur MoS_2/PbS@CdS, MoS_2/PbS@CdS dopés au Zn (5 %, 10 %, 15 %, 20 %, 30 % de dopant Zn) ont été utilisés pour étudier l'effet des dopants Zn sur l'alignement des bandes du hétérojonction et comment cela peut affecter les performances du PEC. Comme le montre la Figure R2a, la densité de photocourant (Jph) augmente avec la polarisation appliquée en raison de l'amélioration de la génération et de la collecte de porteurs de charge photoexcités. Le LSV montre que l'échantillon pur de MoS_2/PbS@CdS génère un photocourant de 0.08 mA cm^{-2} à 0.93 V par rapport à l'électrode à hydrogène réversible (RHE) (0 V par rapport à l'Ag/AgCl) sous un éclairage solaire. L'échantillon à 5 % en poids de Zn présente une densité de photocourant de 0,16 mA cm^{-2}, une valeur intermédiaire entre celle obtenue pour un dopage à 0 % et à 10 % de Zn. En dopant avec 10% de Zn, le Jph a montré une augmentation de 3 fois, atteignant une valeur de photocourant maximale de 0.25 mA cm^{-2} à 0.93 V, alors que pour des quantités plus élevées de dopage au Zn, les performances ont diminué. En particulier, les performances du PEC diminuent progressivement avec une quantité plus élevée de dopage au Zn de 15 %, 20 % et 30 % réduisant le photocourant à 0.21 mA cm^{-2}, 0.18 mA cm^{-2} et 0.13 mA cm^{-2}, respectivement. Ainsi, le photocourant maximal (0.25 mA cm^{-2}) est obtenu pour 10 % de Zn dopé dans du MoS_2, alors que pour des quantités inférieures/élevées de Zn, les performances sont inférieures.

Pour mettre davantage en évidence l'effet du dopage au Zn, le photocourant haché normalisé (i-t ampérométrique normalisé) à 0,93 V vs RHE est présenté à la Figure R2b. Par rapport au courant d'obscurité (état OFF), pour tous les échantillons le Jph sous illumination augmente significativement (état ON). Cela confirme que les Zn-MoS_2 préparés sont généralement de type

n, en accord avec le résultat OCP et les mesures M-S.153 De plus, l'augmentation instantanée du photocourant suggère que les photoanodes à base de film semi-transparent sont sensibles à la lumière et peuvent générer et séparer efficacement des paires électron-trou et transférer des électrons vers la contre-électrode. L'ajout de Zn module la densité de photocourant en modifiant la conductivité et l'alignement des bandes, l'échantillon 10 Zn-MoS_2/PbS@CdS présentant la densité de photocourant la plus élevée. Le Jph plus élevé de 10 Zn-MoS_2/PbS@CdS peut être attribué à des effets synergiques, tels que: (i) la formation d'un alignement de bande approprié qui accélère l'injection de charge des QD vers 10Zn-MoS_2, supprimant la recombinaison électron-trou ; (ii) la couche ultra-mince réduit également le chemin que les charges doivent parcourir, réduisant ainsi la recombinaison des charges.

Nous avons également évalué l'effet des différents chalcogénures métalliques QDs, PbS, CdS et leur composite PbS@CdS, en fixant le dopage Zn à 10%. Comme le montre la Figure R2c, 10 Zn-MoS_2/PbS@CdS présente le photocourant saturé le plus élevé par rapport au 10 Zn-MoS_2 pur, 10 Zn-MoS_2/PbS ou 10 Zn-MoS_2/CdS. Les résultats ont montré que les photoanodes à base de 10 Zn-MoS_2 présentent les valeurs de photocourant les plus élevées. De plus, la photoanode à base de 10 hétérostructures Zn-MoS_2/PbS@CdS présente la densité de photocourant maximale par rapport à toute autre combinaison. Ces résultats démontrent que la conception d'un alignement de bande approprié peut augmenter considérablement les performances du PEC.

EIS a été utilisé pour étudier les propriétés de transfert de charge des différentes photoanodes. La Figure R2d affiche les tracés de Nyquist enregistrés à 0 V par rapport à Ag/AgCl sous 1 soleil (100 mW cm^{-2}) d'échantillons représentatifs de Zn-MoS_2/PbS@CdS, 5 Zn-MoS_2/PbS@CdS, 10 Zn-MoS_2/PbS@CdS, 15 Zn-MoS_2/PbS@CdS, 20 Zn-MoS_2/PbS@CdS et 30 Zn-MoS_2/PbS@CdS QD photoanodes. Tous les échantillons présentent des tracés de Nyquist similaires, avec un seul demi-cercle suivi d'une « queue ». L'objectif principal de l'analyse est le diamètre du demi-cercle car il est inversement corrélé à la résistance de transfert de charge (RCT). En particulier, un rayon plus petit du demi-cercle signifie un RCT inférieur indiquant un transfert de charge amélioré. Une résistance de transfert de charge inférieure et une cinétique de transfert de charge supérieure à l'interface électrolyte/catalyseur. 10%Zn-MoS_2 confirmant que la recombinaison des paires électron/trou est fortement réduite dans ce type d'architecture.

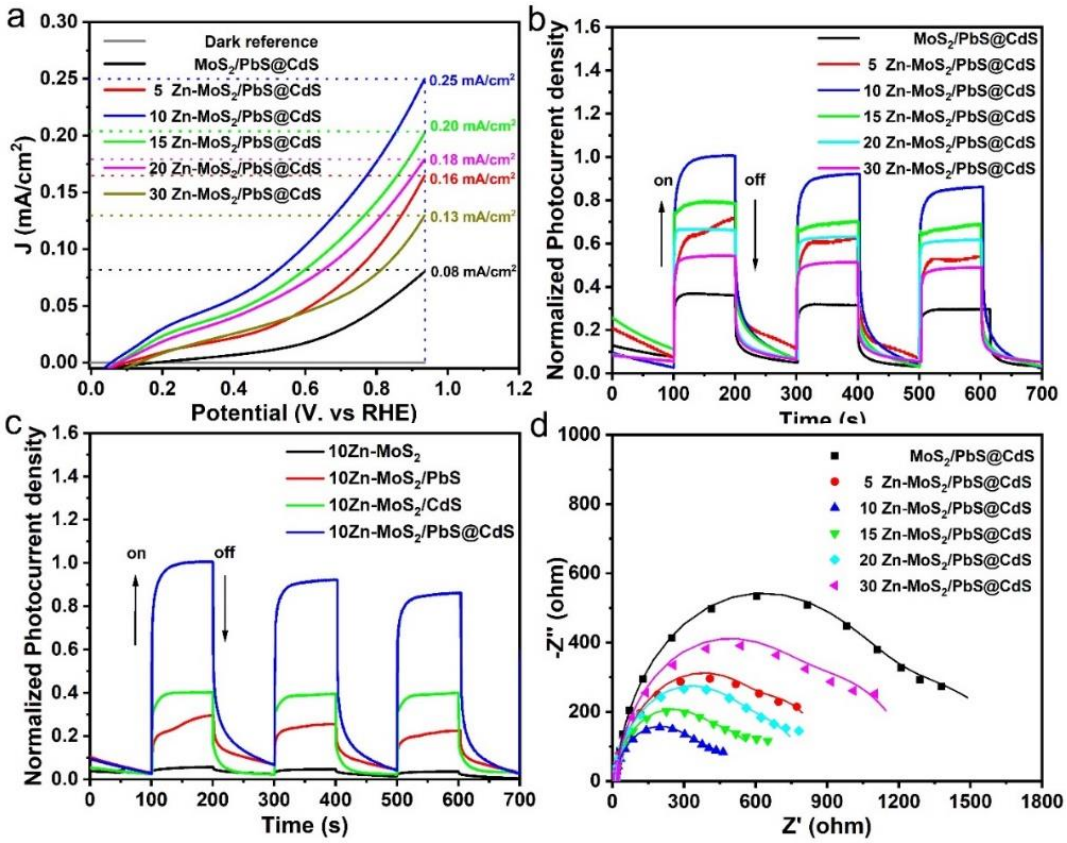

Figure R2. (a) LSV et cycles J-t ampérométriques normalisés pour les PEC avec différentes photo-anodes basées sur différents dopants Zn MoS_2 sensibilisés par les QD PbS @ CdS; (c) photo-anodes à base de différents QD sensibilisés au 10 Zn-MoS_2. (d) Les tracés de Nyquist d'EIS avec différentes électrodes sous éclairage et les résultats d'ajustement sont tracés sous forme de traces solides.

Comparé au MoS_2 pur, le Zn-MoS_2 augmente considérablement la surface et la densité électronique en raison du dopage au Zn. Par conséquent, plus de QD adhèreront à la surface Zn-MoS_2, augmentant l'absorption et conduisant à de meilleures performances PEC. En outre, un dopage Zn approprié peut ajuster la structure de bande de Zn-MoS_2 permettant la formation d'un alignement de bande favorable pour l'injection de charge. Cependant, le dopage doit être limité en dessous d'un certain seuil (dans ce cas précis 10%) pour éviter un alignement de bande défavorable à l'injection de charge et la création d'impuretés, comme le ZnS, qui limiteraient le transfert d'électrons. Dans l'ensemble, une modulation appropriée de l'énergie de bande des deux, les QD avec la formation d'un composite, et une quantité optimale de dopant Zn dans MoS_2 peuvent augmenter les performances finales du PEC.

Points quantiques "verts", dégradés multi-coquilles $CuInSe_2/(CuInSe_xS_{1-x})_5/CuInS_2$ pour la génération d'hydrogène photoélectrochimique

Une approche séquentielle d'échange de cations basée sur un modèle a été appliquée pour préparer des QD gradués colloïdaux sans métaux lourds NIR. Tout d'abord, des QD CdSe avec une taille de rayon uniforme ont été synthétisés selon une approche d'injection à chaud.[96] Par la suite, six couches de coque CdS ont été envahies par la méthode SILAR sur la surface des QD à noyau CdSe pour former un noyau géant $CdSe/(CdS)_6$ QD shell. Pour étendre davantage la région d'absorption des QD CdSe $/(CdS)_6$, le deuxième type de QD multi-coques à gradient a également été préparé: cinq monocouches alliées à gradient de coque $CdSe_xS_{1-x}$ ont été développées sur les QD à noyau CdSe, puis une monocouche de CdS ont été développés sur la coque alliée pour former des QD $CdSe/(CdSe_xS_{1-x})_5/CdS$. Successivement, les QD à base de Cd^{2+} ont été utilisés comme modèles pour l'échange séquentiel de cations afin d'obtenir les QD finaux sans métaux lourds. Comme le montre la Figure R3, le schéma illustre l'approche d'échange détaillée: Cd^{2+} dans $CdSe/(CdSe_xS_{1-x})_5/CdS$ QDs a été entièrement échangé par Cu^+ et $Cu_2Se/(CuSe_xS1\text{-}x)_5/Cu_2S$ QDs ont été partiellement échangés par In^{3+} pour former des QD $CuInSe_2/(CuInSe_xS_{1-x})_5/CuInS_2$. Avec une approche similaire, en utilisant respectivement CdSe et $CdSe/(CdS)_6$, les QD $CuInSe_2$ et $CuInSe_2/(CuInS_2)_6$ ont été préparés et utilisés à titre de comparaison.

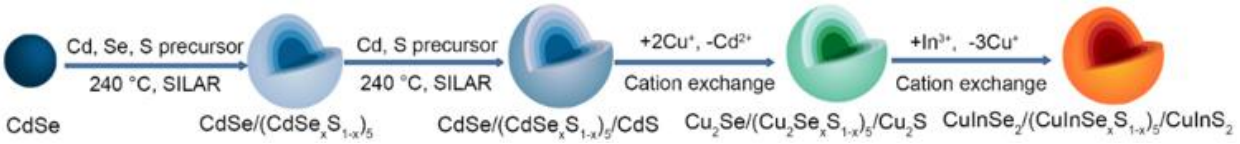

Figure R3. (a) Schéma de principe des procédures séquentielles d'échange de cations pour la synthèse des QD $CuInSe_2/(CuInSe_xS_{1-x})_5/CuInS_2$.

Les propriétés optiques des modèles à base de CdSe et des QD sans métaux lourds dans le toluène sont présentées à la Figure R4. Avant l'échange séquentiel de cations, les spectres d'absorption des QD initiaux s'étendent de la région UV à VIS. Comme le montre la figure R4a, le premier pic excitonique pour les QD CdSe purs et les QD $CdSe/(CdS)_6$ est centré à ~552 nm et 594 nm, respectivement. En ajoutant les couches d'alliage interfaciales, le premier pic d'absorption excitonique des QD $CdSe/(CdSe_xS1\text{-}x)_5/CdS$ se décale vers le rouge vers des

longueurs d'onde plus longues, et il est centré à 626 nm. Le décalage bathochromique est dû à la bande interdite relativement étroite de CdSe par rapport à CdS, et à l'influence de l'effet de taille quantique avec l'augmentation de taille.[174] Simultanément, un décalage vers le rouge similaire a été observé pour le pic PL, en raison d'une fuite accrue d'électrons du cœur vers la région de coque.[175] En fait, en général, dans un système cœur/coque, la fuite d'électrons du cœur vers la région de coque provoque un décalage vers le rouge dans le pic PL, ce qui a été confirmé dans de nombreux QD structurés cœur/coque.[74,176]. Comme mentionné ci-dessus, les QD à base de Cd ont été utilisés comme modèles pour l'approche séquentielle d'échange de cations pour préparer les NIR, les QD multi-coquilles vertes. Après cette procédure (Figure R4b), les spectres d'absorption des QD $CuInSe_2$, $CuInSe_2/(CuInS_2)_6$ et $CuInSe_2/(CuInSe_xS_{1-x})_5/CuInS_2$ se sont déplacés vers le NIR région jusqu'à 1000 nm, respectivement, avec la disparition des pics de première excitonique, indiquant l'échange cationique complet. De plus, le pic PL des QD $CuInSe_2$, $CuInSe_2/(CuInS_2)_6$ et $CuInSe_2/(CuInSe_xS_{1-x})_5/CuInS_2$ présentent également un redshift significatif à ~930 nm, 1040 nm et 1140 nm (Figure R4b), respectivement.

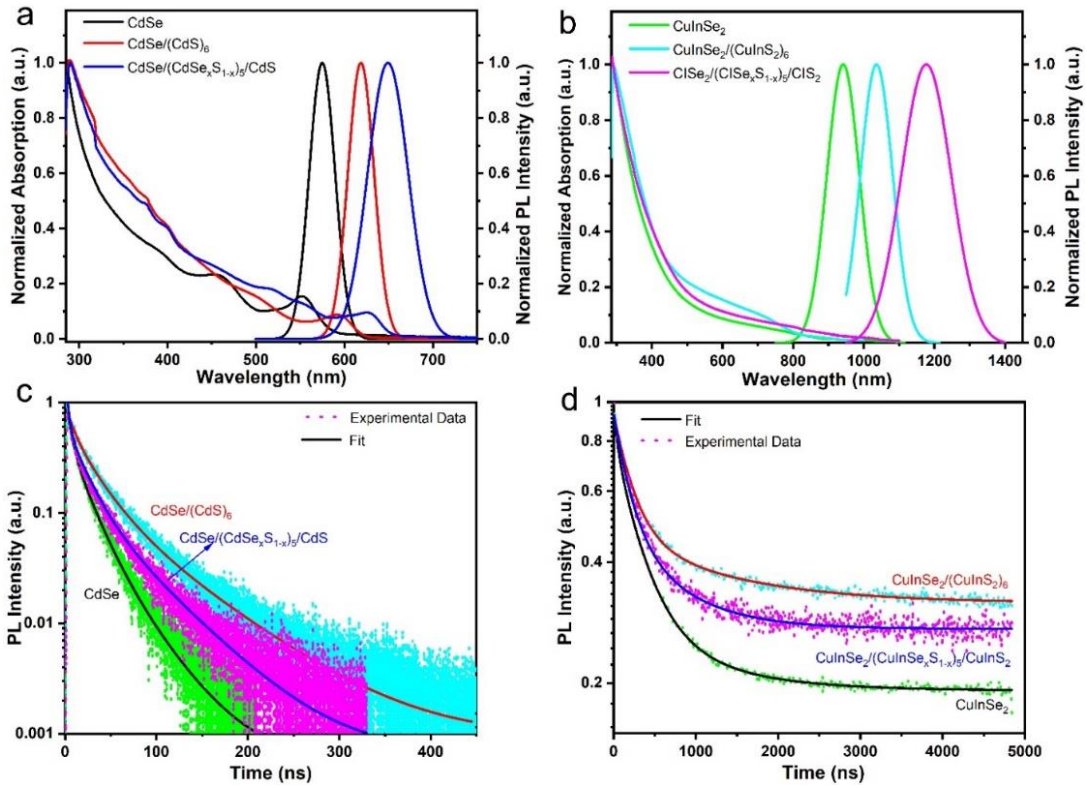

Figure R4 (a) Spectres d'absorption et PL de CdSe, $CdSe/(CdS)_6$ et $CdSe/(CdSe_xS1\text{-}x)_5/CdS$. (b) Absorption et spectres PL de $CuInSe_2$, $CuInSe_2/(CuInS_2)_6$ et $CuInSe_2/(CuInSexS1\text{-}x)_5/CuInS_2$. (c) Spectres PL transitoires de: (c) CdSe, $CdSe/(CdS)_6$ et CdSe / $(CdSe_xS_{1-x})_5/CdS$; (d) $CuInSe_2$, $CuInSe_2/(CuInS_2)_6$ et $CuInSe_2/(CuInSexS_{1-x})_5/CuInS_2$ QD dans le toluène, respectivement.

Le décalage vers le rouge des QD à coquille de gradient par rapport aux QD à noyau et aux QD à noyau-coquille peut être attribué à une fuite d'électrons améliorée du noyau à la coquille, en raison de la formation d'un gradient approprié dans l'alignement des bandes. Pour étudier plus avant la dynamique des excitons des QD tels que synthétisés avant et après l'échange de cations, la spectroscopie de fluorescence transitoire a été appliquée pour étudier leur durée de vie PL dans le toluène. La durée de vie PL des QD avant échange cationique est présentée dans la Figure R4c. Après ajustement avec la fonction de décroissance tri-exponentielle, les modèles de CdSe, CdSe/$(CdS)_6$ et CdSe/$(CdSe_xS_{1-x})_5$/CdS QD présentent une durée de vie moyenne d'environ 29, 54 et 43 ns, respectivement. Les spectres de durée de vie PL des QD après échange cationique sont présentés sur la figure R4d. Après ajustement avec des fonctions de décroissance bi- et tri-exponentielle, les QD $CuInSe_2$ présentent une durée de vie moyenne d'environ 370 ± 5 ns, tandis que les QD $CuInSe_2/(CuInS_2)_6$ core-shell et $CuInSe_2/(CuInSe_xS_{1-x})_5$ /$CuInS_2$ gradués Les QD présentent des durées de vie moyennes plus longues ~ 1180 ± 10 et 630 ± 5 ns, respectivement.

Par rapport à la structure à cœur unique, à mesure que l'épaisseur de la coque augmente, la structure de bande électronique des QD cœur/coque change, conduisant à la formation d'une structure cœur/coque de quasi-type II. La structure spéciale noyau/coquille de quasi-type II accélérera la fuite des électrons du noyau vers la région de la coquille lorsque les trous sont encore principalement confinés dans la région du noyau, diminuant efficacement le chevauchement spatial entre les fonctions d'onde des électrons et des trous, inhibant la recombinaison et conduisant à une durée de vie prolongée. Cependant, lorsque la coque graduée a été ajoutée entre l'interface du noyau et de la coque, l'effet de délocalisation sera réduit car la couche graduée augmente simultanément la fuite d'électrons et de trous vers la surface. Par conséquent, la durée de vie moyenne des QD gradués diminuera par rapport aux QD core-shell. En conclusion, le décalage vers le rouge du pic PL et la durée de vie plus longue confirment la formation d'un alignement de bande quasi de type II entre le noyau et la coque des QD $CuInSe_2/(CuInSe_xS_{1-x})_5/CuInS_2$ après échange séquentiel de cations.[179]

Pour mieux comprendre la cinétique des excitons de ces QD NIR tels que synthétisés, nous avons calculé la fonction d'onde théorique électron/trou (e/h) des QD NIR $CuInSe_2$, $CuInSe_2/(CuInS_2)_6$ et $CuInSe_2/(CuInSe_xS1\text{-}x)_5/CuInS_2$ sur la base de leur alignement de bande en vrac en utilisant la masse effective de e/h en vrac $CuInSe_2$ et $CuInS_2$.[180, 181] Les normes des ψe(r) et ψh(r) calculés en fonction du rayon (nm) sont illustrées à la Figure R5 . Les Figures R5a et R5b montrent la fonction d'onde des électrons et des trous le long d'une ligne commençant au

centre de la structure, dans les trois structures NIR QD différentes. La structure cœur/coque présente un alignement de bande typique de quasi-type II, dans lequel les électrons peuvent fuir dans la couche $CuInS_2$ alors que les trous sont encore principalement confinés dans la région de cœur.[182] Lorsqu'une coque ou une couche d'interface $CuInSe_xS_{1-x}$ à gradient introduites, ψe(r) et ψh(r) montrent une fuite accrue dans la région de la coque en conséquence d'un alignement favorable des bandes. Pour évaluer qualitativement la durée de vie des porteurs photoexcités dans les QD, nous avons calculé l'intégrale de chevauchement (OI) des porteurs photoexcités dans les trois différents QD.

Cette amplitude fournit une estimation de la probabilité de recombinaison de porteurs se produisant dans le QD. Le modèle supposait que la recombinaison se produisait du CBM au VBM sans aucune impureté dans le noyau. La durée de vie PL doit être proportionnelle à l'intégrale de chevauchement inverse, 1/OI. Comme représenté sur la Figure R5c, 1/OI augmente en passant d'une structure cœur à une structure cœur/coque alors que la structure gradient présente une valeur intermédiaire entre les deux autres. Cette tendance est qualitativement en accord avec la durée de vie mesurée, indiquant que la durée de vie plus courte et le léger élargissement du pic PL des QD $CuInSe_2/(CuInSe_xS_{1-x})_5/CuInS_2$ par rapport aux QD $CuInSe_2/(CuInS_2)_6$ peuvent être compris comme résultant de un plus grand chevauchement des e/h dans la région de la coque de la structure alliée à gradient par rapport aux QD cœur/coque. Cependant, le plus grand degré de fuite e/h dans les QD à coque en alliage par rapport aux QD $CuInSe_2/(CuInS_2)_6$, peut être utile pour le transfert e/h des QD vers les accepteurs e/h et pour améliorer encore l'efficacité des dispositifs optoélectroniques. En résumé, dans les QD $CuInSe_2/(CuInSe_xS_{1-x})_5/CuInS_2$, la présence de la couche interfaciale contribue à la fois à une absorption plus large des QD et à une fuite accrue de e/h vers la région de la coque par rapport à $CuInSe_2/(CuInS_2)_6$ QD avec une épaisseur de coque similaire.

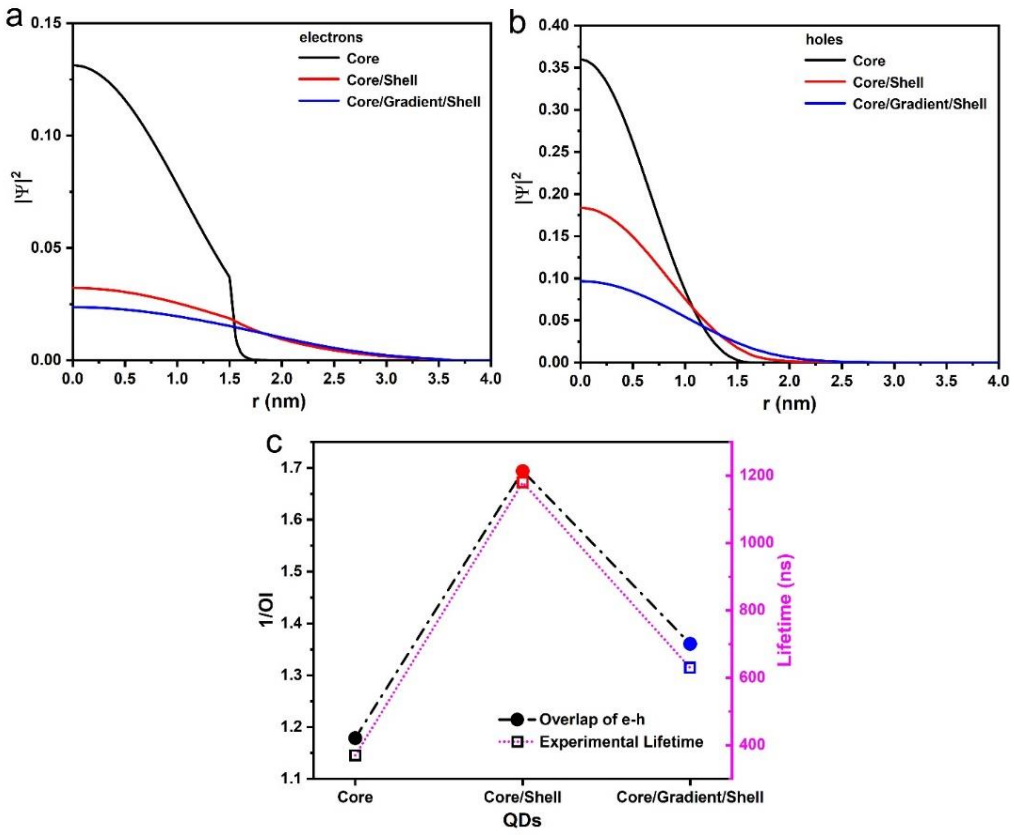

Figure R5 Norme de la fonction d'onde le long d'une coupe radiale commençant au centre du QD, pour (a) les électrons 1s, et (b) les trous 1s. (c) Inverse de l'intégrale de recouvrement entre les électrons et les trous de $CuInSe_2$, $CuInSe_2/(CuInS_2)_6$ et $CuInSe_2/(CuInSe_xS_{1-x})_5/CuInS_2$ avec R = 1.55 nm et Hshell = 2.1 nm, par rapport aux durées de vie expérimentales.

L'analyse PEC a été effectuée à l'aide d'une configuration traditionnelle à trois électrodes, avec un Ag/AgCl avec du KCl saturé comme électrode de référence, une feuille de platine comme électrode auxiliaire et le film épais TiO_2/QDs/ZnS fabriqué comme électrode de travail. L'électrolyte contient du Na_2S 0.25 M et du Na_2SO_3 0.35 M (pH = 12.5), qui servent également de piégeurs de trous sacrificiels pour empêcher la photo-corrosion des points quantiques. Les trois différentes performances de photo-anode basées sur des QD NIR sont évaluées et comparées sur la figure R6a. Pour comparer équitablement les propriétés des QD NIR tels que synthétisés, tous les dispositifs PEC fabriqués ont été mesurés dans des conditions de préparation et de mesure identiques. Les densités de photocourant ont été mesurées dans des conditions d'obscurité, de lumière hachée et d'éclairage en lumière continue (AM 1.5G, 100 mW cm^{-2}). Les résultats sont reportés dans la Figure R6 a. Pour la photo-anode sensibilisée aux QD $CuInSe_2$ à noyau pur, la densité de photocourant est presque nulle dans des conditions sombres (courbe en

pointillés), tandis qu'un photocourant saturé de 1.5 mA cm^{-2} est mesuré à 0.9 V par rapport au RHE. La densité de photocourant saturée de la photo-anode sensibilisée $CuInSe_2/(CuInS_2)_6$ et $CuInSe_2/(CuInSe_xS1\text{-}x)_5/CuInS_2$ peut atteindre ~2.6 mA cm^{-2} et 4.5 mA cm^{-2}, respectivement. En particulier, la structure cœur/coque dégradée montre un incrément de +200% par rapport à la structure monocœur et de +73% par rapport à l'architecture cœur/coque.

Pour démontrer les performances supérieures du gradient core-shell, un test de chronoampérométrie des dispositifs PEC fabriqués a été mesuré à 0,9 V par rapport au RHE. Comme le montre la Figure R6 b, les QD $CuInSe_2/(CuInSe_xS1\text{-}x)_5/CuInS_2$ avec couche de gradient présentent un photocourant saturé qui est 1.7 fois plus élevé que les dispositifs PEC basés sur $CuInSe_2/(CuInS_2)_6$.

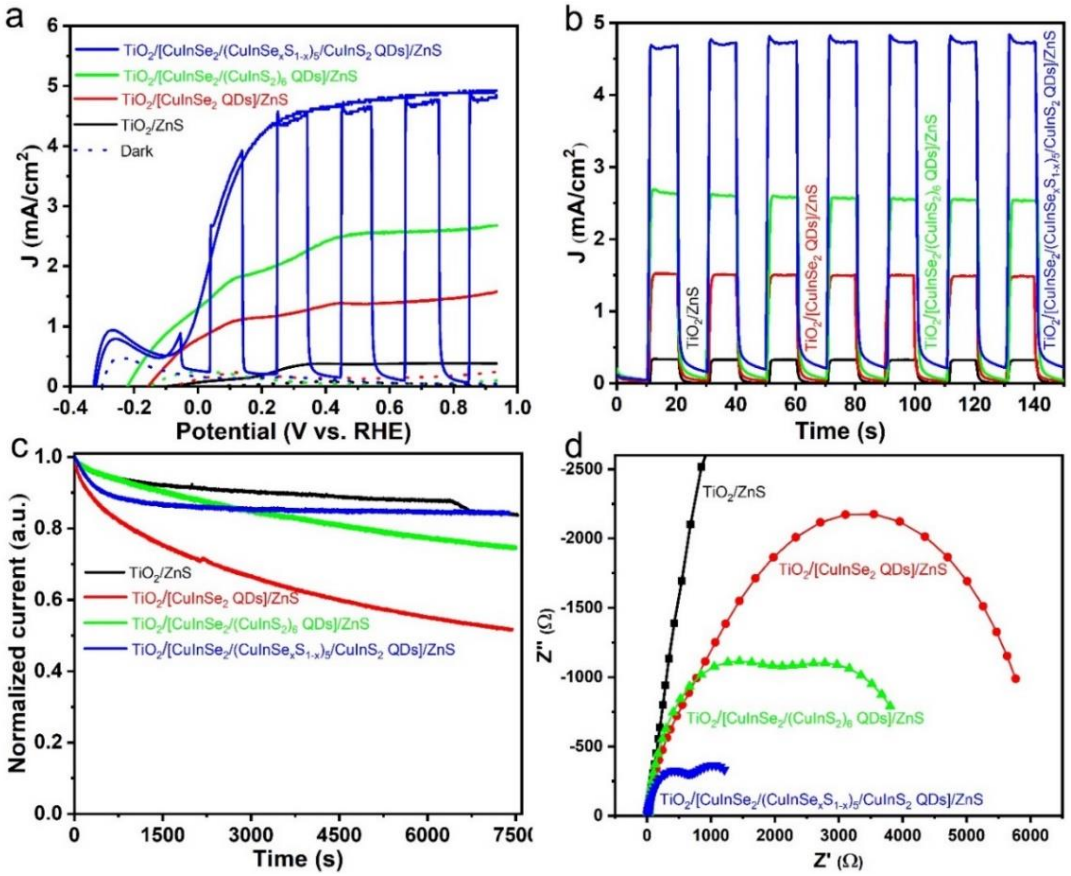

Figure R6 (a) Courbes J-V de TiO_2/ZnS et TiO_2 sensibilisés avec des QD $CuInSe_2$, des QD $CuInSe_2/(CuInS_2)_6$ et des QD $CuInSe_2/(CuInSe_xS1\text{-}x)_5/CuInS_2$, respectivement, sous l'obscurité (courbe en pointillés), hachées et éclairage continu (courbe continue) (AM 1,5 G, 100 mW cm^{-2}). (b) Densité de photocourant en fonction du temps pour les photoanodes telles que synthétisées (c) Photostabilité et (d) Parcelles de Nyquist de photoanodes représentatives sous illumination (100 mW cm^{-2}) à 0V vs Ag/AgCl.

La photo-stabilité du dispositif PEC est également un facteur essentiel pour la génération de H_2. En général, les performances des dispositifs PEC sensibilisés aux QD sont sensibles aux défauts de surface sous illumination qui agissent comme des pièges de charge, limitant la stabilité.[190,191] Les pièges et défauts liés à la surface formeront des canaux de désexcitation non radiatifs rapides pour la photo- porteurs de charge générés, réduisant les performances globales. Cependant, la coque inorganique peut réduire les pièges de surface pour renforcer les performances du PEC. Pour comparer la décroissance du photocourant, la densité initiale du photocourant a été normalisée à son maximum. Comme le montre la figure R6c, la photoanode pure TiO_2/ZnS présente une bonne photo-stabilité, conservant environ ~ 83 % de la valeur initiale après 2 h d'éclairage (courbe noire) en raison de la stabilité inerte du TiO_2 à la corrosion. La densité de photocourant pour les dispositifs PEC sensibilisés aux QD $CuInSe_2$ nus diminue progressivement avec le temps, tombant à ~ 53 % de la valeur initiale après 2 h d'éclairage (courbe rouge). Avec la présence de la coque de protection $CuInS_2$, la densité de photocourant maintient plus de ~74 % de la valeur initiale (courbe verte), tandis qu'une stabilité beaucoup plus élevée, environ ~83 % de la valeur initiale, a été observée pour le $CuInSe_2$/$(CuInSe_xS_{1-x})_5$/$CuInS_2$ QDs (courbe bleue) après 2 h d'illumination. L'amélioration notable est attribuée à la protection de la coque et à l'interaction interfaciale. En fait, en augmentant les quantités de charges qui fuient des QD, la photo-oxydation peut être encore retardée.

Pour confirmer davantage que les performances améliorées observées sont dues à un meilleur mécanisme de transfert de charge dans la structure noyau / coque à gradient, les caractéristiques de transfert de charge des photoélectrodes ont été étudiées à l'aide de l'EIS. La figure R6d affiche les tracés de Nyquist des QD noyau, noyau/coque et noyau/coquille à gradient déposés sur des photoanodes TiO_2 similaires. Dans ce cas, l'objectif principal de l'analyse est le diamètre du demi-cercle à fréquence moyenne (demi-cercle le plus à droite) car il est en corrélation avec la résistance de transfert de charge. En particulier, un rayon plus petit du demi-cercle signifie un RCT inférieur indiquant un transfert de charge amélioré. Comme le montre la figure R6d, le RCT suit la tendance inverse du photocourant, avec des valeurs de 8,8 kΩ, 5,7 kΩ, 2,53 kΩ et 0,87 kΩ pour TiO_2/ZnS, TiO_2/[$CuInSe_2$ QDs]/ZnS, TiO_2/[$CuInSe_2$/($CuInS_2)_6$ QDs]/ZnS et TiO_2/[$CuInSe_2$/$(CuInSe_xS_{1-x})_5$/$CuInS_2$ QDs]/ZnS, respectivement. Comme les photoanodes sont construites de manière similaire avec les mêmes matériaux, le transfert de charge amélioré peut être attribué à la meilleure séparation de charge dans la structure à gradient, confirmant que la recombinaison des paires électron/trou est réduite dans ce type d'architecture.

La meilleure performance PEC des QD à gradient peut être attribuée à plusieurs effets synergiques : (i) la flexion de bande appropriée accélère le transfert d'électrons des QD vers TiO_2, supprimant la recombinaison électron-trou. (ii) avec la formation d'une couche graduée, le transfert d'électrons est relativement élevé par rapport aux QD cœur-coquille basés sur l'analyse dynamique. (iii) La couche protectrice de ZnS inhibe efficacement la photo-corrosion des QD.

Nanocomposite 0D/2D/2D à base de $CuInS_2$ dopé au Zn vert et MoS_2/graphène réduit comme photoélectrodes pour la production d'hydrogène solaire

Un hybride 0D/2D/2D a été synthétisé par auto-assemblage électrostatique sous l'assistance d'ultrasons et d'agitation de QD $CuInS_2$ dopés au Zn 0D et de NS MoS_2/rGO 2D/2D. Une série d'approches de caractérisation ont été utilisées pour étudier la morphologie et la microstructure des composites d'hétérostructure 0D/2D/2D préparés afin de confirmer la préparation réussie de l'hétérostructure 0D/2D/2D. Comme le montre l'image TEM (Figure R7a) de GO, le GO tel que préparé présente une structure froissée semblable à du papier. Au lieu de cela, le MoS_2 pur forme des agrégats denses en raison de l'interaction de Van der Waals, présentant une forme irrégulière avec une taille moyenne d'agrégat de plus de 2 µm (Figure R7b). Cependant, lorsque GO est introduit (et réduit en rGO) dans le processus de synthèse de MoS_2, l'hétérostructure 2D/2D obtenue, MG, présente une morphologie régulière de nano-fleurs d'une taille moyenne de 450 nm, constituée d'une structure hiérarchique de 2D NS en forme de pétale (Figure R7). La raison de la différence de structure entre le MoS_2 pur et le composite MG est due au fait que lors du processus de synthèse du composite MG, le MoS_2 est réduit in situ à la surface des couches de graphène réduit, ainsi le réempilement des couches de MoS_2 est inhibé.[199] De plus, les images TEM (Figure R7 c) et HRTEM (Figure R7d) de MG montrent des ondulations et des rides, suggérant la structure ultrafine des SN hiérarchiques. En particulier, l'apparition de petits NS avec des arêtes vives indique un degré élevé de cristallinité. Le HRTEM des MG NS ressemblant à des pétales 2D préparés présente une distance intercouche de 0.62 nm, qui peut être attribuée au plan cristallin (002) de MoS_2 (Figure R7d). La figure R7e montre l'image TEM des QD ZCIS 0D obtenus. Les QD présentent une morphologie sphéroïde de base avec des tailles uniformes de (4.5 ± 0.6) nm. De plus, les images HRTEM (en médaillon sur la Figure R7e) révèlent un espace de réseau ~ 0.32 nm, qui peut être indexé sur le plan (112) de la chalcopyrite de CIS.

Grâce à la méthode d'auto-assemblage électrostatique, les QD ZCIS adhèrent à la surface MG. Cependant, au cours de ce processus, les QD avaient tendance à former des agrégats. Cela peut être dû à l'énergie de surface élevée générée par la présence d'un grand nombre d'atomes

chimiquement insaturés à la surface des QD.[209] La caractérisation TEM a été utilisée pour analyser la morphologie du nanocomposite 0D/2D/2D tel que produit. La figure R7f montre l'image TEM de l'hétérostructure 0D/2D/2D ZCIS/MG proposée, où les QD ZCIS (5 nm) étaient uniformément répartis sur la surface de la surface du film MG. L'image HRTEM (Figure R7g) obtenue à partir de la vue partiellement agrandie de la zone entourée de bleu (Figure R7f) montre l'assemblage 0D/2D/2D; les QD sont mis en évidence par des cercles superposés, tandis que le MG présente un réseau différent. L'image HRTEM de ZCIS QD montre des franges de réseau avec un espacement de 0.32 nm (Figure R7g), correspondant au plan de la chalcopyrite (112), tandis que l'image HRTEM des NS hiérarchiques 2D montre la nanostructure MG hexagonale attendue, avec un espacement de réseau de 0.62 nm , appartenant au plan (002) de MoS_2.

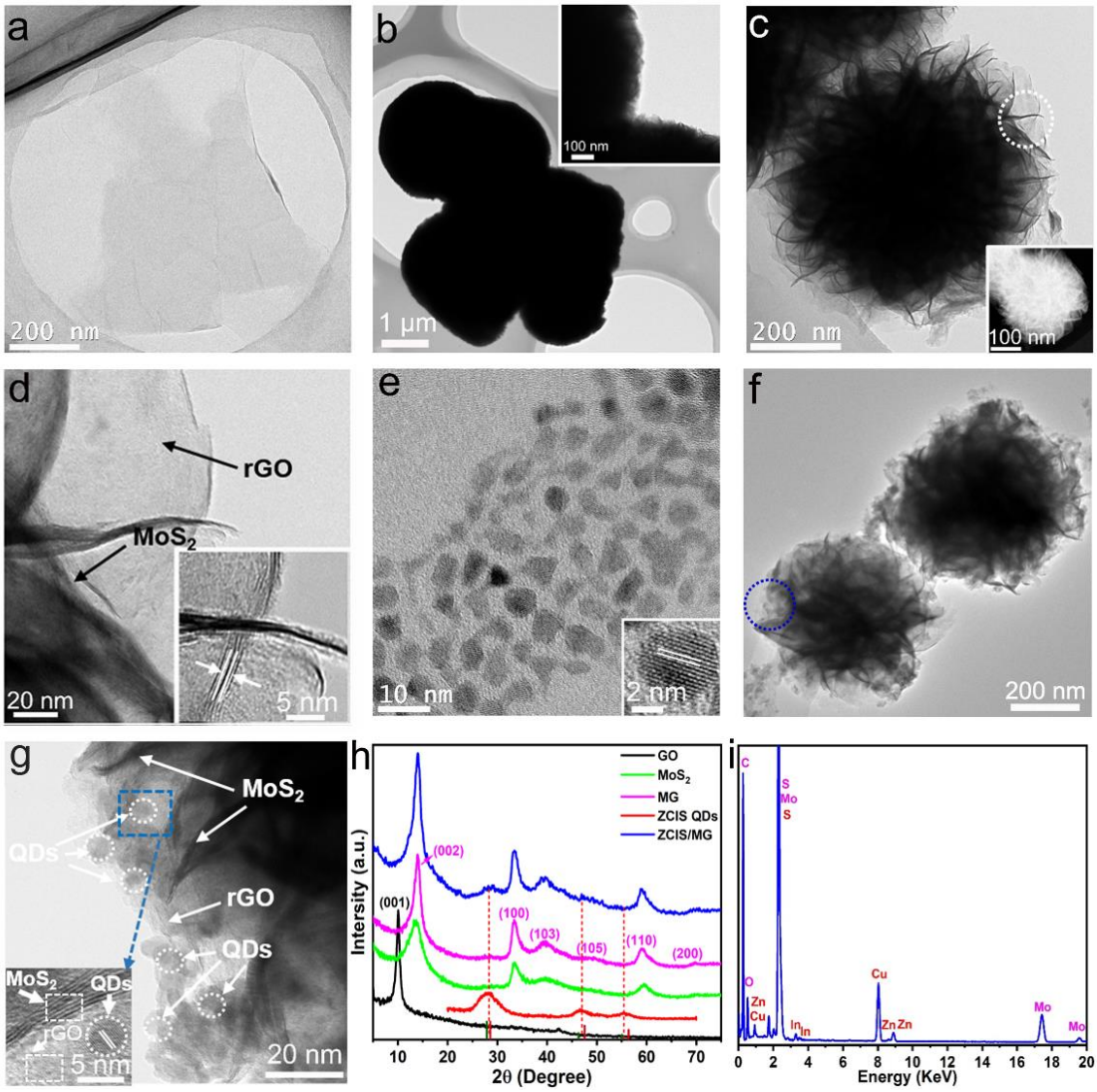

Figure R7. Caractérisations morphologiques des photocatalyseurs 0D/2D/2D proposés : image TEM de (a) GO, (b) MoS_2, (c-d) MG avec différents grossissements, (e) ZCIS QDs, (f-g) ZCIS QDs/MG hétéro-structure avec

différents grossissements ; L'encart dans (b) et (d) est l'image HRTEM de MoS_2 et MoS_2/rGO respectivement. Les encarts dans (e) et (g) sont des images HRTEM de QD ZCIS; (h) modèles XRD et (i) spectres EDX de 0D/ 2D/2D ZCIS/MG NS.

La caractérisation XRD a été utilisée pour étudier la structure cristalline et le processus de synthèse de l'hétérostructure 0D/2D/2D (Figure R7h). Comme le montrent les diagrammes MoS_2 XRD, les pics de diffraction situés à 13.9 °, 33.5 °, 39.8 ° et 59.5 ° peuvent être attribués aux plans (002), (100), (103) et (110), respectivement, qui peut être indexé sur la phase hexagonale MoS_2 (JCPDS NO. 37-1492). La réflexion (002) à 13.9° est indicative de la structure en couches de MoS_2.[210] Le pic de diffraction intense et net de l'oxyde de graphène à 10.0° correspondant au plan cristallin (001), disparaît dans le nanocomposite MG, révélant la réduction de GO au cours du processus hydrothermique. Cependant, il n'y a pas de pic évident correspondant à rGO apparaissant à 24°~30° en raison de la quantité relativement faible de rGO (moins de 5%) présente dans MG. Comme prévu, le spectre de MG/ZCIS est une combinaison de pics de diffraction MG et ZCIS. Dans ce cas, un chevauchement entre les plans de MG et ZCIS est présent. L'analyse par spectroscopie de rayons X à dispersion d'énergie (EDS) effectuée sur MG/ZCIS confirme la coexistence des éléments C, O, Mo, S, Cu, In et Zn (Figure R7i) (N.B. le signal Cu fort est dû à la grille Cu utilisé pour l'imagerie TEM).

L'hétérostructure 0D/2D/2D telle que synthétisée a été utilisée pour préparer la photo-anode en utilisant une approche d'auto-assemblage confiné dans l'espace. Des photoanodes sensibilisées avec différents QD et basées sur un nombre différent de couches de MG ont été étudiées dans un électrolyte (0.25 M $Na_2S{\cdot}9H2O$ et 0.35 M Na_2SO_3), en utilisant une configuration typique à trois électrodes dans des conditions d'obscurité et de lumière, y compris LSV, chronoampérométrie , et EIS. Afin d'obtenir les performances PEC optimales, nous avons optimisé l'épaisseur du film ZCIS/MG déposé sur le substrat FTO/TiO_2. Comme le montre la Figure R8, les photoanodes à trois couches présentaient la densité de photocourant la plus élevée. Pour un film formé avec plus de couches, les performances du photocourant ont diminué. L'augmentation de l'épaisseur du film MG au-delà d'une certaine valeur pourrait conduire à une augmentation de la résistance de transfert de charge de l'interface. Par conséquent, dans cette étude, trois couches de MG sont sélectionnées comme condition optimale pour le substrat.

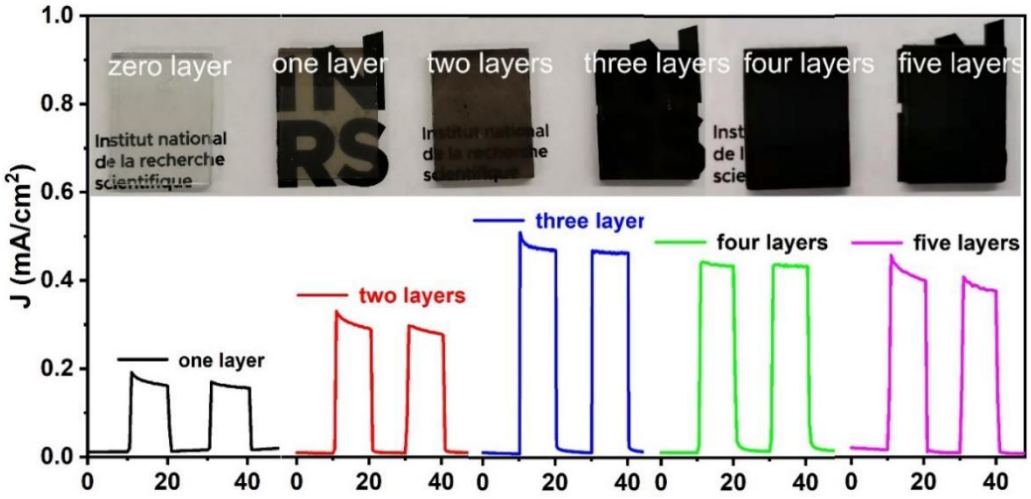

Figure R8 Les cycles i-t ampérométriques correspondants pour différentes couches. L'encart est les photographies de FTO/TiO_2 revêtues de différentes couches de MG-ZCIS, le FTO est de 1.5 cm * 2 cm.

Pour étudier l'effet des dopants au Zn sur l'alignement des bandes de l'hétérojonction proposée et son influence sur les performances du PEC, des échantillons représentatifs de MG/CIS purs, CIS/MG dopés au Zn (Zn:Cu = 1:2, 1:1 , 2:1, 3:1) ont été testés. Comme le montre la figure R9a, la densité de photocourant (Jph) dépend fortement du type de QD utilisé. Par rapport aux QD MG/$CuInS_2$ non dopés (Jph ≈ 0,09 mA cm^{-2} à 0.93 V vs RHE), tous les QD dopés au Zn présentent un photocourant plus élevé, indiquant une plus grande capacité à générer des porteurs de charge. Le photocourant le plus élevé est obtenu pour la photoanode sensibilisée avec un rapport Zn/Cu de 1:1, avec un photocourant saturé de 0.44 mA/cm_2 à 0.93 V (vs. RHE) qui est presque cinq fois plus élevé que les QD CIS purs. L'échantillon avec un rapport 1:2 de Zn/Cu, présente une densité de photocourant de 0.23 mA cm^{-2}, une valeur intermédiaire entre celle obtenue pour un dopage Zn 0:1 et 1:1. Au lieu de cela, les performances du PEC diminuent progressivement avec une plus grande quantité de dopage au Zn, avec des valeurs de photocourant égales à 0.3 et 0.18 mA cm^{-2}, pour des rapports Zn/Cu de 2:1 et 3:1, respectivement.

La figure R9b montre les caractéristiques j-t ampérométriques transitoires marche/arrêt de ces photoanodes, mesurées à 0.93 V par rapport à RHE (0 V par rapport à Ag/AgCl). Par rapport au courant d'obscurité (état OFF), pour tous les échantillons, le Jph est significativement augmenté sous un éclairage clair (état ON). L'augmentation instantanée du photocourant indique que les photoanodes peuvent efficacement générer et séparer des paires électron-trou et transférer des électrons vers la contre-électrode. En particulier, le Jph des photoanodes basées sur le sensibilisateur MG/ZCIS QDs montre une augmentation maximale de 400 % par rapport à la

photoanode sensibilisée MG/CIS QDs. L'ajout de Zn peut en fait moduler la densité de photocourant en modifiant la plage d'absorption de la lumière et la disposition des bandes d'énergie des QD.

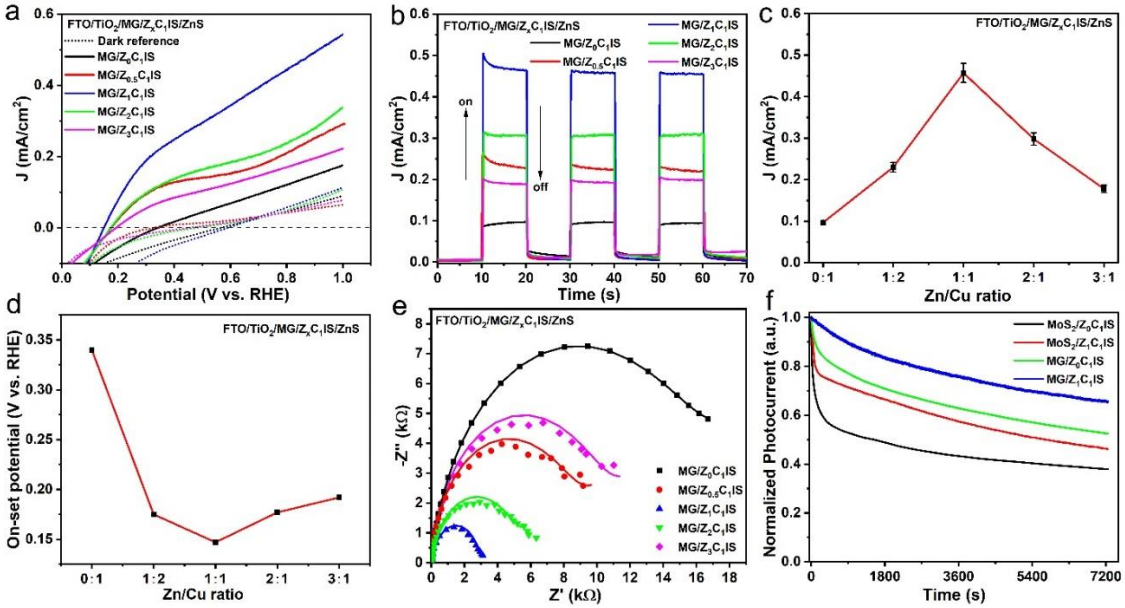

Figure R9 (a) courbes J-V et (b) cycles ampérométriques J-t de différentes quantités de photoanode sensibilisée QDs $CuInS_2$ dopée au Zn dans l'obscurité (courbe en pointillés) et sous éclairage continu (courbe pleine) (AM 1,5 G, 100 mW cm^{-2}); (c) Les tendances de la densité de photocourant et du potentiel d'apparition (d) des photo-anodes MG/Z_xC_1IS en fonction de différentes quantités de dopage au Zn. La ligne rouge est un guide pour les yeux; (e) Parcelles de Nyquist d'EIS et (f) photostabilité de photoanodes représentatives sous illumination à 0V vs Ag/AgCl. Les résultats d'ajustement sont tracés sous forme de traces solides dans EIS.

La tendance générale du photocourant par rapport à la quantité de Zn dopé est indiquée sur la figure R9c: 1:1 $CuInS_2$ dopé au Zn QD est la condition optimale qui produit le photocourant le plus élevé. De plus, le potentiel d'apparition se décale négativement par rapport aux QD purs MG/$CuInS_2$ (Figure R9d), indiquant que davantage d'électrons sont libérés et accumulés dans l'hétérostructure. peut également être attribuée au transport d'électrons plus rapide et à l'efficacité de séparation plus élevée des paires électron-trou photogénérées en raison de l'introduction de graphène.

EIS a été utilisé pour étudier le mécanisme de transfert de charge. Comme le montre la figure R9e, la photoanode basée sur les QD MG/ZCIS présente une résistance au transfert de charge plus faible par rapport aux autres matériaux composites, qui bénéficie de l'excellent alignement des bandes et de l'introduction de graphène pour la séparation des charges aux interfaces, confirmant que le porteur de charge la recombinaison est réduite dans l'architecture MG/ZCIS.

La stabilité des dispositifs PEC est également un aspect important des applications pratiques. Afin de comparer clairement le taux de décroissance du photocourant, la densité initiale du photocourant est normalisée à sa valeur maximale. Comme le montre la figure R9f, le Jph du dispositif MoS_2/CIS QDs chute rapidement, atteignant 38 % de sa valeur initiale après 2 h d'illumination. De même, la densité de photocourant des QD MoS_2/ZCIS (1:1) conserve 46 % de la valeur initiale. La légère augmentation de la stabilité pourrait être attribuée à la diminution des pièges à la surface des QD en raison du dopage au Zn. Au contraire, la densité de photocourant de MG/CIS et MG/ZCIS QD reste respectivement à environ 53 % et 66 % de la valeur initiale. Des travaux antérieurs ont montré que le graphène ainsi que d'autres allotropes de nanocarbone peuvent être utilisés avec succès pour améliorer les performances de plusieurs dispositifs optoélectroniques.[219] En particulier, l'introduction de graphène peut également améliorer de manière significative la stabilité à long terme des dispositifs photovoltaïques.[220] Globalement, la stabilité significative L'amélioration par rapport au PEC basé sur les QD MoS_2/ZCIS peut être attribuée à une excellente interaction interfaciale, à un alignement de bande approprié et à une recombinaison de charge réduite. En général, les dispositifs PEC à base de QD sont sensibles à la photooxydation due aux défauts de surface, qui agissent comme des pièges à charge. Les pièges et les défauts liés à la surface formeront des canaux de désexcitation non radiatifs rapides pour les porteurs de charge photo-générés, réduisant ainsi les performances globales. Par conséquent, une quantité appropriée de dopant peut optimiser l'interface et accélérer le transfert d'électrons, réduire la photooxydation des points quantiques et améliorer la stabilité globale. Simultanément, l'hybride graphène/MoS_2 2D peut également améliorer considérablement les performances du PEC et la stabilité à long terme grâce à la mobilité améliorée des porteurs. Dans l'ensemble, les performances supérieures de MG/ZCIS (1:1) peuvent être attribuées à l'effet synergique de : (i) un alignement de bande approprié entre MG et QD, accélérant l'injection de charge de QD à MG et inhibant la recombinaison électron-trou ; (ii) une épaisseur optimale du film mince, offrant une charge élevée de QD tout en gardant au minimum le chemin de déplacement des charges, réduisant la recombinaison des charges grâce à la présence de graphène. (iii) La couche protectrice de ZnS inhibe efficacement la photo-corrosion des QD.

Sur la base des données DRS et UPS, un mécanisme possible pour l'activité PEC des photoanodes MG/$ZnCuInS_2$ peut être proposé (Figure R10). Le diagramme schématique illustre la structure d'énergie de bande de l'hétérostructure MG/Z_xC_1IS et la séparation et le transport des porteurs de charge. Ces bandes correctement positionnées conviennent au transfert et à la séparation efficace des porteurs de charge, confirmant la capacité de MG/$ZnCuInS_2$ en tant que photocatalyseur convivial pour les dispositifs PEC. Lors de l'irradiation lumineuse, les électrons

photogénérés sont rapidement excités de la bande de cantonnière (VB) des QD ZCIS vers CB, laissant les trous derrière eux. Deux cas peuvent se présenter : si le CB des QD est plus négatif que le CB du MG, aucun transfert d'électron ne peut avoir lieu, et des phénomènes de recombinaison entrent en jeu. Inversement, si le CB du QD est plus positif que le CB du MG, les électrons du CB du QD peuvent être rapidement transférés au CB du MG adjacent. Dans ce dernier cas, la recombinaison des porteurs de charge est réduite et la réduction de H_2O en H_2 est favorisée. L'introduction du graphène favorise également efficacement le processus de transfert de charge. Ensuite, les électrons peuvent être transférés dans le CB de TiO2 et collectés par FTO. La couche de blocage supplémentaire en TiO_2 inhibe le rétrotransfert d'électrons du FTO vers l'électrolyte. De l'autre côté, les trous sont immédiatement capturés par le récupérateur de trous. Dans ce processus, le graphène joue principalement un rôle d'accepteur de charge pour inhiber la recombinaison des porteurs de charge et conduit à des performances PEC efficaces.

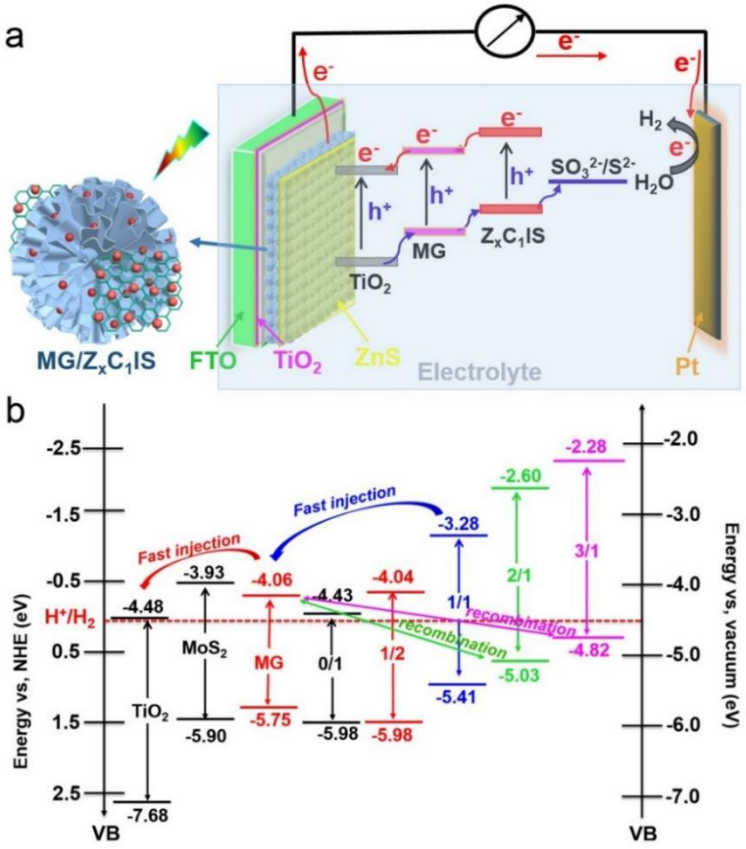

Figure R10 (a) Schémas de principe de formation de photocourant anodique ; (b) Position de l'énergie de la bande de MG et différentes quantités de ZxC1IS et mécanisme de transfert de charge.

La photoanode à base de MoS_2 sans graphène présente de moins bonnes performances en raison de la recombinaison rapide des porteurs de charge. De plus, il est possible d'observer

qu'avec l'augmentation du dopage au Zn, la position du CB des QD devient plus positive, passant de -4.43 eV à -2.28 eV. En particulier, en l'absence de dopage, le CB des QD est positionné en dessous du CB du MG, ainsi un mauvais transfert de charge peut se produire entre les deux matériaux. Au lieu de la valeur du dopage Zn de 1:1, 2:1 et 3:1, le CB des QDs est dans une position favorable pour un transfert de charge efficace entre QDs et MG. Au lieu de cela, pour le rapport 1:2 de Zn / Cu, nous supposons que la force motrice plus petite peut conduire à des performances PEC inférieures par rapport au rapport 1:1. D'autre part, les photoanodes avec des rapports 2:1 et 3:1 présentent un photocourant inférieur par rapport à l'échantillon de rapport 1:1, car les électrons sur le CB de MG se recombinent avec le trou sur le VB des QD ZCIS. Ainsi, en raison du niveau d'énergie de bande approprié, les capacités élevées de transfert de charge et de séparation de l'interface inhibent la recombinaison des porteurs de charge, ce qui explique la photoactivité améliorée et la réponse photocourant améliorée du composite MG/Z_1C_1IS.